Solvothermal Synthesis of Nickel-Based Metal-Organic Framework (Ni-MOF) and its Derivative for Advanced Symmetric Supercapacitor Applications

A Thesis

Submitted for the Degree of Doctor of Philosophy

Name	:	ZHENG SHENGQIANG
Student ID	:	20313371
School/Faculty	:	Faculty of Science and Engineering
Department	:	Mechanical, Materials and Manufacturing Engineering
Supervisors	:	Prof. Dr. Khiew Poi Sim Assoc. Prof. Dr. Lim Siew Shee

September 2023

Solvothermal Synthesis of Nickel-Based Metal-Organic Framework (Ni-MOF) and its Derivative for Advanced Symmetric Supercapacitor Applications

Thesis submitted to

The University of Nottingham Malaysia

in partial fulfillment of the requirement

for the degree of

Doctor of Philosophy

in

Mechanical, Materials and Manufacturing Engineering

by

ZHENG SHENGQIANG

Thesis Supervisors: Prof. Dr. Khiew Poi Sim

Assoc. Prof. Dr. Lim Siew Shee

September 2023

ABSTRACT

Nanomaterials have successfully attracted enormous interest in energy storage systems, such as batteries and supercapacitors (SCs), by virtue of the enhanced electronic and ionic conductivity as compared to traditional electrochemical energy storage materials. Meanwhile, small-sized materials are favorable for improving electrolyte ion diffusion and specific capacity due to the possibility of occupying all available sites in the particle volume. Among a wide range of electrode materials, high-crystalline conductive materials (such as nickel-based metal-organic frameworks (Ni-MOFs)), have been utilized as promising electrode active materials for SCs on the strength of their high porosities, ultra-large specific surface areas and structural tunability. More significantly, these materials are not only able to be utilized as electrode active materials, but also function as precursors to synthesize transition metal oxides and carbonaceous nanomaterials for energy storage systems. Nevertheless, there are still some challenges associated in the application of Ni-MOFs in high-performance SCs, such as inferior electrical conductivity, low energy density and durability. Hence, tremendous efforts have been made to study novel MOF-based nanostructures with enhanced electrochemical performance for their widespread implementation.

In this study, the impact of processing parameters, including synthesis temperature and time, on morphological and electrochemical properties of Ni-MOF nanostructures have been extensively studied. The results annotated that the average size of Ni-MOF nanosheets trended to decrease with increasing reaction temperature, whereas the crystallinity of these nanostructures was shown to have a direct correlation with solvothermal temperature. The symmetric supercapacitor device fabricated from nanostructures synthesized at 160°C exhibited an excellent energy density of 22.44 Wh kg^{-1} and a superior cyclic durability of 118% over 10,000 cycles. Moreover, the effect of different solvent systems on the morphologies and electrochemical properties of Ni-MOFs, which were synthesized via a solvothermal approach, were systematically investigated as well. It was found that binary solvents (Ethylene glycol + DMF) with high polarity and viscosity were favorable for the formation of microspheres, resulting from the self-assembly of ultrathin 2D nanosheets. Besides, the successful incorporation of highly conductive graphene nanosheets with Ni-MOF nanostructures could further enhance electrochemical performance, and a higher specific capacitance of 420.4 F g^{-1} was obtained in 2M KOH electrolyte. To further improve electrochemical performance of Ni-MOF-based SCs, 2D layered molybdenum disulphide (MoS_2) with large surface area and flexibility in the atomic scale dimension, was incorporated onto porous Ni-MOFs via a facile hydrothermal method. Meanwhile, sodium ions were introduced to further improve electronic conductivity and overall electrochemical performance. The results indicated that the as-synthesized porous nanocomposites delivered an excellent supercapacitive performance, in which the delivered maximum energy density was 33.33 Wh kg^{-1}, and the delivered capacitance retention and coulombic efficiency were more than 97% after 10,000 cycles. Additionally, highly porous nanostructured NiO/C yolk-shell nanocomposites via a simple calcination of Ni-MOFs. The porosity and electrochemical property were further enhanced by incorporating Na^+ and hierarchical MoS_2 nanostructures via a facile hydrothermal method. The delivered electrochemical capacitance of NiO/C yolk-shell structure was 1779.50 F g^{-1} in 2M KOH, and a superior specific capacitance of 2540.63 F g^{-1} was acquired after the incorporation of Na^+ and 2D layered MoS_2 onto the nanocomposite. When a symmetric supercapacitor was fabricated, a remarkable energy

density of 36.93 Wh kg^{-1} was recorded in an environmental-friendly aqueous-based electrolyte. More significantly, the outstanding delivered capacitance retention and coulombic efficiency were recorded at 111.92% and 97.6%, respectively after 4,000 continuous GCD cycles.

ACKNOWLEDGEMENTS

I would like to first extend my gratitude to my supervisors, Prof. Dr. Khiew Poi Sim and Assoc. Prof. Dr. Lim Siew Shee. They have provided me with a lot of guiding opinions and invaluable recommendations on my dissertation, carefully helped me to overcome the difficulties and remove the doubts I encountered in the process of writing the dissertation. Undoubtedly, these informative suggestions were beneficial to further improve my project design as well as writing. Meanwhile, Prof. Khiew is a responsible and enthusiastic person and he paid more attention to my work with great enthusiasm. I would like to thank him for his valuable advice and support throughout my work.

Moreover, I would also like to acknowledge the financial supports by the FRGS Grants (FRGS/1/2019/STG02/UNIM/01/1 and FRGS/1/2023/STG07/UNIM/01/1) from Ministry of Higher Education Malaysia and Research Grant (SU/FOSE/PG2020/37) from Faculty of Science and Engineering, the University of Nottingham Malaysia.

I sincerely appreciated the endless support, concern and great encouragement from my family. I could never have achieved such success without your kind support and patience. I love you so much and cannot express how much I appreciate all of you.

I greatly appreciated the technique support from University of Nottingham Malaysia, thanks for all the hard work you put in. And I'd like to thank all my friends and colleagues who have given me support and trust for your selfless support and help.

Finally, I would like to express my heartfelt appreciation to all the experts and scholars who reviewed my thesis and participated in the defense meeting. Thank you for your precious time and the valuable opinions on the improper aspects of my thesis. At the meantime, I would also like to thank all the authors in the references. Through your articles, I have a good starting point and a deeper understanding on my research topic.

RESEARCH PUBLICATIONS

[1] S.Q. Zheng, S.S. Lim, C.Y. Foo, C.Y. Haw, W.S. Chiu, C.H. Chia, P.S. Khiew, Recent Progress on the Applications of Carbonaceous and Metal-Organic Frameworks Nanomaterials for Supercapacitors, Frontiers in Materials (2021) 500.

[2] S.Q. Zheng, S.S. Lim, C.Y. Foo, C.Y. Haw, W.S. Chiu, C.H. Chia, P.S. Khiew, Solvothermal synthesis of nanostructured nickel-based metal–organic frameworks (Ni-MOFs) with enhanced electrochemical performance for symmetric supercapacitors, Journal of Materials Science 58 (2023) 11894 -11913.

[3] S. Qiang Zheng, S. Shee Lim, C. Yi Foo, C. Yian Haw, W. Siong Chiu, C. Hua Chia, P. Sim Khiew, Probing the Effect of Solvents on the Electrochemical Performance of Graphene Incorporated Nickel-Based Metal Organic Frameworks, Journal of Electroanalytical Chemistry (2022) 116860.

[4] S.Q. Zheng, S.S. Lim, C.Y. Foo, C.Y. Haw, W.S. Chiu, C.H. Chia, P.S. Khiew, Fabrication of sodium and MoS_2 incorporated NiO and carbon nanostructures for advanced supercapacitor application, Journal of Energy Storage 63 (2023) 106980.

[5] S.Q. Zheng, S.S. Lim, C.Y. Foo, C.Y. Haw, W.S. Chiu, C.H. Chia, P.S. Khiew, A novel MOF-derived binary metal oxides and carbon nanocomposite for high-performance symmetric supercapacitor application, Journal of Materials Science: Materials in Electronics 34 (2023) 1578.

[6] S.Q. Zheng, S.S. Lim, C.Y. Foo, C.Y. Haw, W.S. Chiu, C.H. Chia, P.S. Khiew, Facile Synthesis of Nanostructured MoS_2 Incorporated Ni-MOFs With Excellent Cyclic Durability for Symmetric Supercapacitor Application, Next Nanotechnology 5 (2024) 100031.

[7] S.Q. Zheng, S.S. Lim, C.Y. M.S.L. Yee, Foo, C.Y. Haw, W.S. Chiu, C.H. Chia, P.S. Khiew, Fundamentals and Advances of Nanostructured Transition Metal Oxides (TMOs) and Their Composites for High-Performance Supercapacitors, Handbook of Energy Materials in Supercapacitors and Storage Devices (Editors: Sarathchandran C, S a Ilangovan, P M Shankar, Sabu Thomas, Accepted).

TABLE OF CONTENT

ABSTRACT i

ACKNOWLEDGEMENT iii

RESEARCH PUBLICATIONS iv

TABLE OF CONTENTS v

LIST OF TABLES ix

LIST OF FIGURES xi

LIST OF SYMBOLS xvii

LIST OF ABBREVATIONS xviii

Chapter 1: Introduction 1

1.1 Background 1

1.2 Scopes and Aims 5

1.2.1 Problem Statement 5

1.2.2 Research Questions/Hypothesis 6

1.2.3 Scope of Study 6

1.2.4 Objectives 7

1.2.5 Thesis Overview 7

1.2.6 Thesis Highlight 9

Chapter 2: Recent Progress on the Synthesis and Application of MOF-Based Nanostructures 10
2.1 Synthesis Strategies of MOFs 10
2.1.1 Solvent Volatilization 11
2.1.2 Hydro/Solvothermal Method 11
2.1.3 Microwave-assisted Approach 13
2.1.4 Sealing Pathway 14
2.1.5 Electrochemical & Mechanical Synthesis 16
2.1.6 Reactor Method 18
2.2 Effect of Critical Parameters on the Performance of MOFs 20
2.2.1 The Impact of Metal Ions and Organic Linkers 20
2.2.1.1 Metal ions 21
2.2.1.2 Organic ligands 23
2.2.2 The Molar Ratio Between Metal Ions and Organic Linkers 25
2.2.3 Template Reagent and Solvent 27
2.2.4 Temperature 32
2.2.5 pH 34
2.3 The Application of MOF Materials in SCs 38
2.3.1 The Electrochemical Performance of Pristine MOFs 38
2.3.1.1 Zr-based MOFs 38
2.3.1.2 Iron-based MOFs and the related nanocomposites 39
2.3.1.3 Cu-based MOFs 40
2.3.1.4 Mn-based MOFs 41
2.3.1.5 Zn-based MOFs 45
2.3.1.6 Co-based MOFs 46
2.3.1.7 Ni-based MOFs 47
2.3.2 Derivations of MOFs for SCs 54
2.3.2.1 Bimetallic and ternary MO nanoporous materials 54

2.3.2.2 MOF-derived carbon nanoporous composites 57
2.4 Summary 63
Chapter 3: Chemicals and Characterization 65
3.1 Chemicals 65
3.2 Synthesis of Graphene Nanosheets 65
3.3 Material Characterizations 65
3.3.1 X-ray Powder Diffraction (XRD) 66
3.3.2 X-ray Photoelectron Spectroscopy (XPS) 66
3.3.3 Fourier Transform Infrared Spectroscopy 67
3.3.4 Field Emission Scanning Electron Microscopy (FESEM)/Transmission Electron Microscopy (TEM) 67
3.3.5 Thermogravimetry Analysis (TGA) 68
3.4 Electrochemical Measurement 68
3.4.1 Cyclic Voltammetry (CV) 69
3.4.2 Electrochemical Impedance Spectroscopy (EIS) 69
3.4.3 Galvanostatic Charge and Discharge 70
Chapter 4: Solvothermal Synthesis of Nanostructured Nickel-based Metal-Organic Frameworks (Ni-MOFs) With Enhanced Electrochemical Performance for Symmetric Supercapacitors 71
4.1 Introduction 71
4.1.1 Synthesis of Ni-MOF Nanomaterials 72
4.2 Results and Discussion 72
4.2.1 Material Characterizations 72
4.2.2 The Impact of Reaction Temperature 83
4.2.3 Electrochemical Analysis 85
4.2.3.1 Cyclic voltammetry (CV) 85
4.2.3.2 Galvanostatic charge-discharge (GCD) 89
4.2.3.3 Cyclic stability 93
4.2.3.4 Electrochemical impedance spectroscopy (EIS) 94

4.3 Summary 95
Chapter 5: Probing the Effect of Solvents on the Electrochemical Performance of Graphene Incorporated Nickel-Based Metal-Organic Frameworks 96
5.1 Introduction 96
5.2 Experimental 96
5.2.1 Synthesis of Ni-MOF Nanomaterials 96
5.2.2 Synthesis of Ni-MOF/Graphene Nanocomposites (FG_Gr$_y$) 97
5.3 Results and Discussion 98
5.3.1 Material Characterization 98
5.3.2 The Impact of Solvents 105
5.3.3 Electrochemical Analysis 106
5.3.3.1 Cyclic voltammetry 106
5.3.3.2 Galvanostatic charge/discharge 112
5.3.3.3 Electrochemical impedance spectroscopy 113
5.3.3.4 Cyclic stability 114
5.4 Summary 116
Chapter 6: Facile Synthesis of Nanostructured MoS_2 Incorporated Ni-MOFs With Excellent Cyclic Durability for Symmetric Supercapacitor Application 117
6.1 Introduction 117
6.1.1 Synthesis of Ni-MOF Nanosheets 118
6.1.2 Synthesis of Na^+-doped MoS_2@Ni-MOFs Nanocomposites 118
6.2 Results and Discussion 118
6.2.1 Material Characterization 118
6.2.2 Electrochemical Performance of Nanocomposites 127
6.2.3 Sodium Storage Mechanism 136
6.3 Summary 139
Chapter 7: Fabrication of Sodium and MoS_2 Incorporated NiO and Carbon Nanostructures for Advanced Supercapacitor Application 140
7.1 Introduction 140
7.1.1 Synthesis of Ni-MOF-derived NiO/C 141

7.1.2 Synthesis of Na-doped MoS_2@NiO/C 141
7.2 Results and Discussion 142
7.2.1 Material Characterization 142
7.2.2 Electrochemical Analysis 151
7.3 Summary 161
Chapter 8: Conclusion and Future Perspectives 162
8.1 Conclusion 162
8.2 Future Perspectives 164
References 165

LIST OF TABLES

2.1 The specific capacitance of various MOFs-derived carbon at different current densities 23

2.2 The physical characteristics of as-developed MILs at different molar ratios..... 26

2.3 The physical and electrochemical properties (over a current density of 1 A g^{-1}) of Ni-MOFs made at different molar ratio of metal to ligand 26

2.4 The physical and chemical properties of Cu-MOFs developed at various concentration of auxiliary template reagent 28

2.5 The textural and electrochemical properties of Co-based MOFs prepared under various solvent conditions 30

2.6 The textural properties of the samples synthesized at different pH..... 37

2.7 Summary of the electrochemical performance of pristine MOFs materials utilized as SCs electrode materials 51

2.8 Summary of the electrochemical performance of bimetallic oxides derived from MOF materials utilized as SCs electrode materials 61

2.9 Summary of the electrochemical performance of MOF-derived carbon materials utilized as SCs electrode materials 62

4.1 EIS parameters for Ni-MOFs synthesized at 160°C for 8, 16, 24 and 32 h after 1 and 10,000 cycles..... 95

5.1 Chemical properties of solvents used, average width and yield of synthesized Ni-MOFs 105

5.2 Solution and charge transfer resistance of Ni-MOFs synthesized in different solvents 114

6.1 Comparison of electrochemical performance of various carbon- and MOF-based electrode for supercapacitor applications 134

6.2 The electrochemical impedance of MoS_2-incorporated nanocomposites..... 135

7.1 The electrochemical performance of NiO-based SC electrode active materials 153

7.2 EIS data of Na-doped MoS_2@NiO/C nanocomposites in 2M Na_2SO_4 aqueous electrolyte 160

8.1 Electrochemical performance of MOF-based nanostructures used in SCs 163

LIST OF FIGURES

1.1 A schematic showing a structure supercapacitor containing cell cases, current collectors, active materials, separator and electrolyte 1
1.2 The characteristics of conventional supercapacitors (SCs) like electrical double-layer capacitors (EDLCs), pseudocapacitors and hybrid capacitors (HCs) 2
1.3 The number of publications per year from Web of Science: the applications of MOFs and Supercapacitors 3

2.1 The overview of various synthesis methods of MOFs 10
2.2 The pH-modulated synthesis of MOF-5 with conditions 13
2.3 The XRD patterns of γ-CD-MOFs synthesized via microwave method at different time comparing with simulated one 14
2.4 (a) Anodic dissolution of nickel foam for the synthesis $Ni_3(BTC)_2$ MOFs via electrochemical approach and (b) $Fe(NO_3)_3 \cdot 9H_2O$ and H_3BTC as precursor for the synthesis of isostructural MIL-100(Fe) through liquid-assisted mechanochemical synthesis 16
2.5 (a) The synthesis of ZIF-8 via continuous-flow hydrothermal system (CFHS). (b) The synthesis of MOF-5 through continuous-stirred tank reactor (CSTR) and (c) A microfluidic system (MFS) producing dicarboxylate based MIL-88B within 20 seconds 19
2.6 The SEM images of microcrystals of Co-MOF (a1-a3) and Mn-MOF (b1-b3) that were developed over various conditions. a1, b1 methanol-water; a2, b2 ethanol-water; a3, b3 n-propanol 22
2.7 The SEM images of (a) ZIF-8 and (b) ZIF-67 with disparate morphologies due to the utilization of Co^{2+} and Zn^{2+} metal ions, respectively 23
2.8 The FESEM images of Ni-MOFs under different organic ligand ratios: PTA : BTC= (a, b) 10 : 0, (c, d) 9 : 1, (e, f) 8 : 2 and (g, h) 7 : 3 25
2.9 The XRD patterns of HP-Cu-BTC_A, HP-Cu-BTC_B. HP-Cu-BTC_C, HP-Cu-BTC_D and C-Cu-BTC, which indicates the structure of Cu-MOFs are not influenced by the template concentration 28
2.10 The SEM images of Co-based MOFs prepared over different solvent mixtures: (a, b) DMF, (c, d) mixture of DMF and ethanol, (e, f) mixture of DMF and water, (g, h) ethanol and mixture of DMF, (i, j) ethanol and water 29
2.11 TGA of ZIF-8 synthesized in various solvents. (a) Mixing method, (b) solvothermal method and (c) sonochemical method 30
2.12 Reaction scheme of (a) the synthesis of ZIF-8 in water, deprotonation of Hmim in (b) methanol and (c) DMF 31

2.13 The SEM images of Co-MOF-74 with different morphologies synthesized at (a) 100 ℃, (b) 120 ℃, (c) 135 ℃ and (d) 150 ℃. Inset: the cross section of Co-MOF-74 33
2.14 The OG degradation curves by different MIL-53(Fe), developed under different synthesis temperature conditions utilized in activated persulfate systems..... 34
2.15 Zn-MOFs synthesized under various pH conditions, in which the ionic components in the solvent with corresponding pH values are labeled. This illustrates that the synthesis environment with different pH values has crucial effect on the morphologies of resulting MOFs..... 35
2.16 The SEM images of zinc-based samples obtained at (a1, a2) pH 4.1, (b1, b2) pH 6.5, (c1, c2) pH 7.6 and (d1, d2) pH 10.3, respectively 36
2.17 The SEM images of MIL-110 (pH 2.1), MIL-100 (pH 2.2 and pH 2.4) the mixtures of MIL-96 and MIL-100 (pH 2.7) 37
2.18 Schematic illustration of the synthesis of UiO-66..... 39
2.19 (a) The galvanostatic charge-discharge curves at various current densities. (b) Cu-LCP at 1 M LiOH and (c) $((Cu_2Cl(OH)(L)_2) \cdot (CH_3OH)_4)_n$ at 6 M KOH. It demonstrates the high stability of Cu-MOF materials as SC electrode materials in different alkaline-based environment..... 41
2.20 The specific capacitance of Mn-LMOF at a current density of 2 A g^{-1} in 1 M KOH and 1 M LiOH, respectively 42
2.21 (a) The CV diagrams of Mn-MOF with a potential window of 1.5 V over various scan rates. (b) Charging and discharging performance of Mn-MOF electrode under different current densities. (c) The impedance diagram before and after cycling and (d) Plot of capacity retention versus cycle number for Mn-MOF electrode over 5000 cycles (inset) and Mn-MOF//rGO HC over 10,000 cycles (blue line), the corresponding efficiencies are 92.3% and 81.18% for Mn-MOF electrode and HC, respectively. It clearly illustrates that Mn-MOF possesses superior cycle life 44
2.22 (a) The schematic illustration of synthesis $Ni_3(HITP)_2$ and the EPD process towards $Ni_3(HITP)_2$ SC electrodes, the SEM images of $Ni_3(HITP)_2$ film which is formed through EPD on Ni foam (10 um) in (b) before cycling and (c) after 100,000 cycles. (d) the CVs after different cycles at a scan rate of 600 mV s^{-1}. (e) Nyquist plot and (f) Cycling stability until 100,000 cycles at 1 mA cm^{-2} of $Ni_3(HITP)_2$..... 49
2.23 Schematic diagram showing the process to develop ZnCoO-G..... 55
2.24 A schematic illustration of the synthesis process of $ZnO/ZnCo_2O_4/NiO$..... 55
2.25 A schematic diagram showing the fabrication process of $ZnCo_2O_4$ and NPC via "all in one" strategy..... 56
2.26 Schematic diagram illustrating (a) the synthesis process of NPC and (b) the SC construction made of MOF-derived NPC..... 58
2.27 A schematic illustration of the fabrication of sandwiched-like MOFs via in-situ growth and the WNPC..... 59
2.28 (a) The Nyquist plot of the 1st cycle and last cycle. (b) The cyclic stability over 10,000 cycles in 1 M KOH..... 60

2.29 A schematic diagram showing the synthesis of (a) ZnO nanorods, (b) ZnO@ZIF-8 via ion exchange, (c) ZnO@C@ZIF-8 via in situ ethanol decomposition and (d) N-doped carbon bubbles on carbon tubes via reduction-evaporation 60

3.1 Schematic illustration for the synthesis of graphene via solvent exfoliation method 65

4.1 The XRD patterns (a, b) and FT-IR spectra (c, d) of Ni-MOFs synthesized at different solvothermal temperatures and times 73
4.2 FESEM images for Ni-MOF nanomaterials synthesized at different solvothermal temperatures of (a, b)120 ℃, (c, d) 140 ℃, (e, f) 180 ℃ and (g, h) 200 ℃..... 75
4.3 FESEM images for Ni-MOFs synthesized at 160 ℃ for (a, b) 8h, (c, d) 16h, (e, f) 24h and (g, h) 32h..... 76
4.4 N_2 adsorption and desorption isotherms and pore size distribution (inset) of FG_{16032} 77
4.5 Elemental mapping and EDX images for Ni-MOF nanomaterials synthesized at different solvothermal temperatures of (a)120 ℃, (b) 140 ℃, (c) 180 ℃ and (d) 200 ℃ 78
4.6 Elemental mapping and EDX images for Ni-MOFs synthesized at 160 ℃ for (a) 8h, (b) 16h, (c) 24h and (d) 32h 79
4.7 (a) TEM images of FG_{16032} nanomaterials, the corresponding (b) FFT pattern and (c) lattice spacing. (d, e) SAED patterns 80
4.8 Thermogravimetric analysis for Ni-MOF nanomaterials synthesized at different solvothermal temperatures (a) and times (b) 81
4.9 Derivative thermogravimetric curves for Ni-MOF nanomaterials synthesized at different temperatures..... 81
4.10 EDX and elemental mapping images for Ni-MOFs synthesized with a molar ratio between Ni^{2+} and H_2BDC of (a, b) 2 : 1 and (c, d) 3 :1..... 82
4.11 EDX and elemental mapping images for Ni-MOFs synthesized with a molar ratio between Ni^{2+} and H_2BDC of (a, b) 4 : 1 and (c, d) 5 :1..... 83
4.12 Solubility of *p*-benzenedicarboxylic acid in DMF solution (a) and the classic Lamer nucleation and growth model (b) 85
4.13 Optimization of potential window of Ni-MOF SC electrode in 2M NaCl. (a) Cyclic voltammetry for Ni-MOF nanomaterials synthesized at different reaction temperatures (b) and times (c) 86
4.14 The (a) CV, (b) GCD profiles and (c) specific capacitance calculated from GCDs of FG_{16032} nanomaterials in 2M KOH electrolyte 86
4.15 Cyclic voltammetry profiles for Ni-MOFs synthesized at 160 ℃ for 8 (a), 16 (b), 24 (c) and 32 hours (d) with different scan rates ranging from 50 to 500 mV s^{-1} 87
4.16 The relationship between peak current and scan rate (a) square root of scan rate (b). The power-law relationship of Ni-MOFs obtained at 160 ℃ for different times (c) and FG_{16032} at different potentials (d) 88
4.17 Capacitive and diffusion-limited capacitance contribution at 50 mV s^{-1} for (a) FG_{16008}, (b) FG_{16016}, (c) FG_{16024} and (d) FG_{16032}, respectively and the proportion of EDLC and diffusion-limited capacitance contribution at different scan rates for Ni-MOFs synthesized at different hydrothermal times: (e) FG_{16008}, (f) FG_{16016}, (g) FG_{16024} and (h) FG_{16032} 89

4.18 The GCD profiles of Ni-MOFs synthesized at various solvothermal temperatures (a) and times (b). Cycling performance of FG_{16032} at a current density of 1.5 A g^{-1} (c) and Nyquist plots before and after cyclic measurement (d) with fitting data (inset). Nyquist plots of electrode active materials synthesized at different solvothermal temperatures (e) and times (f) 91
4.19 Galvanostatic charge/discharge profiles of Ni-MOFs synthesized at different solvothermal times (a, 8h; b, 16h; c, 24h and d, 32h) with different current densities ranging from 0.3 to 3.0 A g^{-1} 92
4.20 Rate performance of Ni-MOFs synthesized at different solvothermal temperatures (a) and times (b) 93

5.1 Schematic illustration of the fabrication for (i) hierarchical Ni-MOFs and views of the layered structure along different axis, (ii) graphene-incorporated Ni-MOFs via a solvothermal method 97
5.2 (a, b) XRD patterns and (c, d) FT-IR spectra of the as-synthesized Ni-MOF and FG_Gr_y nanomaterials 99
5.3 (a) XRD pattern and (b) FT-IR spectra of graphene nanosheets 100
5.4 TG/DTG curves for (a) the as-synthesized Ni-MOF and (b)FG_Gr_y nanocomposites 100
5.5 FESEM images and EDX of Ni-MOFs synthesized in different solvent systems: (a-c) ethanol, (d-f) DMF, (g-i) DMF + D.I. water, (j-l) DMF + ethanol and (m-o) DMF + EG 102
5.6 FESEM images and EDX of FG_Gr_y: (a-c) FG_$Gr_{0.25}$, (d-f) FG_$Gr_{0.5}$, (g-i) FG_$Gr_{0.75}$, (j-l) FG_$Gr_{1.0}$ and (m-o) FG_$Gr_{1.5}$ 103
5.7 (a) N_2 adsorption and desorption isotherms and (b) pore size distributions of FG and FG_$Gr_{1.0}$ samples 104
5.8 (a, b) TEM images and (c) elemental mapping of hierarchical FG_$Gr_{1.0}$ 104
5.9 (a) Cyclic voltammetry profiles at 50 mV s^{-1}, (c) Nyquist plots and (e) Galvanostatic charge/discharges profiles at a current density of 0.3 A g^{-1} of the as-developed Ni-MOFs in different solvent systems. (b) Cyclic voltammetry profiles at 50 mV s^{-1}, (d) Nyquist plots and (f) Galvanostatic charge/discharges profiles at 0.3 A g^{-1} of FG_Gr_y in 2M NaCl electrolyte 108
5.10 (a) Cyclic voltammetry profiles (50 mV s^{-1}), (b) Nyquist plots and (c) Galvanostatic charge/discharges profiles (0.3 A g^{-1}) of FG_$Gr_{1.0}$ in 2M NaCl and 2M KOH aqueous electrolyte, respectively 109
5.11 (a) Cyclic voltammograms at different scanning rates and (b) Galvanostatic charge/discharges profiles at different current densities of FG_$Gr_{1.0}$ in a three-electrode system using 2M KOH aqueous electrolytes 109
5.12 The electrochemical performance of FG_$Gr_{1.0}$ nanocomposites: (a) cyclic voltammograms at different scan rates, (b) CV profiles with different potential windows, (c) linear response of peak current density versus scan rate plot, (d) peak current density versus square root of scan rate at 1.0 V 111

5.13 (a) The plot of log(i_p) versus log(v) with linear fitting and (b) plot of I/ $v^{1/2}$ vs. $v^{1/2}$ at a potential of 1.0 V, (c) The capacitance contributions of EDLC and nondiffusion-controlled process, (d) GCD at different current densities for FG_$Gr_{1.0}$ electrode in both neutral and alkaline aqueous electrolytes 112
5.14 Cycling performance of FG_$Gr_{1.0}$ at 1.5 A g^{-1} in (a) 2M NaCl, (b) 2M KOH, and (c) the coulombic efficiency of FG_$Gr_{1.0}$ 115
5.15 Nyquist plots before and after cycling measurement with fitting data and equivalent circuits (inset) in (a) 2M NaCl, (b) 2M KOH 116

6.1 (a) XRD pattern and (b) FT-IR spectra of the as-synthesized nanocomposites 119
6.2 XRD patterns of pristine Ni-MOFs synthesized via a solvothermal method 120
6.3 The crystal structures of Ni-MOFs viewed along (a) a, (b) b and (c) c directions, respectively 120
6.4 TG/DTG curves of Na and MoS_2 incorporated Ni-MOF nanocomposites 121
6.5 FESEM images of (a, b) MNM_0, (c, d) MNM_1, (e, f) MNM_2 and (g, h) MNM_3 122
6.6 N_2 adsorption and desorption isotherms and pore size distribution (inset) of MNM_1 123
6.7 Elemental mapping of (a) MNM_0 and (b) MNM_1 124
6.8 Elemental mapping of (a) MNM_2 and (b) MNM_3 125
6.9 EDX and elemental composition of (a) MNM_0, (b) MNM_1, (c) MNM_2 and (d) MNM_3 126
6.10 (a, b) Low-resolution and (c, d) HRTEM images showing the lattice spacing of the MNM_1 sample 127
6.11 (a) CV profiles and (b) GCD curves of the prepared electrodes in 2M KOH electrolyte 128
6.12 Electrochemical properties of the as-prepared electrodes in a three-electrode system in 2M KOH electrolyte: (a, b) MNM_0, (c, d) MNM_1, (e, f) MNM_2 and MNM_3 129
6.13 (a) CV profiles, (b) GCD curves, (c) Nyquist plots and (d) the plot of resistance versus frequency 131
6.14 CV curves of the as-prepared electrodes in a two-electrode system at different scan rates: (a) MNM_0, (b) MNM_1, (c) MNM_2 and (d) MNM_3 132
6.15 GCD curves of the as-prepared electrodes in a two-electrode system at different scan rates: (a) MNM_0, (b) MNM_1, (c) MNM_2 and (d) MNM_3 133
6.16 (a) Cycling stability and (b) Nyquist plots before and after performing cyclic stability study with equivalent circuit and fitting (inset) of MNM_1 in 2M Na_2SO_4 electrolyte 136
6.17 The plot of current densities versus (a) scanning rates and (b) square root of scanning rates. The linear relationship between log(i) and log(v) at (c) positive and (d) negative potentials, respectively 137
6.18 (a) Capacitance contribution at 50 mV s^{-1} and (b) the proportion contribution of capacitive and diffusion-limited capacitances at various scan rates for MNM_1 139

7.1 A schematic illustration for the synthesis of Na-doped MoS_2@NiO/C nanocomposites 141
7.2 XRD patterns of (a) NiO/C nanocomposites derived from Ni-MOFs, (b) Na-doped MoS_2@NiO/C nanocomposites prepared at different molar ratio of Ni^{2+} to Mo^{4+}. FT-IR (c) and TG/DTG (d) curves of the as-synthesized Na-doped MoS_2@NiO/C nanocomposites 143
7.3 TG/DTG curves of MOF-derived NiO/C yolk-shell structures under air flow..... 144
7.4 FESEM and EDX images of (a-d) NiO/C yolk-shell derived from Ni-MOFs (MNC_0), (e-h) MNC_1 and (i-l) MNC_3 145
7.5 FESEM and EDX images (a-d), (e, f) lattice fringes and FFT results (inset), (g, h) TEM images and (i) corresponding elemental mapping of MNC_2 nanocomposites 146
7.6 N_2 adsorption and desorption isotherms and pore size distributions (inset) of MNC_2 147
7.7 Elemental mapping of MNC_0, MNC_1 and MNC_3, respectively 149
7.8 XPS spectra of MNC_2: (a) full scanning survey, narrow scan of (b) Ni 2p, (c) O 1s, (d) Mo 3d and (d) S 2p..... 150
7.9 Cyclic voltammograms at various scan rates (a-d) and galvanostatic charge/discharge curves (e-f) of Na-doped MoS_2@NiO/C nanocomposites on nickel foam at 2M KOH electrolyte 152
7.10 (a) CV profile of nickel foam at a scan rate of 5 mV s^{-1} and (b) the specific capacitance obtained for Na-doped MoS_2@NiO/C nanocomposites at various current densities in 2M KOH electrolyte..... 153
7.11 (a) CV profiles of Na-doped MoS_2@NiO/C nanocomposites at 50 mV s^{-1}. (b) Linear response between current densities and square root of scan rates, (c) calculation of b values at various potentials and (d) capacitance contributions at different scan rates of MNC_2 154
7.12 CV curves of (a) MNC_0, (b) MNC_1, (c) MNC_2 and (d) MNC_3 at different scan rates ranging from 50 to 500 mV s^{-1} in 2M Na_2SO_4 aqueous electrolyte 155
7.13 (a) Different potential windows at 50 mV s^{-1}, (b) plots of current density versus scan rate, and (c) plots of $iv^{-0.5}$ versus $v^{0.5}$ at both positive and negative 0.84 and 0.87 V for MNC_2 156
7.14 Schematic illustration of the sodium storage behavior in hierarchical porous Na-doped MoS_2@NiO/C nanocomposites 157
7.15 GCDs at different current densities (0.5 – 5.0 A g^{-1}) for (a) MNC_0, (b) MNC_1, (c) MNC_2 and (d) MNC_3 158
7.16 (a) GCD profiles at 0.5 A g^{-1}, (b) rate performance of Na-doped MoS_2@NiO/C nanomaterials and (c) Ragone plot of the as-fabricated symmetric SC devices and other references. (d) Cyclic performance, (e) Nyquist plot and (f) EIS spectra before and after cycling performance measurement of Na-doped MoS_2@NiO/C nanocomposites 159

LIST OF SYMBOLS

Symbol	Description	Unit
R_s	Equivalent Series Resistance	Ω
R_{ct}	Charge Transfer Resistance	Ω
C_{sp}	Specific Capacitance	F g^{-1}
C_t	Capacitance of Electrodes	F
C_E	Capacitance of Single Electrode	F
M	Mass	g
I	Current	A
Δt	Discharge Time	s
ΔV	Potential Difference	V
E	Specific Energy Density	Wh kg^{-1}
P	Specific Power Density	W kg^{-1}
η	Coulombic Efficiency	%
t_c	Charge Time	s
t_d	Discharge Time	s
C_s	Saturation Concentration	mol L^{-1}
C_{ss}	Supersaturation Concentration	mol L^{-1}
τ	Time Constant	s
f	Frequency	Hz
v	Scan Rate	V s^{-1}

LIST OF ABBREVIATIONS

1D	One-Dimensional
2D	Two-Dimensional
3D	Three-Dimensional
AC	Activated Carbon
BET	Brunauer-Emmett-Teller
C	Carbon
CDI	Capacitive Deionization
CFHS/CFSS	Continuous-Flow Hydro/Solvothermal Systems
CF-OBR	Continuous Flow Oscillatory Baffled Reactor
CH_4	Methane
CO_2	Carbon Dioxide
Co-MOF/NF	Co-MOF on Nickel Foam
CR	Congo red
CS	Core-Shell
CSR	Continuous Flow Reactors
CSTR	Continuous-Stirred Tank Reactors
Cu-LCP	Copper-Based Layered MOFs
CV	Cyclic Voltammetry
DEF	N, N-Diethylformamide
DFT	Density Functional Theory
DMA	N, N-Dimethylacetamide
DMF	N, N-Dimethylformamide

DTG	Derivative Thermogravimetry
EDLCs	Electrical Double-Layer Capacitors
EDX	Energy Dispersive X-Ray Spectroscopy
EG	Ethylene Glycol
EIS	Electrochemical Impedance Spectroscopy
EPD	Electrophoretic Deposition
ESR	Equivalent Series Resistance
ESSs	Energy Storage Systems
EVs	Electrical Vehicles
FESEM	Field Emission Scanning Electron Microscopy
FT-IR	Fourier Transform Infrared Spectroscopy
GAs	Graphene Aerogels
GC	Graphitized Carbon
GCD	Galvanostatic Charge/Discharge
GCMC	Grand Canonical Monte Carlo
H_2	Hydrogen
H_2BDC	Terephthalic/*p*-benzenedicarboxylic Acid
H_2O	Water
Halt	3-amino-1, 2, 4-triazole
HATP·6HCl	2,3,6,7,10,11-Hexaaminotriphenylene Hexahydrochloride
HCs	Hybrid Capacitors
HER	Hydrogen Evolution Reaction
HL	4,2′:6′,4″-terpyridine-4′-carboxylic acid
HOPG	Highly Oriented Pyrolytic Graphite
HSAB	Hard and Soft (Lewis) Acids Bases
HTW	High Temperature Water
ILAG	Ion- and Liquid-Assisted Grinding

IRMOF	Iso-reticular Metal Organic Framework
KOH	Potassium Hydroxide
LAG	Liquid-Assisted Griding
LIBs	Lithium-ion Batteries
LPE	Liquid Phase Epitaxy
MFS	Microfluidic Systems
Mn-BDC	Manganese-1,4- Benzenedicarboxylate
Mn-LMOF	$Mn(tfbdc)(4,4'\text{-}bpy)(H_2O)_2$
MO	Metal Oxides
MOFs	Metal-organic frameworks
MWCNT	Multi-wall Carbon Nanotubes
N_2	Nitrogen
NaCl	Sodium Chloride
NaCOOH	Sodium Formate
NG	Neat Grinding
NH_3	Ammonia
$NiCl_2 \cdot 6H_2O$	Nickel Chloride Hexahydrate
Ni-MOF	Nickel-Based MOF
NMP	N-Methyl-2-Pyrrolidone
NPC	Nanoporous Carbons
OCS	Open Cu(II) Site
PAN	Polyacrylonitrile
PC	Porous Carbon
PSDs	Pore Size Distributions
PSE	Post-Synthetic Exchange
PSM	Post-Synthesis Modification
PVA	Polyvinyl Alcohol

PVDF	Polyvinylidene Fluoride
PVP	Polyvinylpyrrolidone
RBS	Regenerative Braking System
R-BTAsp	(1R,3R,5R)-benzene tricarbonyl tri-(aspartic acid)
rGO	Reduced Graphene Oxide
RT	Room Temperature
SALE	Solvent-Assisted Ligand Exchange
S-BTAsp	(1S,3S,5S)-benzene tricarbonyl tri-(aspartic acid)
SCs	Supercapacitors
SEM	Scanning Electron Microscopy
STP	Standard Temperature and Pressure
STY	Space-Time Yield
SUBs	Secondary Building Units
TEA	Triethylamine
TEA-BF_4/PC	Tetraethylammonium Tetrafluoroboratein/Propylene Carbonate
TEM	Transmission Electron Microscopy
HRTEM	High-Resolution Transmission Electron Microscopy
TG	Thermogravimetry
TGA	Thermogravimetry Analysis
TMOs	Transitional Metal Oxides
UCNs	Ultra-Microporous Carbon Nanoparticles
W	Warburg Impedance
XRD	X-ray Diffraction
ZIF	Zeolitic-Imidazolate Frameworks
Zn-pPDA	Zn-p-Phenylenediamine
Zr	Zirconium
H_3TATB	4,4′,4″-s-Triazine-2,4,6-Triyltribenzoic Acid

MoS_2	Molybdenum Disulfide
SAED	Selected Area Electron Diffraction
IR	Internal Resistance
S	Sulfur
ZZN	$ZnO/ZnCo_2O_4/NiO$
XPS	X-ray Photoelectron Spectroscopy
FFT	Fast Fourier Transform

Chapter 1: Introduction

1.1 Background

With the rapid increase in world population, and fast development of science and technology, conventional energy sources (such as fossil fuels) are consumed rapidly, resulting in energy crisis and severe environmental issues, especially global warming. In response to these challenges, a lot of policies and laws have been introduced to reduce the emission of carbon dioxide (CO_2), the primary contributor to the greenhouse effect. These changes have urged researchers to explore renewable energy resources, such as solar, wind, ocean and geothermal energy, which have been developed rapidly in the past two decades. However, the main limitation of these renewable technologies is their inconsistent power output [1]. This emphasizes reliable and efficient electrochemical energy storage systems for practical applications. Currently, batteries and supercapacitors (SCs) are the two main electrochemical energy storage devices. Despite batteries with high energy density have dominated the energy storage systems (ESSs) for decades, their widespread is hindered by the slow rate capability due to the slow redox process and sluggish charge transport [2, 3]. It is hard to satisfy the energy requirements for sensing devices [4-7], digital cameras [6], regenerative braking systems (RBS) [8, 9] and electrical vehicles (EVs) [9]. SCs are emerging as crucial ESSs since they can provide high power density, exhibit long cycle life and have the capability of quick charging and discharging [10-12]. **Fig. 1.1** shows a schematic illustration of the configuration of SCs.

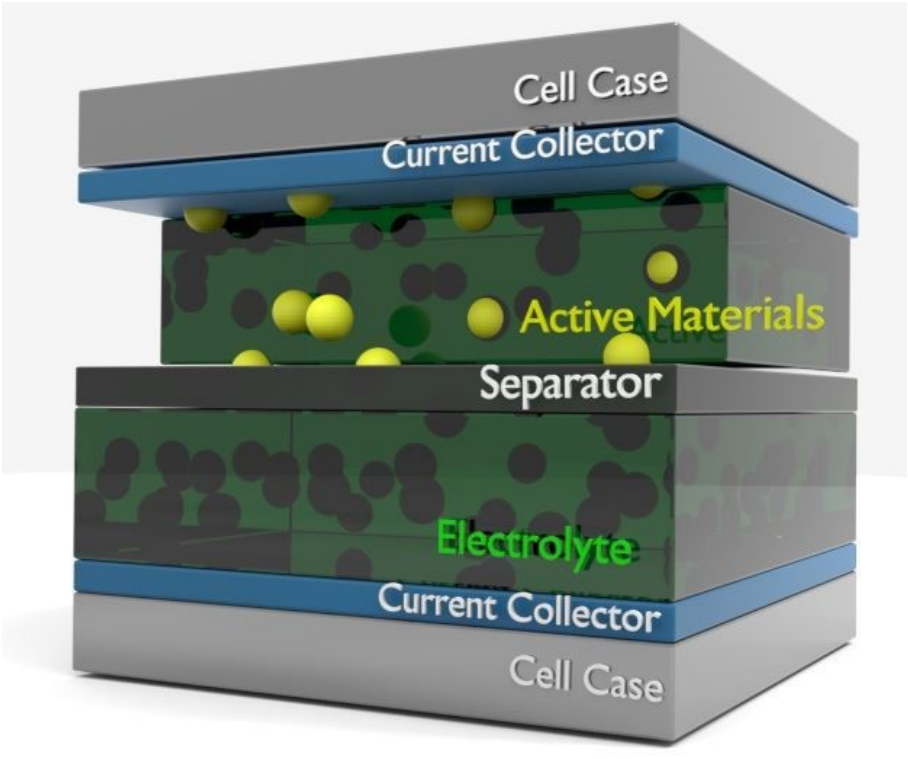


Figure 1.1. A schematic showing a structure supercapacitor containing cell cases, current collectors, active materials, separator and electrolyte.

In general, there are three different types of SCs based on interfacial physics and chemistry, including electrical double-layer capacitors (EDLCs) [11, 13], pseudocapacitors [14] as well as hybrid capacitors (HCs) [15] as illustrated in **Fig. 1.2**. EDLCs store charge through the formation of static electrical double-layer (known as Helmholtz double-layer) with a high diffusion rate, which enables them to possess high power density and excellent cycling life. Nonetheless, they are always characterized by much lower energy densities compared to the other two [16]. Unlike EDLCs, the working principle of pseudocapacitors involves reversible Faradaic redox reactions, which lead to a higher capacitive capability [17]. Most of the pseudocapacitors, however, have low cyclic stability and power density [18]. HCs, formed by combining EDLCs and pseudocapacitors, are subjected to employ higher energy density and longer lifespan. Commonly, carbon-based active materials like carbon nanotubes, activated carbon (AC), graphene and carbon black with large surface areas, are suitable for EDLCs [15, 19-21], whereas conducting polymers [22], transition metal oxides (TMOs) [23] and hydroxides [18] are mainly utilized for pseudocapacitors. Nonetheless, it is hard to achieve a balance between high energy density and high power density. Thus, it is necessary to explore advanced active electrode materials with highly accessible surface areas and enhanced electrochemical performance.

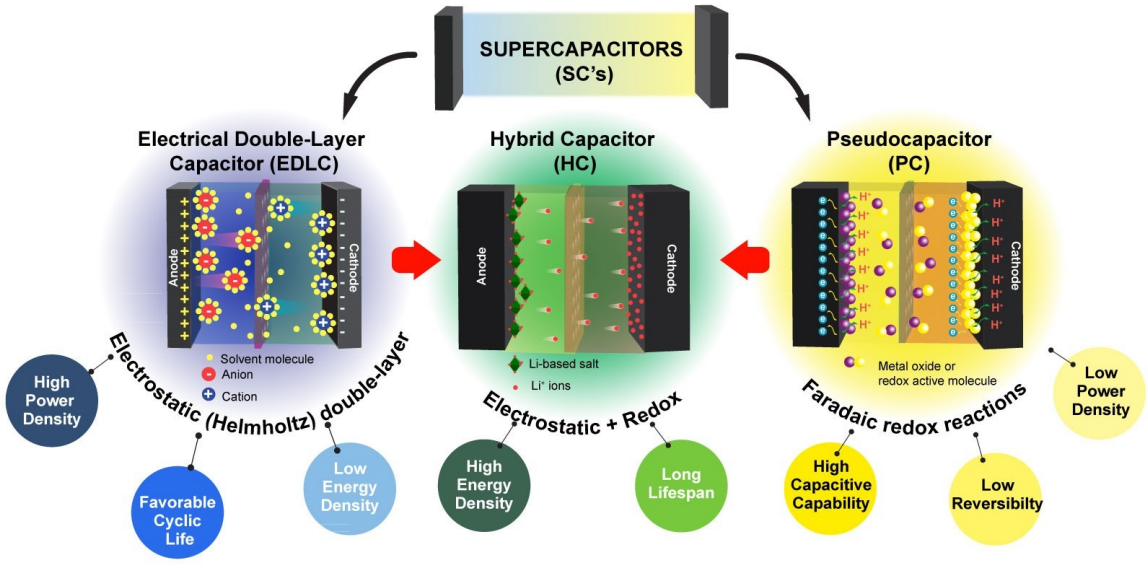


Figure 1.2. The characteristics of conventional supercapacitors (SCs) like electrical double-layer capacitors (EDLCs), pseudocapacitors and hybrid capacitors (HCs).

Metal-Organic Frameworks (MOFs) [24, 25], also known as coordination polymers, are a class of porous crystalline materials and have attracted enormous attention for a variety of applications in drug delivery [25], catalyst [26], gas storage and separations [24, 27, 28], as well as sensors [4, 29]. Recently, they have been reported as promising electrode materials for ESSs, especially for SCs. This is attributed to the tunable pore sizes, large surface areas (up to 10,000 $m^2 g^{-1}$), various structures and diverse functionalities [30-33]. More significantly, MOFs are a type of bifunctional materials, which can be directly employed as both electrode materials and templates/precursors to synthesize various nanostructures for electrochemical applications. Besides, MOF-based materials with desired structures could be generated by tuning the synthesis methods. Taking pristine MOFs for example, the performance is determined by its physical properties such as conductivity, particle

size, specific surface area, as well as the distribution of internal pore size [34]. Notably, during the electrochemical process, it has a preferable ionic transportation for loosely packed MOFs.

Till date, more than 80,000 types of MOFs [35] have been explored in various fields, and the numbers are progressively increasing (**Fig. 1.3**). However, there are three tough problems that the researchers faced in the applications of MOFs as effective electrode materials in SCs: (i) low stability (thermal, mechanical, chemical and water stability), (ii) low conductivity as well as (iii) low specific energy density. In terms of the stability issue, it could be resolved by creating a hydrophobic interface [36]. For achieving environmental protection objectives, the electrolytes used for most SCs are water-based. As the electroactive materials are immersed in the electrolyte, substation reactions might occur and result in the dissociation of MOFs, in which the water molecules or hydroxide would replace metal-coordinated ligands. Therefore, strengthening the coordination bonds between organic linkers and secondary building units (SUBs) [37] is another possible option. In addition, the water stability of MOFs could be improved by modifying the surface of MOFs and their derivatives. For instance, an amorphous carbon layer, formed by heating the surface of MOFs, ameliorated the water stability of MOFs by hindering the hydrolysis of the iso-reticular metal organic framework (IRMOF-1) [38], and water-stable MOF-polymer composites were synthesized by incorporating MOFs onto polymers [39]. Furthermore, it is challenging to fabricate high acid/base stabilized MOFs, which cause serious damage to the skeleton structures of MOFs under acidic or alkaline conditions. According to hard and soft (Lewis) acids bases (HSAB) principles, hard acids/bases tend to bind to hard bases/acids (h-h), while soft acids/bases prefer to bind to soft bases/acids (s-s). The orbital and charge interactions are much stronger than that of either hard Lewis acids to soft bases or hard Lewis bases to soft acids (h-s). At the same time, the molecules are going to restrict the change of pH in a buffer solution when an acid /base is added. In this case, it is a novel strategy to enhance the stability of MOFs in acidic/alkalescent solutions as they are composed of both acidic and alkaline functional groups [40-42].

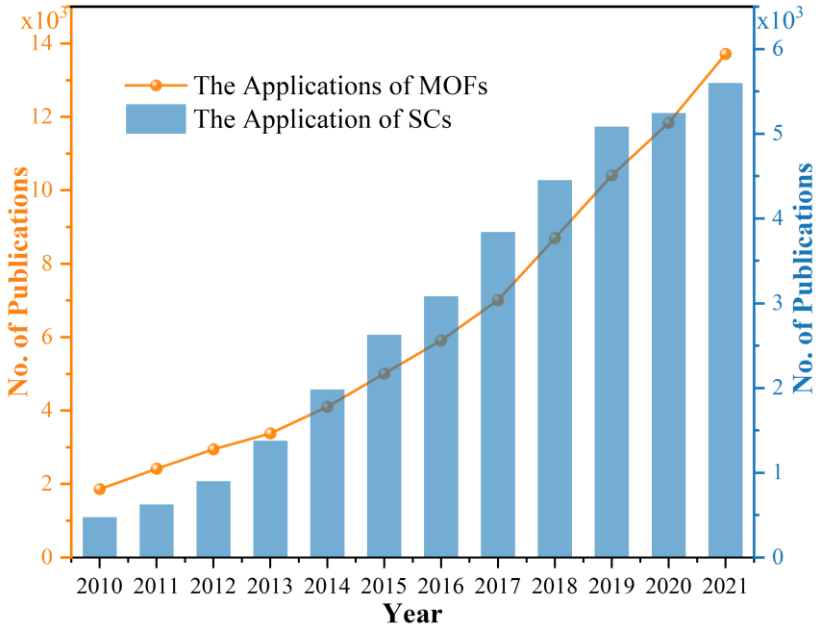


Figure 1.3. The number of publications per year from Web of Science: the applications of MOFs and Supercapacitors.

Despite MOFs are viewed as promising candidates in optical, chemical as well as electrochemical fields, most of them have been characterized by low electrical conductivity (10^{-8} – 10^{-6} S m^{-1}) or even insulators (< 10^{-8} S m^{-1}), which significantly hinders their electrochemical applications. Moreover, it is hard to keep its porosity and conductivity simultaneously. This would limit the electrochemical capacitance as well as its reversibility, when MOFs are utilized as electrode materials in SCs. Hence, great efforts have been made to explore highly conductive MOF nanomaterials for further applications. In general, the conductivity is limited by charge carriers. The higher charge mobility of the charge carriers, the higher electrical conductivity of MOFs. To date, several approaches have been developed to enhance the conductivity of porous MOFs, namely formation of composite and post-synthetic modification. The electron mobility of MOFs could be improved by careful and precise selection of metal clusters and organic linkers, in which the constructed architecture could exhibit long-range charge delocalization through resonance or π - π stacking [43]. Another potential and versatile approach is guest doping through either introduce guest molecules or other nanomaterials with excellent conductivity [43, 44].

Among of reported MOF materials utilized for SCs, Ni-MOFs exhibit large surface area, flexible topology, natural crystalline structure and high theoretical capacity [45, 46], which have been viewed as promising electrode active materials for supercapacitor applications. Nonetheless, several challenges impede their widespread implementation. In particular, the inherently low electrical conductivity, which limits charge-discharge rates, and the issue of stability under electrochemical conditions, leading to degradation over repeated cycles. Moreover, the intricate structures of Ni-MOFs could hinder ion diffusion within their pores, impacting their reversibility. In addition, synthesis reproducibility and scalability are also significant concerns, as the complex synthesis routes and the use of costly or limited components hinder large-scale production. Overcoming these challenges through innovations in material design, synthesis methods, and understanding structure-property relationships is essential for unlocking the full potential of Ni-MOFs in supercapacitor technology.

Over the past two decades, various methods have been adopted for stable MOFs, which are essential to be applied for electrochemical energy storage systems. In this work, various methodologies to synthesize MOFs are briefly discussed, including conventional methods such as solvent volatilization, hydro/solvothermal synthesis, accelerating the synthesis process by microwave radiation, electrochemical and mechanical approaches, sealing pathway to integrate other functional materials and continuous flow to reach industrial production. Moreover, various factors could play crucial roles in the synthesis leading to stable MOFs, ranging from the precursors such as metal salts and organic ligands to synthesizing conditions like temperature, pH, etc. Besides, the applications of MOF materials as SCs electrode materials were discussed in terms of two aspects: (a) the performance of pristine MOFs which are employed directly as electrodes for SCs and (b) the applications of nanoporous composites derived from MOFs, including binary/ternary metal oxides and MOF-derived carbons. In addition, the impact of processing parameters, including solvent systems, reaction temperatures and synthesis duration, on the morphological and electrochemical properties of Ni-MOF nanostructures were systematically studied. Furthermore, pseudocapacitance-rich materials, such as MoS_2 and MOF-derived TMOs and carbonaceous nanocomposites, were introduced to further enhance the electrochemical properties as well. Lastly, a short summary and perspectives were provided.

1.2 Scope and Aims

1.2.1 Problem Statement

With the rising energy demand and environmental pollution in human society, it is essential to develop renewable and economical ESSs. Meanwhile, it is imperative to grow better technology for huge amounts of renewable energy storage and at a faster speed because of the great emphasis on sustainable energy technologies. Among a wide range of ESSs, SCs are one of the most promising and efficient technologies due to their high-power density, low cost, fast charge/discharge rate profiles and extended cyclability. More significantly, it shows a great potential in various technological applications. Firstly, it could be adopted in the automotive industry. For instance, General Motors employ a SC-based voltage stabilization system for start/stop technology and the system can start the engine within 0.4 seconds, which is twice as quick as conventional systems [47]. Mazda utilizes SCs to store surplus energy from RBS in i-ELOOP system [48], which could be fully charged within seven seconds. Secondly, SCs can also be used in public transport systems, an obvious example is that SCs are applied to power CSR trams in China and it is able to run 4 km after charging for 30 seconds and approximately 85% of braking energy is recovered [49]. Thirdly, in the energy sector, Maxwell applies SCs in the wind pitch control system on wind turbines [50], which functions as backup power and it helps to lower the maintenance and operation costs. Lastly, SCs even play a significant role in the aviation industry. Airbus A380 adopted them for emergency doors [51]. Nonetheless, the energy density is relatively low as compared to a battery, which hinders their further applications. To overcome these issues, new materials with high capacitive performance and large potential windows are widely studied.

MOFs have received huge attention in the recent decade in various fields, such as catalyst, drug delivery, gas storage/separation and electrochemical ESSs, due to the features of high porosity, ultra-large specific surface area (up to 10,000 $m^2 g^{-1}$) and adjustable pore size. Recently, MOFs are employed as electrode materials for SCs by virtue of the flexible structures and large surface areas with highly exposed active sites. Nevertheless, the high capacitance and stability have been significantly restricted by the low electrical conductivity and physiochemical stability. Similarly, the applications of Ni-MOF-based nanostructures for SCs also suffer from inferior rate/kinetic performance and cyclic stability due to their low electrical conductivity and stacking characteristics, which significantly hindered their wide exploitation in electrochemistry. Besides, aqueous electrolyte is popularly used in electrochemical ESSs, and most Ni-MOF-based materials cannot stably exist in water. Hence, tremendous systematic structure-performance studies are required to explore modified MOF-based nanomaterials with excellent electrical conductivity, cyclability and stability in water.

This research aims to systematically investigate the synthesis conditions (i.e., solvents used, reaction temperature and duration), characterizations and electrochemical behaviors of Ni-MOF-based nanostructures as electrode active materials for high-performance supercapacitor applications. The study will focus on enhancing the specific capacitance, rate performance and cycling stability of these materials via various strategies, including structural modifications, doping and composite fabrication. The ultimate goal is to synthesize Ni-MOF-based nanostructures with superior electrochemical performance, contributing to the advancement of energy storage devices for diverse applications.

1.2.2 Research Questions/Hypothesis

(a) What is the charge storage efficiency of nanostructured MOF material? Will the 2D Ni-MOF nanosheets provide an excellent electrochemical capacitive performance and lifespan? These questions will be addressed by the current proposed study in which the processing parameters of the synthesis process shall be carefully examined to produce Ni-MOF materials with the optimum electrochemical performance.

(b) What is the effect of graphene incorporated MOF nanomaterials? Will the electrical conductivity and electrochemical performance be further enhanced by incorporating graphene with Ni-MOFs? What are the mechanisms that might contribute to the enhancement of electrochemical performance of the product? All these questions shall be evaluated carefully, from the synthesis process until the physical-chemical properties characterization. The optimized electrochemical performance of the Ni-MOF/graphene nanocomposites shall be investigated comprehensively via a series of analytical techniques.

(c) What is the electrochemical performance of the Ni-MOF-based nanocomposites by incorporating nanomaterials with pseudo-capacitive behaviors, such as MoS_2 and MOF-derived TMOs? Will the electrochemical performance be significantly enhanced? These questions will be answered by synthesizing MoS_2, MOF-derived TMOs and the precise selection of the composition between Ni-MOFs and other nanomaterials. The optimized electrode active materials will be further evaluated by analytical instrument.

1.2.3 Scope of Study

This project will concentrate on the synthesis of Nickel-Based Metal Organic Frameworks (Ni-MOFs)-based nanostructures as electrode active materials for symmetric supercapacitor applications. The chemical composition, pore size distribution and morphology of the as-synthesized Ni-MOFs will be carried out using X-ray diffraction (XRD), Fourier transform infrared (FT-IR) spectroscopy, scanning electron microscopy (SEM) and transmission electron microscopy (TEM). Moreover, the surface areas of the as-synthesized samples are measured by Brunauer–Emmett–Teller (BET). To analyze the electrochemical characteristics of the products, cyclic voltammetry (CV) and electrochemical impedance spectroscopy (EIS) will be carried out in a two-electrode system. In addition, the energy density and power density of the as-synthesized MOF-based nanostructures will be investigated based on symmetric supercapacitor devices. Lastly, graphene and other pseudocapacitance-rich materials (i.e., TMOs and MoS_2) will be incorporated with the MOF to form a nanocomposite, with the target to further improve the stability as well the electrochemical performance of the electrode materials.

1.2.4 Objectives

1. To synthesize and characterize the Ni-MOF and Ni-MOF/graphene nanocomposites for optimum electrochemical performance using solvothermal approach.
2. To optimize the processing parameters (type of solvent systems, processing temperature and reaction duration) for improving the electrochemical properties of the Ni-MOF nanomaterials.
3. To enhance the energy density of MOF-based nanostructures by incorporating pseudocapacitance-rich materials (MoS_2 and MOF-derived TMOs).

1.2.5 Thesis Overview

In this thesis, hierarchical porous Ni-MOFs were synthesized via a facile solvothermal approach, in which the impact of critical synthesis and processing parameters, including different solvents, synthesis temperature as well as time, on the electrochemical performance of Ni-MOF nanostructures have been systematically studied. Meanwhile, graphene nanosheets and MOF-derived carbon matrixes were incorporated to enhance the electronic conductivity and cycling stability. Apart from that, transition metal compounds (i.e., transition metal oxides derived from MOFs and metal dichalcogenide) with enhanced electronic conductivity and superior theoretical capacitance have been explored in this study as well.

Initially, the general background of supercapacitor with current issues is introduced in chapter one. Subsequently, the synthesis conditions and physicochemical properties of MOFs as well as MOF-derived nanomaterials are systematically reviewed in chapter two. Chapter three summarizes the materials and methods used in this thesis, including chemicals, material characterizations, electrochemical analysis, as well as synthesis method.

In chapter four, the impact of processing parameters, including synthesis temperature and time, on the morphological and electrochemical properties of Ni-MOF nanostructures have been extensively studied. Particularly, the synthesis temperature ranged from 100 to 200 °C, while the duration was between 8 and 32 hours. The results annotated that the solvothermal reaction temperature had a significant influence on the morphologies and electrochemical capacitive performance of Ni-MOF nanomaterials, while solvothermal time only had a slight impact on these resultant intrinsic properties. Specifically, the average size of Ni-MOF nanosheets trended to gradually decrease as the reaction temperature was increased, whereas the crystallinity of these nanostructures was shown to have a direct correlation with solvothermal temperature. Noteworthily, when the nanostructures synthesized at 160°C were used as symmetrical supercapacitor electrodes in an environmental-friendly aqueous electrolyte, an excellent energy density of 22.44 Wh kg^{-1} and a superior cyclic durability of 118% over 10,000 cycles were achieved. Hence, the optimized solvothermal reaction temperature (160°C) was selected for the synthesis of nanostructured Ni-MOFs of subsequent works.

Moreover, the impact of critical parameters on the electrochemical properties of nickel-based metal-organic frameworks (Ni-MOFs), which were synthesized via a solvothermal approach, have been systematically studied in chapter five. Firstly, the effect of different solvent systems on the morphologies and electrochemical properties of Ni-MOFs were systematically investigated. It was found that binary solvents (Ethylene glycol + DMF) with high polarity and viscosity were favorable for the formation of microspheres, resulting from the self-assembly of ultrathin 2D nanosheets. The as-synthesized Ni-MOFs exhibited flower-like structures and excellent

electrochemical performance. Meanwhile, the successful incorporation of highly conductive graphene nanosheets with Ni-MOF nanostructures could further enhance the electrochemical performance. A higher specific capacitance of 420.4 F g^{-1} was obtained in 2M KOH electrolyte. In a neutral aqueous electrolyte (2M NaCl), the delivered maximum energy and power density were 14.68 Wh kg^{-1} and 2,852 W kg^{-1}, respectively. Besides, a remarkable capacitance retention of 97.70% over 10,000 cycles was achieved by the nanocomposite electrode. Furthermore, it was worth noting that the coordination ratio between nickel (Ni) and oxygen (O) atoms was 1 : 6 for the most optimized electrode.

In chapter six, molybdenum disulphide (MoS_2), a 2D layered transition metal dichalcogenide with large surface area and flexibility in the atomic scale dimension, was incorporated onto porous Ni-MOFs via a facile hydrothermal approach. Moreover, the sandwiched structure could be beneficial to facilitate the electronic conductivity. To further improve electronic conductivity and overall electrochemical performance, sodium ions were introduced as well. It was found that the as-synthesized porous nanocomposites delivered an excellent supercapacitive performance, in which the obtained maximum energy density was as high as 33.33 Wh kg^{-1}. Besides, the as-fabricated symmetric supercapacitor device delivered a remarkable cycling durability with a capacitance retention of 97.42%, while an outstanding coulombic efficiency of 97.82% was achieved over more than 10,000 cycles in an aqueous electrolyte.

Additionally, transition metal oxides/carbon nanocomposites derived from metal-organic frameworks (MOFs) with enhanced electronic conductivity and superior theoretical capacitance have been viewed as novel nanostructured electrode active materials for high-performance electrochemical energy storage applications. In chapter seven, highly porous nanostructured NiO/C yolk-shell nanocomposites were prepared via a simple calcination of Ni-MOFs. The porosity and electrochemical property were further enhanced by incorporating Na^+ and hierarchical MoS_2 nanostructures via a facile hydrothermal method. The delivered electrochemical capacitance of NiO/C yolk-shell structure was 1779.50 F g^{-1} in 2M KOH, and a superior specific capacitance of 2540.63 F g^{-1} was acquired after the incorporation of Na^+ and 2D layered MoS_2 onto the nanocomposite. When a symmetric supercapacitor was fabricated, a remarkable energy density of 36.93 Wh kg^{-1} was recorded in an environmental-friendly aqueous-based electrolyte. More significantly, the outstanding delivered capacitance retention and coulombic efficiency were recorded at 111.92% and 97.6%, respectively after 4,000 continuous GCD cycles.

Chapter eight summarizes the works that have been conducted throughout the whole thesis and some suggestions for future works are included in this chapter.

Overall, the synthesis parameters, including solvothermal reaction temperature, time and solvent systems, which have a crucial role in the morphologies and electrochemical properties of Ni-MOF nanostructures, have been systematically investigated in the current study. Moreover, to enhance the electrochemical performance, some novel electrochemical active materials (i.e., graphene and MoS_2) were incorporated onto Ni-MOF nanomaterials in optimizing the associated intrinsic properties. Additionally, MOF-derived transition metal oxides/carbon nanocomposites with high specific capacitance and excellent electronic conductivity were also extensively studied in the current research work. The results indicated that MOF-based nanocomposites can be utilized as promising electrode active materials for high efficiency electrochemical energy storage applications.

1.2.6 Thesis Highlights

The thesis generally showed a groundbreaking exploration in the realm of materials science and energy storage technology. In a world increasingly dependent on portable electronics and renewable energy sources, the development of efficient and sustainable energy storage materials, especially MOF-based nanostructures, is crucial. Nevertheless, the excellent functional properties and potential applications of these materials have been significantly hindered by the inferior electronic conductivity, energy density and cyclability. In response to these challenges, this thesis initially focuses on the systematic exploration of the impact of critical processing parameters on morphological and electrochemical properties of Ni-MOF nanostructures. Through comprehensive experimentation, including varying solvent systems, reaction temperatures, and synthesis durations, the study elucidates key insights into optimizing the synthesis process. The results revealed that binary solvent system (DMF+EG) with high polarity and viscosity favors the formation of small-sized nanosheets, and solvothermal reaction temperature played a crucial role in determining morphology and electrochemical performance. In particular, the average size of Ni-MOF nanosheets trended to gradually decrease with increasing reaction temperature, whereas the crystallinity and product yield of these nanostructures were enhanced as reaction time was prolonged. It worth noting that nanostructures synthesized at 160°C exhibited exceptional energy density and cyclability. Moreover, the incorporation of graphene and pseudocapacitance-rich materials, such as MoS_2, MOF-derived TMOs and carbonaceous nanocomposites, could further enhance electrochemical properties, leading to superior energy densities and cycling stability. Hence, through meticulous experimentation and analysis, it elucidated the mechanisms underlying the superior energy storage behavior of Ni-MOF-based nanostructures. In addition, this research not only expands fundamental understanding of these materials but also offers a promising avenue for improving supercapacitor performance. These findings have the potential to facilitate advancements in electrochemical energy storage technologies, with far-reaching implications for diverse fields ranging from portable electronics to renewable energy systems.

Chapter 2: Recent Progress on the Synthesis and Applications of MOF-Based Nanostructures

2.1 Synthesis Strategies of MOFs

MOFs, a type of porous crystalline materials, have successfully attracted enormous attention in the last twenty years owing to their high porosity, ultra-high surface area, structural and functional diversity. Hence, MOFs and their derivatives have been extensively studied in the field of SCs, fuel cells and lithium-ion batteries (LIBs) [52-54]. To ensure the stable and safe operation of these electrochemical ESSs, current studies are focusing on stable MOFs under harsh conditions and the understanding on the synthesis mechanism over structural stability. However, it is still challenging to fabricate MOFs with excellent structural stability and electrochemical properties.

An overview of MOFs fabrication approaches is illustrated in **Fig. 2.1**. Practically, most MOFs are developed through liquid phase syntheses where MOFs are directly formed by mixing metal salts and organic ligands. Among various synthesis routes, solvent volatilization [55, 56] is the most commonly used synthesis method, but it is only suitable for precursors with excellent solubility and the resultant product with a lower solubility in the solvent. To cope with those precursors with low solubilities, Hydro/solvothermal method [57, 58] is employed, in which organic solvents not only act as the reaction medium, but also function as a template agent during the synthesis process. The process could be accelerated through microwave radiation [58, 59] and the resulting MOFs are able to possess high purity. Moreover, sealing pathways are applied to further explore the functionalities by integrating other functional materials with MOFs. To facilitate crystal growth and develop uniform MOFs with micro/nano sizes, even with high yields, electrochemical [60, 61] and mechanical synthesis [62, 63] have been investigated. Furthermore, reactor method [64] is a continuous-flow process to reach the technical-economic purpose for industrialization. It is time-saving and favorable for the product yields which could achieve 100,000 kg on a daily basis.

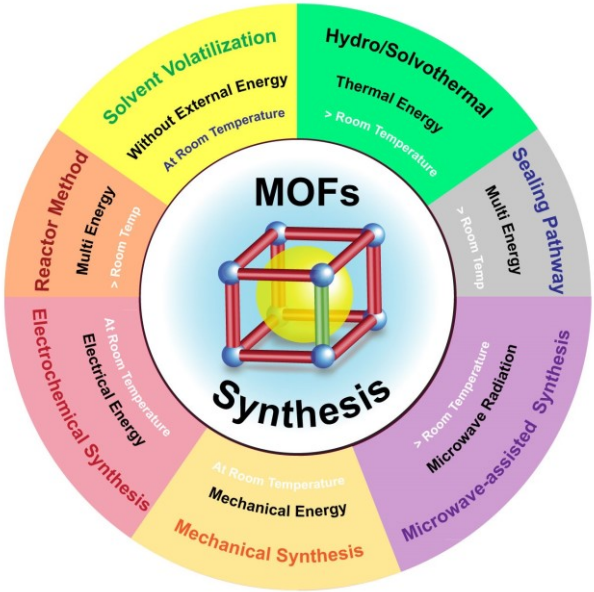


Figure 2.1. The overview of various synthesis methods of MOFs.

2.1.1 Solvent Volatilization

The solvent volatilization method, also known as slow evaporation, is the most commonly employed approach for the synthesis of MOFs. This method does not consume much energy as it mostly occurs at room temperature (RT). During the process, the solvents in a reaction volatilize or diffuse slowly. In general, metal clusters/ions and organic ligands are mixed together in a solvent without any auxiliary compounds. Occasionally, a mixture of more than two solvents is required to speed up this process and enhance the solubility of the reactants. As compared to conventional methods, the main drawback of this process is that it requires a longer synthesis duration. Therefore, the reagents, which act as solvents, with low boiling points are utilized. By applying a reduced evaporating rate, products with a perfect single crystal could be generated via this method [65, 66].

Supersaturation is required for the crystal growth at a constant temperature. For instance, MOFs with well-defined nanoparticles can be developed in a process of slow evaporation, while rapid evaporation of solvent may create a lot of defects, and thus the acquired MOFs materials exhibit high porosity [67, 68]. As a result, the volatilization rate could control the growth rate of active materials. It is possible to directly evaporate nontoxic solvents like water, whereas precautions are necessary to avoid air pollution.

According to Basu's study [69], dense MOFs containing membranes were fabricated via solvent volatilization for the binary gas mixture separation of CO_2-CH_4/N_2, the mechanical and thermal properties of the dense MOFs were improved with the incorporation of fillers. The experimental results indicated that the mechanical and thermal properties were enhanced due to the formation of rigid structure in MOFs and the excellent interactions between MOFs and polyimide matrix, respectively. Through this method and followed by a subsequent annealing under H_2 condition, the partially decomposed cobalt-based zeolitic-imidazolate frameworks (ZIF) supported palladium (Pd) nanoparticles (Pd/PD-ZIF) were synthesized, which was a catalyst for the hydrolysis of $NaBH_4$ [70]. More significantly, it possessed a favorable catalytic activity, high level of structural stability at RT, the H_2 generation rate was 20.61 min^{-1} mg_{Pd}^{-1} and the turnover frequency was 495.0 mol_{Pd}^{-1}, which was the highest performance among other catalysts. Simultaneously, the catalytic activity declined approximately 10% after five operation cycles. Another robust and flexible HKUST-1/polyvinylidene fluoride (PVDF) composite with micro-, meso- and macro structure was prepared via solvent evaporation where the crystallization of MOF and precipitation of polymer occurred together [71]. This porous active material with an improved water stability could enhance the adsorption of CO_2. To achieve the construction with large scale mesopores and macropores, a template-free and simple solvent evaporation method was attempted for carbonization [72]. The resultant carbon material contained a three-dimensional (3D) structure with extensively high specific pore volume of 5.45 cm^3 g^{-1} and surface area of 3000 m^2 g^{-1}. In the heat treatment, solvent evaporation would contribute to the surface defects of MOFs, which is beneficial to form meso- and macropores. The material with hierarchical porosity has the potential to be used as a capacitive deionization (CDI) electrode.

2.1.2 Hydro/solvothermal Method

Hydrothermal synthesis method refers to the chemical reactions taking place in an aqueous solution at a temperature over 100 ℃ (the boiling point of water under atmospheric condition).

The solvothermal and hydrothermal methods are analogous, the only difference is that water is replaced by organic solvent due to the different temperature requirement. The liquid-phase reaction is carried out in a specially sealed vessel, such as Teflon-lined autoclave, for several hours or days at high temperature and pressure. Generally, the temperature ranges from 100 to 1000 ℃ and the pressure in the range of 1-100 MPa. It would reach the supercritical condition and the solvent would possess higher viscosity when the treating temperature is higher than 647.15 K and the pressure is higher than 218 atm for water. The surface tension disappears between metal salts and solvents. As a result, it enhances the dissolving capability of solvent to dissolve the reagents and speeds up the chemical reactions. The advantage of hydrothermal method is that solvent with enhanced solubility could help to produce MOFs with nanoscale morphologies and high purity. Nevertheless, it is hard to control this process well. The as-synthesized MOFs always encounters agglomeration problem due to their high surface energy [73, 74]. To cope with the agglomeration problem, a modulated synthesis was introduced by Kitagawa and co-workers [75].

Usually, chemical modulators are introduced into the synthesis to regulate the sizes and optimize the morphologies of MOFs [76, 77]. The most common modulators are acetic acid, lauric and benzoic acid [78, 79]. It is noted that modulated synthesis is employed to regulate the coordination equilibrium between metal ions and organic ligands. For instance, modulators reduce the crystal growth rate of MOFs, resulting in the formation of smaller MOF crystals. On the other hand, larger crystal particles were synthesized through slowing down nucleation [80]. This can be achieved by using modulators to coordinate with metal clusters or suppress the deprotonation of organic ligands.

The flower-string-like NiCo-MOF/multi-wall carbon nanotubes (MWCNT) composite was synthesized via a facile solvothermal approach [81], in which two-dimensional (2D) NiCo-MOF nanoparticles grew on the surface of MWCNT. Due to the unique structure, it exhibited an excellent electrochemical performance, such as high-power density, appealing rate capability and reversibility as SC electrodes materials. In a three-electrode system, the specific capacitance was 1010 F g^{-1} at a current density of 0.5 A g^{-1}, it could maintain 760 F g^{-1} when the current density was up to 10 A g^{-1}. The coulombic efficiency was around 98 % after 3000 cycles at a current density of 5 A g^{-1}. Moreover, one-pot solvothermal approach was adopted to develop a multifunctional MOF-based heterostructure with magnetic nanospheres, which was composed of one-dimensional (1D) MIL-53(Fe) microrods [82]. This material could be employed as a photoanode with favorable photoelectrochemical performance. For instance, this material had the capability to regenerate effective and constant photocurrent, can be effectively utilized for water oxidation over visible light and had excellent efficiency in a photocatalysis mediated by H_2O_2. Moreover, it is possible to adjust and tailor the structure and performance through hydrothermal synthesis [83]. The crystal growth and morphology of meso- and microporous MOFs were limited by starting coordination complexes of Cu^{2+}-based linkers. Furthermore, crystal MOF-5 ($Zn_4O(BDC)_3$, BDC = terephthalic acid) with high purity was continuously produced at a rate of 1000 kg m^{-3} day^{-1} through solvothermal approach [84]. This indicated that MOF-5 can be cost effective electrode materials.

Unlike NiCo-MOF nanoparticles, MOF-5 square sheet was formed through a pH-modulated solvothermal mechanism, while the uniform sheet was controlled by auxiliary modulator like polyvinylpyrrolidone (PVP) [85]. Meanwhile, monodispersed MOF-5 crystals with tunable sizes and morphology were also fabricated via a modulated synthesis method [86]. The sizes of the crystals ranged from several nanometers to hundreds of micrometers [87], and the morphology included cube, truncated cubes and octahedron were observed. This unique structure was achieved

since the triethylamine (TEA) was used as an auxiliary base for tuning the nucleation of crystals and PVP with amphiphilic surfactant property for modulating the morphologies of MOF-5. The synthesis of MOF-5 is illustrated in **Fig. 2.2**. Notably, the first Zr-MOFs with octahedral crystal were synthesized via another modulated synthesis, in which acetic and benzoic acid were the modulating agents controlling the nucleation rate [88].

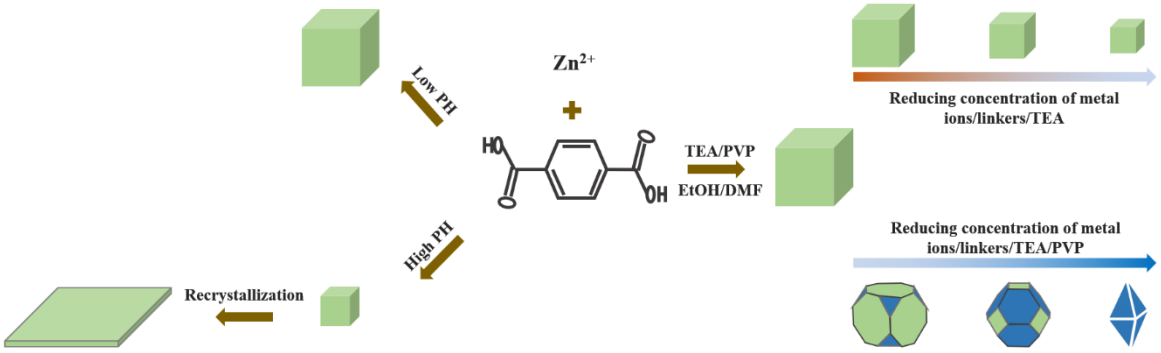


Figure 2.2. The pH-modulated synthesis of MOF-5 with conditions. Reproduced with permission from Ref. [85, 86]. Copyright 2018, Elsevier.

2.1.3 Microwave-Assisted Synthesis

Microwave-assisted method is another route to synthesize MOFs quickly, it could increase the efficiency and yield of the reaction, and ensure ease separation in a time and energy saving manner [89, 90]. This is because metal ions and organic ligands nucleate rapidly and grow into crystalline under microwave radiation. The driving force of this method is the microwave energy with high efficiency, which is capable of altering the electrical and magnetic properties of compounds, and it can also penetrate into the interior of materials rather than being transmitted through the surface [91, 92]. Due to fast crystalline growth kinetics, microwave-assisted synthesis has been extensively employed to develop microcrystalline powders and nanocrystals. However, controlling the size of crystals is the most challenging issue for this method. Large-sized crystals are more difficult to be produced via this method as compared to solvothermal synthesis. Nonetheless, microwave-assisted method was found possible to develop new crystalline materials, owing to its ability of dielectric/volumetric heating [93].

An amine-functionalized MOF was developed in a short period of time through microwave-assisted synthesis [94]. This material was used as a heterogeneous catalyst for Knoevenagel condensation in ethanol with different ketones and aromatic aldehydes. The results indicated that the reactions occurred rapidly and the yields were much higher than those of hydrothermal methods. Moreover, the catalyst could be recycled without further purification and the efficiency remained at 100%. γ-cyclodextrin MOFs (γ-CD-MOFs) of micro- and nanometer size were first synthesized via this facile method [89]. This method has reduced the duration of production from several hours to minutes, and the X-ray diffraction (XRD) patterns of the products for different time scales were illustrated in **Fig. 2.3**. There is not too many differences on the crystallinity within the optimum heating time (< 120 min). In addition, the nanometer sized γ-CD-MOFs possessed the capacity to quickly adsorb of 196 mg Fenbufen within a unit mass in ethanol. To shorten the

process of synthesis with low cost, a microwave-assisted ball milling was applied [95]. The fabricated MOFs were utilized to remove Congo red (CR) from water-based solution and shown an extraordinary CR removal efficiency of 85.54% after five hours. More importantly, zinc-doped nickel-based MOF (Ni-MOF), which was synthesized via the microwave-assisted method, was obtained and employed as SC electrode material with excellent electrochemical performance [96]. The corresponding specific energy densities recorded were 237.4 and 122.3 mA h g^{-1} at 1 and 20 A g^{-1}, respectively. This material also exhibited a preferable cyclic stability of 12% reduction after 4000 charging and discharging cycles. Therefore, it is beneficial to develop MOF-based active materials through microwave-assisted method.

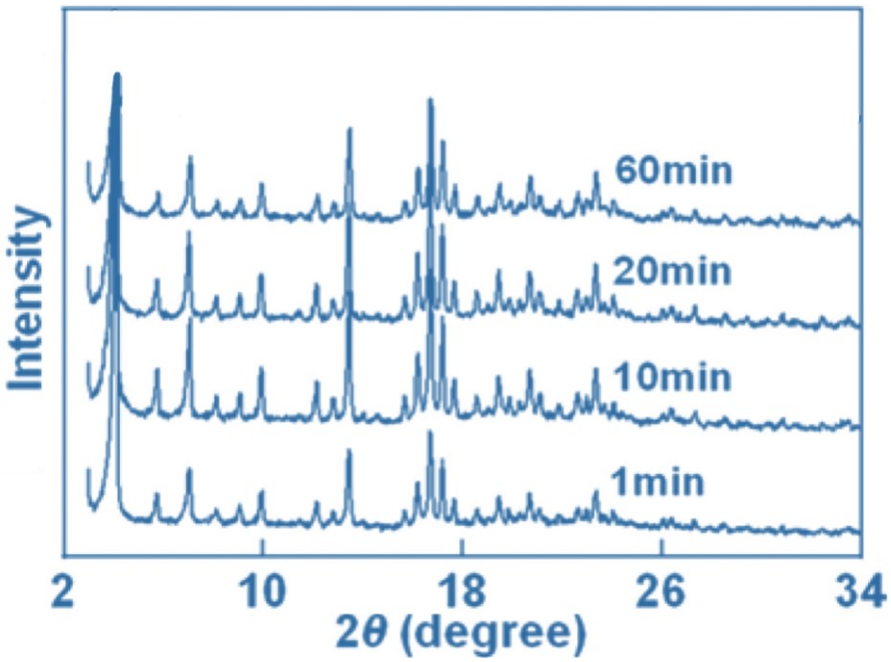


Figure 2.3. The XRD patterns of γ-CD-MOFs synthesized via microwave method at different time. Reproduced with permission from Ref. [89]. Copyright 2017, American Chemical Society.

2.1.4 Sealing Pathway

To further explore the functionalities, integrating other functional species with MOF composites illustrates a bright pathway. Therefore, surface modifications on MOFs have successfully attracted the interest of researchers, especially in the field of chemistry and drug. This method is able to access either by loading functional species into MOFs after deposition or by post-synthesis modification (PSM) [97, 98]. For practical applications of the MOF-based composites, it is crucial to possess both homogeneous films with a well-defined thickness and a high-degree of crystalline orientation during the growth of non-isotropic MOFs. A method known as liquid phase epitaxy (LPE) has been introduced to produce high-oriented crystalline MOFs [99]. However, this layer-by-layer approach is limited by time-consuming deposition process, and the as-synthesized MOF layers are less than 100 layers. For instance, 100-nm (the thickness of one-layer MOF is about 1 nm) MOF layers require 400 times of immersions which takes 36 hours. As MOFs membranes are applied for separation, it is necessary to synthesize the membranes with at least several-micrometer thickness to fulfil the mechanical strength. To cope with this problem, a spray method was utilized

to grow MOF layers on a solid substrate [100]. Most importantly, the processing time was significantly reduced.

PSM and post-synthetic exchange (PSE) processes usually involve solvent-assisted ligand exchange (SALE), which has been recognized as one of the most efficient synthesis approaches in producing MOF materials. PSE was proven able to enhance the stability and functionality of the composites in which metal ions do not form MOFs naturally [101]. Meanwhile, PSM and PSE are beneficial to locate the composition and architecture reasonably, they are effective approaches to form hybrid solids as well.

To further develop the functional materials, synthesis of the composite with a core-shell (CS) structure is another attraction, which plays a vital role in the application in catalyst and energy storage [102]. Furthermore, it provides the properties and functions that cannot be offered by individual building blocks. Currently, there are two major challenges for the formation of CS: (a) It is difficult to control the special structures of CS since the functional material is composed of a core center and surrounded by a cover as shell. (b) MOFs could form undesired inner cores instead of outer shell. Particularly, it is challenging to restrict the crystalline of MOFs in solution and on the surface of core. The reason is that precursors tend to take shape into a composite with various morphologies and sizes. Basically, a template approach could be adopted to control the architecture of composites, in which the size of CS grows according to templates [103]. The shells of CS composites can be controlled via surface modification. However, the process is limited to polymer, metal as well as MO. Fortunately, MOFs are possible to be sealed on various species without size limitation through surface modification of cores, and followed by surface-confined growth [104]. As a result, this has become a new method to design MOF-based composites in various applications.

The MOF layers could be coated on the surface of zeolite 5A beads to form nano-valves shape utilizing a secondary seeding method [105]. This nano-valved composite was employed as an adsorbent for methane (CH_4) storage at low pressure. The results indicated that there was no impact on the performance of composites regardless of the types of metal ions which form MOFs. At the same time, the nano-valved material with the highest performance captured 33.6 L CH_4/L adsorbent at standard temperature and pressure (STP). Through coating the MOFs particles onto a polyacrylonitrile (PAN) membrane, adsorbent of a sandwich-shaped membrane was fabricated for the removal of aflatoxins with high efficiency [106]. As compared to conventional approaches including irradiation, sour alkali soaking and biological methods, MOFs-based membrane has a plenty of outstanding traits such as there is no influence on the nutrient substances, no secondary contamination and it is unnecessary to produce huge amount of wastewater. Meanwhile, the post-synthesis strategies like freestanding could reduce the chemical interactions between enzymes and hollow MOFs that had a higher stability and improved the activity of immobilized enzymes, which was able to be coated inside hollowing MOFs by freestanding [107]. Besides purifications, the resultant MOFs could be applied in photocatalytic systems and ESSs as well. Using PSE processing, nanoscale TMOs were coated onto MOFs [108], which could act as photocatalysts with enhanced catalytic activity. More significantly, the spray approach was adopted to largely develop highly oriented MOF-sealing with several-micrometer thickness [100]. A carbon-based material derived from MOF was developed through vacuum sealing heat treatment [109]. The CS composites were also synthesized with enhanced electrochemical properties [104]. These materials exhibited high energy densities and excellent cyclability when they were employed as anode materials for LIBs.

2.1.5 Electrochemical & Mechanochemical Synthesis

To accelerate the process of crystal growth and develop uniform micro/nano MOFs, many promising alternatives such as electrochemical [110, 111] and mechanochemical synthesis have been explored [112, 113]. The main advantage of these two methods is that the derived MOFs showed favorable electrochemical performance and can be used for industrial applications. The common routes for electrochemical and mechanochemical synthesis of MOFs are demonstrated in **Fig. 2.4a** and **b**, respectively.

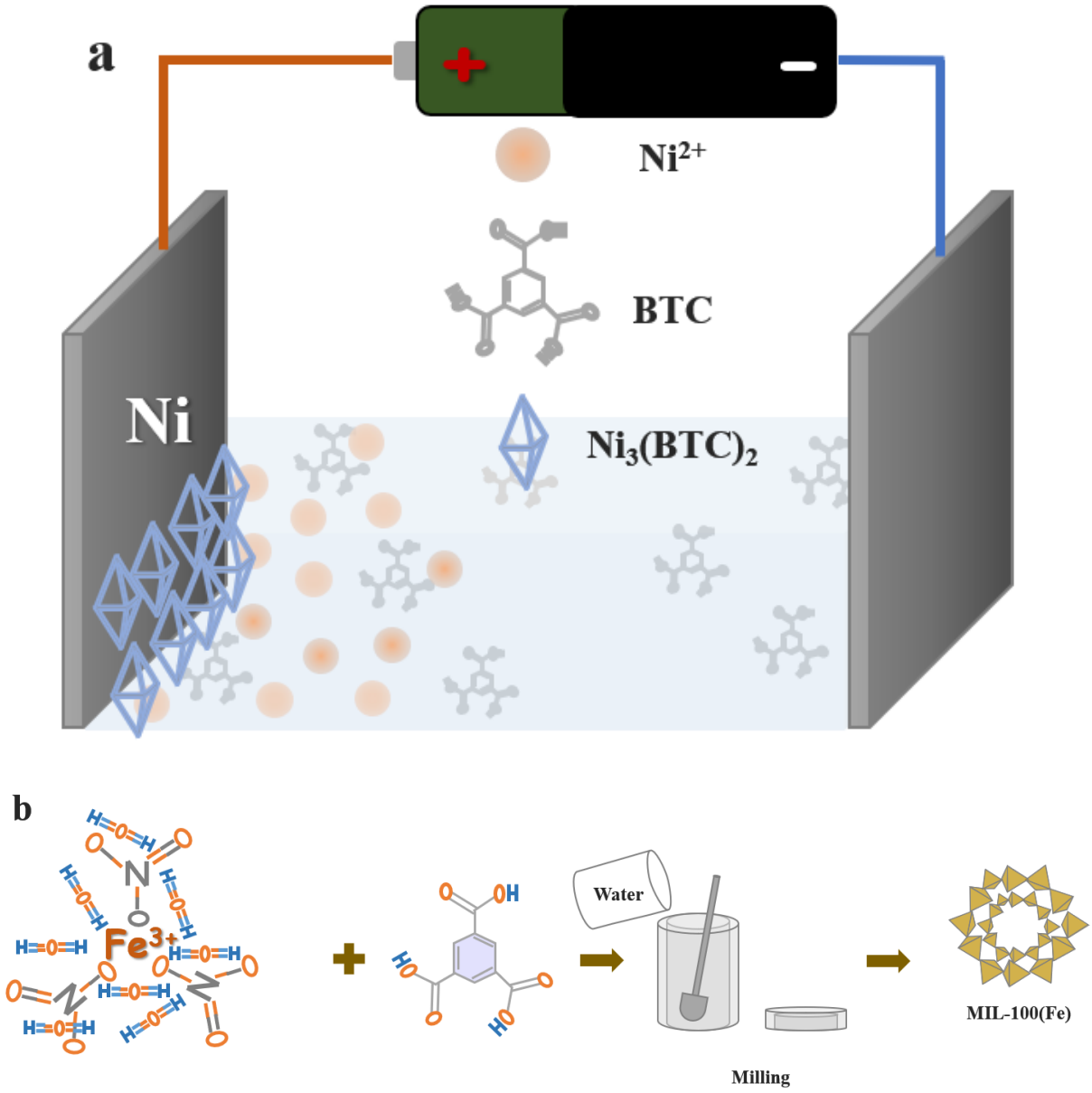


Figure 2.4. (a) Anodic dissolution of nickel foam for the synthesis of $Ni_3(BTC)_2$ MOFs via electrochemical approach [111] and (b) $Fe(NO_3)_3 \cdot 9H_2O$ and H_3BTC as precursors for the synthesis of isostructural MIL-100(Fe) through the liquid-assisted mechanochemical synthesis [112].

In terms of the working mechanisms and properties, electrochemical routes are classified into galvanic displacement [114], self-templated synthesis [115], anodic dissolution [116] and reductive electrosynthesis [117]. In general, electrochemical synthesis is differentiated by direct and indirect electrosynthesis. In direct methods, such as anodic dissolution, cathodic and reductive electrosynthesis, MOFs are directly developed on the surface of electrode through electrochemical reactions, in which the parameters and conditions are tuned during the synthesis process [116, 118].

As for the indirect synthesis, the electrochemical reactions are one of the crucial steps to fabricate MOFs. The working mechanism of electrochemical route indicates that metal ions would be introduced from an electrochemical process instead of being added from the corresponding salts, or the product from a chemical reaction between metal and acid. Consequently, it is essential to start a continuous electrochemical process. Recently, a thin layer structure of $Ni_3(BTC)_2$ MOFs was developed on a nickel foam through an electrochemical approach [111]. This synthesis was conducted at 25 °C in 5 min. The developed material was utilized for hydrogen evolution reaction (HER). Interestingly, this material was found to have much lower charge transfer resistance (R_{ct}) under both acidic and basic conditions. Besides, its stability was satisfactory as it possessed a higher catalytic activity than that of pure Ni foams. Furthermore, a series of characteristic MOFs have been developed in a shorter time with high purity via anodic dissolution [110]. Finally, this synthetic method demonstrated that all the virtual ligands could be utilized with effective Faraday reactions. Moreover, MOFs could also be synthesized with both anode and cathodes. As an illustration, zirconium (Zr) was applied for the deposition of UiO-66 [119]. The result illustrated that UiO-66 was utilized directly for the analytical sampling. However, it is necessary for anodic electrodeposition to occur in a solution, the as-synthesized MOFs must have the same metal as electrode substrate as well. Otherwise, it may cause impurities in the as-synthesized MOFs, which is not recommended for membrane-based separation and adsorption. Nevertheless, it could provide opportunities for MOFs to be used in electrochemical energy storage systems, which allowed higher capacitance with enhanced reversibility.

On the other hand, mechanochemical synthesis has gained popularity due to the ability to form MOFs instantly with high yield. More significantly, this synthesis is conducted on a dry basis or with a little amount of solvent [113, 120]. This helps to reduce the synthesis time as well as the side effect of organic solvents on the environment. Also, the new synthetic route enables screening new MOFs in a scalable and efficient manner. Currently, mechanical synthesis requires neat grinding (NG) [121], liquid-assisted grinding (LAG) [122], ion- and liquid-assisted grinding (ILAG) [112], compression [123] and extrusion [124]. Basically, it is possible to synthesize MOFs with little (or without) solvents via NG, LAG and ILAG which are considered to be versatile as these processes could be accelerated by the utilization of catalysts. Meanwhile it has the ability to bring the production of MOFs to industrial scale through compression and extrusion. According to Thorne et al., [120] ZIF-62, a MOF containing binary linkers (imidazolate and benzimidazolate), was developed through non-catalyzed route which was considered as a green synthesis. By grinding calcium oxide (CaO) and squaric acid in a mortar with a little aqueous liquid, UTSA-280 ($Ca(C_4O_4)(H_2O)$) was obtained [113]. The resultant material is one of the super-microporous MOFs, demonstrating the capability to separate ethylene from ethane with high efficiency. Following the similar approach, H_3BTC and $Ag_6Mo_7O_{24}$ were ground in ethanol solution to produce $Ag_6Mo_7O_{24}$@Ag-MOF [125], which was used as a potential electrode material for SC. As $Ag_6Mo_7O_{24}$@Ag-MOF was utilized as symmetrical SC electrodes, it had excellent capacitive

performance by showing the rate capability of approximately 60% and specific capacitance of as high as 971 F g^{-1}. Profoundly, it possessed a remarkable cycling stability, with 98% retention after charging and discharging for 5000 cycles. LAG is also an effective strategy to synthesize high-quality MOFs with quantitative yields and low energy consumption. The ball-milled iso-structure of MIL-100(Fe) was obtained at room temperature, which exhibited large surface area, excellent crystallinity and thermal stability [112]. Since it is beneficial to accelerate the mechanical synthesis process, ILAG is formed through adding simple ion/salt into LAG. MOFs could be easily produced in 30 min [120, 126], while they might have different structures obtained from different salts. Moreover, ZIF-8 could be developed by both single- and twin-screw extrusion with a space-time yield (STY) up to 144 x 10^3 kg m^{-3} day^{-1} [127].

2.1.6 Reactor Method

Despite a wide range of MOFs with extraordinary performances have been developed, most are produced on laboratory scale. To achieve the technical-economic purpose for industrialization, reactor synthesis methods such as batch reactors and continuous flow reactors (CSR) have been studied intensively [128-130]. Generally, laboratory-scale synthesis of MOFs involves mixing metal salt and organic linkers in a sealed reactor, followed by heating for several hours or days. This process is time-consuming and not ideal for industrialization. The synthesis by continuous-flow processing has few obvious advantages, as it is cost-efficient and makes industrial-scale production of MOFs-based materials possible. Furthermore, MOFs can be utilized as a reactor to develop other types of nanomaterials as well [131].

The continuous flow systems are usually classified into three types, which are continuous-flow hydro/solvothermal systems (CFHS/CFSS) [132], continuous-stirred tank reactors (CSTR) [84] as well as microfluidic systems (MFS) [133]. The experimental layout of these three reactors is shown in **Fig. 2.5**. Initially, the CFHS was utilized to produce fine nano-powders of TMOs. As compared to CFSS, CFHS is beneficial for cost saving and environmental protection seeing as the utilization of green solvent. Nevertheless, CFSS exhibits a high operation temperature and was combined with microwave and mechanochemical syntheses, leading to a shorter process time. CSTR, also known as vat- or back-mix reactor, is a traditional reactor consisting of a huge vessel and a mechanical stirrer in which the reactants are loaded continuously and mixed well. In contrast, MFS has a smaller reactor tank, which has been extensively employed owing to the high degree of control [133].

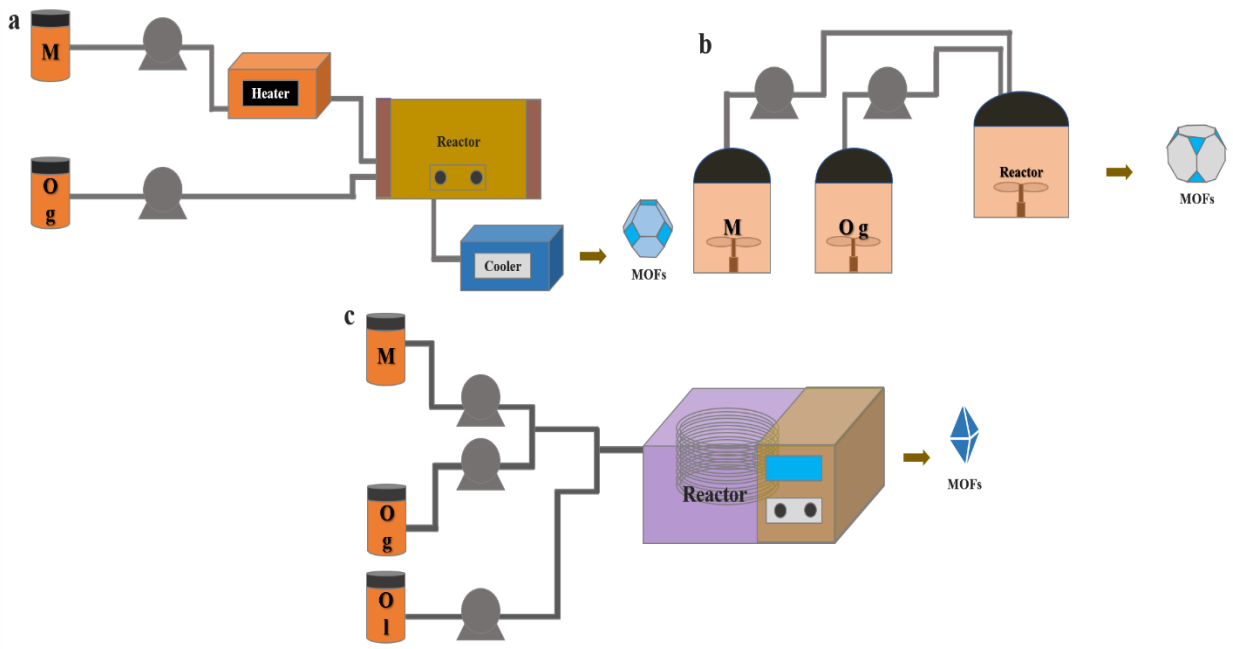


Figure 2.5. (a) Synthesis of ZIF-8 via continuous-flow hydrothermal system (CFHS). [134] - Published by The Royal Society of Chemistry. (b) The synthesis of MOF-5 through continuous-stirred tank reactor (CSTR) [84] and (c) A microfluidic system (MFS) producing dicarboxylate based MIL-88B within 20 seconds. Reprinted with permission from Ref. [133]. Copyright 2013, American Chemistry Society. (M: metal ions; Og: Organic ligands; Ol: oil)

A functionalized zirconium-base MOF (Zr-MOF) was developed in a upscaled synthesis using a batch reactor and employed for ammonia (NH_3) purification [128]. It was entirely a green process, since only water was used for washing, and the initializing reagents were non-corrosive and environmentally friendly. The daily yield was 350 kg m^{-3} with an overall efficiency of 89%. Recently, ZIF-8 was prepared by a large-scale CFHS with a countercurrent mixing reactor. The production rate was slightly low, in which one hour could only fabricate less than one kilogram of product [134]. After optimization, the STY of high quality aluminum fumarate MOF (Al-Fum) could reach as high as 97159 kg m^{-3} per day, solely based on an aqueous synthesis [135]. At the same time, high temperature water (HTW) was utilized in CFHS process, MIL-53(Al) was largely produced within 5-6 min [132]. It is possible to employ CSTR to synthesize high purity MOF-5 at ambient pressure with a STY of approximately 1000 kg m^{-3} per day [84]. This is particularly helpful to reduce the cost of industrial production. As the homogeneous and adjustable microwave device was equipped, the processing of HKUST-1 could be accelerated in a continuous flow oscillatory baffled reactor (CF-OBR) [129]. The yield was 6.32 x 10^5 kg m^{-3} per day and the corresponding surface area was around 1.12 x 10^{12} m^2. This process indicated that it only requires 2.2 seconds of the process time, implying the fascinating high-productivity characteristic. Besides CFHS/CFSS and CSTR, MFS is another approach to speed up the process. Dicarboxylate based MIL-88B with well-defined crystal size was synthesized in 20 seconds [133]. However, only some MIL-88B was modified to have long-term porosity such that nitrogen gas (N_2) is hence unsuitable to be adsorbed. Furthermore, a 2D phosphorus material could be directly fabricated by a MOF-

based 2D nano-reactor in which a pillar-layer MOF was formed via this approach [131]. This method offers the production of multi-dimensional materials.

Though it is possible to scale up the laboratory synthesis to industrial production, there are some limitations of the process that need to be addressed. For example, it is necessary to consider the size distribution of the materials with lower specific surface areas. More importantly, there is no additional treatment of defects from reactor synthesis, mainly due to the rigid synthesis design. On the other hand, the properties should not have too much difference between the MOFs synthesized from laboratories and industries. Therefore, a comprehensive understanding on the optimization and a systematic investigation is hence crucial.

2.2 Effects of Critical Parameters on the Performance of MOFs

MOF materials are mainly composed of nodes and linkages. In porous coordination polymers, metal ions and organic ligands are commonly viewed as the nodes and bridging linkages, respectively. Meanwhile, the network structures of MOFs could be seen as the combination of different nodes and bridging linkages with various numbers. Therefore, the coordination tendency of metal ions and the geometric configuration of organic ligands play a vital role in the structures and performance of MOFs. It is hard to predict the molecular interactions during the synthesis of MOFs, it is hence necessary to recognize and amend the synthesis conditions such that metal ions and organic linkers could interact in a desired manner. Even small changes in the concentration of metal ions and organic ligands, solvent polarity, temperature and pH values could lead to changes in the quality, yields, as well as the structures of MOFs, it is hence crucial to control the size and morphology of MOFs structures for their applications. The reasons are that: Firstly, the coordination configurations of metal centers and the chemical structures of organic ligands play a decisive role in the final structures of MOFs. Secondly, different solvents exhibit different polarities, solubilities and viscosities, which influence the crystallization of MOFs. Other factors, such as the molar ratio and properties of metal ions and organic ligands, could also affect the synthesis process of MOF materials. Moreover, appropriate reaction temperature not only can provide enough power for the synthesis of MOFs, but also avoid secondary reactions which occur at high temperature. Furthermore, a suitable pH condition could deprotonate the organic ligands effectively for coordination with metal ions, as protons and hydroxides are likely to compete and substitute metal clusters.

2.2.1 The Impact of Metal ions and Organic Linkers

The attractive properties of MOFs materials, including large surface areas, high porosity and controllable pore size, are determined by their structures [136, 137]. In fact, the skeleton structures and topologies of MOFs can be regulated by carefully adjusting the metal ions, selecting appropriate organic ligands, as well as the solvent condition [138]. MOFs with various morphologies can be developed through aforementioned methods like slow solvent evaporation, hydro/solvothermal synthesis, microwave-assisted and even reactor methods. However, it is hard to control the molecular interactions during the process of synthesis due to the unpredictable intermolecular force between metal cations and organic linkers. Therefore, it is crucial to understand the impact of various operation parameters on the resultant MOFs.

2.2.1.1 Metal ions

Till date, more than 40 types of pristine MOFs used for SCs have been developed, which are composed of mostly transition metal ions, including nickel (Ni^{2+}), cobalt (Co^{2+}), copper (Cu^{2+}), zinc (Zn^{2+}), manganese (Mn^{2+}), iron (Fe^{3+}), aluminum (Al^{3+}), chromium (Cr^{3+}), zirconium (Zr^{4+}) and etc. An increase in charge could lead to the reduction of lability. Hence, it is better for MOFs to possess high-valence metal cations, such as Fe^{3+}, Al^{3+} and Zr^{4+} [139]. The reason is that these metal ions exhibit high coordination numbers and charge densities, which is favorable for the formation of stable coordination bonds between metal ions and organic ligands. This could make a rigid structure, in which there is a low possibility for other molecules, like water or other solvent molecules, to substitute the organic linkers in MOFs [139]. Meanwhile, divalent metal ions tend to form robust MOFs structures with soft nitrogen-containing ligands [140]. Commonly, these nitrogen-donor ligands are contained in metal azolate frameworks, such as triazolates, pyrazolates and imidazolates. These show how the selection of metal cations determines the morphologies, skeleton structures as well as the properties of resulting MOFs.

Nickel (II) and cobalt (II) are promising metal ions to develop layered MOFs, which are used as active electrode materials for SCs with long-term stability and high capacitance. A layered Ni-TDA ($Ni_3(OH)_2(C_2H_6O_4S_2)$) was successfully fabricated and firstly employed as a SC electrode, in which the electrolyte used was 2M KOH [141]. It was found that the as-fabricated Ni-MOF had a high specific capacitance of 1518.8 F g^{-1} over 1 A g^{-1}. Although the current density rose to 20 A g^{-1}, the capacitance could still remain at 483.3 F g^{-1}. This was further signified by the capacitance retention which was as high as 95.5% after 10,000 cycles. Following the similar approach, a layered Co-MOF was synthesized by an oil-bath route [42]. The as-synthesized Co-MOF was utilized as electrode for a SC for the first time and possessed preferable specific capacitance of 2564 F g^{-1} and 1164 F g^{-1} at current densities of 1 A g^{-1} and 20 A g^{-1}, respectively. Moreover, it could retain 95.8% of its initial capacitance after 3000 cycles. Different ion-based MOFs have disparate functions, even isostructural MOFs made via the same method. Through solvent diffusion method, Co- and Mn-based MOFs were synthesized with 2D network topologies [142]. Interestingly, Co-MOF possessed the properties of catalytic oxidation to degrade malachite green dye, while Mn-MOF could only function for methylene blue. This is because iminium organic dyes contain C=N group, the Co^{2+} and Mn^{2+} have different energy to break C=N bond. According to the structures of these two different dyes, malachite green exhibits a greater π electronic conjugate than that of methylene blue. Meanwhile, the energy of coordinated hexa-coordinate Co is higher than that of Mn (**Fig. 2.6**). ZIF-67 and ZIF-8 with high porosity were prepared for uranium U(VI) removal by Liu and his coworkers [140], in which the ZIF-67 and ZIF-8 had the same organic linkers but the metal ions were Co^{2+} and Zn^{2+}, respectively. It was found that ZIF-8 possessed higher performance than ZIF-67, ZIF-8 had a U(VI) removal capability of 540.4 mg g^{-1}, whereas one gram of ZIF-67 could only capture 368.2 mg U(VI), and the morphologies are revealed in **Fig. 2.7**. The influence of four different metal cations, including Zn^{2+}, Ca^{2+}, Ba^{2+} and Cd^{2+}, on photoinduced electron-transfer was investigated in another study [143]. The results indicate that: Firstly, the yields were different using different metal cations, which ranged from 31% to 63%. Secondly, the photosensitive properties were tested in terms of electron spin resonance, the amount of photogenerated radicals was in the order of Ba < Ca < Cd < Zn. This could be determined by the electronegativity values of metal ions, since the result was in accordance with the electron withdrawing abilities as $Ba^{2+} < Ca^{2+} < Cd^{2+} < Zn^{2+}$. Furthermore, the selection of metal ions not only affects the morphologies and structures of the resulting MOFs, but

also has a crucial role to play in MOF-derived carbon. Six isomorphous MOFs with a 3D structure and various metals, including Ni, Co, Zn, Mn, Cd and Cu, were employed as precursors to synthesize MOF-derived carbon [144]. It was found that there were three disparate morphologies, known as carbon (C), porous carbon (PC) and graphitized carbon (GC). Even only three kinds of carbon morphologies emerged, they exhibited totally different properties. To intensively investigate these properties, the as-derived materials were fabricated as electrode materials for SCs and the respective specific capacitance is shown in **Table 2.1**. It is obvious that Zn-based MOF-derived carbon possessed the highest specific capacitance as compared to others.

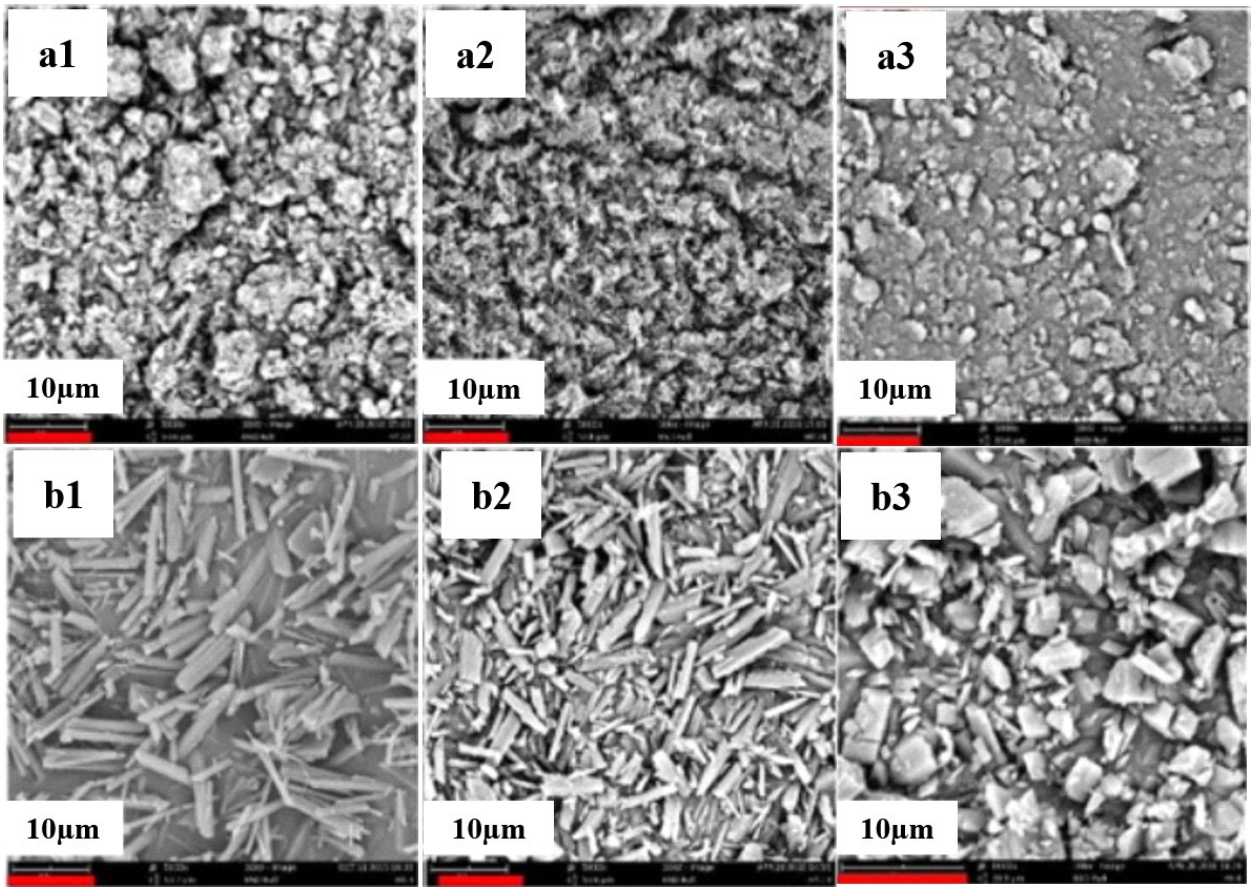


Figure 2.6. The SEM images of microcrystals of Co-MOF (a1-a3) and Mn-MOF (b1-b3) developed under various conditions. a1, b1 methanol-water; a2, b2 ethanol-water; a3, b3 n-propanol. Adapted with permission from Ref. [142]. Copyright 2018, Elsevier.

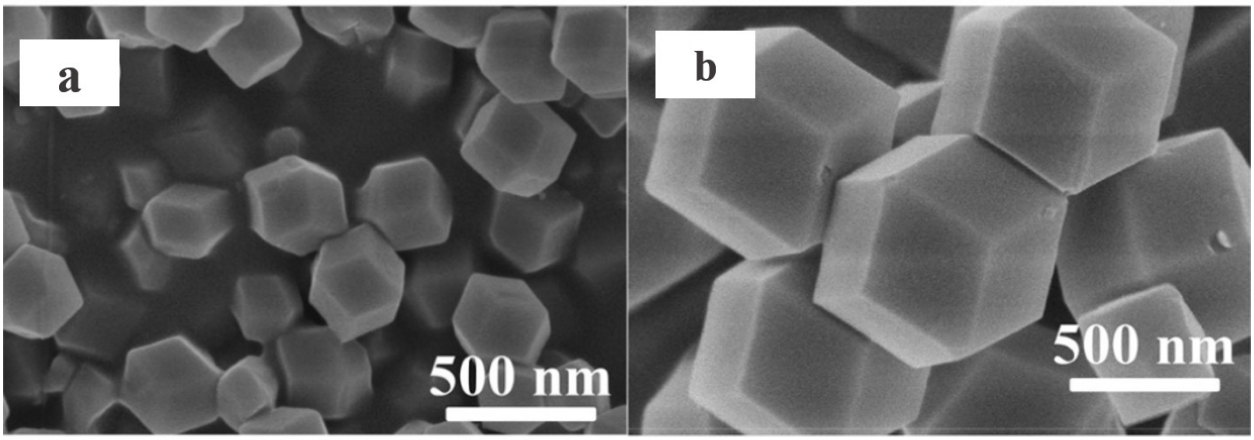


Figure 2.7. The SEM images of (a) ZIF-8 and (b) ZIF-67 with disparate morphologies due to the utilization of Zn^{2+} (ZIF-8) and Co^{2+} (ZIF-67) metal ions, respectively. Reprinted with permission from Ref. [140]. Copyright 2021, Elsevier.

Table 2.1. The specific capacitance of various MOFs-derived carbon at different current densities. Adapted with permission from Ref. [144]. Copyright 2018, John Wiley and Sons.

Current Densities ($A\ g^{-1}$)	**Specific Capacitance ($F\ g^{-1}$)**					
	Cu-C	Mn-GC	Co-GC	Ni-GC	Cd-PC	Zn-PC
0.5	24	50	40	42	126	138
1	23	40	37	39	120	125
2	22	31	35	37	114	115
5	21	20	32	34	106	106
10	19	12	27	29	95	94

2.2.1.2 Organic ligands

Besides the precise control of metal cations, the selection of organic linkers is also crucial for the synthesis of MOFs with desired functionalities. In general, organic ligands have significant impact on the surface areas, volumes, topologies and structures of MOFs [145, 146]. Notably, it is necessary for organic linkers to contain a polydentate functional group, such as -COOH, $-NO_2$, $-PO_3H$ and $-CS_2H$. This is owing to the fact that these linkers can assemble supramolecular architectures acting as both hydrogen-bond acceptors and donors [147]. As compared to other organic linkers, ligands containing carboxyl groups have a large negative charge density, which offers a strong coordination with metal ions. In addition, multi-carboxylate ligands have various coordination modes to take shape into metal-carboxylate clusters or bridging structures which in turn enhance the stability and rigidity of MOFs. Therefore, the appropriate organic linkers help to synthesize novel structural MOFs with favorable physical and chemical properties.

Generally, chiral ligands are exploited to develop homochiral porous MOFs, in which the enantiopurity of a chiral linker controls the chirality and structure of MOFs [148]. In this case, (1S,3S,5S)-benzene tricarbonyl tri-(aspartic acid) (S-BTAsp) and (1R,3R,5R)-benzene tricarbonyl tri-(aspartic acid) (R-BTAsp) were employed to combine with copper (II) under the same synthesis condition to investigate the properties variation [146]. It was found that Cu^{2+} reacted with S-BTAsp and R-BTAsp. The two resulting 3D and homochiral MOFs were iso-structures, but with disparate optical activity. When Cu^{2+} was combined with the mixture of S-BTAsp and R-BTAsp, the final product was 1D and achiral MOF. Meanwhile, the yields were 35%, 67% and 70% for S/R-BTAsp mixture, S-BTAsp and R-BTAsp. Following the similar approach, silver(I)-based MOFs were developed with three different carboxylate anions and various architectures [145]. $(Ag_4(bpy)_2(bpdc)_2)\cdot 13H_2O$ with a 3D sandwich-like network was formed through connecting the neighboring 2D sheets (made by the joint of adjacent strands) with rich hydrogen-bonding interactions, while for $(Ag_2(bpy)(bqdc)(H_2O))\cdot 4.5H_2O$, the interactions were intermolecular hydrogen-bonding and rich π-π stacking. By grouping adjacent anodic and cationic sheets through electrostatic interactions, $(Ag_2(bpy)_2(H_2O)_2)(bpdc)\cdot 3H_2O$ was produced. The resulting Ag-MOFs exhibited different thermal stability as well. The dimensions and functional sites of the organic linkers could also have an essential influence on the properties of MOFs. According to Grand Canonical Monte Carlo (GCMC) simulation and density functional theory (DFT), a series of open Cu(II) site (OCS)-based-MOFs prepared with various ligands for gas separation were investigated [149]. The results indicated that the C_2H_2 separation and storage ability differ from each MOF. Particularly, MOF-505 exhibited the highest C_2H_2 storage capacity and C_2H_2/CH_4 selectivity at two bars due to the compact pores. In another study, ZIF-67 and ZIF-9 with identical metal ion (Co^{2+}) but different organic linkers were fabricated and utilized for U(VI) removal [140]. It was found that ZIF-9 had a higher adsorption capacity than ZIF-67. This was due to ZIF-9 containing more oxygen-containing groups. Hence, it is crucial to take various organic linkers into consideration when synthesizing MOFs for different applications. Interestingly, nitrogen in the function groups was proven to have the capability to improve the wettability of resulting materials, specifically for SC, and thus enhanced the ionic transport process between the electrodes and electrolyte [150]. In 2014, the electrochemical performance of 23 different MOFs were studied by O. M. Yaghi et al. [151] Among MOFs, MOF-867 possessed the highest specific capacitance. Even though both MOF-867 and UiO-67 exhibited identical architectures, they were synthesized using different organic linkers and the electrochemical performance of MOF-867 was much better than that of UiO-67. Specifically, the specific capacitance of MOF-867 could reach 726 F g^{-1} at 1 A g^{-1} and it was able to cycle more than 10,000 time over a large voltage window of 0 - 2.7 V.

Additionally, the morphology can also be modulated by using more than one organic linker owing to the competitive interactions. To improve the charge storage capability by designing unique structures of MOF, BTC was introduced to partially replace PTA linkers [152]. As shown in **Fig. 2.8**, the aggregated nanosheet morphology was transferred into nanosheets with inserted albizia flower-like hierarchical nanostructure when BTC was introduced. Meanwhile, the internal space between nanosheets was beneficial to expose more active sites and provide buffer strains during the long-term cycling. Nonetheless, nanowires were viewed as the molar ratio between PTA and BTC was more than 7 : 3, suggesting the nanosheet structures were destroyed by adding excess BTC. In a three-electrode system (6 M KOH), Ni-MOF synthesized with a mole ratio of 8 : 2 (PTA : BTC) exhibited a specific capacitance of 920 F g^{-1} at 1 A g^{-1}. A high-rate capability of 61% even at a high current density of 20 A g^{-1} was achieved, indicating the introduction of BTC could

enhance redox reaction kinetics. Moreover, approximately 80% of capacitance retention was achieved after 3,000 cycles at 5 A g^{-1}.

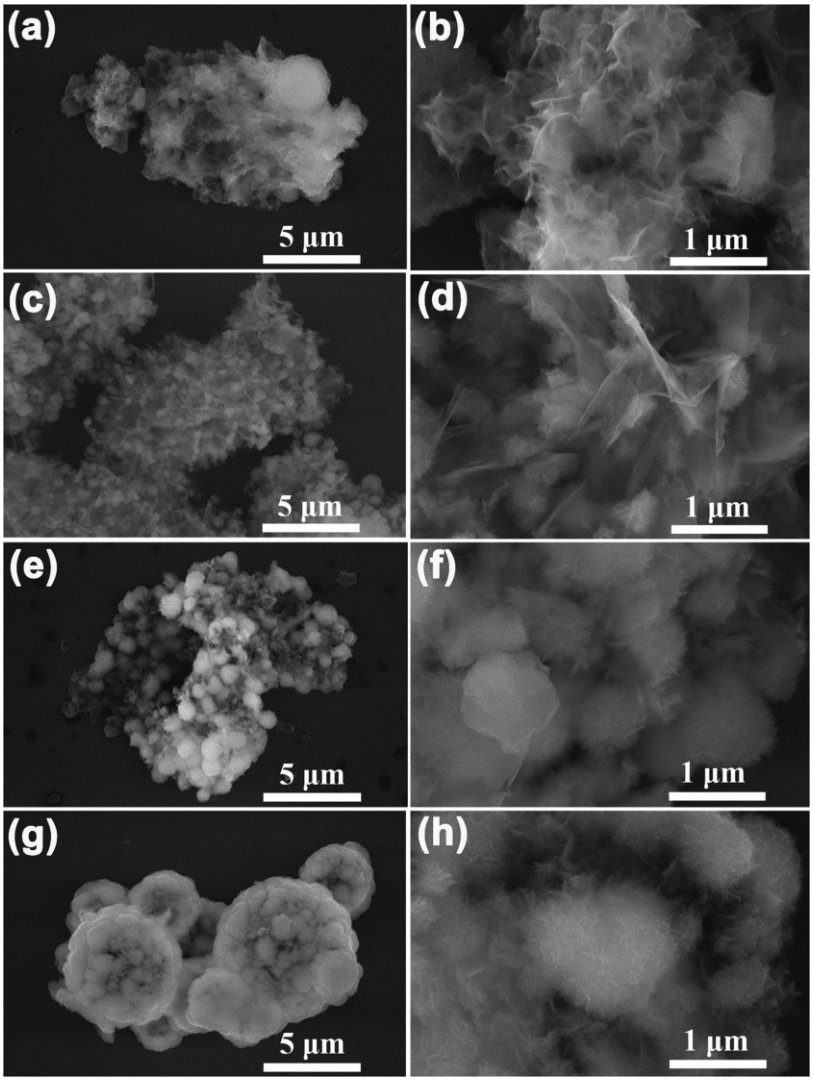


Figure 2.8. The FESEM images of Ni-MOFs under different organic ligand ratios: PTA : BTC= (a, b) 10 : 0, (c, d) 9 : 1, (e, f) 8 : 2 and (g, h) 7 : 3. Reprinted with permission from Ref. [152]. Copyright 2021, Elsevier.

2.2.2 Molar Ratio of Metal Ions and Organic Ligands

In the synthesis of MOFs, the selection of metal cations or organic ligands can independently influence the architectures and properties of the resulting products due to the disparate characteristics of different metal clusters and organic linkers. Generally, the molar ratio of metal ions to organic ligands ranges from 1 : 10 to 10 : 1 owing to the stoichiometric ratio of chemical coordination. As the proportion of metal ions exceeds the stoichiometric ratio of the organic ligand coordination, they will sufficiently coordinate as polydentate ligands. In contrast, it may be fully

or partially monodentate, such that there is no or only few unsaturated metal cations in the resulting MOFs. However, the structures may not be as stable as those containing polydentate ligands.

The utilization of various amount of ligands and metals could affect the porosities, architectures and surface areas of corresponding MOFs. Here, a series of Cu-BTC MOFs were developed by employing copper nitrate and BTC at ratios of 1.81 : 1, 1.45 : 1, 1.09 : 1 and 0.72 : 1 [153]. All the as-synthesized Cu-BTC MOFs were in accordance with the reference sample with octahedral morphologies. This confirmed that the metal-ligand ratio did not have impact on the morphology. However, the pore sizes, surface areas, as well as the performance on CO_2 absorption of the resultant MOFs were different. To study the ratio of metal ion to organic linker on the morphology, MIL-125(Ti) was synthesized through a modified solvothermal approach at a molar ratio of 1 : 3, 2 : 3 and 3 : 3, namely MIL-1, MIL-2 and MIL-3 respectively [136]. Consequently, both the adsorption removal and photocatalytic degradation efficiencies were shown in the following order, MIL-1 < MIL-3 < MIL-2 (as summarized in **Table 2.2**). This might be attributed to the excellent crystallinity, more electrostatic charges and high surface area of MIL-2 with appropriate ratio of Ti^{4+} and terephthalic acid (PTA) (2 : 3). Similarly, hierarchical porous Ni-MOFs were constructed as asymmetrical SC electrode materials with high performance. These uniform layered porous Ni-MOFs were developed by controlling the molar ratio of nickel cation to trimesic acid ligand [137]. During the synthesis, the mole ratio of ligand to metal was set as 1 : 1, 1 : 2, 1 : 4 and 1 : 6, and the corresponding MOFs were labeled as: Ni-MOF 1-1, Ni-MOF 1-2, Ni-MOF 1-4 and Ni-MOF 1-6, respectively. The results from XRD indicated that the crystallinity of resulting Ni-MOF was enhanced as the Ni^{2+} concentration increased. It is noteworthy that the specific capacitance and retention capability are in the order of Ni-MOF 1-1 < Ni-MOF 1-2 < Ni-MOF 1-4 < Ni-MOF 1-6, as showed in **Table 2.3**.

Table 2.2. The physical characteristics of as-developed MILs at different molar ratios. Reproduced with permission from Ref. [136]. Copyright 2020, Elsevier.

Samples	Ratios (Ti:PTA)	Pore size (Å)	Pore Volume ($cm^3\ g^{-1}$)	Surface Area ($cm^2\ g^{-1}$)	Efficiency (%) @90 min
MIL-1	1 : 3	24	0.05	49	72
MIL-2	2 : 3	21	0.41	574	94
MIL-3	3 : 3	21	0.19	214	75

Table 2.3. The physical and electrochemical properties (over a current density of 1 A g^{-1}) of Ni-MOFs made at different molar ratio of ligand to metal. Reproduced with permission from Ref. [137]. Copyright 2018, Elsevier.

Samples	Pore Size (nm)	Surface Area ($cm^2\ g^{-1}$)	Specific Capacitance (F g^{-1} at 1 A g^{-1})	Retention Capability (%)
Ni-MOF 1-1	5.40	5.24	554.3	61.5
Ni-MOF 1-2	13.22	23.36	581.2	58.1
Ni-MOF 1-4	23.62	28.28	828.2	57.4
Ni-MOF 1-6	19.03	40.36	1057.2	49.1

2.2.3 Template Reagent and Solvent

Most MOFs have been developed with the utilization of solvents, such that the impact of solvent is worthwhile to be investigated. Solvents have a great influence on the crystalline process since they could affect the solubility of organic linkers which made solvent molecules get involved in coordination. As for those ligands like carboxylic acid with low solubility, an alkaline-based solvent with the capability to deprotonate should be added. To satisfy the charge conservation of resulting products, addition of some ions and even auxiliary molecules becomes necessary [154]. In general, solvents function as template reagents and the molecules could be incorporated in the resulting products. They can also be utilized as structure directing agents for the crystal growth of MOFs. Solvents could affect the assembly of MOFs and are responsible for disparate architectures of MOFs. The most commonly used solvents with high boiling point and polar nature are N, N-dimethylformamide (DMF), N, N-dimethylacetamide (DMA) and N, N-diethylformamide (DEF). Meanwhile, some other single solvent (i.e., acetone, methanol, ethanol and water) or solvent mixture (i.e., methanol/DMF, ethanol/water/DMF, methanol/water) are frequently employed to synthesize MOFs as well, relying on the solubility of the selected metal ions and organic linkers [155].

The formation of MOF with mesoporous and multi-functional luminescent properties highly relies on the type of solvent used in the synthesis. For instance, 3-amino-1, 2, 4-triazole (Hatz) was selected as the solvent for the synthesis of Tb(III)-based MOF [156]. It acted as a template reagent and directed the formation of Tb-MOF material. The as-developed Tb-MOF had a three-fold interpenetrated architecture, in which single-stranded and double-stranded helical chains co-exist along the c axis. This stable MOF material was employed as sensor and showed excellent efficiency on detecting aluminum and iron ions in aqueous solvent. Meanwhile, it could discriminate p-xylene vapor, as well as sense the presence of nitrobenzene vapor. An auxiliary reagent could also be applied to adjust the pore sizes and structures of MOFs. Hierarchically porous copper-based MOFs were synthesized through hydrothermal method [157], in which sodium dodecylbenzene sulfonate (SDBS), a novel anionic surfactant, was employed as a template reagent. In the synthesis process, the ratios of SDBS to Cu^{2+} were set at 0.08, 0.25, 0.35 and 0.40 and the corresponding products were denoted as HP-Cu-BTC_A, HP-Cu-BTC_B. HP-Cu-BTC_C and HP-Cu-BTC_D, respectively. Another organic solvent used in the same synthesis was H_3BTC. Based on the XRD patterns, the crystal structures of as-developed HP-Cu-BTCs were similar, which implied that the concentration of template reagent did not affect the architectures of resulting materials (the XRD patterns are illustrated in **Fig. 2.9**). However, it did have influential impact on the physical properties such as pore size, surface area and specific volume as compared to conventional Cu-BTC (C-Cu-BTC). Moreover, as the synthesized MOFs were utilized as catalyst, they showed different performance as well. These related properties are summarized in **Table 2.4**. Besides, the amount of water, which is miscible with solvent, could induce the formation of different structures. Through Yue's research work [158], it was found that when the amount of water in the solvent was between 5.5 to 15.5 mL, TbPDBA-9 was formed. By just increasing the amount of water to 16.5 mL. TbPDBA-8 was produced in the same study. Interestingly, both TbPDBA-8 and TbPDBA-9 were obtained when 10.5 mL water was utilized. The process of structural transformation would be achieved by adding sodium formate (NaCOOH). The results also indicated that TbPDBA-8 and TbPDBA-9 had distinctive property differences, which might be due to the addition of different components. HCOOH and H_2O were detected in TbPDBA-9 and TbPDBA-8, respectively. Specifically, Tb-PDBA-8 possessed high selectivity for H_2O in

dioxane, while Tb-PDBA-9 was able to detect ascorbic with fluorescence quenching. Furthermore, different hydrogen bond donors in the template solvent could influence the assembly process resulting MOF materials with various frameworks. This observation is evidenced by another study, when similar amount of urea, e-urea and m-urea was employed to produce Zn-, Co- and Mn-based MOFs under identical condition, respectively [159]. The resulting MOFs had disparate structures, as Zn-MOF and Co-MOF possessed 1D chains but with different directions, while Mn-MOF exhibited 3D architecture.

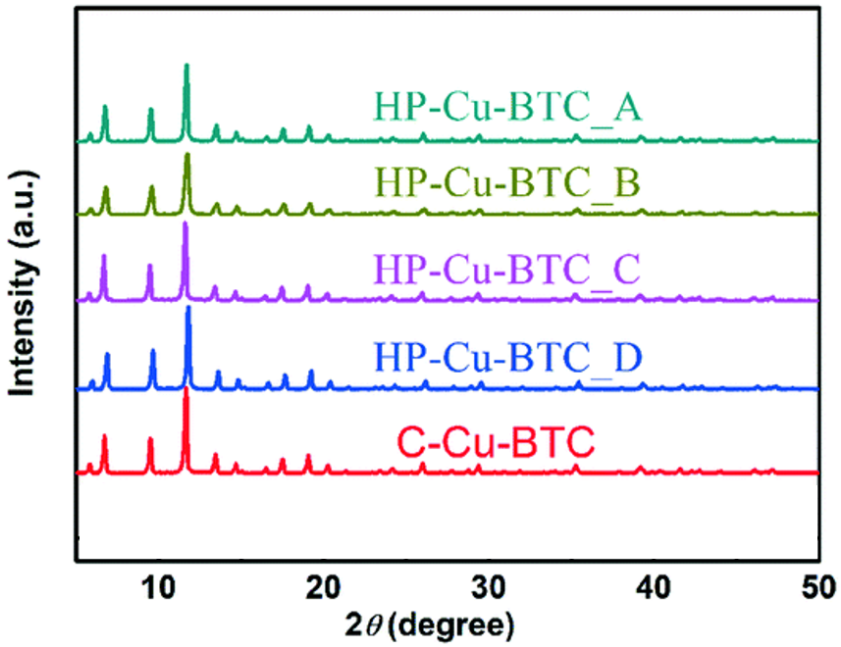


Figure 2.9. The XRD patterns of HP-Cu-BTC_A, HP-Cu-BTC_B. HP-Cu-BTC_C, HP-Cu-BTC_D and C-Cu-BTC, indicating the structure of Cu-MOFs not being influenced by the template concentration. Reproduced from Ref. [157] with permission from The Royal Society of Chemistry.

Table 2.4. The physical and chemical properties of Cu-MOFs developed at various concentrations of auxiliary template reagent. Reproduced from Ref. [157] with permission from The Royal Society of Chemistry.

Sample	C-Cu-BTC	HP-Cu-BTC-A	HP-Cu-BTC-B	HP-Cu-BTC-C	HP-Cu-BTC-D
Ratio of SDBS to Cu^{2+}	-	0.08	0.25	0.35	0.40
Specific Surface Area ($m^2\ g^{-1}$)	1360	1216	812	659	1218
Specific Volume ($cm^3\ g^{-1}$)	0.63	0.59	0.54	0.55	0.59
Pore Diameter (nm)	0.85	24	18	12	7
Conversion rate (%)	17.3	20.2	25.0	25.7	-

To study the effect of solvents as well as the volume ratios on the morphologies and size of MOFs, Co-MOFs were developed using various mixed solvent systems and their electrochemical performance was investigated in a three-electrode system [160]. According to XRD patterns (**Fig. 2.10**), all Co-MOFs exhibited excellent crystallinity with high purity. Meanwhile, it could be evidently observed that MOF samples synthesized using different mixture solvents exhibited significant variations in terms of morphologies and crystal sizes, as indicated in the SEM images. Co-MOF synthesized in pure dimethylformamide (DMF) exhibited uneven size of rod architecture but with a smooth surface. Nano-needles and rods hybrids were formed as ethanol was mixed with DMF, in which the widths of nanoneedles and nanorods were less than 2 micrometers. It clearly indicated that the hydrogen bond strength of the solvent was enhanced by ethanol molecules. When the water molecules were involved, bulk rods with length about 15 micrometers were viewed, which might be attributed to the slow nucleation. Interestingly, nano needles appeared again as ethanol was used alone, which illustrated that it was beneficial to employ ethanol as solvent for the synthesis of nano-sized MOFs. In addition, the Co-MOF prepared in the mixture of water, ethanol and DMF demonstrated a hybrid structure with nanoneedles and rods structures. The morphological variation could be further corroborated with the Brunauer-Emmett-Teller (BET) surface areas analysis. As summarized in **Table 2.5**, the specific surface areas for Co-MOF/D-W-E, Co-MOF/D-W, Co-MOF/D, Co-MOF/E and Co-MOF/D-E were 1.81, 2.27, 3.84, 5.73 and 31.98 m^2 g^{-1}, respectively. The specific capacitances were 393.4, 428.3, 626.9, 654.4 and 958.1 F g^{-1} for Co-MOF/D, Co-MOF/D-W-E. Co-MOF/D-W, Co-MOF/E and Co-MOF/D-E over a current density of 2 A g^{-1}, respectively. Co-MOF/D-E sample was found to have the most desirable cyclic stability with a capacitance retention of 92.3% over 3000 cycles. It is clearly demonstrated that the large surface area and pore size of Co-MOF were responsible for improving the specific capacitance, while the solvent used affected the structural stability. Therefore, all these results confirmed the significance of solvent by either acting as a template reagent or structure directing reagent in the synthesis of MOFs.

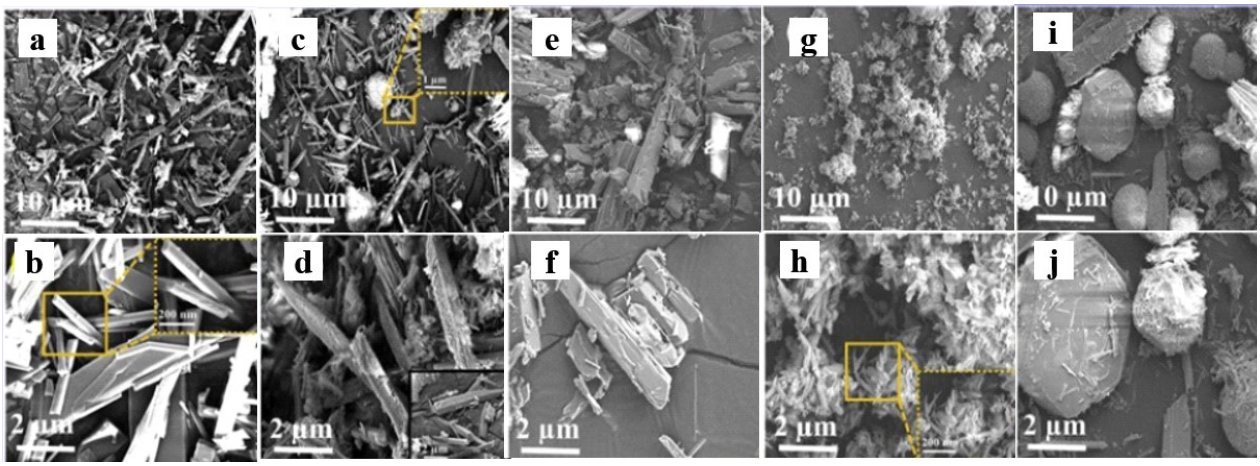


Figure 2.10. The SEM images of Co-based MOFs prepared with different solvent mixtures: (a, b) DMF, (c, d) mixture of DMF and ethanol, (e, f) mixture of DMF and water, (g, h) ethanol and mixture of DMF, (i, j) ethanol and water. Reused with permission from Ref. [160]. Copyright 2018, Elsevier.

Table 2.5. The textural and electrochemical properties of Co-based MOFs prepared utilizing different solvent combinations. Reproduced with permission from Ref. [160]. Copyright 2018, Elsevier.

Samples	BET areas ($m^2\ g^{-1}$)	R_{ct} (Ω)	Specific Capacitance ($F\ g^{-1}$)
Co-MOF/D-W-E	1.81	10.3	428.3
Co-MOF/D-W	2.27	7.5	626.9
Co-MOF/D	3.84	4.7	393.4
Co-MOF/E	5.73	2.6	654.4
Co-MOF/D-E	31.98	1.7	958.1

Lately, the impact of the solvent on the crystal architecture and properties of ZIF-8 was investigated [155]. The results indicated that MOF synthesized via solvothermal method in DMF exhibited relatively high product yield and crystallinity, consequently, a lower pore volume and specific surface area was obtained as compared to that in methanol. Nonetheless, these samples synthesized by solvothermal were found to possess high stability and less defect due to the high crystallinity and more organic linkers, proven by the thermal gravimetric analysis (TGA) as shown in **Fig. 2.11**. These might be ascribed to three reasons. (a) the low interfacial tension of DMF could enhance the crystallization of ZIF-8, while water with the highest interfacial tension might create a high surface barrier for nuclei and crystallization. (b) the extreme high polarity of water was not beneficial for the synthesis of ZIF-8 since the formation of ZIF-8 could be postponed and hydrolyzed. DMF exhibited slightly higher dielectric (38) and dipole moment (3.82) than methanol (33 & 1.7), which could help to dissolve metal salts in the reactants, subsequently resulted in a large number of nuclei and a quicker nucleation process. The reaction schemes are illustrated in **Fig. 2.12**. (c) Methanol with lowest viscosity (0.544 mPa·s) among DMF (0.802 mPa·s) and water (0.8949 mPa·s) might allow further mass transfer and lead to a high crystalline rate. Thus, defects could be induced by the high crystal growth rate.

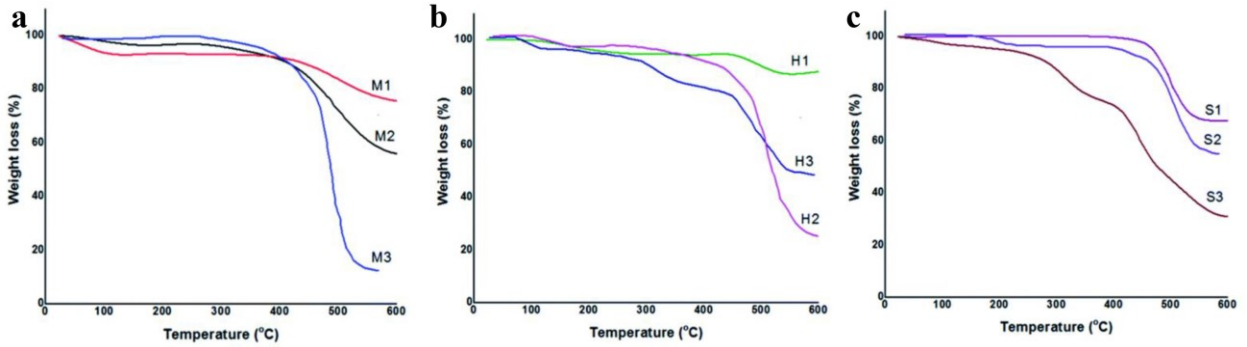


Figure 2.11. TGA of ZIF-8 synthesized in various solvents. (a) Mixing method, (b) solvothermal method and (c) sonochemical method. Reproduced from Ref. [155] with permission from the Royal Society of Chemistry.

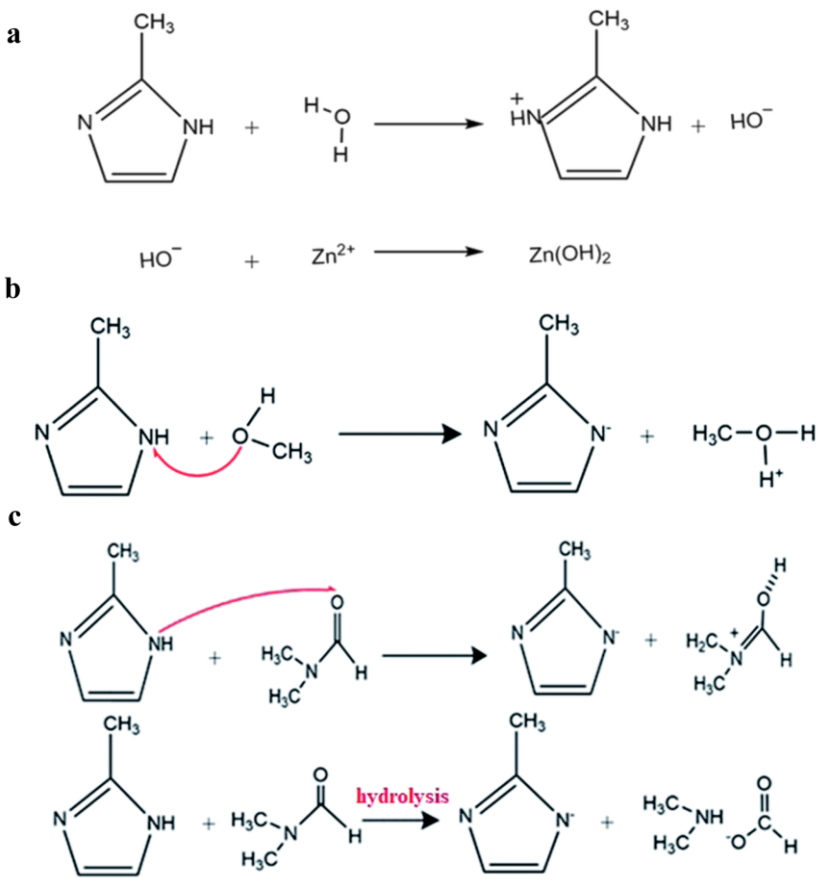


Figure 2.12. Reaction scheme of (a) the synthesis of ZIF-8 in water, deprotonation of Hmim in (b) methanol and (c) DMF. Reproduced from Ref. [155] with permission from the Royal Society of Chemistry.

Additionally, the adsorption properties of MOFs synthesized at different solvent systems can also be changed by the variation of texture properties. To study the impact of MOFs developed in different solvent systems (pure DMF, mixture of ethanol and D.I. water (v/v = 1 : 1) on the adsorption of CO_2, Zn-based MOFs were fabricated via solvothermal approach [161]. It was found that the as-synthesized Zn-BTC had different morphology, thermal stability as well as CO_2 adsorption capability. Firstly, Zn-BTC synthesized in ethanol and D.I. water possessed well-defined cuboidal morphology, whereas it expressed random architecture in DMF. Secondly, the sample developed using DMF exhibited higher thermal stability but with lower capability to absorb CO_2, which might be caused by the strong bond between Zn^{2+} and carboxylate groups, leading to densified layers on the surface and lower the adsorption of CO_2. This was further confirmed by the BET surface area where a high specific surface area (272.64 m^2 g^{-1}) was acquired for the samples synthesized in the mixture of ethanol and D.I. water, which was much higher than that developed in DMF (137.4 m^2 g^{-1}). As a result, Zn-MOF developed in DMF had a lower ability to absorb CO_2 as it exhibited a lower specific surface area as compared to that developed in the mixture of D.I. water and ethanol.

2.2.4 Temperature

Different synthesis temperatures could offer different energy for the formation of coordination bonds, it is hence able to influence the interactions between metal cations and organic linkers. When an identical solvent was employed, different MOFs could be formed at different temperatures [162, 163]. The reaction temperature can affect the solubility of organic linkers, especially in hydro/solvothermal synthesis [164]. Hydrothermal synthesized materials usually exhibit favorable morphologies and crystalline sizes since the synthesis is carried out in a sealed container at high temperature and pressure (T > 100 ℃ and P > 1 atm), at which the reagents, such as 3,3′,4,4′-biphenyltetracarboxylic acid (H_4bptc) [165], Thiophene-2, 5-dicarboxylic acid [166], are found to have high solubility. The desired MOFs materials cannot be formed when the temperature is too low, whereas the formed MOFs were possible to be destroyed at a high temperature [167]. As a consequence, it is possible to adjust the morphologies and architectures of MOFs through controlling the reaction temperatures.

The effect of synthesis temperature on the morphology of MOF is more dominant than on the formation of crystal. The impact of temperature on the synthesis of Co-MOF-74 via hydrothermal route was investigated by Jiang and coworkers [168]. The PXRD patterns indicated that Co-MOF-74-100, 120, 135 and 150 exhibited an identical architecture (the postfix number, such as 100, 120 and 150, means the synthesis temperature, the same as following). However, the Co-MOFs obtained at different temperatures showed different shapes. Co-MOF-74-100 exhibited flower-like shape, which was attributed to the aggregation of small polyhedral crystals, while the rest had bar-like morphologies with different sizes. The corresponding lengths were approximately 25, 35 and 40 μm, and diameters were 5, 8 and 6.5 μm for Co-MOF-74-120, 135 and 150 (**Fig. 2.13**). Similar results were demonstrated in another study involving the fabrication of Co-MOFs [163]. Similarly, Co-MOFs with different morphologies and sizes were developed at different temperatures in a solvothermal synthesis. Temperature change did not have an apparent effect on the crystallinity, but on the textural characteristics and electrochemical performance of the resultant MOFs. The specific surface areas of the as-developed Co-MOFs were in an order of Co-MOF-150 > Co-MOF-210 > Co-MOF-180 > Co-MOF-120, while the micropore areas were in the sequence of Co-MOF-150 > Co-MOF-120 > Co-MOF-180 > Co-MOF-210. As for the electrochemical performance, however, showed a different order as follows: Co-MOF-150 > Co-MOF-120 > Co-MOF-210 > Co-MOF-180. The outstanding charge storage performance of Co-MOF-150 was attributed to the large specific surface area and specific pore area, beneficial for enhancing the ionic transport efficiency boosting the Faradaic redox reactions [169]. Furthermore, the control of activation temperature determines the removal of solvent reagent in pores and coordination. Four different temperatures were applied on three types of iron-based MOFs for activation purposes [170]. The activation temperature (below the decomposition point) did not have too much impact on the crystallinity of iron-based MOFs (MIL-88B and MIL-101), but greatly influenced the shapes and textural properties of MOFs. These results implied that even though the synthesis temperature has lower impact on the structures of as-developed MOFs, the variation of temperature does have crucial influence on the textural and chemical characteristics.

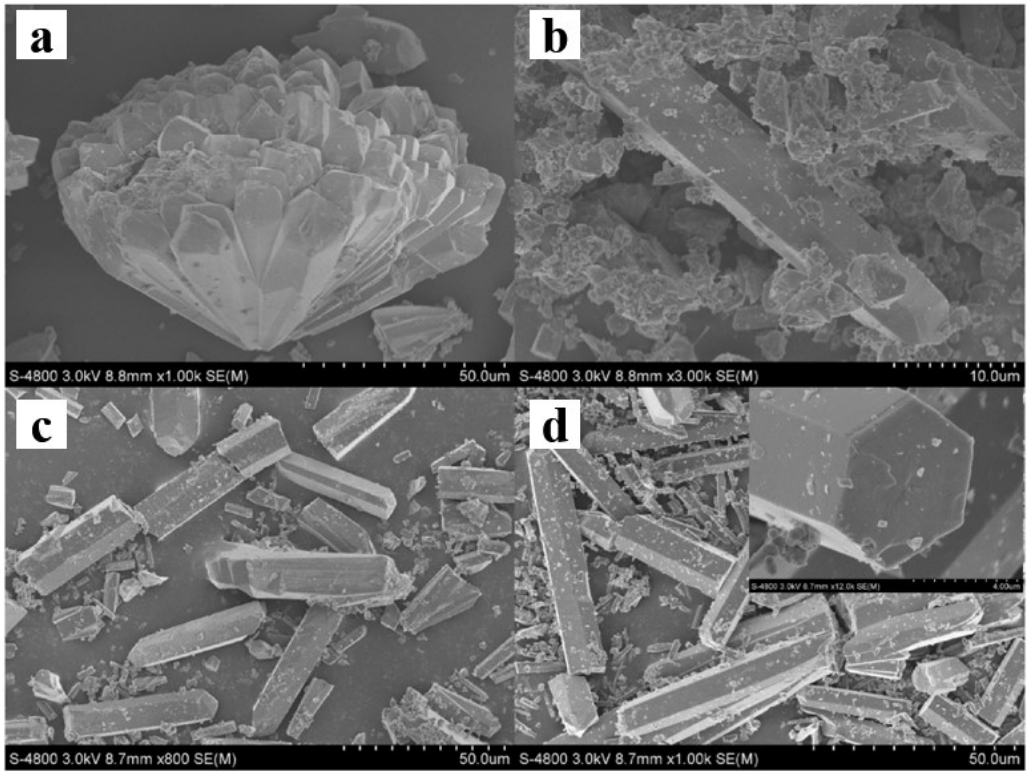


Figure 2.13. The SEM images of Co-MOF-74 with different morphologies synthesized at (a) 100 ℃, (b) 120 ℃, (c) 135 ℃ and (d) 150 ℃, insert: the cross section of Co-MOF-74. Reused with permission from Ref. [168]. Copyright 2016, Elsevier.

Metal-organic frameworks assembled at different temperatures could have disparate morphologies and architectures. A porous Nickel(II) Dihydroterephthalate MOF was developed at 90 ℃, 110 ℃ and 130 ℃ with the assistance of microwave [162]. The corresponding MOF materials were denoted as MW-90, MW-110 and MW-130, accordingly. It was found that MW-90 was well crystallized and exhibited slightly smaller particle size compared to the other two samples, mainly due to the higher synthesis temperature. This might be caused by the quick nucleation and crystallization of precursors at higher temperatures. Similarly, MW-130 exhibited a lower BET surface area of 913 $m^2 g^{-1}$ and followed by MW-100 of 1050 $m^2 g^{-1}$ and MW-90 of 1148 $m^2 g^{-1}$. According to Yu's study [171], they demonstrated that the reaction temperature had influential impact on the architecture formation of MOFs. Specifically, polymer $(Co(imta)_2)_n$ was developed as the synthesis temperature was between 95 - 120 ℃, and a 3-D architecture was observed around 105 ℃. Nevertheless, polymer $(Co(imta)_2)_n$ was transferred into complex $(Co(imta)_2(H_2O)_4)\cdot 2H_2O$ as the temperature was in a range of 130 – 160 ℃. In another study, a series of MIL-53(Fe) were obtained at different temperatures [167]. The resulting MOF materials were found to exhibit great variation in both physical and chemical properties. When the temperature was lower than certain critical value, such as 150 ℃ for MIL-53(Fe), metal clusters and organic linkers were found not able to coordinate successfully, leading to poor product formation. On the contrary, when the synthesis temperature was too high (higher than 170 ℃), the structure of the samples could be destroyed. The as-obtained MOFs were employed as catalyst and the corresponding performance was illustrated by decolorization of Orange G (OG) as shown in **Fig. 2.14**. The removal efficiencies of MIL-53(Fe)-150 and MIL-53(Fe)-170 were similar, and

followed by MIL-53(Fe)-200 and MIL-53(Fe)-220. The results indicated that the synthesis of MOFs had an optimum temperature range. If the temperature is higher than the critical temperature or lower than the formation temperature, the corresponding MOFs cannot be assembled successfully.

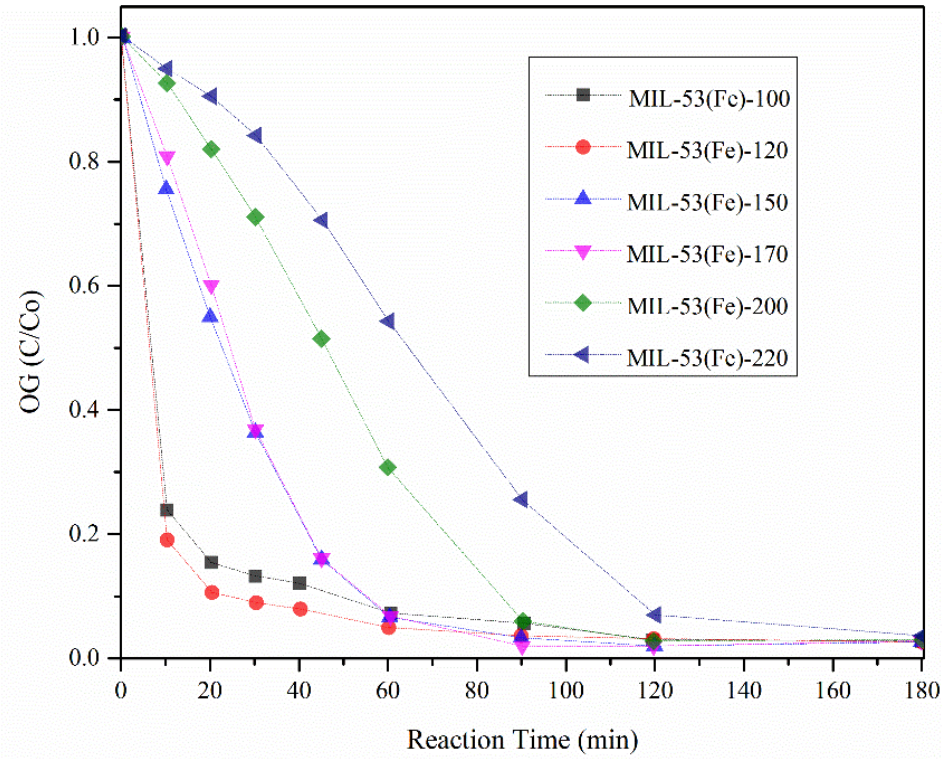


Figure 2.14. The OG degradation curves by different MIL-53(Fe), developed at different synthesis temperatures utilized in activated persulfate systems. Reproduced with permission from Ref. [167]. Copyright 2018, Elsevier.

2.2.5 pH

Besides aforementioned parameters, pH also has a remarkable impact on morphologies and structures of MOFs. It not only plays a crucial role in determining the coordination mode of carboxylic ligands, but also controls the architectures of the resulting MOF materials [172]. A slightly lower pH value resulted in MOFs of higher purity, while a higher pH value could lead to a higher dimensionality [173, 174]. When pH value is low (< 2), the hydrogen and covalent bonds could be coordinated to form compounds. On the other hand, small solvent molecules are not able to occupy the coordinative metal centers at high pH, leading to the formation of multi-dimensional framework structures linked by covalent bonds. In addition, it is noteworthy that the functional groups in organic ligands could be reversibly deprotonated or protonated through tuning the pH values of the reaction systems. Therefore, it is possible that there is a reversible transformation of the resulting MOF architectures. However, MOFs could not be formed in strongly basic solution [173]. Additionally, through altering the pH value, the resulting materials could exhibit various colors as well [175]. **Fig. 2.15** shows that Zn-based MOFs with various morphologies were developed at different pH values.

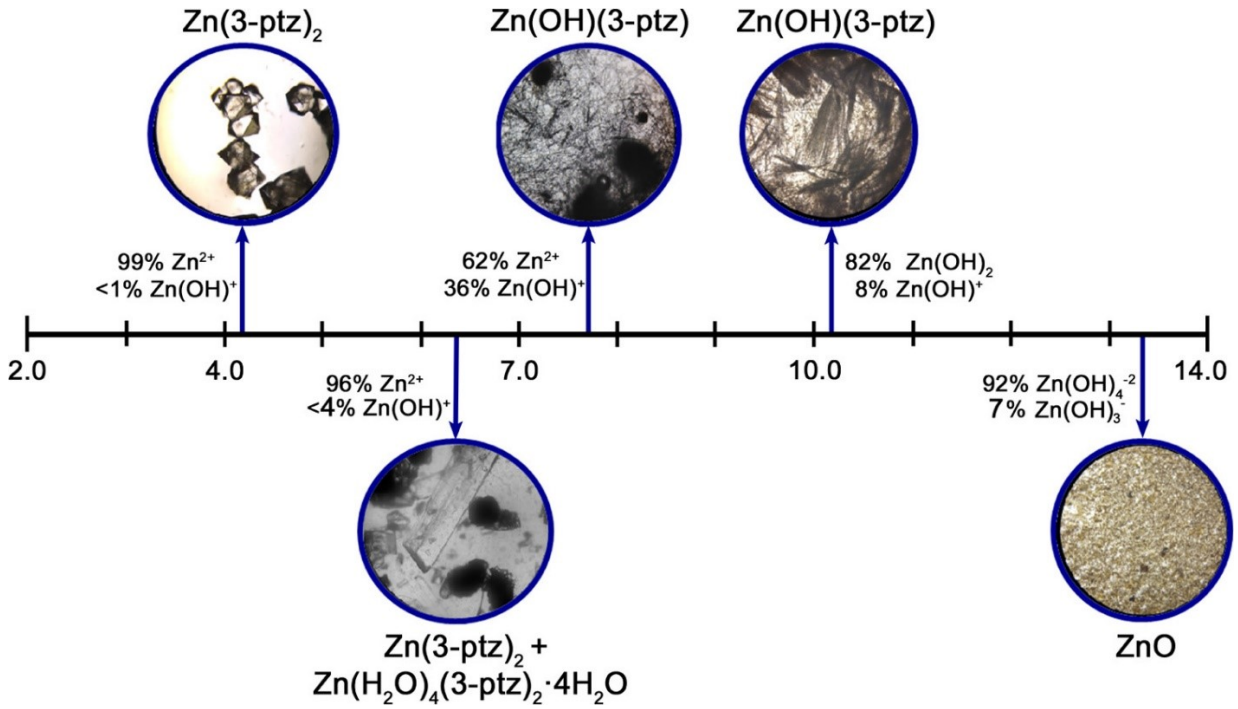


Figure 2.15. Zn-MOFs synthesized under various pH conditions, in which the ionic components in the solvent with corresponding pH values are labelled. This illustrates that the synthesis environment at different pH has a crucial role in the morphologies of resulting MOFs. Reproduced with permission from Ref. [173]. Copyright 2018, American Chemical Society.

The metal clusters and organic ligands could connect in different ways under different pH environments. For instance, aluminum ions and pyromellitic acid combined via μ_2-hydroxo corner of AlO_6 octahedra at pH values of 2.0 and 1.4 to form MIL-118 and MIL-121, respectively. However, two μ_2-hydroxo groups would be linked to develop MIL-120 at pH 12.2 [176]. As the pH values rose from 1.4, 2.0 to 12.2, the number of carboxyl oxygen-atoms coordinated with Al^{3+} increased from 4, 6 to 8 as well. The corresponding MOFs were MIL-121, MIL-118 and MIL-120. When the pH value was changed from 5 to neutral (pH 7), the structure of Mg-based MOF was changed from a 1D zigzag chain to a 3D architecture, in which the yields increased from 35% to 45% [174]. Moreover, Zn-based MOFs followed a similar trend under different pH conditions. The well-defined octahedra crystals were under acidic environment with high purity, while thin and long microrods were obtained under alkaline condition [173]. It was found that 3D MOF bis(5-(3-pyridyl)tetrazolato)zinc(II) was formed at pH 4.1 due to the large amount of octahedral Zn^{2+} ion existing in strong Lewis acid. As the pH of solvent was slightly below 7, a mixture of 3D MOF and $Zn(H_2O)_4(3\text{-ptz})_2\cdot 4H_2O$ was obtained. Under nonacidic conditions, another mixture of $Zn(H_2O)_4(3\text{-ptz})_2\cdot 4H_2O$ and 2D MOF Zn(OH)(3-ptz) was generated. When the pH value was between 10 and 12, the formation of 2D MOF microrods was reported in the same study. However, metal oxide (ZnO) was synthesized as the pH higher than 12 (the SEM images of products at different pH are illustrated in **Fig. 2.16**) The reason behind could be the change of ionic components with increasing pH values as follows: Zn^{2+} (pH 4.1) → $Zn(OH)^{+}_{aq}$ (pH 6.5) → $Zn(OH)_{2\ aq}$ (pH 7.0) → $Zn(OH)^{-}_{3\ aq}$ (pH 7.6) → $Zn(OH)^{2-}_{4\ aq}$ (pH 10.3) (Fig. 13).

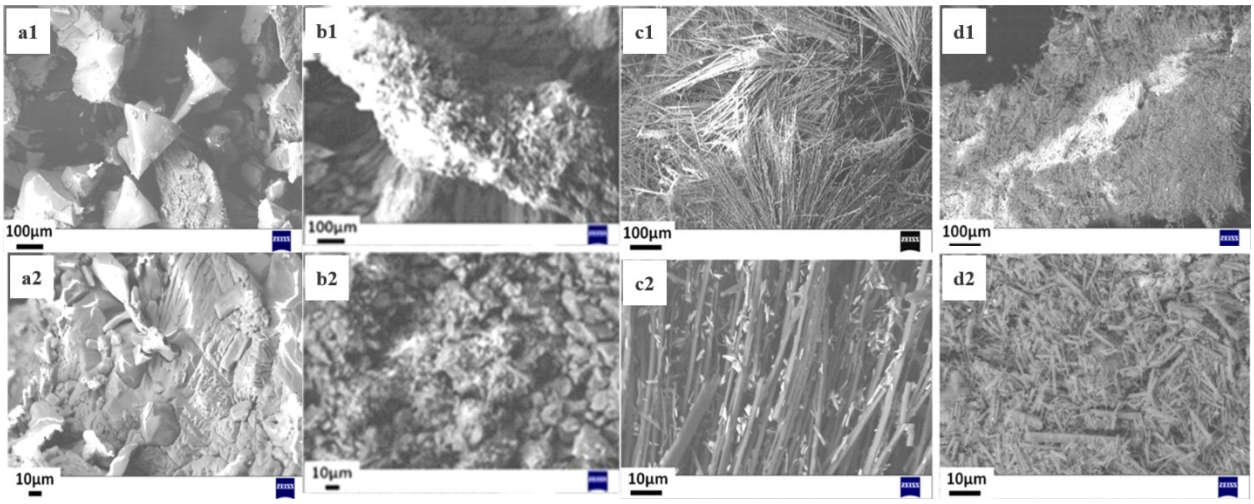


Figure 2.16. The SEM images of zinc-based samples obtained at (a1, a2) pH 4.1, (b1, b2) pH 6.5, (c1, c2) pH 7.6 and (d1, d2) pH 10.3, respectively. Reused with permission from Ref. [173]. Copyright 2018, American Chemical Society.

Different pH conditions could result in disparate framework architectures due to the change in the coordination modes of carboxylic organic linkers. The resulting samples were found to exhibit different properties, particularly in luminescent and thermal stability. Approximately 0.1 mmol $CdCl_2 \cdot 2.5H_2O$, 0.1 mmol Hctpy (4'-carboxy-4,2':6',4''-terpyridine) and the same amount of oxalic acid were employed to develop Cd-MOFs by heating to 160 ℃ for three days and cooling down at a rate of 5 ℃ h^{-1} except varying pH values [172]. It was found that the resultant products were totally different, $(Cd_2(ctpy)_2(ox))_n$ and $(Cd_2(ctpy)_4)_n \cdot 2nH_2O$ were obtained at pH values of 5.5 and 7.5, respectively. The results also indicated that the decomposition temperature of resultant $(Cd_2(ctpy)_4)_n \cdot 2nH_2O$ was 400 ℃, while $(Cd_2(ctpy)_2(ox))_n$ as another MOF material decomposed at 420 ℃. To further investigate the impact of pH, Seoane and coworkers [177] changed the pH from 2.1 to 2.7 in their study. When starting pH of 2.1 was utilized, MIL-110 was developed with elongated hexagonal crystals, but with impurities. MIL-100 was dominant with a well-defined octahedral shape in the pH range of 2.3 – 2.5, whereas a mixture of MIL-96 and MIL-100 with small octahedra and hexagonal crystals was generated at a pH higher than 2.5. This is demonstrated by the SEM images of various samples developed over different pH values, as shown in **Fig. 2.17**. It illustrates that higher starting pH would lead to the formation of hierarchical MOF materials owing to the small aggregation and quick ligand deprotonation. The BET surface areas of these MOFs were reported to be 1365 $m^2\ g^{-1}$, 1970 $m^2\ g^{-1}$ and 990 $m^2\ g^{-1}$ at pH values of 2.1, 2.4 and 2.7, respectively. Three complexes, namely $(Co_2(L)(HBTC)_2(\mu_2\text{-}H_2O)(H_2O)_2) \cdot 3H_2O$ (**1**), $(Co_3(L)_2(BTC)_2) \cdot 4H_2O$ (**2**) and $(Co_2(L)(BTC)(\mu_2\text{-}OH)(H_2O)_2) \cdot 2H_2O$ (**3**) were synthesized in another study via hydrothermal method at pH 5, pH 7 and pH 9, respectively [175]. Specifically, complexes **1** and **2** exhibited the same monoclinic structures, whereas **1** had a space group of P2/c and C2/c for **2**. However, **3** was found to possess a crystal system of orthorhombic and a space group of Pccn, which was entirely different from complexes **1** and **2**. According to UV-visible spectra, the reflection of 1 and 2 was 506 and 550 nm, respectively. The crystal and structural refinements of these three complexes are summarized in **Table 2.6**. Therefore, it is evidenced that pH could affect the architectures and morphologies of MOF materials, leading to the alteration of either physical (such as surface areas, pore sizes, colors) or chemical properties (like luminescent and thermal stabilities).

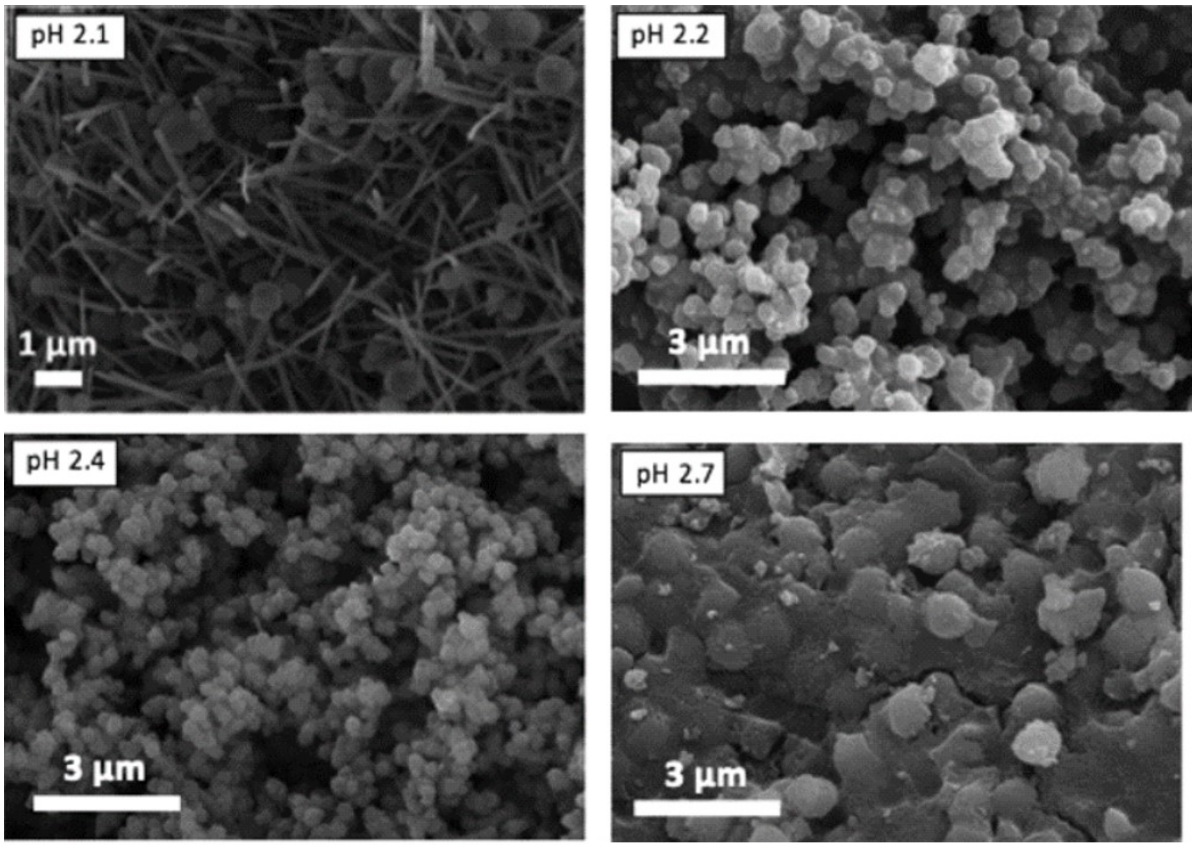


Figure 2.17. The SEM images of MIL-110 (pH 2.1), MIL-100 (pH 2.2 and pH 2.4) the mixtures of MIL-96 and MIL-100 (pH 2.7). Reproduced with permission from Ref. [177] – Published by The Royal Society of Chemistry.

Table 2.6. The crystallinity of MOF samples synthesized at different pH. Reproduced from Ref. [175] with permission from The Royal Society of Chemistry.

Sample	**1**	**2**	**3**
pH	5	7	9
Crystal System	Monoclinic	Monoclinic	Orthorhombic
Space Group	P2/c	C2/c	Pccn
a(Å)	15.9990(15)	27.882(3)	20.0960(10)
b(Å)	10.6917(14)	13.2793(16)	23.0880(10)
c(Å)	14.4959(19)	18.463(2)	14.6160(10)
β (°)	116.938(8)	107.198(2)	90.00
V (Å^3)	2210.6(5)	6530.2(14)	6781.5(6)
Z	2	4	8
Color	Pink	Purple	Brown

2.3 The Application of MOF Materials in SCs

To date, a large number of MOF-based materials have been synthesized and applied across a wide array of fields. For instance, they can be utilized for separation and adsorption processes, serve as photocatalysts in chemical applications, and play a crucial role in drug delivery [25, 108, 119, 140, 178]. Nevertheless, most of them are limited to low-valence transition metal ions. While MOFs comprising high-valence transition metal ions are generally believed to exhibit enhanced electrochemical performance, only limited literatures proved this feature. Typically, the electrochemical performance of MOF-based SCs is dominated by the selection of electrode active materials, in which these active materials should exhibit attractive properties such as large specific surface areas, high porosity and excellent electric conductivity. In general, MOF-based materials are classified into three categories in the practical applications: (a) Pristine MOFs which are directly exploited after being synthesized through various approaches. (b) Corresponding TMOs are obtained by calcination of MOF materials. (c) Pyrolysis of MOFs to nano-carbon materials where these carbon materials employ favorable conductivity and stability [45, 179, 180].

2.3.1 The Electrochemical Performance of Pristine MOFs

High-valence metal ions such as Zr^{4+}, Cr^{3+}, Fe^{3+} are usually viewed as favorable cations to form stable coordination bonds among the resulting MOF materials since they possess high coordination numbers and charge densities. The problem faced is that only limited studies have been done on these materials. Various studies have been proceeded on low valence-based MOFs, such as Mn^{2+}, Cu^{2+}, Zn^{2+}, Co^{2+} and Ni^{2+}. Nonetheless, the majority of pristine MOF materials exhibit low electrical conductivities and unstable structures during the long-term charging and discharging cycles.

2.3.1.1 Zr-based MOFs

UiO-66 as a Zr-based MOF has been studied recently as electrode material for electrochemical capacitors, owing to its unique stability feature in aqueous environment [181]. Nonetheless, the potential of the Zr-based MOFs as effective electrode material is greatly hampered by its low electrical conductivity and microporous structure with limited ions mobility [182, 183]. Hence, to tackle these shortcomings, UiO-66 material with hierarchical porous structure was prepared through solvothermal method at atmospheric pressure (**Fig. 2.18**) [184]. The electrochemical behavior was tested in a three-electrode system in 6 M KOH. The specific capacitance of the as-synthesized material was 849 F g^{-1} at a current density of 0.2 A g^{-1}, significantly higher than the bare UiO-66 material (101.5 F g^{-1}) with microporous structure. This clearly indicates that the hierarchical porous structure was beneficial to greatly improve the electrochemical performance of UiO-66. The unique architecture was not only able to enhance the specific surface area and volumes, but it has also shortened the ionic migration distance and decreased the diffusion resistance between the electrolyte and reactive sites of the electrode material. It is essential to ensure unimpeded channels for charge transfer process to take place and speed up the redox process. The recorded energy density and power density of this material was 32 Wh kg^{-1} and 240 W kg^{-1}, respectively.

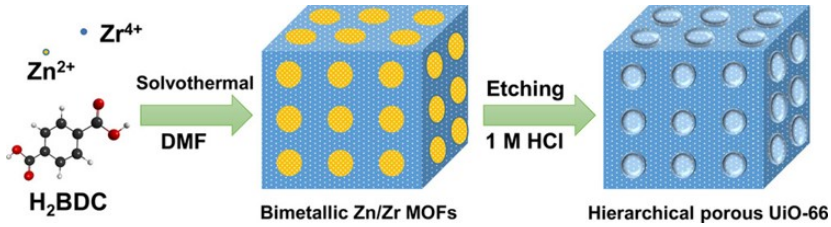


Figure 2.18. Schematic illustration of the synthesis of UiO-66. Reprinted with permission from Ref. [184]. Copyright 2017, American Chemical Society.

Another similar study was conducted with improved properties, while Zr-MOFs were synthesized without the addition of $Zn(NO_3)_2$ [185]. It delivered an electrochemical capacitance of 1144 F g^{-1} at a scan rate of 5 mV s^{-1}, which was much higher than that of UiO-66. This is ascribed to two main reasons: Firstly, the homogeneous Zr-MOFs with small particle sizes of 100 nm could be beneficial to enhance the BET surface area, which was 1047 m^2 g^{-1}. Such a high surface area could efficiently store large number of charges and eventually improve the capacitive performance. Secondly, the 3D structure of Zr-MOFs could reduce the diffusion resistance of the electrolyte and provide smooth channels for ion transport, since the R_s was only 0.42 **Ω**. More importantly, it could maintain 57.2% of its initial capacitance after 2000 cycles at 10 mV s^{-1} in alkaline environment, suggesting the high stability of the electrode active materials. In addition, the stability of Zr-based MOFs materials for SCs electrodes can be further enhanced through a careful selection of organic functionality and control of the nanocrystals. For instance, $Zr_6O_4(OH)_4$-$(BPYDC)_6$ (MOF-867) has been successfully synthesized and was employed as SCs electrodes materials [151]. It was found that the areal capacitance was 5.085 mF cm^{-2}, which is 10 times that of graphene (0.515 mF cm^{-2}). Meanwhile, the structure of the active material is fairly stable, approximately 90% of the capacitance could be retained after 10,000 charge/discharge cycles at a current density of 12.7 mA cm^{-2} within the working voltage window of 0 – 2.7 V. This could be attributed to the existence of sp^2 nitrogen atoms, which are capable of significantly enhancing the ionic interactions and ameliorate the electrochemical property.

2.3.1.2 Iron-based MOFs and the related nanocomposites

In general, iron-based MOFs exhibit low conductivity and these materials are seldom to be studied for electrochemical applications, particularly for SC electrode materials. Nonetheless, the relatively low cost of the material has still attracted a number of studies in this area. For example, MIL-88(Fe) on graphene aerogels (GAs) has been developed through in situ growth method [186]. The electrode was able to deliver a high capacitance of 389 F g^{-1} at 1 A g^{-1} in 1 M H_2SO_4 aqueous electrolyte solution, and the rate capability was as high as 90.7% (353 F g^{-1}) at a current density of 20 A g^{-1}. This indicated that the architecture of GA with high porosity and the directed orientation of MOF on graphene sheets could enhance the capacitive performance. MOF-88(Fe) with micropores evidently showed to store electrolyte, while the GA with both meso- and macro-pores improved the efficiency of ion transfer [187]. In addition, the homogeneous distributed rod-like MOFs could provide a large surface area (414 m^2 g^{-1}) and eventually boost the electrochemical capacitance. More significantly, it could maintain 74.4% of its starting capacitance over 10,000 cycles at a current density of 1 A g^{-1} in aqueous-based electrolyte, indicating the superior stability

of the active electrode materials. The direction-oriented architecture of MOFs and the strong interface force were responsible for the excellent stability. Besides, the energy storage property of the as-obtained active material was investigated in sulfuric acid (H_2SO_4) and organic (tetraethylammonium tetrafluoroboratein/propylene carbonate (TEA-BF_4/PC)) electrolytes within a potential window of 0 – 1 V. In 1 M H_2SO_4, the recorded energy density and power density were 36 Wh kg^{-1} and 588 W kg^{-1}, respectively. While in 1 M TEA-BF_4/PC, a much higher power density of 4300 W kg^{-1} was achieved at a high energy density of 27 Wh kg^{-1}.

2.3.1.3 Cu-based MOFs

The Cu-MOFs normally exhibit low electrochemical performance due to the small pore sizes and surface areas. Hence, the studies on MOFs that directly utilized as electrode active materials for SCs are rarely explored. Nonetheless, novel Cu-MOFs with pseudo-capacitive redox metal centers and sufficient interspace for storage and diffusion of electrolyte were investigated. For example, 2D copper-based layered MOFs (Cu-LCP) were synthesized by a slow evaporation approach [188]. The as-obtained Cu-LCP delivered a specific capacitance of 1274 F g^{-1} at 1 A g^{-1}, and a capacitance of 568 F g^{-1} could be achieved when the current density was increased to 20 A g^{-1}, indicating the high capacitance and rate capability of Cu-LCP electrode. The high current capacitive behavior was mainly attributed to the special 2D layered structure with nanorods ranging from 100 nm to 700 nm, which is beneficial to provide large surface area, and hence enhanced the electrochemical performance of Cu-LCP. Moreover, the layered structure not only could provide large surface area with plenty Cu(II) active sites, but also offers sufficient interspace for electrolyte storage and diffusion. The discharge profile was shown in **Fig. 2.19a**, the high electrochemical capacitance was contributed by both electrical double-layer capacitance and pseudo-capacitance. There are two distinctive stages which were observed during the process of discharge: Firstly, a quick voltage drop was observed between 0.5 and 0.35 V, which was caused by the EDLC behavior from the charge separation on the interface of electrode and electrolyte. Secondly, a slow potential decline appeared from 0.35 to 0 V due to the redox activities (pseudo-capacitance) of Cu(II) ions on the large surface area. Moreover, the R_s and R_{ct} were recorded as 0.13 **Ω** and 1.7 **Ω**, respectively. The phase angle of the Nyquist plot was larger than 45°, indicating an excellent accessibility of electrolyte as Cu-LCP offered enough interlayer space. Most importantly, approximately 88% of its starting capacitance could be retained after cycling for 2000 circles over a current density of 2 A g^{-1} (**Fig. 2.19b**), reflecting the excellent stability of Cu-LCP active material. This high stability might be owing to the ferromagnetic interaction between metal centers and bridging tfbdc, hmt molecules, originating from the mixed bridging linkers of hexamethylenetetramine (hmt) and tetrafluoroterephthalic acid (H_2tfbdc). Consequently, the structural stability was strengthened.

In another study, halogen-bridged 3D Cu-MOFs ($(((Cu_2Cl(OH)(L)_2)\cdot(CH_3OH)_4)_n$) with high stability were developed through a solvothermal route, in which the selected organic ligand was a bifunctional ligand, HL: 4,2′:6′,4″-terpyridine-4′-carboxylic acid [189]. The reported specific capacitance of the Cu-MOF electrode was 1148 F g^{-1} at a low current density of 0.5 A g^{-1}, and it still could maintain 886 F g^{-1} at a high current density of 20 A g^{-1}. Such high performance was likely attributed to two main reasons: (a) The 3D porous architecture provided appropriate surface area (302 m^2 g^{-1}) and pore volume (80 cm^3 g^{-1}), which was not only helpful to form an electrostatic charge separation layer and enhanced the facile intercalation/deintercalation of OH^- ions, it has also offered more active sites with redox activities for pseudo-capacitance enhancement. (b) The

existence of oxygen and halogen polar sites on the surface was beneficial to ameliorate the surface properties and enhance electron transfer resulting in a lower electron-transfer resistance. Meanwhile, the decrease of capacitance at a high current density should be ascribed to the low availability of active materials at fast charging cycle. As for the cycling stability, around 90 % of the initial capacitance was retained after 2000 cycles at a high current density of 10 A g^{-1}, as illustrated in **Fig. 2.19c**, suggesting the excellent cyclic stability over continuous charging and discharging.

Moreover, the ohmic electrical resistance of MOF thin-film electrodes can be tuned by the doping strategy on utilizing the electron acceptor molecules. He et al. [190] found the electrical conductivity of Cu-MOF thin film could be improved up to over 40 times by doping with 7,7,8,8-tetracyanoquinododimethane, in which the attained maximum electrical conductivity was 0.463 mS m^{-1}. Owing to the large specific surface area, rich redox-active sites and improved conductivity of the doped Cu-MOF thin films, a remarkable areal capacitance of 95.1 mF cm^{-2} was achieved at a rate of 5 mV s^{-1} for the as-fabricated flexible asymmetric micro-supercapacitors. At the meantime, it delivered a good long-term cycling stability where the capacitance retention was 94.1% after 5,000 cycles at 10 mA cm^{-2}.

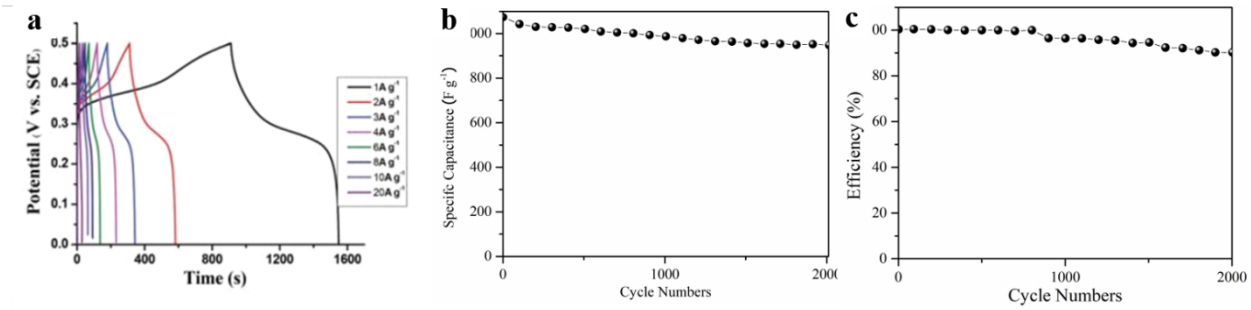


Figure 2.19. (a) The galvanostatic charge-discharge curves of Cu-LCP at various current densities, (b) Cu-LCP in 1 M LiOH and (c) $((Cu_2Cl(OH)(L)_2) \cdot (CH_3OH)_4)_n$ at 6 M KOH. It demonstrates the high stability of Cu-MOF materials as SC electrode materials in different alkaline environment. Reproduced from Ref. [188, 189] with permission from The Royal Society of Chemistry.

2.3.1.4 Mn-based MOFs

Based on the energy storage mechanism of SCs, metal-based nanomaterials are viewed to exhibit higher performance, especially those which possess tunable pose sizes and large surface areas, since it is favorable for quick charge transfer and electrolyte diffusion. Among them, Mn-based MOFs with carboxylic acids linkers are the most promising materials due to the low cost, wide operating potential window and low toxicity [191]. A 3D Mn-MOF was reported by Feng and coworkers in 2020 [192]. The electrochemical performance of the as-developed Mn-MOF electrode material was tested in a three-electrode system in 6 M KOH, it could deliver a maximum capacitance of 433 F g^{-1} at 1 A g^{-1}. The enhanced electrochemical performance was caused by the 3D architectures of Mn-MOFs bridged by carboxylic functional group, which could provide appropriate carriers for charge transfer and conductive channels for electrolyte. In addition, it exhibited good stability and was able to retain 86% of its initial capacitance after 1000 cycle at a current density of 5 A g^{-1}. The capacity was found to decline during the galvanostatic

charge/discharge (GCD) cycles, owing to the shedding or dissolution of active materials in alkaline solution. In another study, a layered and colorless Mn-based MOF (Mn-LMOF: Mn(tfbdc)(4,4'-bpy)(H_2O)$_2$, 4,4'-bpy = 4,4'-bipyridine) was synthesized through a slow volatilization method, and fabricated as electrodes for SCs using different electrolytes [193]. After cycling for 2000 cycles, approximately 92.6% (2 A g^{-1}, 1 M KOH) and 94.6% (2 A g^{-1}, 1 M LiOH) of the initial electrochemical capacitance could be retained, respectively (**Fig. 2.20**). Such excellent cycling stability could be ascribed to the existence of hydrogen bonds, which act as linkers to bond those 2D layers, formed by Mn(II) bridging with $tfbdc^{2-}$ and 4,4'-bpy molecules, into 3D supramolecular structure.

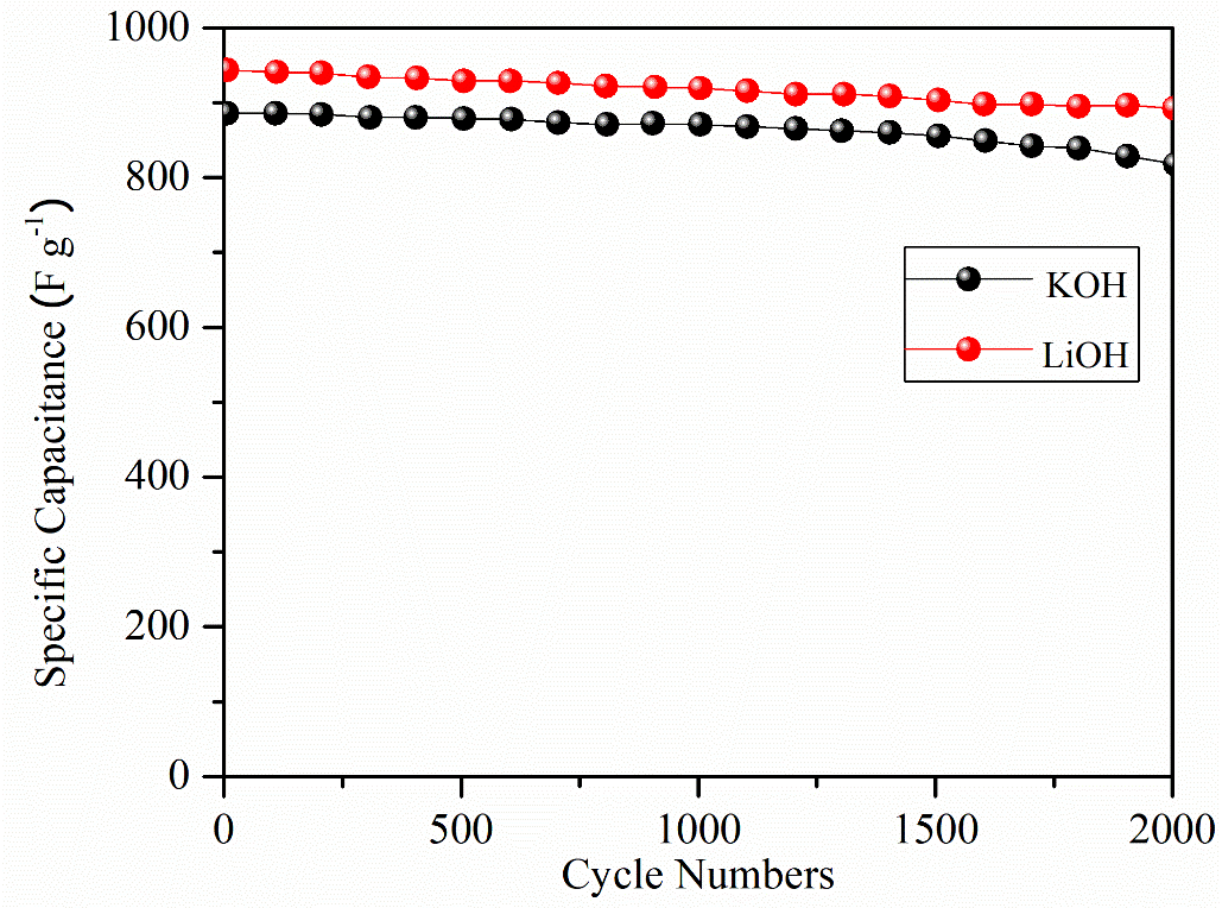


Figure 2.20. The specific capacitance of Mn-LMOF at a current density of 2 A g^{-1} in 1 M KOH and 1 M LiOH, respectively [193]. – Published by The Royal Society of Chemistry.

Pristine Mn-based coordination polymers have attracted lots of attention due to their controllable pore size and high porosity. Nonetheless, their performance in practical application has been limited by the low specific energy density. Hence, HCs with enhanced performance in energy density have been investigated. Through hydrothermal technique, Shinde and co-workers [194] successfully synthesized layered $(Mn(BDC)\cdot nDMF)_n$ with high stability. Meanwhile, the electrochemical performance was tested using a three-electrode system in 2 M KOH, and the electrochemical performance of the nanocomposite is depicted in **Fig. 2.21**. It was found that Mn-

MOF delivered an areal capacitance of 10.22 F cm^{-2} at 1 A g^{-1} within a wide voltage window of 1.2 V (vs. Hg/HgO), and could maintain 5.72 F cm^{-2} as the current density rose to 12 A g^{-1}, indicating high rate capability of Mn-MOF electrode. This could be ascribed to two main reasons: Firstly, the ultrathin nanosheets with a 2D layered architecture of Mn-MOF would ameliorate the accessibility and storage of electrolyte. Secondly, the large surface area (202 m^2 g^{-1}) and high porosity nature of the as-obtained Mn-MOFs effectively provided more active sites and speed up the surface redox reactions. Meanwhile, a low R_s value of 1.11 **Ω** was obtained. This clearly indicates the low resistance and good conductivity of active materials. It could be attributed to three aspects: (a) The mesoporous nature was helpful for ion diffusion. (b) The large surface area to volume ratio enhanced the interactions between electrode active materials and electrolyte, hence the diffusion distance could be reduced. (c) The mesh-like cavities provided enough interspace for ion diffusion during GCD process. More significantly, Mn-MOF could maintain 92.3% of its initial capacitance over 5000 charging and discharging cycles at 10 A g^{-1} (**Fig. 2.21d**, inset). It was due to hydrogen bonding, which not only ensures the consistency of frameworks, but also significantly contribute to cyclic stability.

On the other hand, the as-synthesized Mn-MOF and reduced graphene oxide (rGO) were employed to assemble HC (Mn-MOF//rGO) with a mass ratio of 1 : 0.92 in 2 M KOH solution. Mn-MOF functioned as the cathode while rGO served as the anode. The as-assembled HC possessed a capacitance of 211.4 F g^{-1} at a current density of 5 A g^{-1} within a wide voltage window of 1.5 V, and was able to retain 62% of its starting capacitance when the scanning rate was increased to 40 A g^{-1}, suggesting a superior rate capability. The high-rate capability was contributed by the special 2D layered architecture that facilitates better charge transfer, while the overall conductivity of the device was enhanced by rGO. The HC maintained 81.18% of its initial capacitance after 10,000 cycles at a large current density of 10 A g^{-1}, indicating the long lifespan of this electrode (**Fig. 2.21d**, blue line). The superior performance was attributed to the integration of various characteristics of both 2D layered MOF with mesh-like cavities and rGO. The recorded energy density and power density of this material were 66 Wh kg^{-1} and 441 W kg^{-1}, respectively.

In a similar study, the Mn-MOF-based HC was found to have a longer cycle life when graphene was employed as anode [195]. The BET surface area of the mesoporous material was 102.6 m^2 g^{-1} and the pore volume was 0.78 cm^3 g^{-1}. The high surface area was attributed to the ordered nanorods structure with uniform size. The delivered electrochemical capacitance of the Mn-MOFs microrod electrode was 371 F g^{-1} at a current density of 0.5 A g^{-1} in 6 M KOH. The high capacitance and excellent rate capability were mainly contributed by the high specific surface area and pore volume. The large surface area of Mn-MOFs offered sufficient active sites for electroactive redox activities. The high pore volume provided enough interspace for electrolyte storage and diffusion. Meanwhile, the internal resistance and R_{ct} were 3.112 **Ω** and 0.367 **Ω**, respectively, indicating the relatively high conductivity and quick charge transport. The mesoporous structure with nanorods of the electrode offered more contact areas, while the electrolyte ions diffusion is ameliorated. The Mn-MOF active materials were employed to assemble HC and the performance was tested in 6 M KOH electrolyte solution within a potential window of 1.6 V. The superior stability of Mn-MOF electrode was evidently demonstrated by showing 91.8% of its initial capacitance after 10,000 GCD cycles.

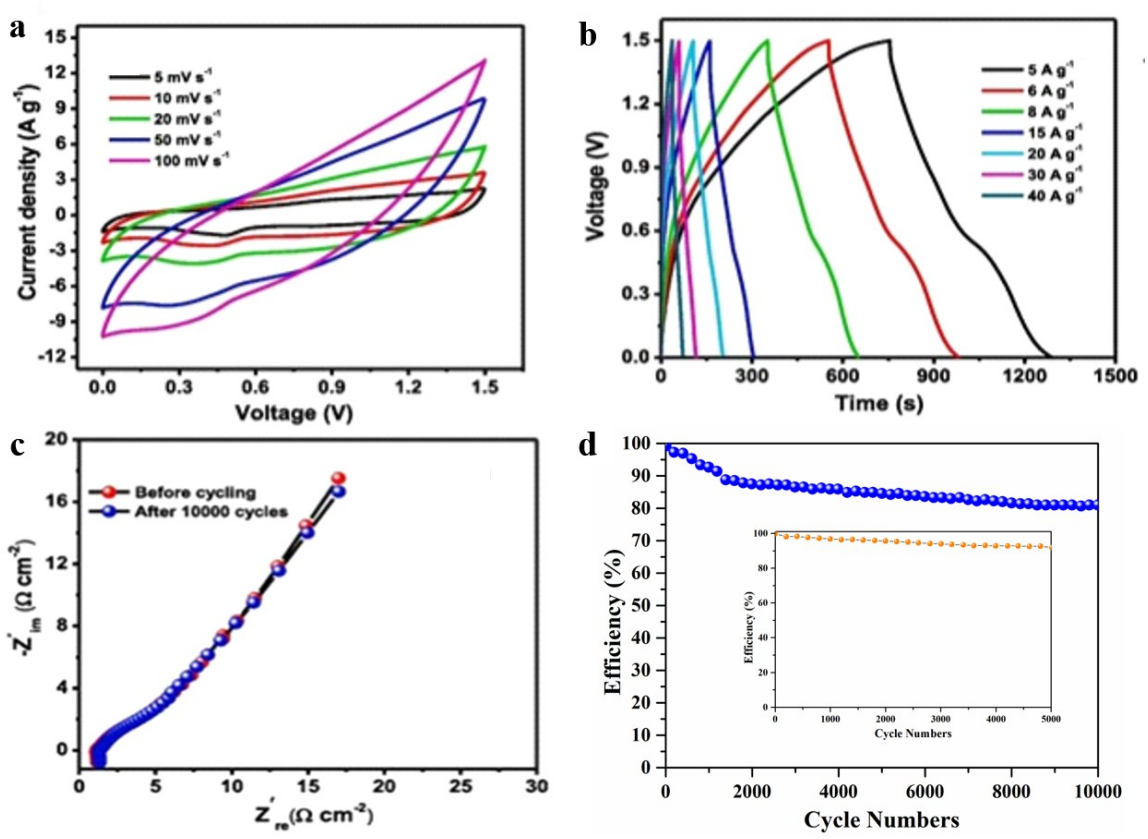


Figure 2.21. (a) The CV diagrams of Mn-MOF with a potential window of 1.5 V over various scan rates. (b) Charging and discharging performance of Mn-MOF electrode under different current densities. (c) The impedance diagram before and after cycling and (d) Plot of capacity retention versus cycle number for Mn-MOF electrode over 5000 cycles (inset) and Mn-MOF//rGO HC over 10,000 cycles (blue line), the corresponding efficiencies are 92.3% and 81.18% for Mn-MOF electrode and HC, respectively. Reproduced with permission from Ref. [194]. Copyright 2020, Elsevier.

Furthermore, Mn-based MOF can also be fabricated into SCs in solid state with a wide potential window, which is potential to be employed in wearable devices. Manganese-1,4-Benzenedicarboxylate MOF (Mn-BDC MOF) was prepared via hydrothermal approach and the as-fabricated electrode possessed a specific capacitance of 177.9 F g^{-1} at 0.5 A g^{-1} in three-electrode system, using 1 M Na_2SO_4 as the electrolyte [196]. During the assembling of SC, polyvinyl alcohol (PVA) - 1 M Na_2SO_4 polymer gel was chosen as the electrolyte instead. In this particular study, the polymer gel served as the separator and electrolyte simultaneously, to ensure the overall cell was in solid state without any leakage. Nonetheless, the as-assembled device could only deliver a capacitance of 64.5 F g^{-1} at the same current density, which is much lower than that in a three-electrode system. The deteriorated capacitive performance was due to the utilization of less active materials and electrolyte in the fabricated cell design. This was still subjected for further optimization and improvement. However, it exhibited a very high-capacity retention percentage (about 98%) over 2000 cycles at a current density of 0.25 A g^{-1}, suggesting a long-term cycling stability. The extraordinary performance of Mn-based MOFs dictates their potential to be applied

as an effective electrode material for SCs, and offers a promising route for the development of future electrochemical energy storage systems.

2.3.1.5 Zn-based MOFs

Aqueous Zn-based batteries and SCs have been recognized as promising candidates for electrochemical energy storage systems due to the low cost, high capacity and environmental friendliness. Nonetheless, the practical applications of Zn-based anodes in aqueous-based electrolyte are limited by the low stability. The undesired dendrite growth during plating and stripping process, unwanted hydrogen evolution and the formation of $Zn(OH)_x$ on the surface are the main shortcomings of Zn-based materials as anodes. This urged the synthesis of Zn@ZIF-8-500 with porous structure through electrochemical depositing with 10.0 mAh cm^{-2} Zn [197]. The HC (Zn@ZIF-8-500//AC) was assembled by employing Zn@ZIF-8-500 as anode and commercial AC as cathode in 2 M $ZnSO_4$. The as-fabricated HC delivered an energy density of 140.8 Wh kg^{-1} at 70 W kg^{-1} and could reach 46.6 Wh kg^{-1} when the power density was increased up to 2850 W kg^{-1}. This high performance was attributed to the device that integrated various characteristics of Zn, ZIF-8-500 and AC. Meanwhile, the as-assembled HC possessed an excellent cyclic stability of 72% after 20,000 cycles at a current density of 4.0 A g^{-1}. This superior stability was owing to the porous ZIF-8-500 that exhibited large surface area (750 m^2 g^{-1}) and pore volume (0.443 cm^3 g^{-1}), which was beneficial to be the host for Zn plating and stripping. It also possessed a small amount of Zn^0 (converted from Zn^{2+} during heat treatment), providing nuclei for the plating of Zn and the high over-potential to reduce hydrogen evolution. Additionally, Zn-8-500 uniformly coated with Zn, which was plated at the first cycle, could function as a substrate for further Zn plating, avoiding the formation of dendrite.

In another study, 2D multi-layered Zn-p-phenylenediamine (Zn-pPDA) MOFs, namely Zn-pPDA MOF-5, Zn-pPDA MOF-8 and Zn-pPDA MOF-12, were synthesized using a facile and green method [198]. These three materials possessed good conductivities, which were 1.05 S cm^{-1} for Zn-pPDA MOF-5, 0.7 S cm^{-1} for Zn-pPDA MOF-8 and 0.3 S cm^{-1} for Zn-pPDA MOF-12. Meanwhile, R_s and R_{ct} values were 4.03 Ω and 0.43 Ω for Zn-pPDA MOF-5, 4.15 Ω and 0.54 Ω for Zn-pPDA MOF-8, 4.36 Ω and 0.6 Ω for Zn-pPDA MOF-12, respectively. Both the R_s and R_{ct} values increased as the concentration of $Zn(acac)_2$ raised, suggesting that the electrical conductivity of Zn-pPDA MOFs was diminished by the $Zn(acac)_2$ residues. The possible factors are: (a) Fourier transform infrared spectroscopy (FTIR) demonstrated that the amount of unreacted acetylacetonate/triad salt negative ions went up as the concentration of Zn triad salt rose, while there was no excess of $Zn(asas)_2$ in Zn-pPDA MOF-5. (b) Zn-pPDA MOF-5 exhibited a 2D layered morphology, the compact layered structure prohibited the infiltration of $Zn(asas)_2$.

These three active materials were employed as positive electrodes and GC was used as negative electrodes. The electrochemical performance was tested in 1 M KOH with a potential gap of 1.5 V (0 – 1.5 V). The delivered energy densities were 62.75 Wh kg^{-1} for Zn-pPDA MOF-5, 57.52 Wh kg^{-1} for Zn-pPDA MOF-8, and 52.25 Wh kg^{-1} for Zn-pPDA MOF-12, respectively. In addition, the Zn-pPDA MOF-5//GC, Zn-pPDA MOF-8//GC and Zn-pPDA MOF-12//GC devices retained 96.2%, 96.81% and 96.79% of their initial capacitances after 2000 cycles at 1 A g^{-1}, respectively. These results indicated the high energy density and stability of Zn-pPDA MOF-5 were actually caused by the 2D multi-layered structure, which enhanced the surface area and eventually ameliorated the capacitance and stability. All of these results confirmed that Zn-MOFs can be

potential active materials for the application in electrochemical energy storage. The dendrite formation of zinc in batteries can be avoided through careful design of the stable 3D porous skeleton architecture with large cages, which is advantageous to be a host material for Zn plating and stripping in aqueous Zn-based electrolyte.

2.3.1.6 Co-based MOFs

Cobalt offers redox-active sites and is readily to be employed for developing MOFs with good electrochemical performance. Hence Co-based MOFs have been widely investigated. The capacitive performance can be further enhanced by Co-MOF-based materials with layered structures as it not only possesses wide and stable interlayers, but also exhibits conductive networks, which is favorable to accelerate the pseudocapacitive process with fast electron transfer and facile electrolyte diffusion. For example, Zhu and his colleagues [199] successfully synthesized a 3D hierarchically structured Co-MOF on nickel foam (Co-MOF/NF) using a one-step solvothermal approach. The electrochemical behavior was tested in a three-electrode system in 2 M KOH. The areal capacitance of the as-synthesized material was 13.6 F cm^{-2} at a current density of 2 mA cm^{-2}, significantly higher than the Co-MOF powder material (1.2 F cm^{-2}). Meanwhile, it also maintained 10.8 F cm^{-2} (79.4%) at 20 mA cm^{-2}, suggesting the high-rate capability of Co-MOF/NF. Such high performance was ascribed to three main reasons: Firstly, no binder was utilized in the self-supported Co-MOF ensuring the maximum utilization of the active material. Secondly, the in-situ crystal growth of Co-MOF/NF could enhance the excellent mechanical adhesion and electrical conductivity, since Co-MOF/NF exhibited a smaller radius at the high-frequency semicircle than Co-MOF powder. Lastly, the 3D hierarchical nanosheets facilitated large accessible surface area with much more electroactive sites. Nonetheless, the recorded cyclic stability was unfavorable, which could only retain 47% over 10,000 continuous charge/discharge cycles. This was owing to the transformation of Co-MOF to MO and hydroxide during continuous charging and discharging.

Moreover, the performance of Co-based MOFs materials for SCs electrodes can be further enhanced through precise control of the architecture and nanocrystals. In another study, hierarchical hollow microsphere were formed by 1D nanorods with an average size of 20 nm and were characterized with a surface area of 93.6 m^2 g^{-1} [163]. Besides, mesoporous voids between the nanorods in the same Co-based MOF materials were discovered. These two key features ensured high availability of active sites and diffusion of electrolyte. As a result, the electrochemical capacitance of 952.5 F g^{-1} was reported at a current density of 0.25 A g^{-1} in 3 M KOH. A minor R_s was viewed and the phase angle is in the range of 50° - 70°. In addition, it could maintain 85% of its initial capacitance after 2000 cycles at 5 A g^{-1}, suggesting a good electrochemical reversibility of the as developed Co-MOF. Nevertheless, this was then followed by the decline in the charge storage efficiency due to the aggregation of the microspheres of Co-MOF over continuous cycles.

Apart from single nanosheet and nanorod morphology, a hybrid structure with both nanorods and nanoneedles is also a promising material which further ameliorates the electrochemical performance. Hence, Co-MOFs with a hybrid architecture and a large number of nanorods and nanoneedles were developed via a normal hydrothermal approach, in which the solvent was a mixture of DMF and ethanol (v : v = 1 : 1) [160]. It exhibited a specific capacitance of 958.1 F g^{-1} at 2 A g^{-1} in 3M KOH, which is much higher than Co-MOF/D (393.4 F g^{-1}, developed in single DMF) and Co-MOF/E (654.4 F g^{-1}, developed in single ethanol). The BET surface area of the

nanosized needles on the 1D nanorods was reported to be 31.98 $m^2 g^{-1}$ which was much higher than Co-MOF/D (3.84 $m^2 g^{-1}$) and Co-MOF/E (5.73 $m^2 g^{-1}$). The high surface area of the electrode material greatly reduced the diffusion path of electrolyte ions offering more contact between electrode active material and electrolyte. The microporous architecture of Co-MOF further improved its supercapacitive performance resulting in an ionic resistance of approximately 0.5 – 0.6 Ω. Notably, the as-generated Co-MOF possessed an ultrahigh cycling stability under a current density of 10 A g^{-1}. The retained specific capacitance was approximately 92.3% after 3000 cycles. The acquired energy density and power density of this material was 24.4 Wh kg^{-1} and 429 W kg^{-1}, respectively. Additionally, another coordination polymer with outstanding performance was synthesized through a facile synthesis route [42]. A maximum electrochemical capacitance of 2564 F g^{-1} over 1 A g^{-1} in 5 M KOH was reported, and it could still achieve 1164 F g^{-1} at a current density of 20 A g^{-1}, indicating the excellent rate capability of the MOF materials. There are three rationalizations which lead to high electrochemical performance. First and foremost, a large number of nanosheet agglomerations contributed to large surface area which are not only feasible to offer sufficient contact between electrode active materials and electrolyte, it has also shortened the migration distance of OH^-. Besides that, the as-synthesized Co-MOFs with a high conductivity of 3.75 x 10^{-3} S cm^{-1} could speed up the electron transfer at the interface of electrode and electrolyte, eventually enhanced the specific capacitance. Furthermore, the large volume between interlayers, which were formed on the bc plane through the interaction of Co-O-Co chain and the double chains of CoO_6, were capable to store electrolyte and improve the intercalation and de-intercalation efficiency of OH^-. In addition, it exhibited a desired cyclic stability with a retention capacitance of 95.8% over 3000 continuous charging and discharging cycles at a current density of 2 A g^{-1}. The extraordinary cycling stability could be ascribed to the unique layered structure with conductive network frames, in which the existence of terephthalate groups between the layers could serve as supportive pillars to avoid the collapse of the architecture.

2.3.1.7 Ni-based MOFs

The application of the majority of MOFs, including Fe-MOFs, Cu-MOFs, and Mn-MOFs, as SCs electrode active materials is largely hampered by their poor electrical conductivity and low chemical stability. Hence, to tackle these weaknesses, nickel-based MOFs with good electrolyte compatibility and high electrochemical performance have been widely explored. This is because Ni-MOFs exhibit ultrahigh conductivity of up to 800 S m^{-1} [200], high capacitive performance and extremely long-term cycling stability, and the retention capability is approximately 84% over 100,000 cycles [46].

Du and his co-workers successfully synthesized hierarchical porous Ni-MOFs and utilized them as electrode active material for SC [137]. These Ni-MOFs were characterized with hierarchical porous structure and specific surface area as high as 40.36 $m^2 g^{-1}$ and their electrochemical behavior was tested in a three-electrode cell in 3 M KOH electrolyte solution. A specific capacitance of 1057.2 F g^{-1} at a current density of 1 A g^{-1} and a rate capability of 61.5% at 30 A g^{-1} were reported, revealing the good rate capability. Meanwhile, the electrical conductivity was further improved by the addition of 20% conductive additive (acetylene black) [201]. As a result, the R_s and R_{ct} were recorded at 1.141 Ω and 1.371 Ω, respectively indicative of a good conductivity. In addition, it delivered a fascinating cyclic stability, in which the capacitance retention was 70% after 2500 cycles at 10 A g^{-1}.

Another study involved the synthesis of pristine nickel hexaaminobenzene ($Ni_3(HAB)_2$) via electrophoretic deposition (EPD) and this pristine MOF exhibited an enhanced electrochemical performance in 0.5 M Na_2SO_4 [202]. The delivered areal capacitance was 13.65 F cm^{-2} at a rate of 0.1 mA cm^{-2} within a voltage window of 0 – 1 V. It was noteworthy that a good rate capability of 76.5% at 1 mA cm^{-2} was acquired. Such high electrochemical capacitance and rate capability could be owing to the large number of in-plane pores and extraordinary conductivity of $Ni_3(HAB)_2$, which ameliorated the accessibility of electrolyte to active sites and accelarated the charge transfer. More significantly, the capacitance retention was as high as 81.2% after 50,000 cycles, indicating its superior cyclic stability. The capacitance fading (~ 19%) was resulted from the loss of active material through either detachment or dissolution during continuous cycling. In addition, the equivalent series resistance (ESR) was 2.96 **Ω**, owing to the low contact resistance. This was due to the utilization of zero binder during the assembly of $Ni_3(HAB)_2$ sheets on current collector (nickel foam) through EPD, as well as the low diffusion resistance resulting from the decreased ion diffusion distance. Nonetheless, the ESR was further reduced to 2.41 **Ω** after long-term GCD cycles, which could be elucidated by the activation of $Ni_3(HAB)_2$ electrode active material.

Through the similar approach, ultrathin 2D Ni_3(2,3,6,7,10,11-hexaaminotriphenelene)$_2$ ($Ni_3(HITP)_2$) was synthesized via the reaction between nickel chloride hexahydrate ($NiCl_2 \cdot 6H_2O$) and 2,3,6,7,10,11-hexaaminotriphenylene hexahydrochloride (HATP·6HCl) [46]. The relevant synthesis process and electrochemical properties are illustrated in **Fig. 2.22**. The specific areal capacitance of the as-obtained MOF material was 15.69 F cm^{-2} at 0.1 mA cm^{-2} in 0.5 M Na_2SO_4. This is attributed to the 3D porous $Ni_3(HITP)_2$ with micrometer-large pores, in which the large pore sizes could offer enough interspace to store electrolyte and boost ion transport. Moreover, the electrode active material showed an excellent capacitive behavior with high electrical conductivity, since the cyclic voltammetry (CV) curve with closely quasi-rectangular shape was maintained even at a very high scan rate of 4000 mV s^{-1}. More crucially, the structure of the active material is ultra-stable, approximately 84.14% of the initial capacitance was retained after 100,000 charge/discharge cycles at a low current density of 1 mA cm^{-2}. This was attributed to the layer-by-layer nanosheet structures, contributing towards the electrical double-layer capacitive behavior. Meanwhile, a low ESR of 1.47 **Ω** was gained, which might be elucidated by two factors: (a) The layer-by-layer nanosheets of $Ni_3(HITP)_2$ without any addition of binder. (b) Nanopores on the structure shortened electrolyte diffusion distance. It is the highest cycle life among the recent reports on MOF-based SCs.

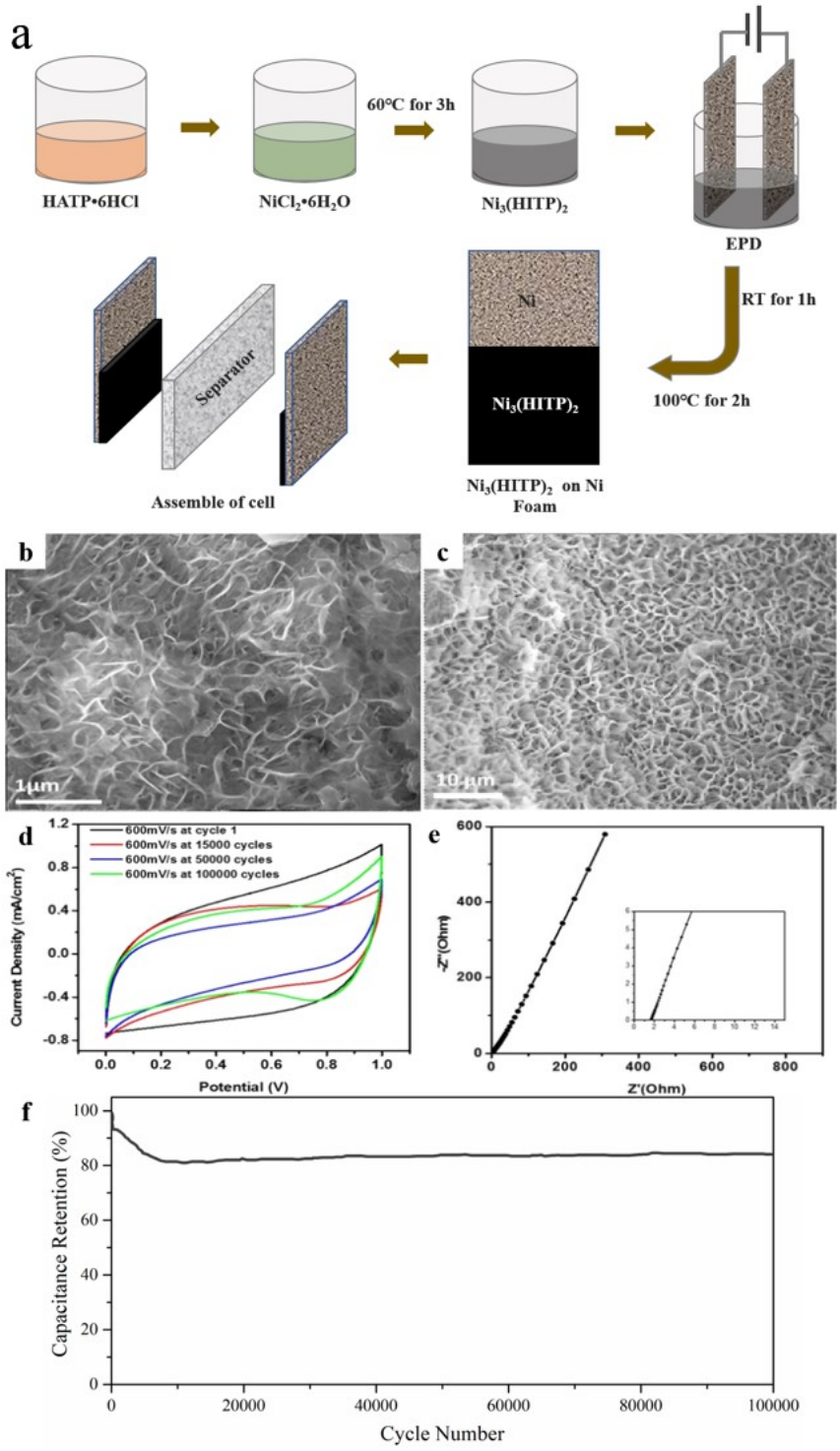


Figure 2.22. (a) The schematic illustration of synthesis $Ni_3(HITP)_2$ and the EPD process for synthesizing $Ni_3(HITP)_2$ SC electrodes, the SEM images of $Ni_3(HITP)_2$ film which was formed through EPD on Ni foam (10 um) in (b) before cycling and (c) after 100,000 cycles. (d) The CVs after different cycles at a scan rate of 600 mV s^{-1}. (e) Nyquist plot and (f) cycling stability until 100,000 cycles at 1 mA cm^{-2} of $Ni_3(HITP)_2$. Reproduced with permission from Ref. [46]. Copyright 2019, Elsevier.

It is also possible to employ Ni-MOFs as all-solid-state SCs since wearable devices are another attraction in the application of electrochemical energy storage systems. Generally, all-solid-state SCs exhibit a relatively lower electrochemical performance and stability due to the utilization of limited electrolyte as compared to normal SCs [203]. Recently, a layered nanosheet Ni-MOF was developed, and being utilized for flexible solid-state SC [45]. The electrode material showed a high electrochemical capacitance of 1518.8 F g^{-1} at 1 A g^{-1}, and a good rate capability of 483.3 F g^{-1} at 20 A g^{-1}. Meanwhile, an outstanding capacitance retention of 95.5% over 10,000 cycles at a current density of 20 A g^{-1} was reported. As the HC was assembled by employing the as-obtained material as cathode and AC as anode, this device delivered an areal capacitance of 244 mF cm^{-2} at 0.5 mA cm^{-2} and reasonably good cycling stability (97.2% was retained over 2000 cycles) in a potential range of 0 - 1.5 V. These ultra-high electrochemical performances could be resulted from the following factors: (a) The stable structure of Ni-MOFs in alkaline environment. (b) The large space offered between layers is beneficial to store electrolyte and enhance the facile intercalation and de-intercalation of OH^-. (c) Unit cells were formed along bc plane, which improved the transport of electron and diffusion of electrolyte.

Hence, the architectures of the synthesized MOFs have a crucial role to play in the electrochemical related properties, it is necessary to understand the interactions between the active materials and electrolyte. Meanwhile, the other factors, including morphologies and pore sizes, also need to be taken into consideration. These factors could affect the diffusion rate of electrolyte and therefore affect the lifespan of the device. As compared to other MOF electrode active materials (i.e., Co^{2+}, Fe^{2+}, Zn^{2+} and Al^{3+}), Ni-based MOFs have attracted tremendous attention in the field of high-performance electrochemical capacitors. This can be ascribed to four reasons: (i) the economic cost results from an abundant reserve of nickel. (ii) The ultrahigh conductivity of Ni-MOFs could enhance the capacitive performance. (iii) The extremely high cyclability could extend their further application. (iv) They not only possess tunable architectures and large specific surface areas, but also are easy to form 2D mesoporous structures, which is beneficial to promote the diffusion of ions and electrolyte for enhancing the electrochemical performance. Consequently, nickel is selected as precursor to synthesize Ni-MOF nanomaterials.

Table 2.7. Summary of the electrochemical performance of pristine MOFs materials utilized as SCs electrode materials.

Material	Specific Capacitance	Electrolyte	Current Density	Potential Window (V)	Reference Electrode	Cycle	Efficiency (%) /Current Density	Reference
SC								
UiO-66(Zr)	101.5 F g^{-1}	6 M KOH	0.2 A g^{-1}	0.6	Hg/HgO	-	-	[184]
UiO-66(Zr)	1144 F g^{-1}	6 M KOH	5 mV s^{-1}	0.75	SCE	2000	57.2/10 mV s^{-1}	[185]
MOF-867	5.085 mF cm^{-2}	-	5 mV s^{-1}	2.7	-	10,000	92/12.7 mA cm^{-2}	[151]
Cu-LCP	1274 F g^{-1}	1 M LiOH	1 A g^{-1}	0.5	SCE	2000	88/2 A g^{-1}	[188]
	568 F g^{-1}		20 A g^{-1}			-	-	
Cu-MOF	1148 F g^{-1}	6 M KOH	0.5 A g^{-1}	0.5	SCE	2000	90/10 A g^{-1}	[189]
Mn-MOF	443 F g^{-1}	6 M KOH	1 A g^{-1}	0.5	SCE	1000	86/5 A g^{-1}	[192]
Mn-LMOF	1098 F g^{-1}	1 M KOH	1 A g^{-1}	0.45	SCE	2000	92.6/2 A g^{-1}	[193]
	396 F g^{-1}		20 A g^{-1}			-	-	
	1178 F g^{-1}	1 M LiOH	1 A g^{-1}	0.5	SCE	2000	94.6/2 A g^{-1}	
	425.26 F g^{-1}		20 A g^{-1}			-	-	
Mn-MOF	10.25 F cm^{-2}	2 M KOH	2 A g^{-1}	0.6	Hg/HgO	5000	92.6/2 A g^{-1}	[194]
	5.72 F cm^{-2}		12 A g^{-1}			-	-	
Mn-MOF	371 F g^{-1}	6 M KOH	0.5 A g^{-1}	0.6	Hg/HgO	-	-	[195]
	248 F g^{-1}		10 A g^{-1}					
Mn-BDC MOF	64.5 F g^{-1}	PVA-1 M Na_2SO_4	0.25 A g^{-1}	1.5	Ag/AgCl	2000	98/0.25 A g^{-1}	[196]

Co-MOF/NF	13.6 F cm^{-2}	2 M KOH	2 mA cm^{-2}	0.8	Hg/HgO	10,000	47/50 mA cm^{-2}	[199]
Co-MOF	952.5 F g^{-1}	3 M KOH	0.25 A g^{-1}	0.5	Ag/AgCl	2000	85/5 A g^{-1}	[163]
Co-MOF	958.1 F g^{-1}	3 M KOH	2 A g^{-1}	0.5	Ag/AgCl	3000	92.3/2 A g^{-1}	[160]
Co-MOF	2564 F g^{-1} 1164 F g^{-1}	5 M KOH	1 A g^{-1} 20 A g^{-1}	0.35	SCE	3000 -	95.8/1 A g^{-1} -	[42]
Ni-MOF	1057.2 F g^{-1} 649 F g^{-1}	3 M KOH	1 A g^{-1} 30 A g^{-1}	0.4	SCE	2500 -	75/10 A g^{-1} -	[137]
$Ni_3(HAB)_2$	13.65 F cm^{-2}	0.5 M Na_2SO_4	0.1 mA cm^{-2}	1	-	50,000	81.2/0.1 mA cm^{-2}	[202]
$Ni_3(HITP)_2$	15.69 F cm^{-2}	0.5 M Na_2SO_4	0.1 mA cm^{-2}	1	-	100,000	84.14/0.1 mA cm^{-2}	[46]
Ni-MOF	1518.8 F g^{-1} 483.3 F g^{-1}	2 M KOH	1 A g^{-1} 20 A g^{-1}	0.5	-	10,000 -	95.5/20 A g^{-1} -	[45]
Mn-BGPD	832.6 F g^{-1}	1 M KOH	1 A g^{-1}	0.8	SCE	2,000	41.2/2 A g^{-1}	[204]
Co-BTC	657 F g^{-1}	1 M NaOH	0.5 A g^{-1}	0.5	SCE	3,000	81.4/10 A g^{-1}	[205]
Co-MOF	75.7 F g^{-1}	3 M KOH	0.5 A g^{-1}	0.4	SCE	3,000	94/1 A g^{-1}	[206]
Ni-MOF	1361 F g^{-1}	2 M KOH	0.5 A g^{-1}	0.6	SCE	4,000	94/0.1 V s^{-1}	[207]
Ni-MOF	2.38 C cm^{-2}	2 M KOH	1 mA cm^{-2}	0.5	Hg/HgO	10,000	88/40 mA cm^{-2}	[208]
HC								
Mn-MOF//rGO	211.4 F g^{-1} 131.07 F g^{-1}	2 M KOH	5 A g^{-1} 40 A g^{-1}	1.5	Hg/HgO	10,000 -	81.18/10 A g^{-1} -	[194]

Mn-MOF //graphene	89 F g^{-1}	6 M KOH	1 A g^{-1}	1.6	Hg/HgO	10,000	91.8/1 A g^{-1}	[195]
Ni-MOF//AC	85.5 F g^{-1}	6 M KOH	0.5 A g^{-1}	1.6	Hg/HgO	1,000	58/5 A g^{-1}	[209]
Mn-BGPD//rGO	100 F g^{-1}	1 M KOH	1 A g^{-1}	1.6	SCE	4,000	46.7/1 A g^{-1}	[204]
Zn-MOF//AC	140.8 Wh kg^{-1} / 46.6 Wh kg^{-1}	2 M $ZnSO_4$	70.0 W kg^{-1} / 2850 W kg^{-1}	1.6	-	20,000 / -	72/4 A g^{-1} / -	[197]
Zn-pPDA MOF-5//GC	62.75 Wh kg^{-1}	1 M KOH	4501.1 W kg^{-1}	1.5	Ag/AgCl	2,000	96.2/1 A g^{-1}	[198]
Zn-pPDA MOF-8//GC	57.52 Wh kg^{-1}		4499.03 W kg^{-1}			-	96.81/1 A g^{-1}	
Zn-pPDA MOF-12//GC	52.25 Wh kg^{-1}		4498.92 W kg^{-1}			-	96.79/1 A g^{-1}	
Ni-MOF//AC	244 mF cm^{-2}	KOH-PVA	0.5 mA cm^{-2}	1.5	-	2,000	97.2/10 mA cm^{-2}	[45]

2.3.2 Derivations of MOFs for SCs

Apart from the direct utilization of pristine MOFs for electrochemical applications, MOF-based materials have been employed as precursors to derive various materials such as TMOs and carbon materials. Generally, TMOs can be obtained through either thermal or chemical treatment of MOFs, and the derived TMOs usually exhibit the same architectures as their precursors. Hence, TMOs with high porosity and large surface areas could be synthesized. Meanwhile, carbons with large surface areas are often viewed as high-conductive materials, which are promising for the development of high-performance SC electrodes. The TMOs derived from MOFs are usually applied in alkaline based electrolyte, while MOF-derived carbon could operate in both acidic and basic electrolyte solutions. These compounds derived from MOFs have expanded their potential applications in electrochemical ESSs.

2.3.2.1 Bimetallic and ternary MO nanoporous materials

It is challenging to directly use most of the pristine MOFs due to the low electrical conductivity and unstable structures, the as-fabricated energy storage devices cannot achieve a desired performance. Hence, MOFs are employed as precursors to derive various nanomaterials (including TMOs and porous carbon) with high porosity and specific surface areas instead of direct utilization. In fact, TMOs derived from MOFs usually exhibit high storage capacity and low cost, which is appropriate for the application in electrochemical energy storage systems [210]. Nevertheless, a recent study showed that the performance of single TMO was limited by the low conductivity and large volume expansion during charge and discharge process over a constant current density [211], eventually the architecture broke and consequently shortened the device lifespan. Hence, this part mainly concentrates on bimetallic and ternary TMOs, which exhibit excellent electrochemical properties due to higher electrical conductivity and multiple redox sites.

Bimetallic composites usually exhibit higher electrochemical activity and stability than its single TMO. As an illustration, NiO/Ni_6MnO_8 composite with a 3D mesoporous and flower-like structure was prepared by Zhang's team [212]. The as-fabricated electrode exhibited a specific capacitance of 433 F g^{-1} and an excellent cyclic stability (91.9% retained after 1000 cycles) at a current density of 1 A g^{-1} in 6 M KOH, which was much higher than that of single component (193 F g^{-1} for NiO and 201 F g^{-1} for Ni_6MnO_8). Meanwhile, both ESR and R_{ct} values of the electrode of 0.3 **Ω** were recorded. These results indicated that the integration of mesoporous (NiO) and flower-like structure (Ni_6MnO_8) not only shortened the charge diffusion path, but also provided more electrochemically active sites with a high surface area of 74 m^2 g^{-1}. In another study, a 2D binary TMO nanosheet (ZnCoO-G) derived from Co-ZIF with GO was synthesized (**Fig. 2.23**), in which nanoparticles ZnO and Co_3O_4 were well distributed on the surface of the GO [213]. As the active material was fabricated as a SC electrode, it delivered a capacitance of 711.6 F g^{-1} at 1 A g^{-1} in 2 M KOH, the rate capability was 64.4% as the current density increased from 1 to 10 A g^{-1}. The high capacitance and rate capability were ascribed to the incorporation of zinc and GO, which leads to the uniform distribution of Co_3O_4, larger surface area and good electrical conductivity. After 1000 continuous charging and discharging cycles over a current density of 5 A g^{-1}, a capacitance retention of 63.6% was obtained, suggesting the remarkable stability of ZnCoO-G. The incorporation of GO was found to restrict the agglomeration of TMOs, and hence enhanced the specific surface area (67.85 m^2 g^{-1}) and electrical conductivity (R_s = 0.76 **Ω**) of the electrode. In another study, mesoporous $ZnCo_2O_4$ was obtained by annealing mixed metal MOF at a

temperature of 400 °C for 2 h [214]. The electrode active material exhibited a specific capacitance of 457 F g^{-1} at 1 A g^{-1} in 6 M KOH. Even though the current density rose to 20 A g^{-1}, it still delivered a capacitance of 368 F g^{-1}, in which the rate capability was as high as 80.5%. Meanwhile, the capacitance loss was only 2.1% after 1500 cycles at 2 A g^{-1}, which revealed the long-term stability of the binary TMOs ($ZnCo_2O_4$). Such electrochemical performance enhancement could be attributed to the porous structure that facilitates charge transport and electrolyte diffusion. Nonetheless, the operating potential window was as low as 0.35 V (0.05 – 0.4 V vs. Ag/AgCl), and the as-derived TMOs exhibited a fairly low surface area of 55 cm^2 g^{-1}.

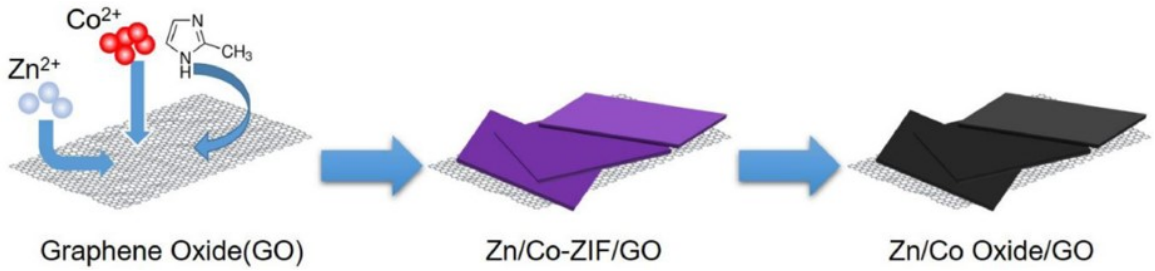


Figure 2.23. Schematic diagram showing the process to develop ZnCoO-G. Reprinted with permission from Ref. [213]. Copyright 2020, Elsevier.

Apart from symmetrical SCs, HCs with improved energy density without fading their power density have been widely explored. Huang et al., [180] has prepared ternary $ZnO/ZnCo_2O_4/NiO$ (ZZN) nanosheets, which were derived from ZIF-8 (**Fig. 2.24**). By virtue of the unique structure, the as-fabricated electrode exhibited high electrochemical capacitance and rate capability with specific capacitance of 1136.4 F g^{-1} and 354 F g^{-1} at current densities of 1 A g^{-1} and 30 A g^{-1}, respectively. Moreover, a low R_s of 0.92 Ω, a Warburg impedance (W) of 2.13 and an excellent capacitance retention of 86.54% over 5000 cycles at a high current density of 10 A g^{-1} were obtained. The enhanced electrochemical properties are due to the following two factors: (a) The ultrathin nanosheet-based hollow microspheres could ameliorate the accessibility of electrolyte, which was not only beneficial to enhance contact between electrode and electrolyte, but also speeded up the diffusion rate and improve the electrochemical property. (b) A large number of tiny holes on the nanosheets increased the surface area and volume during the charging and discharging process.

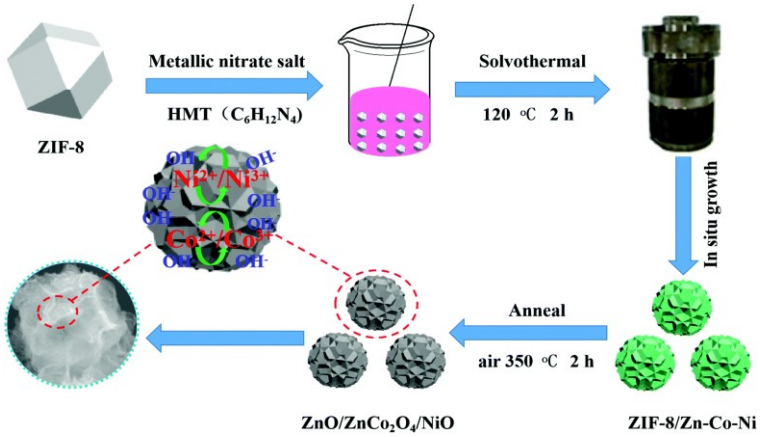


Figure 2.24. A schematic illustration of the synthesis process of $ZnO/ZnCo_2O_4/NiO$. Adapted from Ref. [180] with permission from The Royal Society of Chemistry.

Besides, HC with remarkable performance can also be assembled through "all in one" strategy where two different derivatives were obtained from the same precursor (**Fig. 2.25**) [215]. Zn/Co-MOF, synthesized through dissolving $Zn(NO_3)_2 \cdot 6H_2O$, $Co(NO_3)_2 \cdot 6H_2O$ and methylimidazole (MIM) precursors into methanol, was prepared from both nanoporous carbons (NPC) and bimetallic oxides ($ZnCo_2O_4$). The as-synthesized samples were analyzed in terms of pore size distributions (PSDs). In the analysis, both TMO ($ZnCo_2O_4$) and NPC exhibited hierarchical porous architectures with micro-, meso- and even macro-pores. Hence, the BET surface area of $ZnCo_2O_4$ and NPC were 440 $m^2\ g^{-1}$ and 1137$m^2\ g^{-1}$, respectively, confirming that nanoporous TMOs and NPC could be obtained from a single MOF precursor. Meanwhile, $ZnCo_2O_4$ and NPC were recorded with high specific capacitance of 420 F g^{-1} and 270 F g^{-1}, respectively. The enhanced electrochemical performances could be attributed to the hierarchically porous architectures where micropores were to accumulate ions while mesopore structures could improve the transfer of the ions. When HC (NPC//$ZnCo_2O_4$) was assembled by employing binary TMOs as cathode and NPC as anode, it delivered a maximum energy density of 28.6 Wh kg^{-1} at 100 W kg^{-1} within a wide voltage window of 0 – 1.45 V (vs. Hg/HgO) in 6 M KOH. An energy density of 18 Wh kg^{-1} was achieved when the power density was increased up to 2.5 kW kg^{-1}. As compared to symmetrical SCs consisting of both $ZnCo_2O_4$ and NPC electrodes under the same condition, the energy density was only approximately 8 Wh kg^{-1}, mainly due to the low operating potential window of 0.45 V. Additionally, the HC device possessed a superior cyclic stability of 87.2% over 5000 charging and discharging cycles at 1 A g^{-1}. The excellent electrochemical performance was ascribed to the porous architectures that derived from the same precursor with large surface areas offering large number of active sites. Meanwhile, the micro- and mesoporous structure in the composite was capable of shortening the charge transfer distance and wide operating potential window can be achieved, resulting from both anodic and cathodic materials.

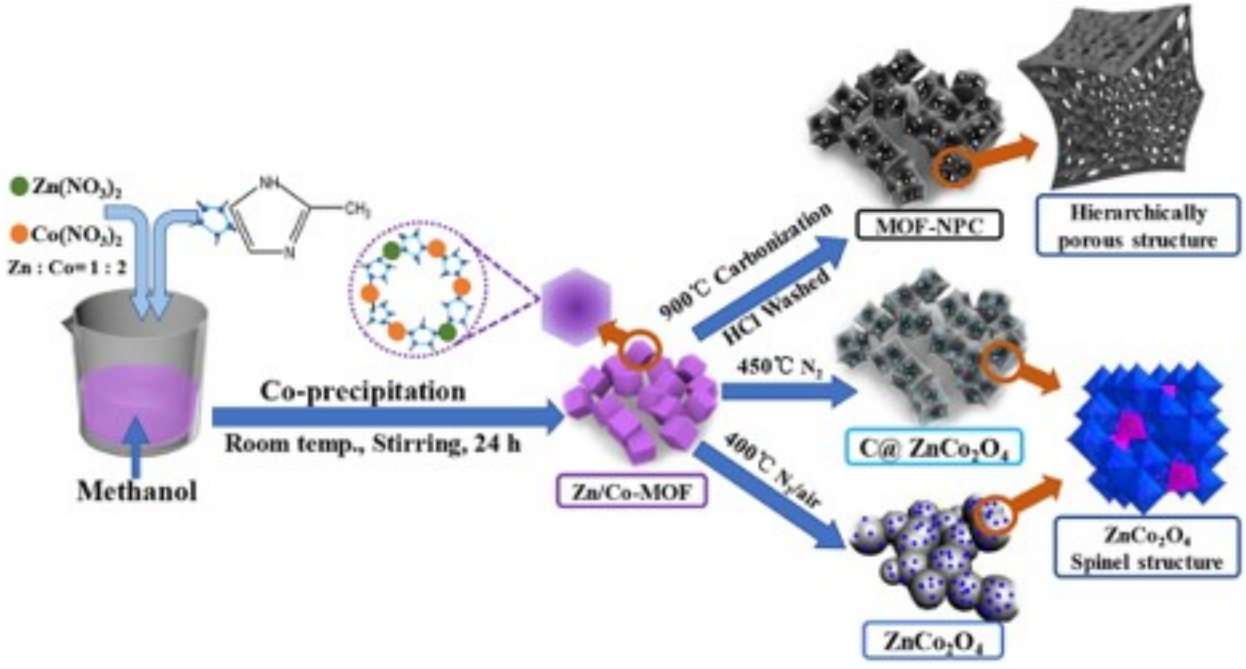


Figure 2.25. A schematic diagram showing the fabrication process of $ZnCo_2O_4$ and NPC via "all in one" strategy. Reused with permission from Ref. [215]. Copyright © 2020 He, Gao, Yao, Wu, Zhang, Huang and Wang.

In summary, binary and ternary TMOs exhibit good electrical conductivity and favorable electrochemical performance. The resulting morphologies of the active materials play a significant role in the electrochemical properties. Particularly, the mesoporous structures could help to store more electrolyte and shorten the charge transport path, and hence to enhance the capacitance and reversibility. Meanwhile, bimetallic oxides and ternary TMOs could offer more charge states, which significantly improve the specific capacitance. However, the specific surface areas of TMOs are not preferable, which might limit the electrochemical property. Another problem encountered is that most MOF-derived bimetallic oxides and ternary TMOs as SC electrode generally suffered from the low cyclic stability as compared to pristine MOFs materials. Usually, TMOs suffer from low operating potential window, while it can be efficiently solved by assembling the electrodes in HC configuration with highly conductive materials, such as NPC. Therefore, the interaction mechanism between TMOs and highly conductive materials still needs to be further explored.

2.3.2.2 MOF-derived carbon nanoporous composites

Currently, carbonaceous materials, developed through direct carbonizing from organic materials, have been widely investigated in electrochemical energy storage devices such as fuel cells [216], batteries [217] and SCs [218] due to their nontoxicity and excellent electrical conductivity. However, their potential applications are greatly limited by the low surface areas, non-uniform particle sizes and chaotic structures [219]. To tackle these shortcomings, MOF-derived NPC with nanoporous architectures and ultra-large ionic accessible surface areas have been synthesized [220]. Micro and mesoporous carbon-based materials such as graphene, activated carbon, carbon nanotubes and etc. possess a significant role to play in SCs, since they offer enough interspace to store electrolyte and shorten the path for ionic transportation [221]. As MOF materials have a wide range of applications owing to their unique structures, MOF-derived carbon is another attraction in the application of SCs.

Carbons can be obtained from MOFs through a simple heat-treatment, and these active materials often exhibit micro/mesoporous architectures and large specific surface areas, which are crucial characteristics to optimize the electrochemical performance of SCs electrodes. Thus, the as-derived carbon materials could have good electrochemical performance. NPC with interconnected hierarchical meso- and micro-porous architecture was synthesized by Chang et al. [218] A specific capacitance of 425 F g^{-1} was acquired at a current density of 2 A g^{-1} within an operating voltage window of 1 V (vs. Ag/AgCl) in 1 M H_2SO_4, which is almost twice that of MOF-derived TMOs [188, 193]. The capacitance was recorded as 244 F g^{-1} (57.4%) when the current density was increased up to 10 A g^{-1}, which clearly indicated the good rate capability of MOF-525-derived NPC. The high capacitance could be caused by the pseudo-capacitance of functional groups and unique structure. Firstly, oxygen-containing groups, forming during the process of pyrolysis, were not only beneficial to generate pseudo-capacitance, but also enhanced the wettability of active materials. Nitrogen-containing functional groups could be responsible for the redox pseudo-capacitance due to the existence of pyridinic and pyrrolic groups. Secondly, the hierarchical micro- and meso-porous architecture with a large number of sp^2 bonded carbon accelerated the diffusion of ions and eventually enhanced the capacitive performance. Lastly, it possessed a large surface area of 786 m^2 g^{-1}, which was able to provide more active sites for electrochemical reactions.

NPC could be also obtained from Zn-MOF at 800 ℃ (**Fig. 2.26**), and the performance was tested under the same condition, while it was mixed with 20% PVDF in N-Methyl-2-Pyrrolidone (NMP)

[222]. As the obtained material was fabricated into electrode for SCs, it delivered an electrochemical capacitance of 251 F g^{-1} at a scan rate of 5 mV s^{-1}. Meanwhile, there was a capacitance retention of approximately 50% at a high scan rate of 1000 mV s^{-1}, which revealed the excellent transport and conductive properties. This was ascribed to the high content of nitrogen (15%) and ultra-large surface area of 1523 m^2 g^{-1}. The large surface area is owing to the special microporous architecture, in which NPC exhibited uniform and symmetric geometry with polyhedral morphology. Additionally, it could maintain 92% of its initial capacitance after 2000 cycles at 7.5 A g^{-1}, indicating its good cyclic stability. The acquired energy density and power density of the as-obtained active electrode material was 10.86 Wh kg^{-1} at 225 W kg^{-1}, respectively.

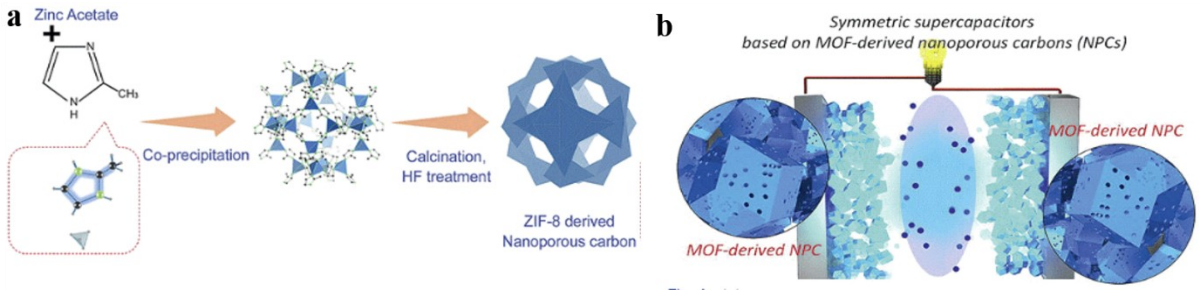


Figure 2.26. Schematic diagram illustrating (a) the synthesis process of NPC and (b) the SC construction made of MOF-derived NPC. Adapted from Ref. [222] with permission from The Royal Society of Chemistry.

The electrochemical property of MOF-derived carbon can be improved by the addition of heteroatoms that are derived from organic ligands. These heteroatoms are able to strengthen the interactions between ions and surfaces, which is beneficial to stabilize the structures. For instance, NC900, nanoporous nitrogen-doped carbon, was developed by heating its precursor, Cd-MOF ($Cd(NIPA)(CH_3CH_2OH)_3$, NIPA = 5-nitroisophthalic acid), at 900 °C [223]. The as-obtained electrode possessed a specific capacitance of 367 F g^{-1} at 1 A g^{-1} and retained 95% capacitance after 3000 cycles in a three-electrode system, revealing a good stability of the nanoporous structure. Meanwhile, low R_s of 0.43 Ω and R_{ct} of 4.57 Ω were recorded in the same study. This was attributed to nanostructure with an average pore size of 800 nm, which increased the diffusion rate of electrolyte and offered a higher number of active sites. In addition, when NC900 was employed to assemble SC cell, it exhibited a specific capacitance of 46 F g^{-1} at 0.5 A g^{-1} over a potential window of 1.6 V, while the energy and power densities were 6.3 Wh kg^{-1} and 246.9 W kg^{-1}, respectively. After cycling for 1000 cycles at 0.5 A g^{-1}, the capacitance retention was 96%.

In another study, waffle-like nanoporous carbons (WNPC) were synthesized (**Fig. 2.27**) with high contents of nitrogen (7.5 wt%) and oxygen (9.1 wt%) and the electrochemical property of this material was tested in a three-electrode system in 1 M H_2SO_4 [224]. During the electrochemical test, the CV curves of WNPC delivered a pair of redox peaks, owing to the pseudo-capacitance of doped nitrogen and oxygen. At the same time, this electrode displayed a capacitance of 300.7 F g^{-1} at 1 A g^{-1} and retained 72% of its initial capacitance at 20 A g^{-1}, which was higher than that of NPC, suggesting the fast electrode kinetics. Moreover, the efficiency loss was only 13% after cycling for 10,000 cycles at a current density of 4 A g^{-1} within 0 – 1 V (vs. Ag/AgCl), which indicated excellent cycling stability. Such outstanding performance was attributed to the existence of micro- and meso-pores, in which the mesopores are able to accelerate ionic diffusion, micropores offer a large BET surface area of 594 m^2 g^{-1}. As WNPC was fabricated into SC

electrode in 1 M organic electrolyte ($TEABF_4$), the working potential was changed to 1.5 – 2.5 V. It was found that this device possessed an energy density and power density of 27 Wh kg^{-1} and 500 W kg^{-1} at 0.5 A g^{-1}. Even though the current density was increased up to 4 A g^{-1}, it was capable of maintaining an energy density of 19.7 Wh kg^{-1} and a power density of 4000 W kg^{-1}. Moreover, the capacitance retention was just 2% lower than that in aqueous electrolyte over the identical current density, showing the favorable stability of WNPC.

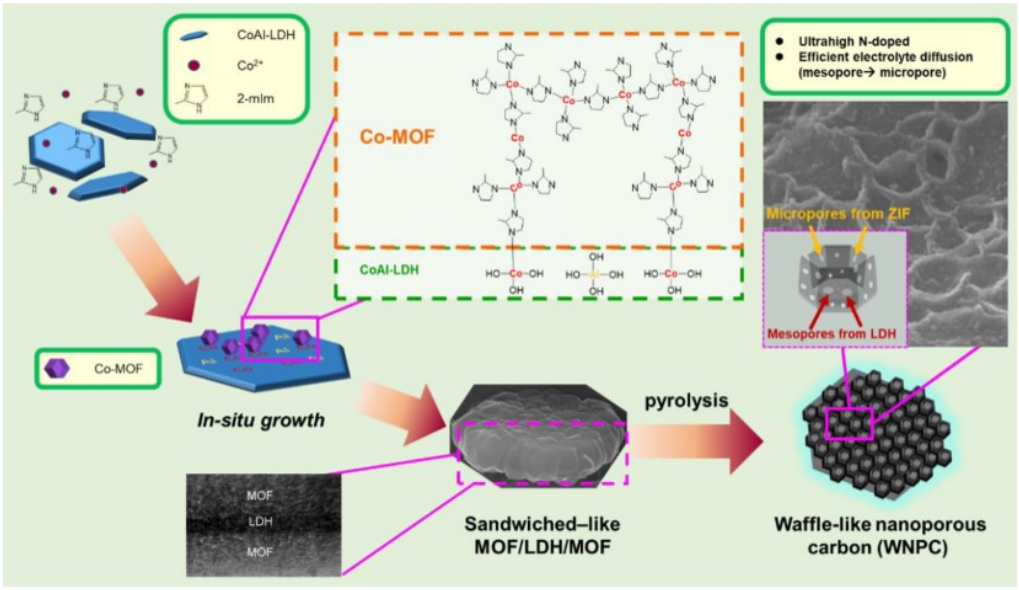


Figure 2.27. A schematic illustration of the fabrication of sandwiched-like MOFs via in-situ growth and the WNPC [224]. Copyright © 2020 Wu, Chang, Chou, Huang, Liu and Peng.

Additionally, the stability of carbon derived from MOFs materials for SCs electrodes can be further enhanced through precise control of the structural pore size. For example, Liu and his co-workers [225] have synthesized ultra-microporous carbon nanoparticles (UCNs) from UiO-67 at a slightly low carbonization temperature (750 ℃). The as-derived carbon was characterized with a BET surface area of 843 m^2 g^{-1} and a pore size of 0.53 nm. Meanwhile, a specific electrochemical capacitance of 256 F g^{-1} at 1 A g^{-1} in 6 M KOH was obtained, and the-fabricated electrode could retain 91% of its starting value over 10,000 cycles at a current density of 2 A g^{-1}. The attractive electrochemical performance of the electrode could be due to the diffusion channel within the ultra-micropores and packing mesopores, leading to fast ion transfer and reduction of diffusion path.

Through rational design, 3D hybrid-hierarchical porous carbon with high ionic accessible surface area and long-term cyclic stability was obtained from ZIF-8 [179]. The electrochemical property of this nanomaterial was shown in **Fig. 2.28**. The derived hybrid-porous carbon displayed a high surface area of 1056.8 m^2 g^{-1} and a pore volume of 0.693 cm^3 g^{-1} resulting from both micro- and meso-pores. Meanwhile, the electrochemical behavior was tested in a three-electrode configuration with 6 M KOH electrolyte. It exhibited a specific capacitance of 215 F g^{-1} at 5 A g^{-1}. More importantly, this value was maintained at 100% even over 10,000 cycles under the same current density. This extraordinary stability was attributed to the micropore structures that ensure

the short distance between the surface of electrode and center of ions, which boosted both charges and electrolyte transfer. Simultaneously, macropores also offer a channel for ions to access the double-layer capacitive carbon materials.

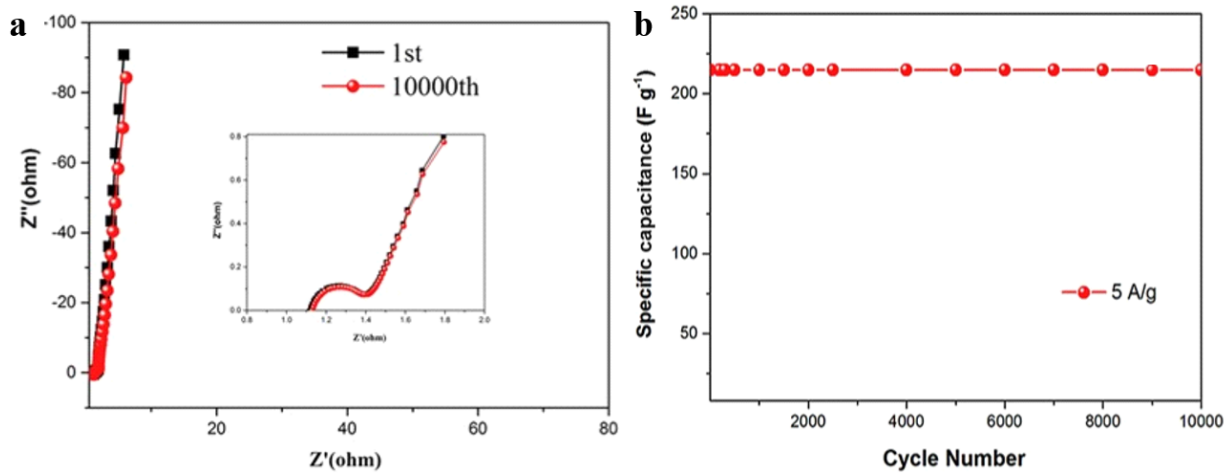


Figure 2.28. (a) The Nyquist plot of the 1st cycle and last cycle. (b) The cyclic stability of 3D hybrid-hierarchical porous carbon derived from ZIF-8 over 10,000 cycles in 1 M KOH. Reused with permission from Ref. [179]. Copyright 2016, Elsevier.

It is also possible to employ MOF-derived carbon for flexible SCs. For example, N-doped carbon nanostructures were developed (**Fig. 2.29**) with a BET surface area of 905 m^2 g^{-1} by Tang et al. [226] The large surface area was attributed to the co-existence of micro- and meso-pores. The acquired electrochemical capacitance were 244 F g^{-1} at 0.67 A g^{-1} and 139 F g^{-1} (56.97%) at an ultra-high current of 134 A g^{-1} within 0 – 1 V (vs. Hg/Hg_2SO_4). Additionally, the capacitance retention was as high as 98.5% over 10,000 cycles at 20 mA cm^{-2}, suggesting the preferable cycling stability of N-doped MOF-derived carbon. These excellent capacitive performances were ascribed to three factors: (a) The binder-free carbon electrode reduced the interfacial resistance. (b) Micropores could provide large surface area and mesopores facilitate low-resistant ion transport channels for electrolyte. (c) The doped nitrogen atoms not only accelerated the kinetics of ion diffusion and transport of charges, but also enhanced the wettability and conductivity of the as-developed carbon materials.

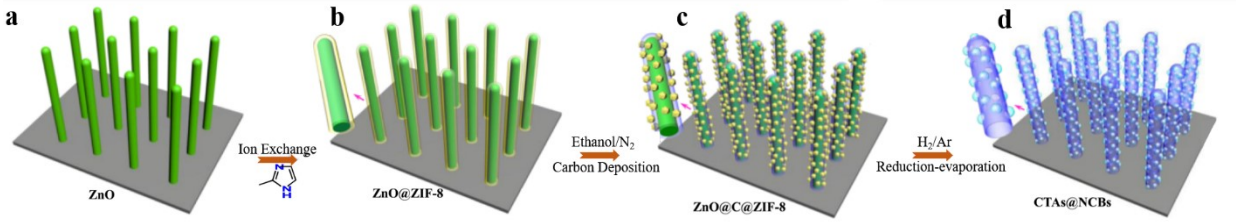


Figure 2.29. A schematic diagram showing the synthesis of (a) ZnO nanorods, (b) ZnO@ZIF-8 via ion exchange, (c) ZnO@C@ZIF-8 via in situ ethanol decomposition, (d) N-doped carbon bubbles on carbon tubes via reduction-evaporation. Reproduced with permission from Ref. [226]. Copyright 2017, Elsevier

Table 2.8. Summary of the electrochemical performance of bimetallic oxides derived from MOF materials utilized as SCs electrode materials.

Samples	Specific Capacitance ($F\ g^{-1}$)	Electrolyte	Current Density	Potential Window (V)	Cycle	Reference Electrode	Efficiency/ Current Density	Reference
SC								
NiO/Ni_6MnO_8	433	6 M KOH	1 A g^{-1}	0.6	1000	SCE	91.9/1 A g^{-1}	[212]
ZnCoO-G	711.6	2 M KOH	1 A g^{-1}	0.6	1000	Hg/HgO	63.6/5 A g^{-1}	[213]
$NiMn_2O_4$	356	1 M Na_2SO_4	0.5 A g^{-1}	2.0	5000	AgCl/Ag	86/10 A g^{-1}	[227]
$NiCo_2O_4$	1191.2	2 M KOH	1 A g^{-1}	0.6	1500	Hg/HgO	78.4/2 A g^{-1}	[228]
65Ni-MDH	875 C g^{-1}	2 M KOH	1 A g^{-1}	0.5	5000	AgCl/Ag	90.1/20 A g^{-1}	[229]
$MnCo_2O_4$	1763	2 M KOH	1 A g^{-1}	0.6	4500	Hg/HgO	95/1 A g^{-1}	[230]
$ZnCo_2O_4$	457 368	6 M KOH	1 A g^{-1} 20 A g^{-1}	0.35	1500 -	Ag/AgCl	97.9/2 A g^{-1} -	[214]
ZZN	1136.4 354	2 M KOH	1 A g^{-1} 30 A g^{-1}	0.5	5000 -	SCE	85.64/10 A g^{-1} -	[180]
$Co_3O_4/ZnFe_2O_4$	326.7	6 M KOH	1 A g^{-1}	1.35	1000	Hg/HgO	80.7/10 A g^{-1}	[231]
HC								
ZZN	-	-	-	1.6	5000	SCE	104.17/10 A g^{-1}	[180]
$ZnCo_2O_4$	420	6 M KOH	0.5 A g^{-1}	1.45	5000	Hg/HgO	87.2/1 A g^{-1}	[215]
65Ni-MDH	215	2 M KOH	2 A g^{-1}	1.7	10,000	AgCl/Ag	91.3/13.5 A g^{-1}	[229]
Co-Ni-CuO_x	188	2M NaOH	0.03 A g^{-1}	1.6	5000	-	98/0.03	[232]
ZNC	247	6 M KOH	0.1 A g^{-1}	1.5	5000	Hg/Hg_2Cl_2	99/0.3 A g^{-1}	[233]

Table 2.9. Summary of the electrochemical performance of MOF-derived carbon materials utilized as SCs electrode materials.

Samples	Specific Capacitance ($F\ g^{-1}$)	Electrolyte	Current Density	Potential Window (V)	Cycle	Reference Electrode	Efficiency/ Current Density	Reference
NPC	425 244	1 M H_2SO_4	2 A g^{-1} 10 A g^{-1}	1	-	Ag/AgCl	-	[218]
NPC	98 62	1 M H_2SO_4	0.5 A g^{-1} 5 A g^{-1}	0.9	2000 -	Ag/AgCl	92/7.5 A g^{-1} -	[222]
NC900	367 46 F	6 M KOH	1 A g^{-1} 0.5 A g^{-1}	1 1.6	3000 1000	Hg/HgO -	95/1 A g^{-1} 96/0.5 A g^{-1}	[223]
WNPC	300.7 216.5	1 M H_2SO_4	1 A g^{-1} 20 A g^{-1}	1	10,000 -	Ag/AgCl	87/4 A g^{-1} -	[224]
UCNs	256	6 M KOH	1 A g^{-1}	1	10,000	Hg/HgO	91/2 A g^{-1}	[225]
Hybrid-porous C	215	6 M KOH	5 A g^{-1}	1	10,000	SCE	100/5 A g^{-1}	[179]
N-doped C	244 139	1 M H_2SO_4	0.67 A g^{-1} 134 A g^{-1}	1	10,000 -	Hg/Hg_2SO_4	98.5/20 mA cm^{-2} -	[226]
PC-Zn	138	6 M KOH	0.5 A g^{-1}	1	5000	SCE	91.8/1 A g^{-1}	[234]
c-CN	333.8	1 M LiTFSI	5 mV s^{-1}	1.2	12,000	Ag/AgCl	88.1/8 A g^{-1}	[235]

2.4 Summary

In summary, this chapter provides an overview of the development of highly stable MOF materials with micro- and meso-porous structures for the application of electrochemical energy storage systems, particularly for SCs in the recent decade. The synthesis approaches to achieve either highly stable architectures or industrial production were introduced. A series of significant parameters that play a crucial role in the process of MOFs synthesis were included. Lastly, the application of the pristine MOFs materials and their derivatives, such as binary/ternary metal oxides and carbon materials derived from MOFs, have been presented as well. Even though it is obvious that MOF-based materials exhibit many positive aspects, including large surface areas, high porosity, tunable sizes and structures, the application of MOFs in SC still faces a lot of challenges. For instance, most of the pristine MOFs possess low conductivities and cycling stabilities, rare studies of high-valence metal ions-based MOFs are found in the application of SCs, derivatives like binary TMOs and carbons have a low electrochemical capacitance.

Firstly, a wide range of synthesizing approaches towards stable MOFs were introduced, including conventional routes such as slow solvent evaporation and hydro/solvothermal synthesis. These are the most versatile and facile methods, in which the synthesis conditions (temperature, solvents, metal and organic precursors, as well as pH) can be fully controlled and eventually results in the production of MOF materials of high purity. Microwave-assisted methods, electrochemical and mechanical syntheses, on the one hand, are employed to speed up the synthesis process. Besides, they are employed to produce micro- and meso-porous MOFs with high yields. In general, these micro- and meso-porous architectures help to increase the surface areas and offer large ion-assessable volume such that more electrolyte is stored and the electrochemical performance would be enhanced. Meanwhile, sealing method is utilized to integrate other functional materials with MOFs for extending their applications. For practical applications of the porous materials and technique-economic purpose, a continuous-flow process was roughly discussed.

Secondly, the electrochemical properties of MOFs could be enhanced through a rational design of the skeleton structures and topologies. To provide proper crystalline structures for targeting applications, it is necessary to precisely control the synthesis environment. For instance, different metal clusters and organic ligands would result in disparate architectures, synthesis temperature could affect the crystal sizes of resulting MOFs and solvent template could function as an architecture directing agent and etc. As a result, all the impact factors should be taken into consideration during the synthesis of MOF materials to reach a desired performance.

Lastly, the performance of pristine MOFs and their derivatives (TMOs and NPC) as electrode materials were summarized. In general, the majority of pristine MOF materials possessed low conductivity, poor specific capacitance in aqueous-based electrolyte and working in low operating voltage windows. Meanwhile, bimetallic oxides derived from MOFs had an improved conductivity and specific capacitance. Nonetheless, they possessed unstable structures. Although MOF-derived carbon delivered a low capacitance of approximately 300 F g^{-1}, the cycling stability was improved. When TMOs and carbon derived from the same MOF precursor are assembled into electrodes for HCs, it is helpful to enhance both the electrochemical capacitance and cyclic stability.

As illustrated by many previous studies, MOF materials with meso-porous (2 nm – 50 nm) structures displayed favorable performance in both specific capacitance and cyclic stability, owing to the enhanced ionic transport and highly accessible areas active sites. It offers a promising route that the future design of MOFs architectures for SCs should be mesoporous, while most of studies

concentrate on low-valence-based MOFs. Thus, it is necessary to explore the pristine MOFs with high-valence coordination such as Cr^{3+} and Zr^{4+} for SCs. Meanwhile, the interaction mechanism among metal cations and organic linkers with various molar ratios remains unclear in the process of synthesis. As for nanocomposites derived from MOFs, "all in one" strategy is an efficient approach to cope with low working voltage window and performance. Most importantly, cyclic stability has become a main challenge for practical applications of MOF materials. Though some efforts have been put on and an increasing number of stable MOFs are reported, MOFs with various metal precursors have not achieved the same electrochemical performance. Hence, it is still crucial to further investigate the associated major impact factors, and thus to investigate new MOF materials for SCs with both high electrochemical performance and long-term lifespan.

Consequently, the utilization of room-temperature aqueous-based electrolyte could tremendously enhance the energy and power density for SCs. It is rational as aqueous electrolyte exhibits high thermal stability, environmental-friendly character, wide working temperature range and potential window. It is not only beneficial to improve the electrochemical performance, but also advantageous to sustain the safe operation of the device. Here, Na_2SO_4 aqueous electrolyte will be applied as electrolyte for fabricating SC devices. Meanwhile, Ni-MOF-based electrode active materials have been viewed as promising candidates for high-performance SCs by virtue of their appealing physiochemical properties (i.e., good thermal stability, controllable and diverse structures). Meanwhile, nickel is not only naturally abundant, but also it exhibits high coordination number, which could result in excellent electrochemical performance. In addition to metal ions, the selection of organic ligand is vital as well. Among a wide variety of ligands, terephthalic acid as a polycarboxylate ligand has received great attention by reason of its various coordination modes, good thermal and chemical stability. For the same reason, carboxylate linkers have been widely utilized as bridging linkers for fabricating mesoporous MOFs. Besides, MOFs assembled by carboxylate ligands normally exhibit neutral skeletons, in which the possibility of the framework collapse is greatly reduced during activation. Thus, Ni-MOFs will be synthesized based on Ni^{2+} and carboxylate linkers in this project. Besides, most MOFs were found to be fabricated via a solvothermal approach using pure DMF or mixing with water, in which very few studies reported the synthesis of MOFs by adopting two organic solvents (DMF & ethylene glycol). Therefore, the electrochemical performance of Ni-MOFs synthesized via this method as SC electrode active materials will be extensively explored.

In addition, graphene can be incorporated to enhance the electric conductivity of Ni-MOFs as it is a single-layer carbonaceous nanomaterial with the properties of relatively low electric resistivity, high chemical and thermal stability, large surface area and superb mechanical flexibility. Furthermore, due to the high porosity, structural tunability and capability to encapsulate guest nanostructures, other functional components, such as charge carriers (like sodium ions) and pseudocapacitance-rich materials (i.e., molybdenum disulfide and MOF-derived transition metal oxides), could be incorporated onto Ni-MOFs and their derivatives via post-synthetic modifications for promoting energy density as well as cyclic durability of the electrode materials.

Chapter 3: Chemicals and Characterizations

3.1 Chemicals

Nickel nitrate hexahydrate ($Ni(NO_3)\cdot 6H_2O$), N, N-Dimethylformamide (DMF, C_3H_7NO), ethylene glycol (EG, $C_2H_6O_2$), sodium chloride (NaCl), potassium hydroxide (KOH) and sodium sulfate (Na_2SO_4) were received from R&M chemicals. *P*-benzenedicarboxylic acid (BDC, $C_8H_6O_4$), polyvinylidene fluoride (PVDF) and N-methyl-2-pyrrolidone (NMP), sodium molybdate (Na_2MoO_4) and thioacetamide (CH_3CSNH_2) were purchased from Sigma-Aldrich. Acetylene black (C) was acquired from Alfa Aesar. High pyrolytic graphite flakes (HOPG) were obtained from Bay Carbon, USA and all the materials were purchased and utilized without further purification. Highly pure water (~18.2 MΩ cm) from Millipore system was employed throughout this study.

3.2 Synthesis of Graphene Nanosheets

Graphene nanosheets were fabricated through a modified sonochemical-assisted solvent exfoliation method, as illustrated in **Fig. 3.1** [236]. Typically, 10 mg of HOPG was dissolved in 100 mL solution composed of deionized water and ethanol (v : v = 3 : 2). This mixture was then sonicated for 4 hours via ultrasonic bath under ambient condition. The resultant graphene solution was centrifuged at 1000 rpm for half an hour and dried at 80 °C overnight.

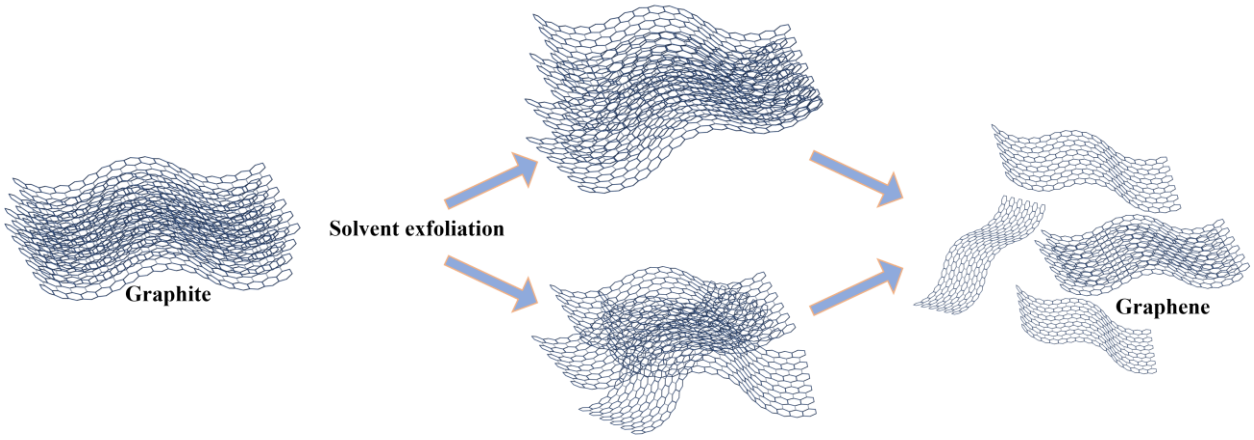


Figure 3.1. Schematic illustration for the synthesis of graphene via solvent exfoliation method.

3.3 Material Characterizations

The crystalline structures of the as-synthesized nanostructures were analyzed using power X-ray diffraction (XRD) with Cu-Kα radiation (λ=1.5406 Å) from 10 to 80°. Field Emission Scanning Electron Microscopy (FESEM, Quanta 400 F) and Transmission Electron Microscopy (TEM,

JEOL 2100 F, USA) were utilized to examine the surface morphology and internal structure of nanocomposites at 20 kV and 200 kV, respectively. An elemental study and mapping were conducted by using energy-dispersive X-ray spectroscopy (EDX). Moreover, elemental composition and chemical states of the nanocomposites were also examined by X-ray photoelectron spectroscopy (XPS, Axis Ultra DLD, UK). The Fourier transform infrared (FT-IR, Perkin Elmer Instrument) of these samples were obtained at wavenumber of 4000 to 400 cm^{-1} on a Universal Sampling Accessory. Additionally, thermogravimetry/derivative thermogravimetry was evaluated by using a thermogravimetry analyzer (TG-DTG, 'STA 409' NETZSCH) from 30 to 800 ℃ at a ramping rate of 10 ℃ min^{-1} and nitrogen (N_2) flow (10 mL min^{-1}).

3.3.1 X-ray Powder Diffraction (XRD)

XRD is a rapid and non-destructive analytical technique for the identification of atomic spacing and crystal structures, in which the dimensional information on a unit cell can be provided through x-ray irradiation and measurement of intensity and scattering angle. It has a wide application in identifying crystalline phase, determining atomic arrangement as well as textural characteristics, such as phase composition, lattice space, growth orientation and grain size. Basically, the incident x-ray could be scattered by crystals, a periodic array of atoms, via interactions with electrons (also known as scatterers) of atoms. A constant array of orbicular waves is produced by a regular array of scatterers. These waves are able to eliminate each other through destructive interference in the main directions, whereas they constructively combine in a few explicit directions as determined by Bragg's law:

$$n\lambda = 2dsin\theta \quad (1)$$

where n is a constant, λ is the wavelength, d is the lattice spacing and θ is the incident angle.

All possible diffraction patterns could be detected by scanning a sample within a range of 2θ angles. These attained diffraction directions can then be converted to d spacing, which allows the identification of the crystal material as each material possesses a set of unique d spacing. Hence, the crystalline material can be identified by comparison of d-spacing with standard reference.

3.3.2 X-ray Photoelectron Spectroscopy (XPS)

XPS is a surface sensitive technique utilized to identify the chemical composition of material surfaces (10 nm). Meanwhile, it can also be employed to analyze the chemical state of polyvalent ions through measuring the binding energies of these elements. This instrumental analysis is based on photoelectric effect, in which electrons are subsequently emitted from atoms when it is under impingement of electromagnetic radiation. Specifically, photoelectrons can be produced when the energy of impinging photons is higher than the binding energy of electrons, and the energy is directly proportional to the frequency. As a result, XPS spectrum is generated as the kinetic energy of the emitted electron is related to the binding energy as represented by **Eq. (2)**.

$$KE = h\upsilon - BE - \varphi \quad (2)$$

where KE represents kinetic energy of the ejected photoelectron, hυ is the energy of the incident photon, BE is the binding energy of the emitted electron and φ stands for spectrometer work function, which is normally stated as the energy between the vacuum energy level and Fermi level.

3.3.3 Fourier Transform Infrared Spectroscopy (FT-IR)

FT-IR is a versatile technique for surface characterization of materials. Basically, it is a mathematical process where infrared spectrum of transmission/absorption of a sample material is obtained by translating interferogram into actual spectrum. Chemical functional groups tend to adsorb infrared radiation with certain intensity and chemical bonds between atoms will bend, stretch and contract when the energy of infrared radiation is adsorbed by sample materials. These vibrations of chemical functional groups can be detected by infrared spectroscopy. Hence, it is beneficial to gain information about the intensity and wavelength of the adsorption, and hence the existing functional groups can be investigated.

To eliminate the impact of environments as well as the instrument, a background spectrum, a spectrum measured without any sample, must be obtained before analyzing samples. A transmittance spectrum is derived (**Eq. (3)**) by normalizing the FT-IR spectrum of sample.

$$\%T = I/I_o \tag{3}$$

where %T stands for the transmittance, I and I_o are the intensity obtained from sample materials and background spectrum.

Besides, the absorbance spectrum (A) can also be obtained from the calculated transmittance by following formula:

$$A = -\log_{10} T \tag{4}$$

3.3.4 Field Emission Scanning Electron Microscopy (FESEM)/Transmission Electron Microscopy (TEM)

FESEM/TEM are utilized for observing the surface of a material, in which morphology, topology and metallographic details can be investigated. During the measurement, the surface of the specimen is scanned by electrons with negative charges, which are liberated from a field emission source. Electrons are scattered and the secondary electrons can be collected by a detector, in which the speed of secondary electrons are reduced due to hitting the surface. Subsequently, a magnified image will be created by these secondary electrons. As a result, the topology as well as morphology of the sample can be illustrated. Meanwhile, the electron, which is backscattered, from the surface is beneficial to differentiate the composition of the sample.

The core difference between these two instruments is that FESEM focuses on the surface of a sample while TEM is able to analyze the internal structure. In fact, the image created by FESEM is through detecting the reflected electrons on the surface. The electron from TEM, on the other hand, can penetrate through the sample material and the emitted electron can be captured. Consequently, TEM normally exhibits a higher resolution (~0.5 Å) as compared to FESEM (0.4 nm).

3.3.5 Thermogravimetry Analysis (TGA)

The changes in physiochemical properties can be analyzed by TGA. Specifically, the physical properties, such as vaporization, desorption and the second-order phase transition can be investigated by performing TGA. Moreover, dehydration, oxidation and decomposition of a sample can be easily determined by thermal analysis. In general, there are two kinds of thermal analysis: (i) The temperature increases continuously while the heating rate is a constant, which is favorable for ensuring the temperature where the gas is removed and identifying the amount of removed gas. (ii) The temperature is fixed and the mass against time is being measured, which offers information on the temperature where a decomposition occurs.

3.4 Electrochemical Measurement

The working electrode was fabricated by mixing active materials (70%), acetylene black (10%) and PVDF binder (20%), with the assistance of 0.2 mL of NMP. The active material, Ni-MOFs and Ni-MOFs/graphene nanocomposites, were mixed with AC at a mass ratio of 80 : 20 (w/w) to further enhance the surface area. Subsequently, the homogeneously mixed black slurry was then coated on a clean piece of glass substrate and heated at 60 ℃ overnight. When the electrode material was completely dried, it was then soaked in D.I. water for around 10 min and the glass substrate was removed. Finally, the as-obtained electrode was dried in oven at 70 ℃ for 5 hours to remove the residue water molecules.

The electrochemical measurement was carried out in a sodium chloride/sulfate ($NaCl/Na_2SO_4$, 2M) aqueous electrolyte on a PGSTAT302F Metrohm Autolab workstation, in which two-electrode configuration was adopted due to its resemblances to real application. For comparison purpose, 2M KOH electrolyte was used in a similar setup. During the fabrication of cell, the as-fabricated electrode was tightly contacted on stainless steel (current collector) by mechanical force and a nylon membrane (Sigma-Aldrich) was used as separator. The electrochemical properties of the as-synthesized MOF-based nanomaterials were investigated using Cyclic Voltammetry (CV) at various sweeping rates ranging from 50 to 500 mV s^{-1} within a potential window of 2.0 V (-1.0 – 1.0 V), Electrochemical Impedance Spectroscopy (EIS) was carried out in a frequency range of 0.01 – 10^5 Hz with an AC signal of 10 mV amplitude, while the Galvanostatic Charge-Discharge (GCD) analysis was conducted at different current densities (i.e., 0.3 – 3.0 A g^{-1}).

The specific capacitance for symmetrical capacitors is calculated from **Eq. (5 – 7)**, and the corresponding energy density (E, Wh kg^{-1}) and power density (P, W kg^{-1}) of electrodes are calculated from **Eq. (8)** and (**9**) [237, 238]. Additionally, the energy deliverable efficiency (η), also known as coulombic efficiency, was acquired from **Eq. (10)** as follows:

$$C_{sp} = \frac{C_t}{2M} = \frac{C_E}{4M} \tag{5}$$

$$C_E = \frac{I\Delta t}{\Delta V} \tag{6}$$

$$C_t = \frac{C_E}{2} \tag{7}$$

$$E = \frac{1}{2} C_{sp} V^2 \tag{8}$$

$$P = \frac{E}{\Delta t} \tag{9}$$

$$\eta = \frac{t_d}{t_c} \times 100\% \tag{10}$$

where C_{sp} is the specific capacitance of the cell (F g^{-1}); C_t, with a unit of F, stands for the capacitance of the electrodes; M (g) denotes the average loading mass of active materials by assuming the mass loading on each electrode is identical; C_E (F) is the electrochemical capacitance of one single electrode. Meanwhile, I, with a unit of A, is the discharge current and Δt (s) is the discharging duration, in which the time period for internal resistance drop is excluded. ΔV (V) represents the potential difference between the end of IR drop and fully discharge. Lastly, η is the coulombic efficiency (%), t_d and t_c are the charging and discharging time, respectively.

3.4.1 Cyclic Voltammetry (CV)

CV is common employed for evaluating the electrochemical behavior of an electrochemical system, which is a kind of potentiodynamic electrochemical measurement measuring the developed current in an electrochemical system when the applied potential is higher than that predicted by the Nernst equation. Generally, ramp signal is provided during CV measurement, and a current-voltage profile consisting of two branches is obtained. If a negative ramp signal is applied for the forward scan, a reduction wave could be detected due to the reduction of active materials on the electrode. The applied voltage is switched after completing the first half-cycle and a positive ramp signal is offered for the second half-cycle, in which the reduced electrode active materials are oxidized and oxidation wave is recorded. The signal will come back to the same position where it started as the system is going to achieve the equilibrium state. Hence, the information on the potential range and the electrochemical reaction parameters, such as reversibility and electron transfer kinetics, can be observed and estimated by applying CV analysis.

3.4.2 Electrochemical Impedance Spectroscopy (EIS)

EIS is helpful to revolutionize research in the area of electrochemistry, and it is considered as one of the crucial techniques to characterize electrochemical reaction mechanisms. The electrochemical impedance is analyzed through applying an oscillating (alternating current) electric signal to an electrochemical cell to investigate the interfacial effects between electrode and electrolyte. Commonly, a sinusoidal current with a relatively small amplitude is utilized as the disturbance signal owing to two reasons: (i) A significant impact on the electrochemical system can be avoided. (ii) An approximately linear relationship between the corresponding response and disturbance can be acquired, which is beneficial to simplify the mathematical process of the resultant signals. As a result, the electrochemical system can be studied by an equivalent circuit.

3.4.3 Galvanostatic Charge and Discharge (GCD)

Galvanostatic charge and discharge analysis, also known as constant current charge and discharge, is usually utilized to examine the electrochemical energy storage properties of electrode active materials and energy storage systems, such as irreversibility, capacitive response, energy and power density. The utilization of this technique involves applying a constant current (both positive and negative) to charge and discharge the material or system under certain potential range.

Typically, the potential of a working electrode is recorded by applying a constant current between working and counter electrodes. To maintain the balance of the system, redox active species start to diffuse to the surface on the working electrode until the diffusion-limited concentration of the redox species is depleted. Meanwhile, the potential of the working electrode would switch to characteristic value based on Nernstian fashion, and followed by a dramatic change to a more negative value until a second reduction taking place. The shift is called the transition time. Hence, the potential of the cell, including both anode and cathode, can be measured accurately. Additionally, the cycling performance of a given cell can be studied as well.

Chapter 4: Solvothermal Synthesis of Nanostructured Nickel-based Metal-Organic Frameworks (Ni-MOFs) With Enhanced Electrochemical Performance for Symmetric Supercapacitors

4.1 Introduction

Wearable and portable gadgets have been emerging as a new trend for electronic devices nowadays for efficient and convenient human life, as the interactions between human and computer have become a potential prospect. The availability of energy storage with light weight, high power and energy density is the most challenging issue to drive intelligent devices. Among a wide range of energy storage systems, SCs are emerging as one of the potential solutions on the strength of superior charging and discharging rate performance, excellent power density and long-term cycling life [239, 240]. Despite the appealing high-power density and rate performance of MOF-based SCs, the relatively low cyclability and energy density have greatly hampered their real applications. As a result, the investigation and development of promising electrode active materials with large surface areas and high porosity are still crucial for high-performance SCs.

Among a variety of reported porous MOF materials, Ni-MOF nanostructures s are found to possess excellent electrochemical performance owing to the high electrical conductivity and excellent cyclability [245]. Nevertheless, it is hard to predict the bulk architectures, morphologies and porosities as there are numerous bonding interactions between metal sites and organic ligands. Moreover, only a few studies were carried out to systematically investigate the impact of reaction duration and processing temperature on the supercapacitive property of the electrode material. Besides, in our previous study [241], it was found that binary solvent with high viscosity and dielectric constant was favorable for size reduction of the Ni-MOFs from micrometers to nanomaterials. The micro-structures have been reported to provide large surface areas and effective channels for the storage and diffusion of electrolyte ions. Therefore, it is crucial to explore synthetic methods and conditions that yield MOFs with desirable structures and morphologies for high-performance SCs.

Herein, the impact of two crucial processing parameters including the temperature and duration of solvothermal reaction, on the electrochemical performance of benzene dicarboxylic acid-based MOFs were systematically studied. Ni-MOFs were first prepared at different temperatures ranging from 100 to 200 ℃ and with different reaction duration (8 – 32 h), while the corresponding electrochemical performance was studied accordingly. It was found that negligible amount of product was produced when the isothermal temperature was low (100 ℃), mainly due to the high energy barrier. In contrast, the decomposition of MOFs to corresponding metal oxides were observed at a high reaction temperature of 200℃. Meanwhile, the average sizes of Ni-MOF nanosheets tended to decrease with increasing reaction temperatures, and the crystallinity of these nanostructures was enhanced as reaction time was prolonged. The Ni-MOF nanomaterials synthesized at an optimum solvothermal temperature of 160 ℃ exhibited excellent electrochemical properties. In particular, a superior cycling durability (118% after 10,000 cycles) was achieved in an aqueous electrolyte. Additionally, the maximum delivered energy density of the electrode was recorded at 22.44 Wh kg^{-1}.

4.1.1 Synthesis of Ni-MOF Nanomaterials

The Ni-MOF nanomaterials were synthesized via a facile and low-cost solvothermal method, as reported elsewhere [241]. Meanwhile, in our previous study, it was found that the optimum coordination ratio between nickel (Ni) and oxygen (O) atoms was 1:6. Hence, a similar molar ratio between metal precursors and organic ligands was adopted in the current study. In a typical synthesis, 0.314 g of $Ni(NO_3)_2 \cdot 6H_2O$ and 0.030 g of H_2BDC were dissolved in a binary solvent (5 mL EG + 8 mL DMF) under ambient conditions. After stirring for 60 min, the green mixture was subsequently transferred into a Teflon-lined stainless-steel autoclave, which was then heated at 160 ℃ for 32 h. When it was cooled down to room temperature, the light green precipitates were centrifuged and washed with DMF and ethanol several times. The obtained green products were then subjected to solvent exchange for 96 h at a temperature of 60 ℃. Lastly, the resultant products were centrifuged and dried in vacuum oven overnight.

Similarly, other Ni-MOF samples were synthesized via this synthetic procedure by adjusting different solvothermal time and temperatures, respectively. The corresponding nanomaterials were denoted as FG_{12032}, FG_{14032}, FG_{18032} and FG_{20032} for Ni-MOFs synthesized at 120, 140, 180 and 200 ℃ for 32 h, respectively. Besides, FG_{16008}, FG_{16016}, FG_{16024} and FG_{16032} were synthesized at an optimum temperature of 160 ℃ for 8, 16, 24 and 32 h, respectively.

4.2 Results and Discussion

4.2.1 Material Characterizations

X-ray single-crystal diffraction patterns were obtained for Ni-MOF samples synthesized at different solvothermal temperatures and times, as shown in **Fig. 4.1a** and **b**. Two distinct broad peaks at 8.93° and 15.75° were observed, which could be related to the (100) and $(\bar{1}01)$ planes of Ni-MOF, respectively. A relatively weak peak at 11.93°, 31.73° and 40.29° were noticed as well, corresponding to the (010), $(3\bar{1}1)$ and $(4\bar{1}1)$ planes respectively. All these peaks were similar to the XRD patterns of Ni-MOFs reported in the literatures [242-244]. Meanwhile, the (100) plane was identified as the largest exposed facet besides the one synthesized at a high solvothermal temperature of 200 ℃. Besides, the diffraction planes (111) and (200) of NiO (JCPDS. 89-3080) were detected at 37.39° and 43.44°, respectively [245]. This finding indicated that the Ni-MOF nanostructures partially decomposed at such high temperature, leading to the formation of NiO. Additionally, these XRD patterns of Ni-MOFs synthesized at 120 and 140 ℃for 8 h exhibited weak crystalline nature. The crystalline intensity gradually increased with both reaction temperature and time (**Fig. 4.1a** and **b**).

The formation of Ni-MOFs was also confirmed by using FT-IR spectra, as depicted in **Fig. 4.1c** and **d**. The wide bands at approximately 3426, 3364 and 3088 cm^{-1} were ascribed to the existence of coordinated H_2O molecules within these nanomaterials [246]. Meanwhile, the stretching vibrations of OH^- could be observed at around 3612 cm^{-1}. Two strong peaks at 1576 and 1382 cm^{-1} were attributed to the asymmetric and symmetric stretching vibrations of the coordinated –COO- groups, respectively. The separation between these two peaks evidently indicated that the coordination between organic ligands (H_2BDC) and metal cations (Ni^{2+}) was in a bidentate mode

[246]. The bands in the range of 1006 – 1120 cm^{-1} in the IR spectra were assigned to the bending vibrations of C-O groups and the stretching O-Ni-O could be observed from 435 to 545 cm^{-1}. The presence of C-N stretching, resulting from the stretching vibration of aromatic amines, was detected in the range of 1290 – 1310 cm^{-1} for Ni-MOFs synthesized at different reaction times, which indicated that DMF molecules were incorporated during the formation of Ni-MOF crystals [247]. However, the C-N stretching peaks were shifted from 1290 to 1324 cm^{-1} when the solvothermal temperature was increased from 120 to 200 °C, suggesting a weakening of the bond between metal precursors and DMF solvent, and less amount of DMF molecules were coordinated into the Ni-MOF crystals which synthesized at a high solvothermal reaction temperature.

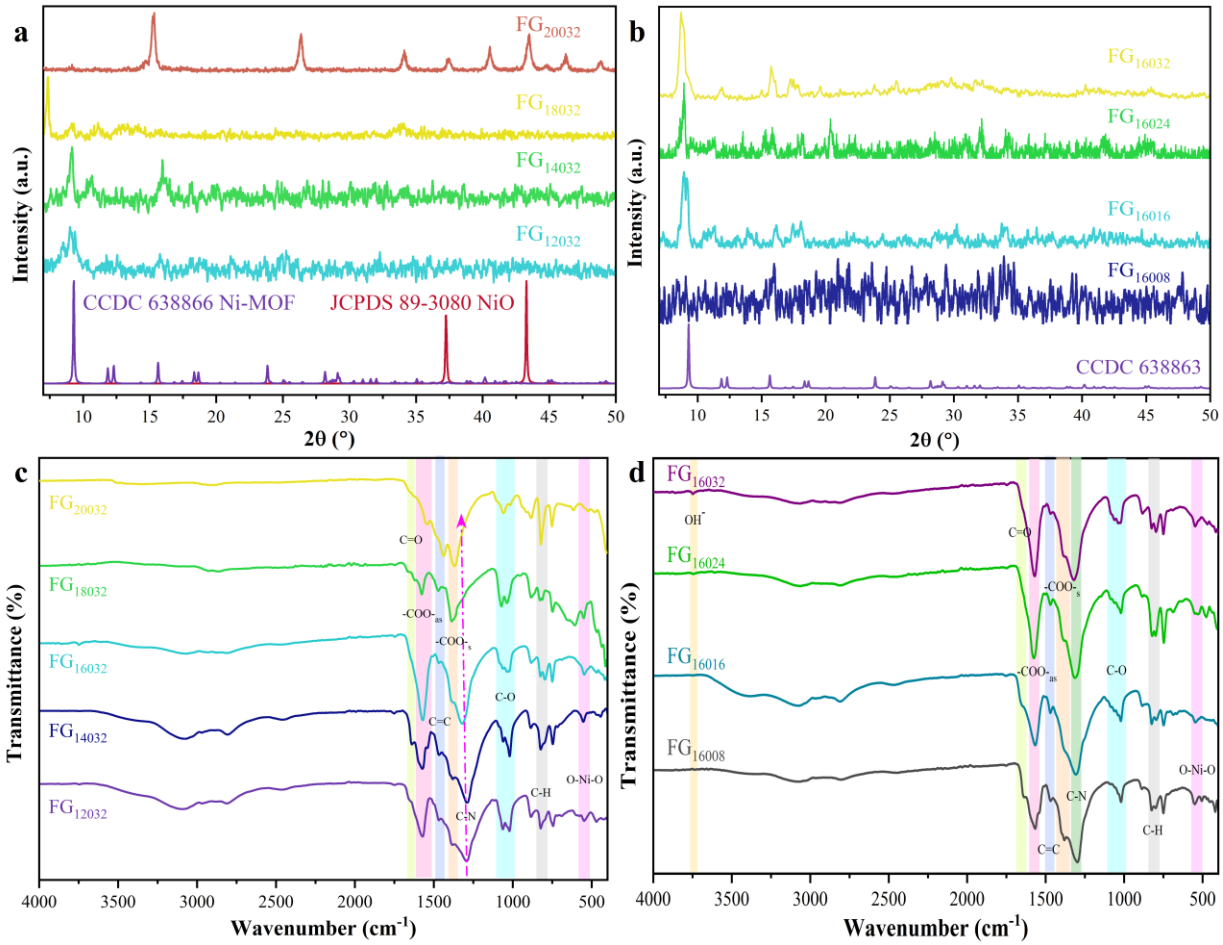


Figure 4.1. The XRD patterns (a, b) and FT-IR spectra (c, d) of Ni-MOFs synthesized at different solvothermal temperatures and times.

FESEM was carried out to investigate the morphologies and nanostructures of as-synthesized Ni-MOF nanomaterials. **Fig. 4.2** illustrates the FESEM images of Ni-MOFs prepared at different reaction temperatures. Ni-MOFs possessed hierarchical hollow microstructures owing to the aggregation of Ni-MOF nanosheets. Meanwhile, it was observed the sizes of holes within the hierarchical nanostructures decreased with increasing solvothermal temperatures from 120 to

200 °C. Particularly, randomly distributed and small-sized nanosheets were seen in FG_{18032} (**Fig. 4.2e**), and the hierarchical structure was slightly changed to hierarchical microsphere morphology with diameters in the range of 0.92 – 1.26 μm. More significantly, the nanosheet-like structure disappeared when the Ni-MOFs were synthesized at 200 °C (**Fig. 4.2g** and **h**), which could be attributed to the high nucleation rate at a high solvothermal temperature. Hence, it evidently revealed the reaction temperature was responsible for the change in the structure and morphology of Ni-MOFs owing to the different nucleation rates.

Fig. 4.3 shows the FESEM images for Ni-MOF nanomaterials synthesized at 160 °C for different solvothermal reaction times. All the nanomaterials exhibited hierarchical hollow microstructures, in which Ni-MOFs were formed by the densely stacked two-dimensional nanosheets, even though the solvothermal reaction time was prolonged from 8 to 32 h. This could be explained by crystalized-dissolved equilibrium as proposed by Seo et al. [248] Once the reaction reaches equilibrium, the crystallization rate and dissolution rate are the same. As a result, the extension of the reaction time only increased the product yields from 62.74% (FG_{16008}), 63.71% (FG_{16016}), 67.06% (FG_{16024}) to 73.04% (FG_{16032}), but did not cause any significant impact on the changes of the structure and morphology of the products. Moreover, N_2 adsorption/desorption isotherm was conducted to investigate the surface area and porosity as demonstrated in **Fig. 4.4**. The estimated BET surface area and pore volume of FG_{16032} were 3.48 m^2 g^{-1} and 0.038 m^3 g^{-1}, respectively. Additionally, the obtained mean pore size was 25.8 nm.

Besides, Energy-dispersive X-ray spectroscopy and elemental mapping analysis were conducted to examine the elemental compositions of the Ni-MOFs. As depicted in **Fig. 4.5** and **4.6**, a uniform distribution of Ni, C, O and N was clearly observed. The appearance of small amount of N could be derived from DMF solvent, manifesting DMF molecules were incorporated into the as-synthesized Ni-MOFs. As illustrated in **Fig. 4.5**, it was worth noting that the N content decreased when the solvothermal reaction temperatures were increased, revealing a high solvothermal temperature was unfavorable for the coordination of DMF solvent molecules. These results are in consistent with FT-IR finding and confirmed that solvothermal treatment temperature not only had a crucial role to play in the structures and morphologies of Ni-MOFs, but also had an important impact on the content of coordinated solvent molecules.

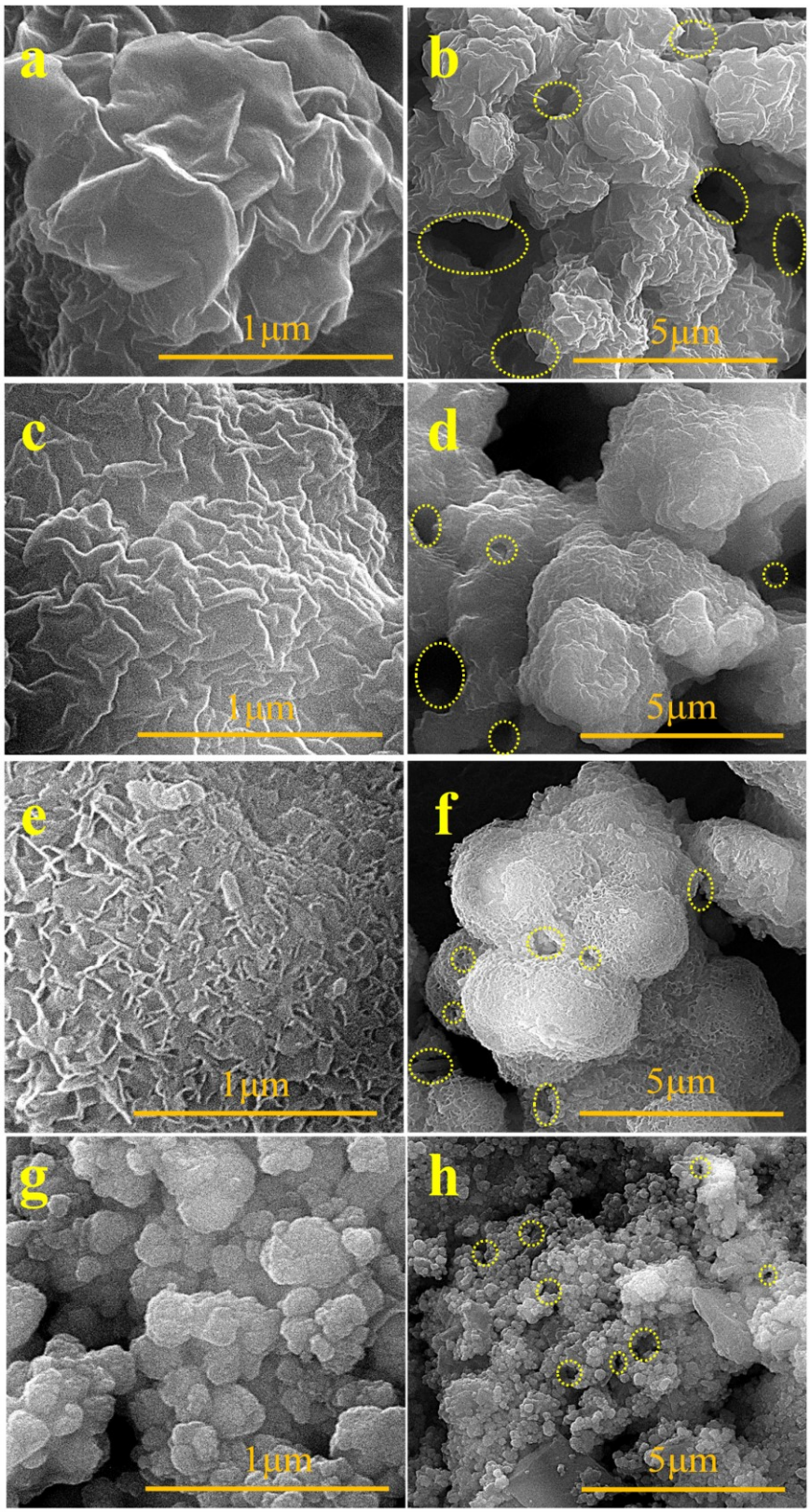


Figure 4.2. FESEM for Ni-MOF nanomaterials synthesized at different solvothermal temperatures of (a, b)120 ℃, (c, d) 140 ℃, (e, f) 180 ℃ and (g, h) 200 ℃.

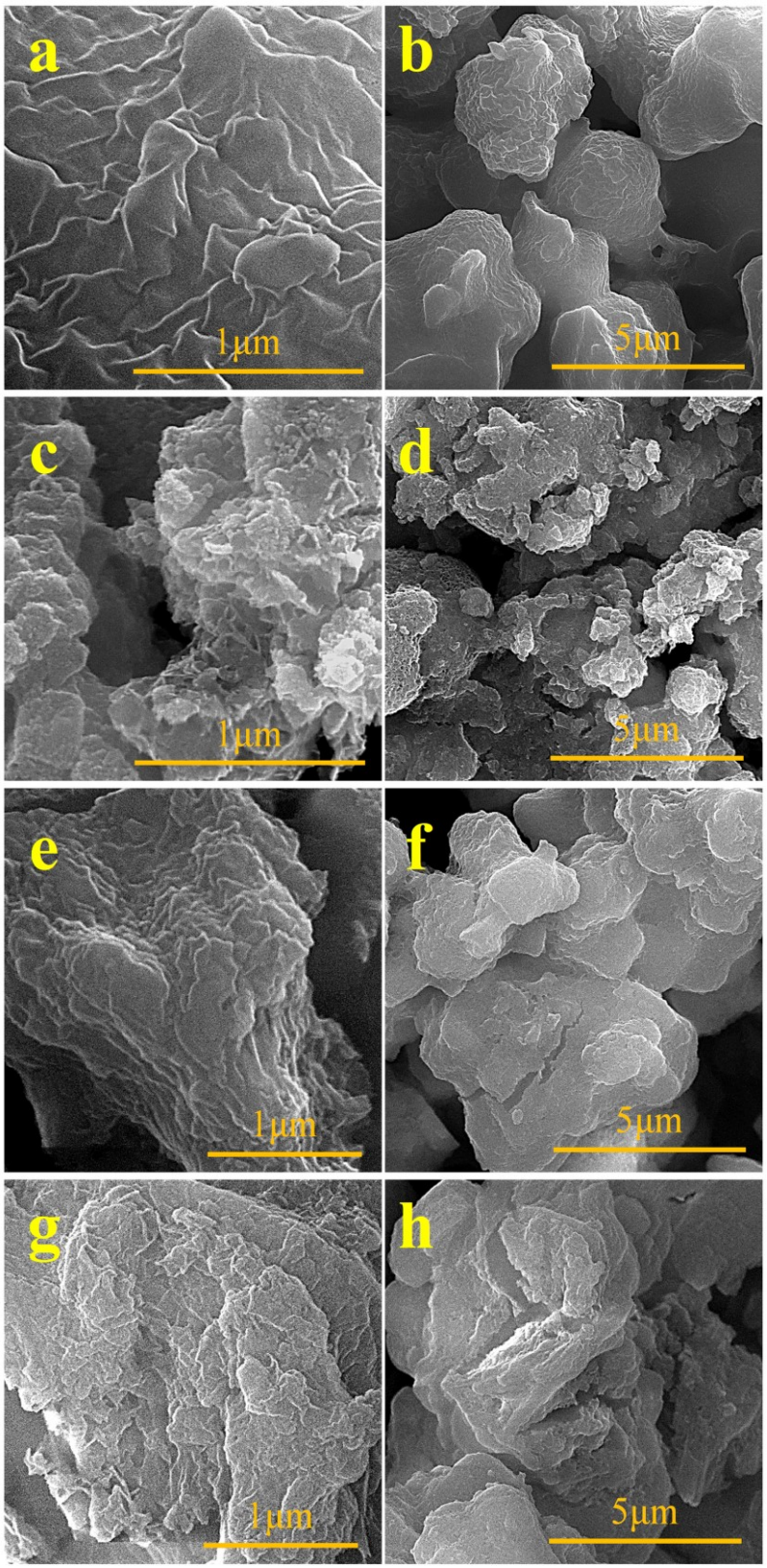


Figure 4.3. FESEM images for Ni-MOFs synthesized at 160 ℃ for (a, b) 8h, (c, d) 16h, (e, f) 24h and (g, h) 32h.

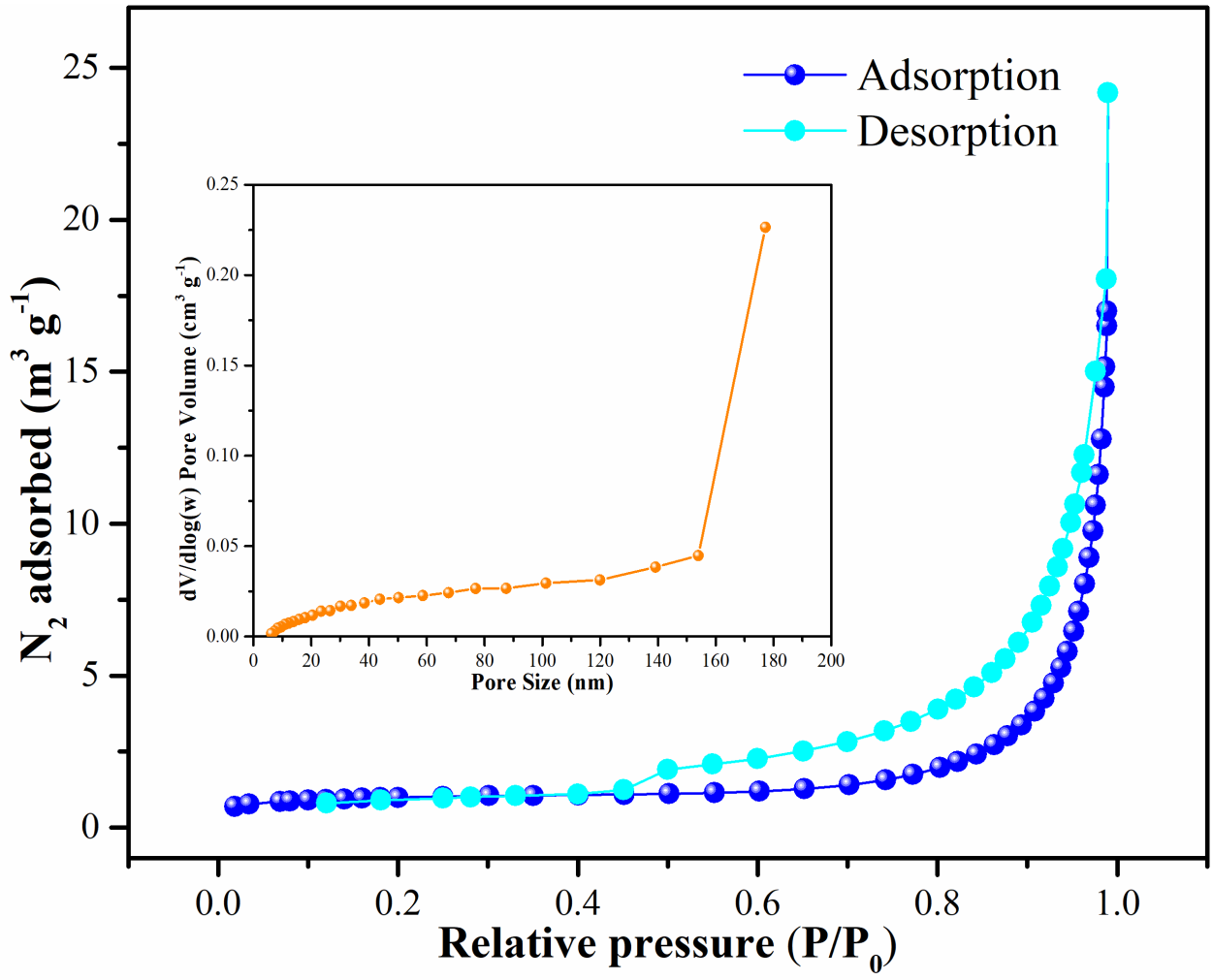


Figure 4.4. N_2 adsorption and desorption isotherms and pore size distribution (inset) of FG_{16032}.

The Ni-MOF nanostructures synthesized at 160 for 32h were further characterized by transmission electron microscopy (TEM). The typical low magnification TEM images were depicted in **Fig. 4.7**, which illustrated the aggregated nanosheet structures. To observe the lattice compression of as-synthesized Ni-MOFs, fast Fourier transform (FFT) analysis was performed at a selected area indicated in **Fig. 4.7a**, and the corresponding results were displayed in **Fig. 4.7b** and **c**. The calculated d spacing was 5.26 Å, corresponding to the plane of $(\bar{1}12)$. The obtained result was in good agreement with the selected area electron diffraction (SAED) pattern as shown in **Fig. 4.7d**, confirming the excellent crystallinity of FG_{16032} nanostructures. Additionally, high-resolution TEM (HRTEM) was carried out to evaluate the lattice fringes of FG_{16032} (**Fig. 4.7e**). The detected diffraction planes matched well with diffraction data from CCDC 638866.

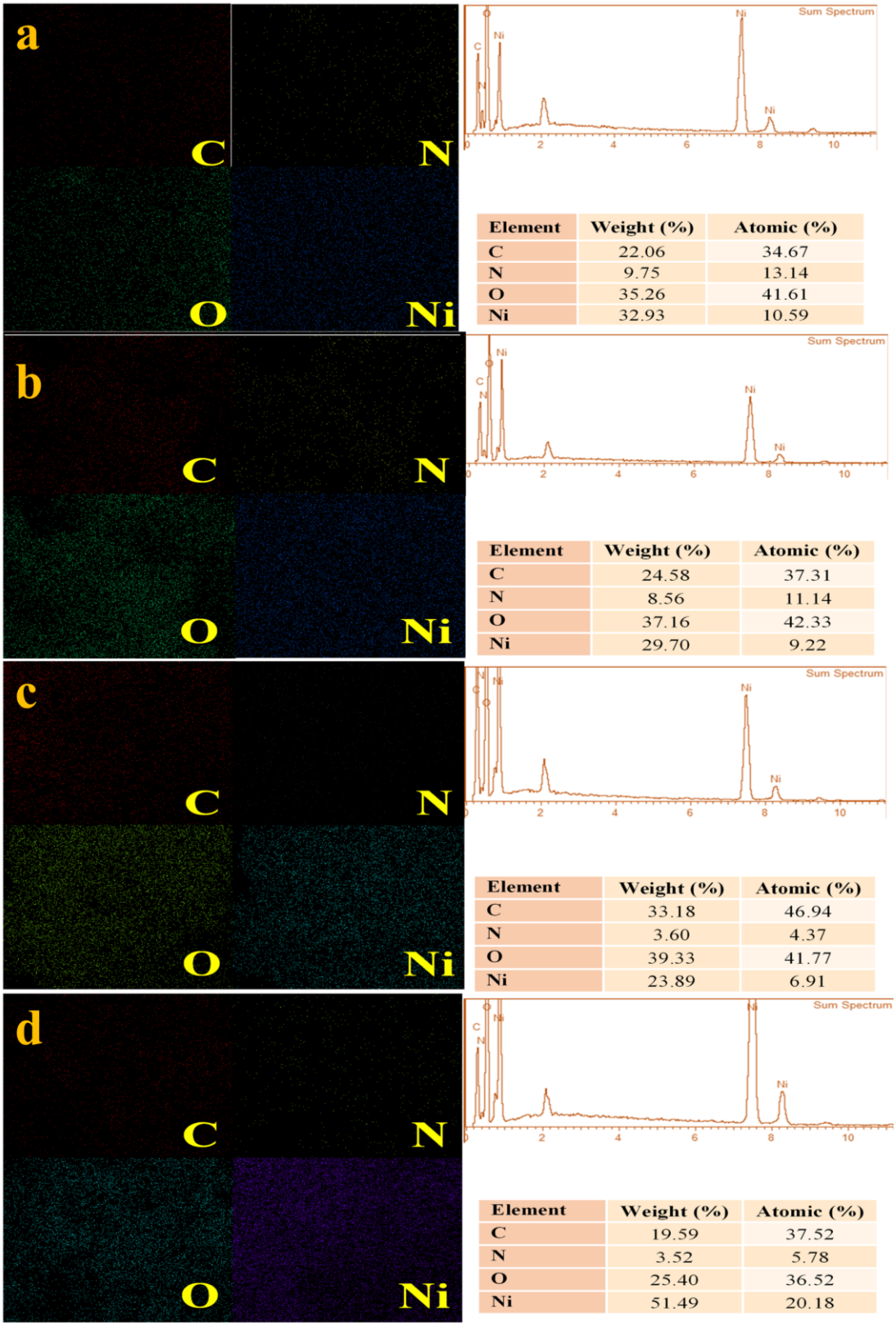


Figure 4.5. Elemental mapping and EDX images for Ni-MOF nanomaterials synthesized at different solvothermal temperatures of (a)120 ℃, (b) 140 ℃, (c) 180 ℃ and (d) 200 ℃.

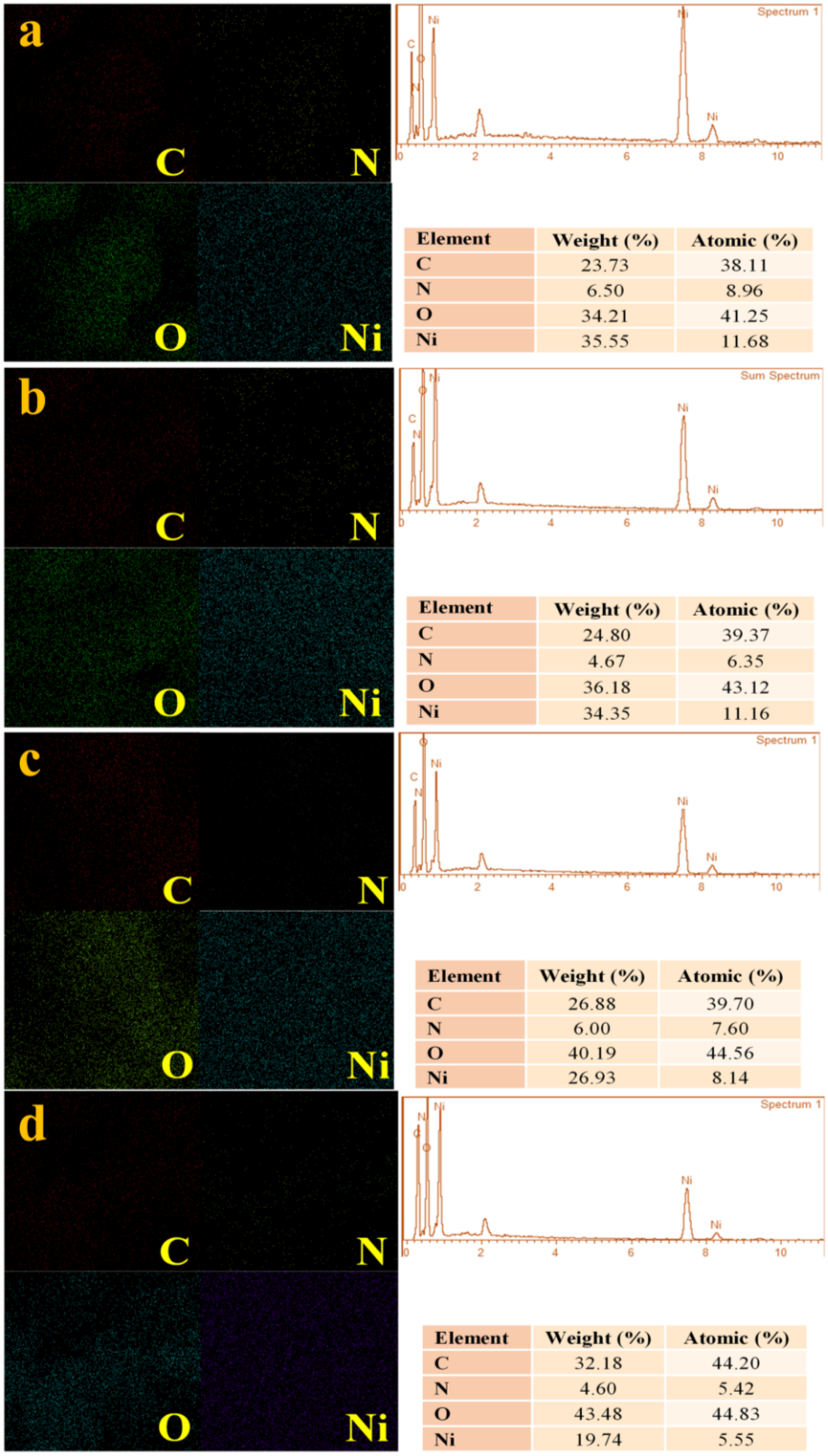


Figure 4.6. Elemental mapping and EDX images for Ni-MOFs synthesized at 160 ℃ for (a) 8h, (b) 16h, (c) 24h and (d) 32h.

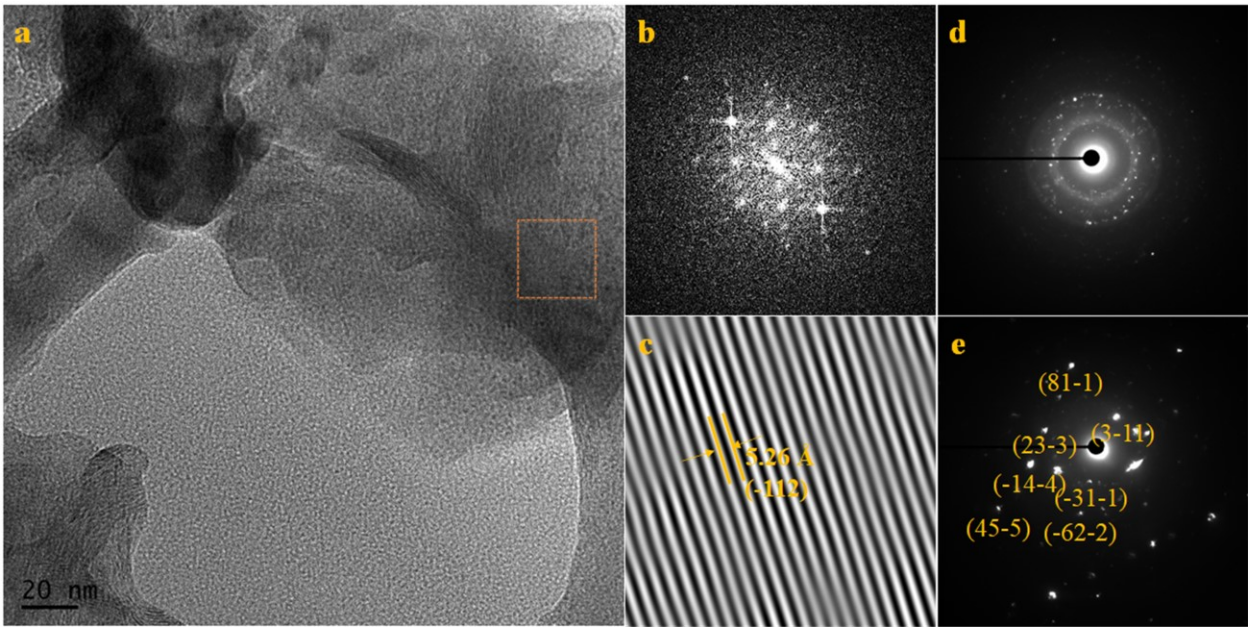


Figure 4.7. (a) TEM images of FG_{16032} nanomaterials, the corresponding (b) FFT pattern and (c) lattice spacing. (d, e) SAED patterns.

To evaluate the thermal stability of Ni-MOFs prepared at different solvothermal times and temperatures, TG-DTA analysis was performed and the finding was shown in **Fig. 4.8** and **4.9**. It could be clearly seen that Ni-MOFs synthesized at different solvothermal temperatures had different thermographic profiles. It was obvious that FG_{12032} possessed a very unstable structure, and the structure collapsed at temperature over 200 ℃. Meanwhile, FG_{14032} had a similar thermal degradation trend as those obtained at 160 ℃, while the main difference was the weight loss in the range of 170 – 250 ℃. This suggested the number of solvent molecules adsorbed in the pores were reduced when the solvothermal temperature was increased. Besides, for samples synthesized above 160 ℃, a gradual weight loss was observed between 30 and 350 ℃ because of the removal of physically and chemically adsorbed water and organic solvent molecules on the surface [249]. A rapid weight loss was identified when the temperature was higher than 350 ℃ owing to the conversion of Ni-MOF to its metal oxide (NiO). In addition, all samples (FG_{16008} – FG_{16032}) prepared at 160 ℃ showed similar TGA profiles, indicating these samples exhibited similar chemical composition and architectures.

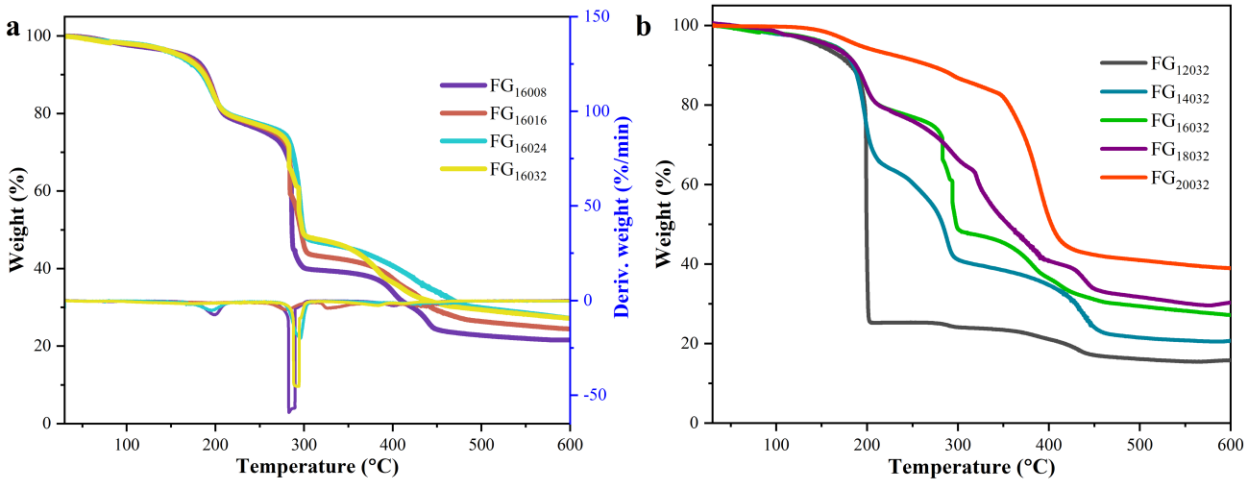


Figure 4.8. Thermogravimetric analysis for Ni-MOF nanomaterials synthesized at different solvothermal temperatures (a) and times (b).

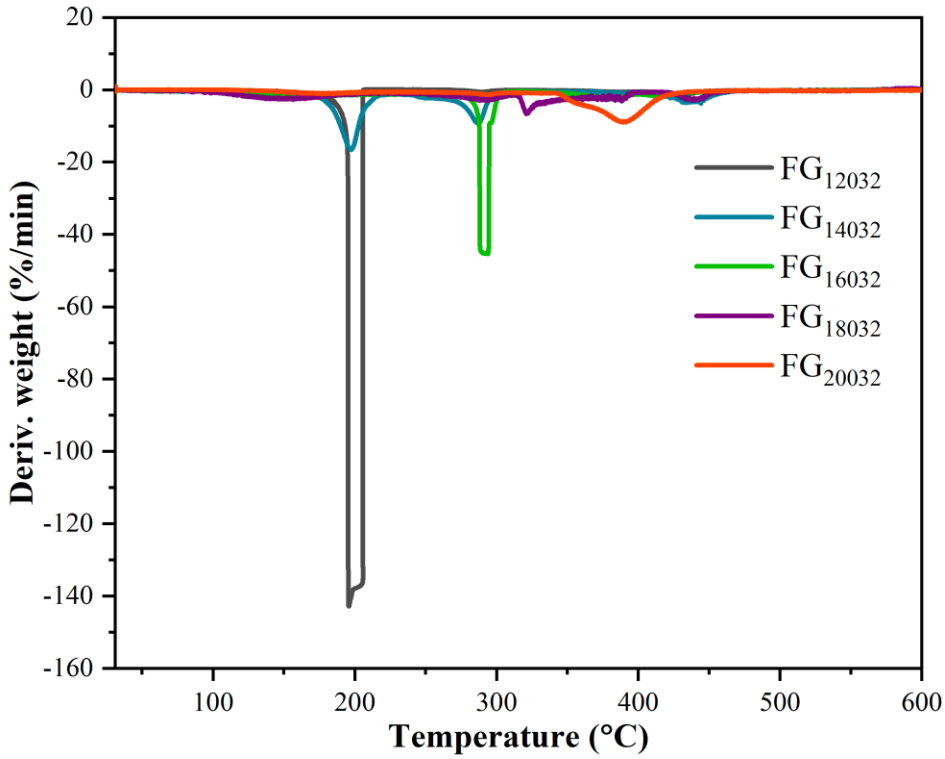
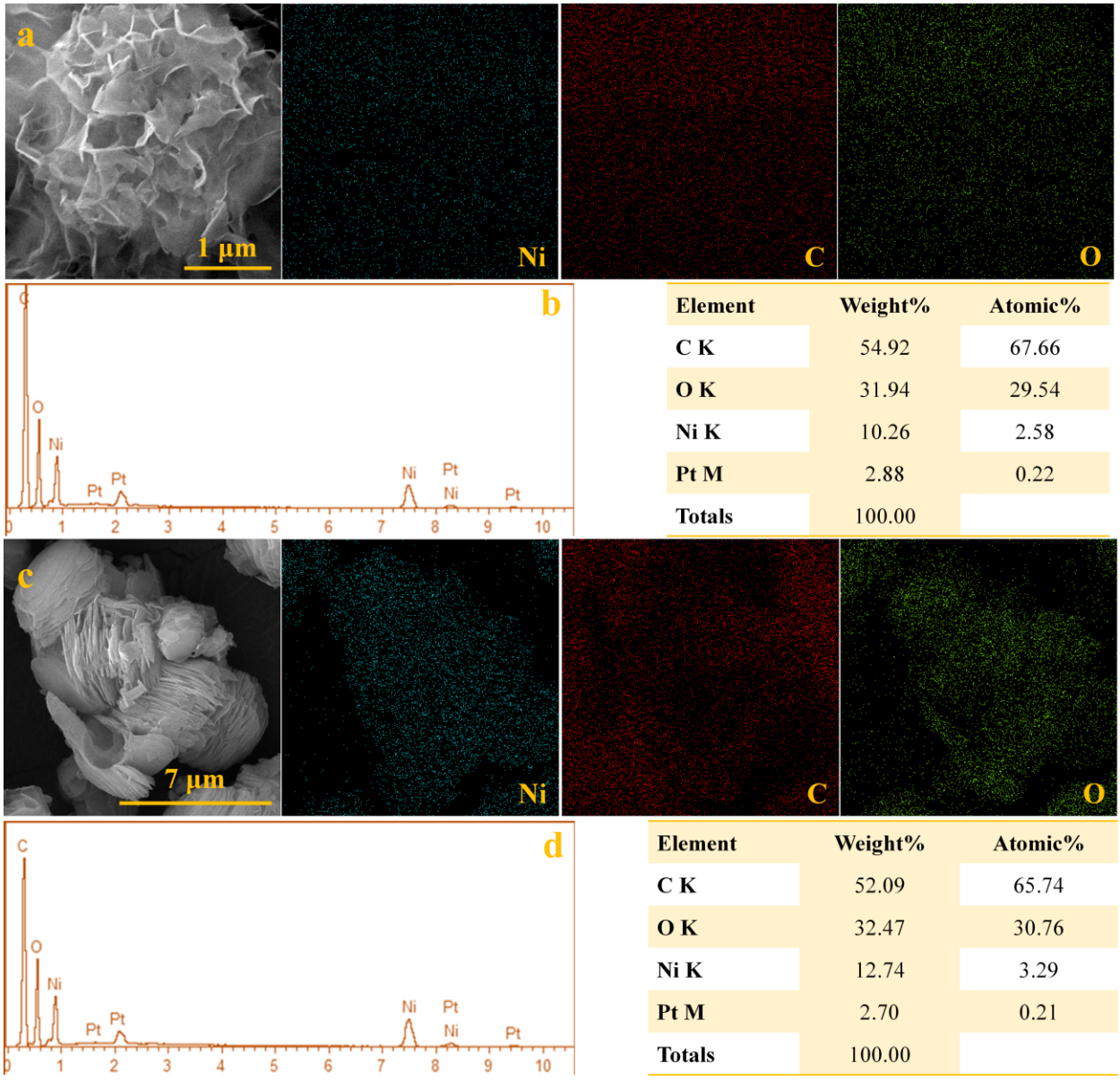


Figure 4.9. Derivative thermogravimetric curves for Ni-MOF nanomaterials synthesized at different temperatures.

In the current study, it was found that DMF molecules could react and coordinate with metal precursors at the ratio of 6 : 1 (Ni^{2+} : H_2BDC), although the reaction temperature was as low as 120 ℃. To further prove this finding, Ni-MOFs were prepared at 160 ℃ for 6 h at molar ratios of Ni^{2+} to H_2BDC ranging from 1:1 to 5:1. The EDX and elemental mapping of the resultant Ni-

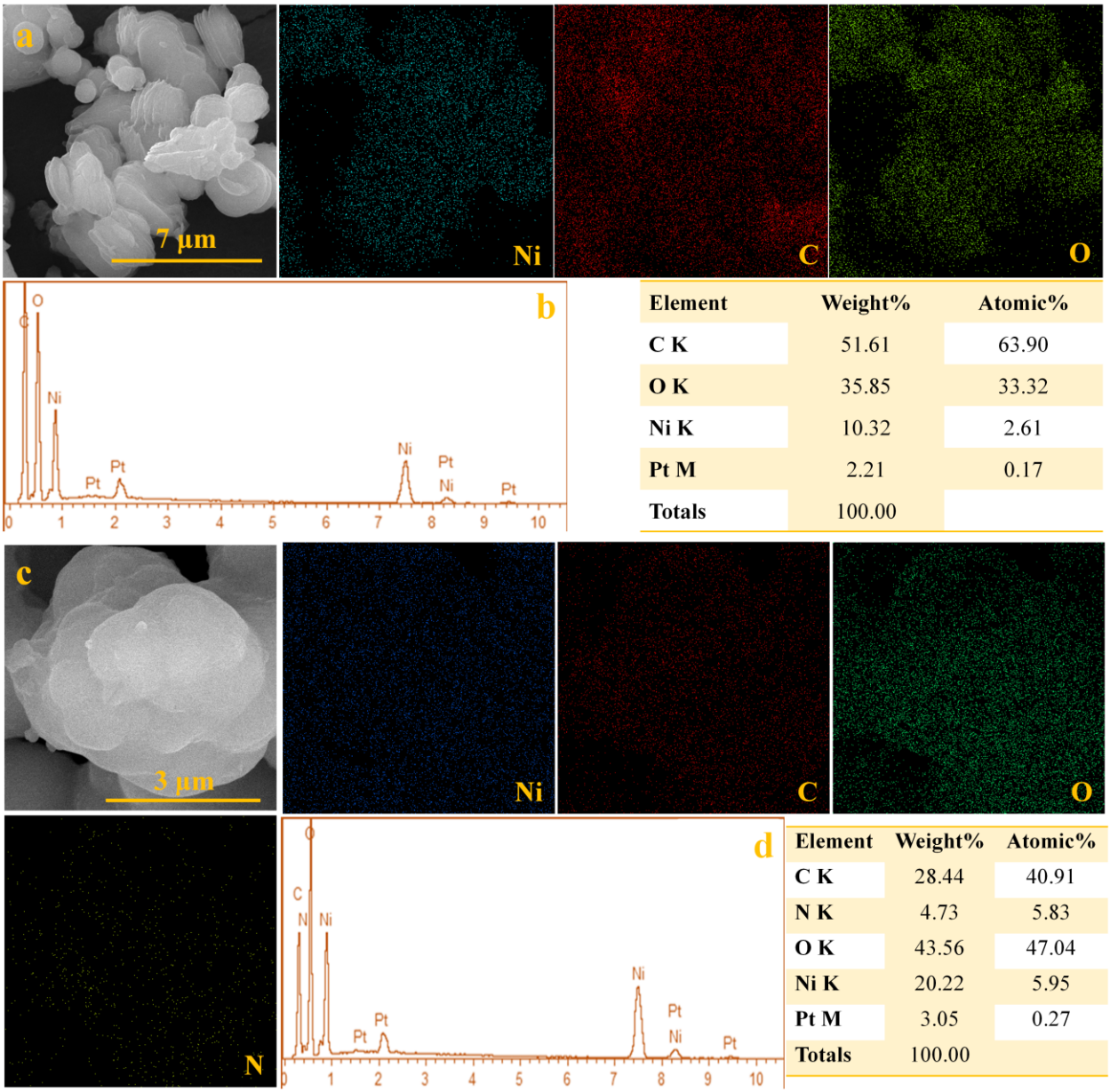
MOFs were demonstrated in **Fig. 4.10** and **4.11**. It was found that element N started to appear when the ratio exceeded 4:1. Hence, we could conclude that solvent molecules (DMF) could coordinate with metal ions during the synthesis when the metal cations were in excess. When only a few numbers of metal precursors appeared in a system, the main coordination occurred between Ni^{2+} and H_2BDC. DMF could interact with Ni^{2+} as organic ligand was completely consumed. As a result, the variation could be observed in terms of topology, morphology and electrochemical property of the as-synthesized Ni-MOF nanomaterials. Besides, it was worth noting that the coordination of DMF molecules did not alter the crystallinity but changed the porous structures and morphologies of Ni-MOFs, as a result of coordination complex formation [250, 251].



Element	Weight%	Atomic%
C K	54.92	67.66
O K	31.94	29.54
Ni K	10.26	2.58
Pt M	2.88	0.22
Totals	100.00	

Element	Weight%	Atomic%
C K	52.09	65.74
O K	32.47	30.76
Ni K	12.74	3.29
Pt M	2.70	0.21
Totals	100.00	

Figure 4.10. EDX and elemental mapping images for Ni-MOFs synthesized with a molar ratio between Ni^{2+} and H_2BDC of (a, b) 2 : 1 and (c, d) 3 :1.



Element	Weight%	Atomic%
C K	51.61	63.90
O K	35.85	33.32
Ni K	10.32	2.61
Pt M	2.21	0.17
Totals	100.00	

Element	Weight%	Atomic%
C K	28.44	40.91
N K	4.73	5.83
O K	43.56	47.04
Ni K	20.22	5.95
Pt M	3.05	0.27
Totals	100.00	

Figure 4.11. EDX and elemental mapping images for Ni-MOFs synthesized with a molar ratio between Ni^{2+} and H_2BDC of (a, b) 4 : 1 and (c, d) 5 :1.

4.2.2 The Impact of Reaction Temperature

In the current study, it was found that only negligible number of Ni-MOF precipitates were obtained, when the isothermal temperature was 100 °C. This could be attributed to the high Gibbs free energy barriers for the coordination of Ni^{2+} and H_2BDC at this temperature. Moreover, this could be interpreted by the fundamental mechanisms of crystal growth as well [252]. Initially, crystal nucleus starts to form once the surface energy is overcome, and the generation of crystal nuclei can only take place when the solution reaches supersaturation [253]. In a saturated solution,

a dynamic equilibrium is reached where the solvation and reformulation rates are the same. Hence, a stable existence of nuclei only occurs in supersaturated solution. Besides, these nuclei start to concurrently or sequentially grow to large-sized units with different structures and morphologies. As a result, the formation of MOF crystals with desired morphology and structures greatly relies on supersaturation [254]. Additionally, it is known that solubility of organic ligands would increase with the solvothermal temperature due to the increase in pressure. It is also found the solubility of H_2BDC was quite low at a lower temperature [255], as shown in **Fig. 4.12a**. In this case, the supersaturation could not be reached at such reaction temperature (**Fig. 4.12b**, green trace), the coordination between metal precursors (Ni^{2+}) and organic ligands (BDC^{2-}) was hence hindered.

The average dimensions of these Ni-MOF nanosheets decreased with increasing reaction temperatures from 120 to 200 ℃. Similar result was observed in Tsai' s study as well [256], in which the average particle sizes of nZIF-8 nanoparticles declined from 78 nm to 27 nm as the reaction temperature raised from -15 to 60 ℃. This could be due to the fact that the formation of Ni-MOF nuclei was limited at a lower synthesis temperature, and majority of precursors was able to access a small number of nuclei and grow into larger sheets. Nonetheless, the nucleation rate was further enhanced when the treatment temperature was increased, leading to a higher concentration of nuclei. Consequently, the average sizes were further reduced. It can be concluded that the nucleation rate of Ni-MOFs was mainly dependent on the solvothermal temperature.

Based on the classic Lamer nucleation and growth model [257, 258], the nucleation and crystal growth of MOF nanostructures go through three stages, as demonstrated in **Fig. 4.12b**. (i) The concentration of reactive monomers increases rapidly when metal precursors and organic ligands are well mixed (stage I). (ii) Subsequently, MOF nuclei are formed quickly as the concentration of reactive monomers reaches supersaturation concentration (C_{ss}), which is also known as critical nucleation concentration (stage II). Meanwhile, the concentration of monomers decreases drastically since nucleation can take place immediately. (iii) Lastly, generated nuclei start to grow when the concentration returns back to saturation (stage III), in which solvation rate is the same as crystal growth rate. When Ni-MOFs were synthesized at slightly low solvothermal temperatures, such as 120 and 140 ℃ (**Fig. 4.12b**, blue trace), majority of precursors (Ni^{2+} and BDC^{2-}) were able to react with very few nuclei due to the slow nucleation rate. Consequently, large pieces of nanosheets could be produced. Additionally, these nuclei start to aggregate due to van der Waals forces [259]. Nonetheless, nucleation rate could be fastened with increasing reaction temperature [260], a large number of nuclei could be generated quickly (**Fig. 4.12b**, red trace). Only a small number of precursors could react with generated nuclei owing to the rapid consumption of metal precursors and organic ligands. Moreover, high supersaturation could be achieved at high pressure and elevated temperature (i.e., 180 and 200 ℃), which was also favorable for the generation of small-sized crystals [261]. Consequently, the resultant average sizes of the Ni-MOF particles were reduced. These generated stable Ni-MOF nanoparticles would contact with each other to form clusters with different morphologies by taking advantage of the high surface energy [262] and inevitable random coagulations.

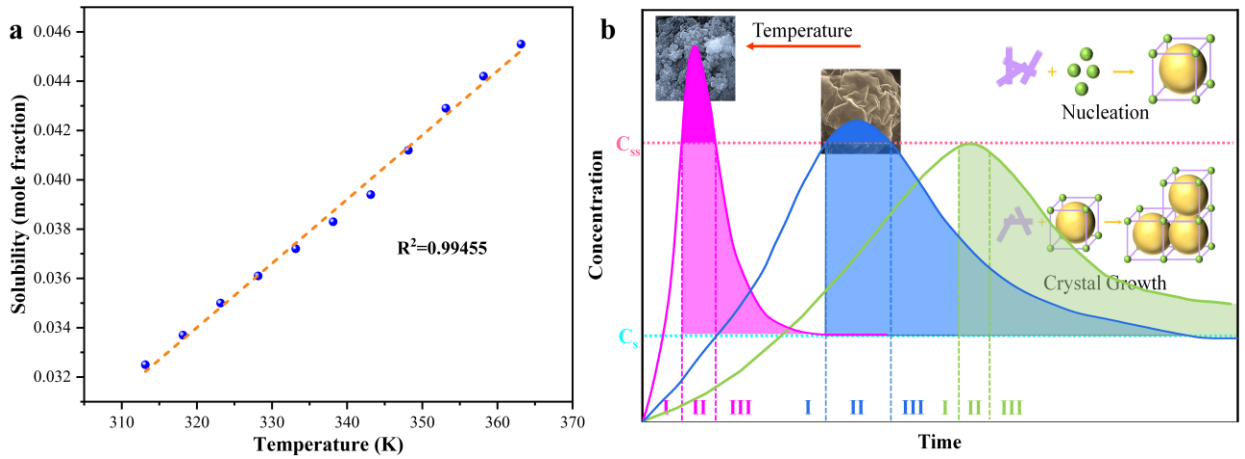


Figure 4.12. Solubility of *p*-benzenedicarboxylic acid in DMF solution (a) and the classic Lamer nucleation and growth model (b).

4.2.3 Electrochemical Analysis

4.2.3.1 Cyclic voltammetry (CV)

To examine the electrochemical performance of these electrode materials, CV analysis was performed at various scan rates ranging from 50 to 500 mV s^{-1} in 2M NaCl aqueous electrolyte. The operating potential window of the as-fabricated SC device was analyzed at a sweeping rate of 50 mV s^{-1} (**Fig. 4.13a**). It was obvious that the CV profiles presented quasi-rectangular shapes without any Faradaic redox peaks within the potential windows from -1.0 to 1.0 V, suggesting the electrode could operate stably within this operating electrochemical window range. **Fig. 4.13b** and **c** show the cyclic voltammograms of Ni-MOF nanomaterials synthesized at different solvothermal times and temperatures at a scan rate of 50 mV s^{-1} within -1.0 – 1.0 V potential range. The existence of any oxidation and reduction peaks were not observed within the scanning range, suggesting these electrode active materials possessed electric double-layer capacitive (EDLC) behavior. Meanwhile, similar CV curves with approximately same encircled areas were found for Ni-MOFs synthesized at various solvothermal times. However, an obvious variation in the CVs was observed for Ni-MOFs synthesized at different solvothermal temperatures. Specifically, the enclosed areas as well as peak current densities gradually increased from 120 ℃ to 160 ℃ but then started to decrease until 200 ℃. The amorphous structure of Ni-MOFs obtained at a low temperature was unfavorable for the fast diffusion of ions due to the tightly contacted layers. Moreover, the partially broken structure was not able to store enough electrolyte, leading to the reduction in capacitance. On the other hand, the small-sized 2D nanosheets could enlarge the area for charge storage and hence improved the capacitive performance, and the electrolyte ion transport could be significantly hampered by the narrowed hollow structures resulting from a higher reaction temperature. For comparison, the CV of FG_{16032} was also evaluated in a three-electrode system using 2M KOH aqueous electrolyte. The appearance of a pair of redox peaks (**Fig. 4.14a**) indicated the predominance of pseudocapacitance in the charge storage. Furthermore, the delivered maximum specific capacitance was 619.62 F g^{-1} and 73.7% (**Fig. 4.14b** & **c**) of its initial capacitance could be retained when the current density was increased by 10 folds, indicating the outstanding electrochemical property of FG_{16032} nanomaterials. Hence, the solvothermal temperature at 160 ℃

was identified as the optimum temperature for the synthesis of Ni-MOF nanomaterials in the current study.

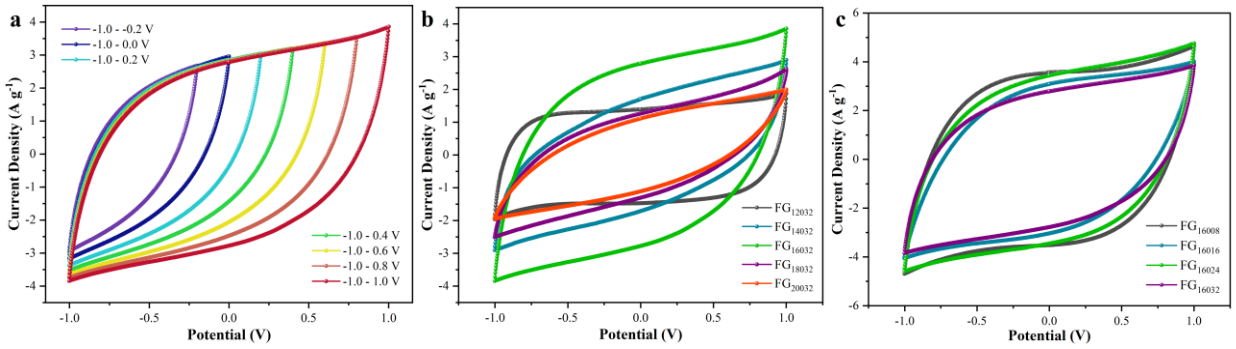


Figure 4.13. Optimization of potential window of Ni-MOF SC electrode in 2M NaCl (a). Cyclic voltammetry for Ni-MOF nanomaterials synthesized at different reaction temperatures (b) and times (c).

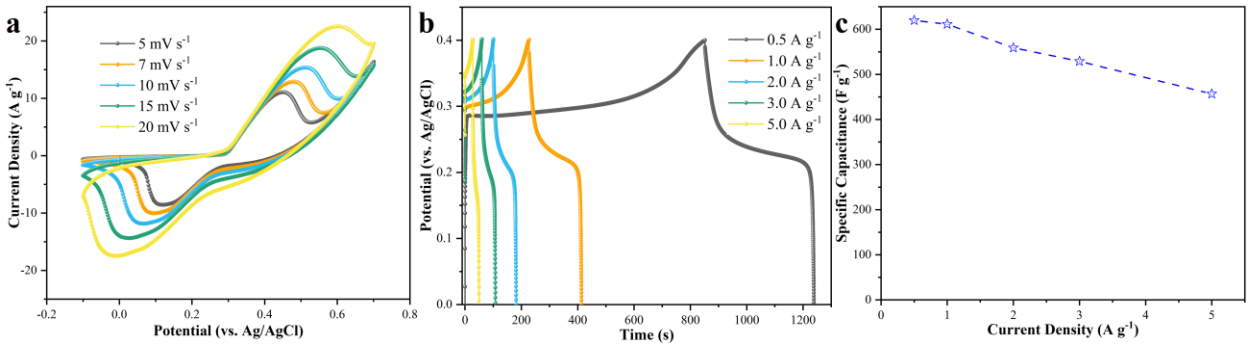


Figure 4.14. The (a) CV, (b) GCD profiles and (c) specific capacitance calculated from GCDs of FG_{16032} nanomaterials in 2M KOH electrolyte.

The CV profiles of Ni-MOF nanomaterials synthesized at different solvothermal times at scan rates between 50 and 500 mV s^{-1} were shown in **Fig. 4.15**. Clearly, quasi-rectangular shapes were retained by all samples, annotating the sodium storage was controlled by EDLC behavior. Meanwhile, the corresponding current density rose with increasing scan rates, and the quasi-rectangular shape could be maintained by these nanomaterials even though the scan rate reached up to 500 mV s^{-1}. This was a good indication of the excellent charge/ionic kinetics of the as-synthesized electrode active materials [263]. The deviation from fairly rectangular shape at high scan rates could be ascribed to the diffusion-limited process, in which electrolyte ions (Na^+/Cl^-) did not have sufficient time to completely access the internal pores of the fabricated electrode at a high scan rate [264]. The lack of smooth inner-pore transfer channels could eventually result in a higher internal resistance (IR) drop at a high current density. Besides, a higher specific capacitance was acquired at a lower scan rate, suggesting the crucial role of micro- and meso-pore structures in the ion transfer and charge storage, respectively [265].

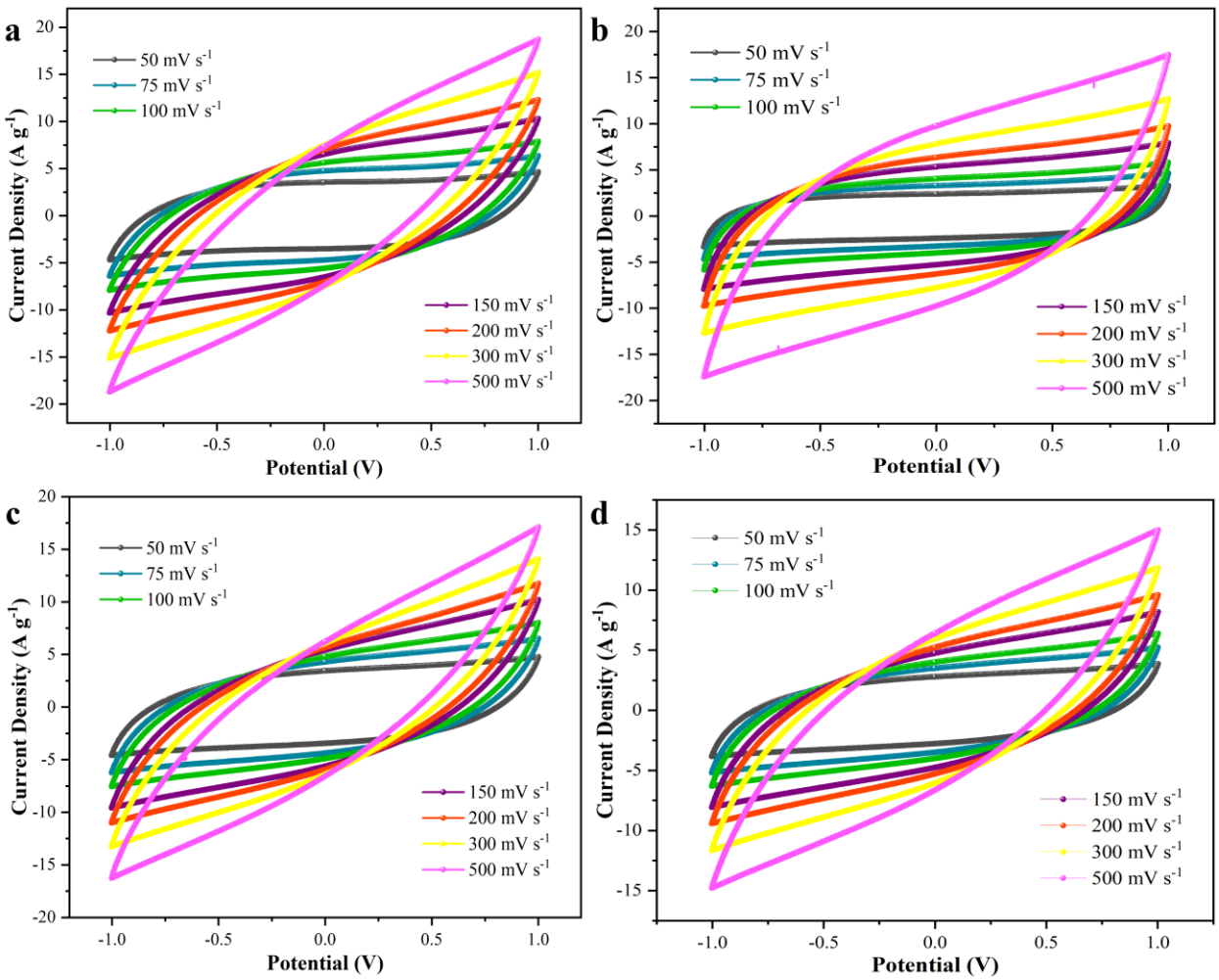


Figure 4.15. Cyclic voltammetry profiles for Ni-MOFs synthesized at 160 °C for 8 (a), 16 (b), 24 (c) and 32 hours (d) with different scan rates ranging from 50 to 500 mV s^{-1}.

To further investigate the charge and energy storage mechanisms of Ni-MOF nanomaterials synthesized at 160 °C, the relationship between peak current and scan rate/square root of scan rate was studied ranging from 50 to 500 mV s^{-1} (**Fig. 4.16a** and **b**). According to the linear fitting, it was obvious that both plots (i vs. υ and i vs. $\upsilon^{1/2}$) presented a linear trend, whereas the R^2 values were found to be slightly higher for i vs. $\upsilon^{1/2}$ plots, indicating the dominance of diffusion-controlled process in energy storage, in which the insertion and deinsertion of electrolyte ions showed great influence on the charge storage. Hence, it could be interpreted that diffusion-limited process was the favorable fit mechanism for Ni-MOFs synthesized from different solvothermal times at 160 °C in neutral aqueous electrolyte.

Dunn's power-law method was employed to better understand the charge storage mechanism in the electrode active materials [266], as given in **Eq. (11)**:

$$i = av^b \qquad (11)$$

where a and b are two constants, i is the potential-dependent current and υ denotes the scan rate.

To obtain the value of b, ln(i) vs. ln(v) ($ln(i) = bln(v) + ln\ (a)$) was plotted in **Fig. 4.16c** and the value of b could be obtained from the slope of the plot. In general, nondiffusion-limited process is responsible for charge storage if b is close to 1.0, while diffusion-limited process is dominant if b is approximately 0.5. According to the linear plots of ln(i) vs. ln(v), the values were found to be in the range of $0.44 < b < 0.61$ at 1.0 V, manifesting the diffusion-limited process was the dominance in charge storage for Ni-MOF nanomaterials synthesized at 160 ℃. The linear relationship of Ni-MOF$_{16032}$ at different potentials (from 0.5 to 1.0 V) was shown in **Fig. 4.16d**. The b-value was found to rise gradually with an increasing potential but not more than 0.6, which were 0.525, 0.544, 0.559, 0.573, 0.582 and 0.597 at 0.5, 0.6, 0.7, 0.8, 0.9 and 1.0 V, respectively. It evidently annotated the energy and charge storage were mainly dominated by diffusion-limited process for these Ni-MOFs synthesized at 160 ℃.

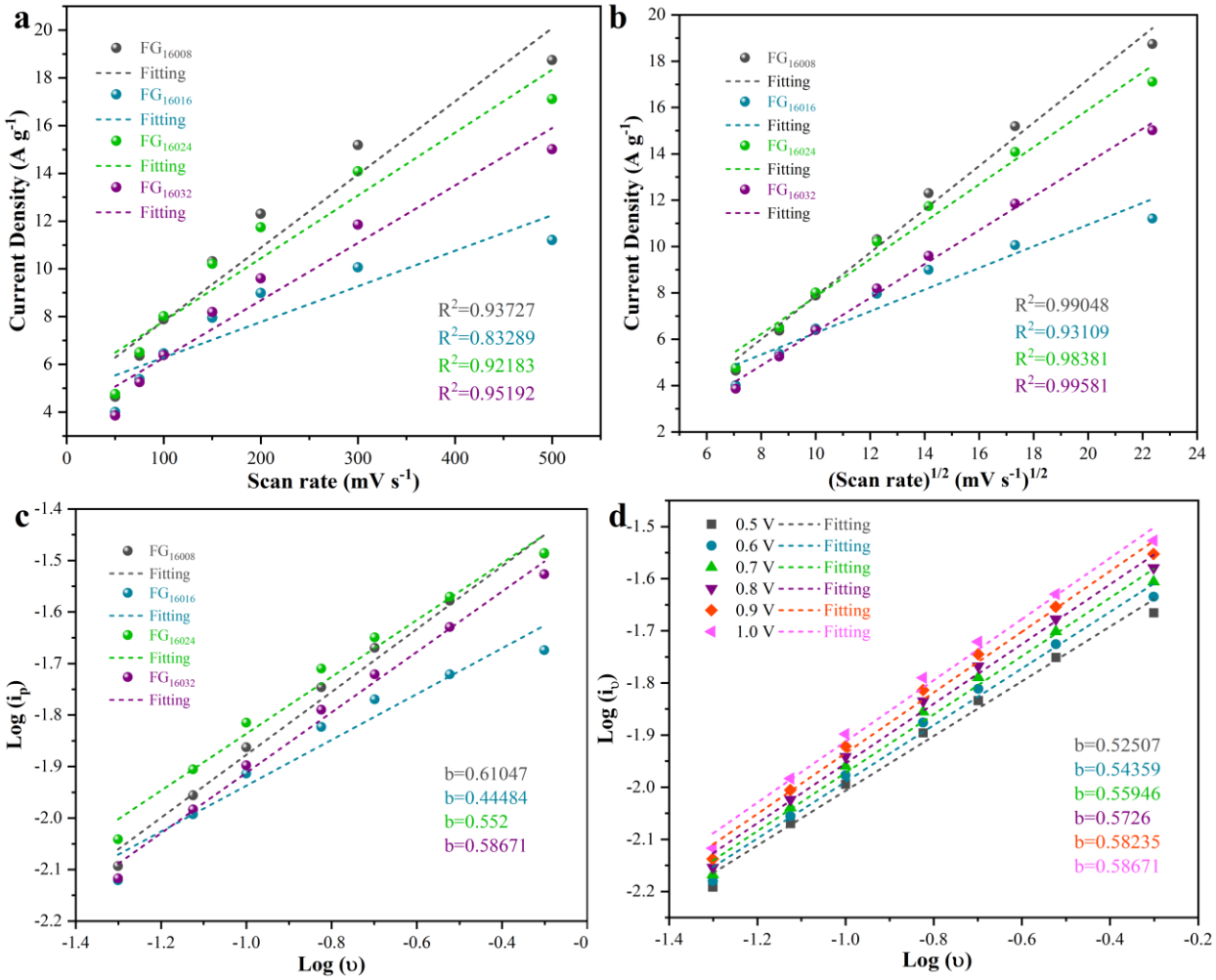


Figure 4.16. The relationship between peak current and scan rate (a) square root of scan rate (b). The power-law relationship of Ni-MOFs obtained at 160 ℃ for different times (c) and FG$_{16032}$ at different potentials (d).

The quantitative contribution of capacitive and diffusion-limited processes could be further evaluated by a modified power-law. Typically, the current at a particular voltage could be subdivided into capacitive current (i_{cap}) and diffusion-limited current (i_{diff}) as given in **Eq. (12)**:

$$i = i_{cap} + i_{diff} = k_1 v + k_2 v^{0.5} \quad (12)$$

where k_1 and k_2 are constants for capacitive and diffusion-limited processes, respectively.

Fig. 4.17(a – d) displays the proportion of current contributions from both capacitive and diffusion-limited processes at a scan rate of 50 mV s^{-1}. The contribution from capacitive process was less than one quarter of the total current contribution, demonstrating the dominance of diffusion-limited process. It could be observed that the closed capacitive contributions lied beyond the primary CV curves, mainly owing to the electrode polarization [267, 268]. Moreover, the calculated percentage contribution of capacitive and diffusion-limited processes was depicted in **Fig. 4.17(e – h)** for Ni-MOFs synthesized for different solvothermal durations. The current contribution from diffusion-limited behavior was dominant in all Ni-MOF nanomaterials at low scan rates (<200 mV s^{-1}). However, at a high scan rate, the charge contribution was mainly from capacitive process due to the slow diffusion in bulk materials.

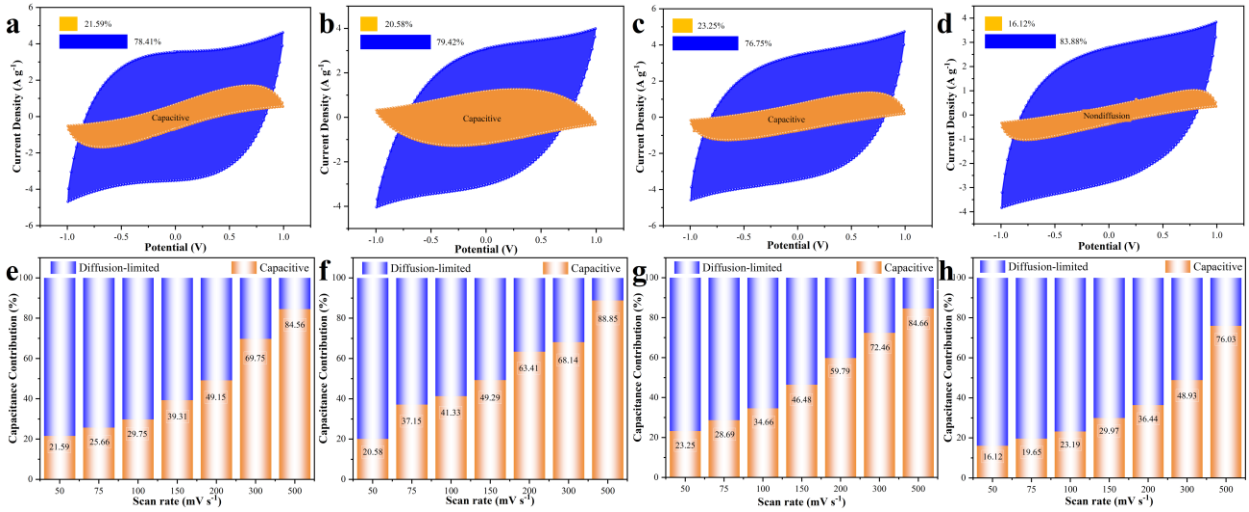


Figure 4.17. Capacitive and diffusion-limited capacitance contribution at 50 mV s^{-1} for (a) FG_{16008}, (b) FG_{16016}, (c) FG_{16024} and (d) FG_{16032}, respectively and the proportion of EDLC and diffusion-limited capacitance contribution at different scan rates for Ni-MOFs synthesized at different hydrothermal times: (e) FG_{16008}, (f) FG_{16016}, (g) FG_{16024} and (h) FG_{16032}.

4.2.3.2 Galvanostatic charge-discharge (GCD)

The electrochemical performance of Ni-MOF nanostructures synthesized at different solvothermal temperatures and times in 2M NaCl electrolyte was quantitatively evaluated by employing GCD technique within 0 – 1.0 V. The GCD measurement was performed to investigate the rate capability of the as-fabricated electrode at various current densities of 0.3, 0.6, 0.9, 1.2, 1.5 and 3.0 A g^{-1}. As depicted in **Fig. 4.18**, all the GCD curves showed feckly symmetrical triangular shapes, indicating

the charge storage mechanism was based on electrostatic ion adsorption/desorption at the electrode and electrolyte interface [269]. A slight potential drop (also known as IR drop) was observed at the beginning of discharging. The small IR drop might be caused by the Ni-MOFs with cross-linked structures. All the obtained results are in accordance with the behavior shown on the CV profiles.

The charging and discharging profiles of Ni-MOF nanomaterials synthesized at different solvothermal temperatures were demonstrated in **Fig. 4.18a** at a current density of 0.3 A g^{-1}. FG_{16032} possessed the longest discharge time among other samples, indicating the outstanding electrochemical capacitance. The calculated specific capacitances of the different samples were found to follow the order of FG_{20032} (63.19 F g^{-1}) < FG_{12032} (105.56 F g^{-1}) < FG_{18032} (108.21 F g^{-1}) < FG_{14032} (116.31 F g^{-1}) < FG_{16032} (167.49 F g^{-1}). The least electrochemical capacitance of FG_{20032} could be caused by the broken structure over high-temperature solvothermal process, in which the porosity and surface area were greatly reduced. Even though Ni-MOF_{12032} was synthesized at 120 ℃ (low isothermal temperature), a relatively low specific capacitance was obtained. Such low temperature was found to be unfavorable to form a stable structure. The loosely aggregated Ni-MOF nanosheets could not tolerate the stress during charging/discharging process [270], which was confirmed by XRD and TGA analysis. Another reason could be that the large-sized nanosheets were not able to provide large accessible surface area for electrolyte ions buffering [271]. Noteworthily, both Ni-MOFs synthesized at 140 and 160 ℃ exhibited a higher capacitive performance than that synthesized at 180 ℃, which could be ascribed to two reasons: (i) The existence of crystalline water in the Ni-MOF nanomaterials was beneficial to enhance the electrochemical property, since the protonic conduction could be significantly strengthened in the hydrous regions of a material [272]. Hence, it was an advantage for the enhancement of electrical conductivity where the charge transfer could be facilitated. (ii) The highly hierarchical hollow Ni-MOFs with large specific surface areas provide more active surface sites, offering more electrolyte ion diffusion channels to promote the electrochemical performance [273].

Besides, the GCD profiles of Ni-MOFs synthesized at various solvothermal times (8 h, 16 h, 24 h and 32 h) at 0.3 A g^{-1} were presented in **Fig. 4.18b**. Similar isosceles triangular shapes without any distortion were observed, suggesting the ideal reversible capacitive behavior. Moreover, it was noted that these electrode active materials possessed similar discharge time, indicating these materials had a comparable specific capacitance. The acquired specific capacitances of 167.54, 165.52, 165.77 and 167.49 F g^{-1} were observed for FG_{16008}, FG_{16016}, FG_{16024} and FG_{16032}, respectively. These high capacitances could be contributed by the hierarchical architectures with abundant micro- and meso-pores, which could store large amount of electrolyte ions [264, 274]. The existence of micropores could be thoroughly saturated with the electrolyte ions (Na^+/Cl^-) during charging process, while mesopores could facilitate charge/ion transfer. Hence, the co-existence of micro- and meso-pores crucially enhanced the electrochemical performance.

In addition, the specific capacitances obtained at multiple current densities were displayed in **Fig. 4.19**. Notably, FG_{16032} possessed a slightly higher rate capability than other nanomaterials obtained at both low (<160 ℃) and high (>160 ℃) solvothermal temperatures. The reason could

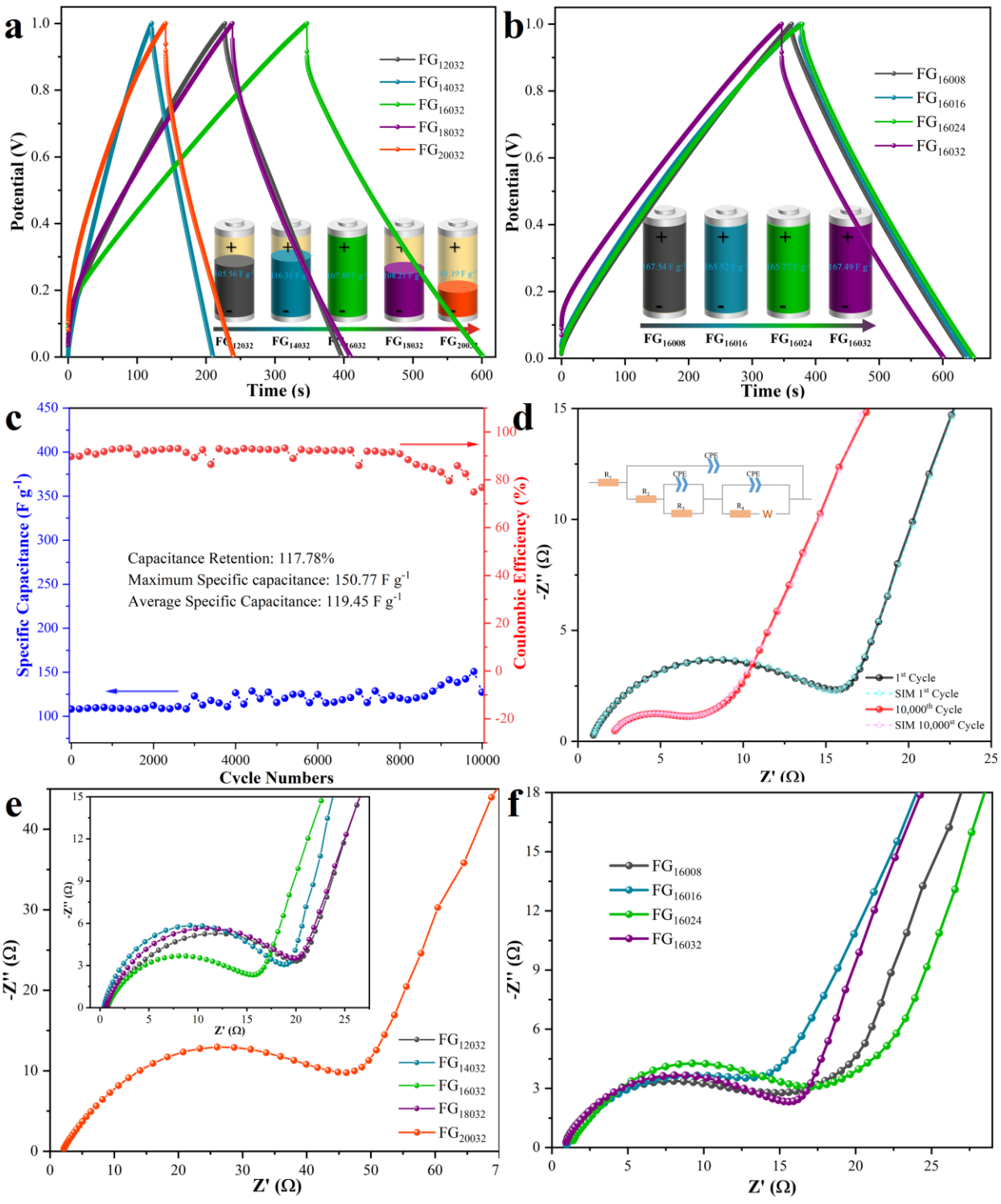


Figure 4.18. The GCD profiles of Ni-MOFs synthesized at various solvothermal temperatures (a) and times (b). Cycling performance of FG_{16032} at a current density of 1.5 A g^{-1} (c) and Nyquist plots before and after cyclic measurement (d) with fitting data (inset). Nyquist plots of electrode active materials synthesized at different solvothermal temperatures (e) and times (f).

be that a stable structure with large surface area could not be formed at temperature below 160°C [275]. On the other hand, a well-constructed MOF structure was thermally decomposed at the reaction temperature above 160 °C [276]. Interestingly, it was noted that the rate performance (**Fig. 4.20**) was reduced as the solvothermal time increased, which followed the order when the applied current density was increased by 10 folds: FG_{16008} (76.74%) > FG_{16016} (72.85%) > FG_{16024} (68.46%) > FG_{16032} (48.19%). This was because the prolonged solvothermal time could lead to the decrease in porosity as well as mesopore/micropore ratio in Ni-MOFs. This was also followed by the declined rate performance, when treatment duration was increased in a solvothermal process [277]. Nonetheless, such excellent rate performance could be ascribed to the hierarchically porous structure, which was favorable for boosting the fast transport of electrolyte ions and enlarging the specific surface area for energy storage [278]. More significantly, the delivered specific energies were as high as 22.44 Wh kg^{-1} at 294.6 W kg^{-1}, 21.23 Wh kg^{-1} at 288.3 W kg^{-1}, 22.02 Wh kg^{-1} at 293.4 W kg^{-1}, 19.52 Wh kg^{-1} at 274.8 W kg^{-1} for Ni-MOFs synthesized for 8 h, 16 h, 24 h and 32 h at 160 °C, respectively. These values are comparable to those reported elsewhere utilizing MOF nanomaterials as SC electrodes [279-283], confirming the excellent energy storage performance and its potential applications in energy storage systems.

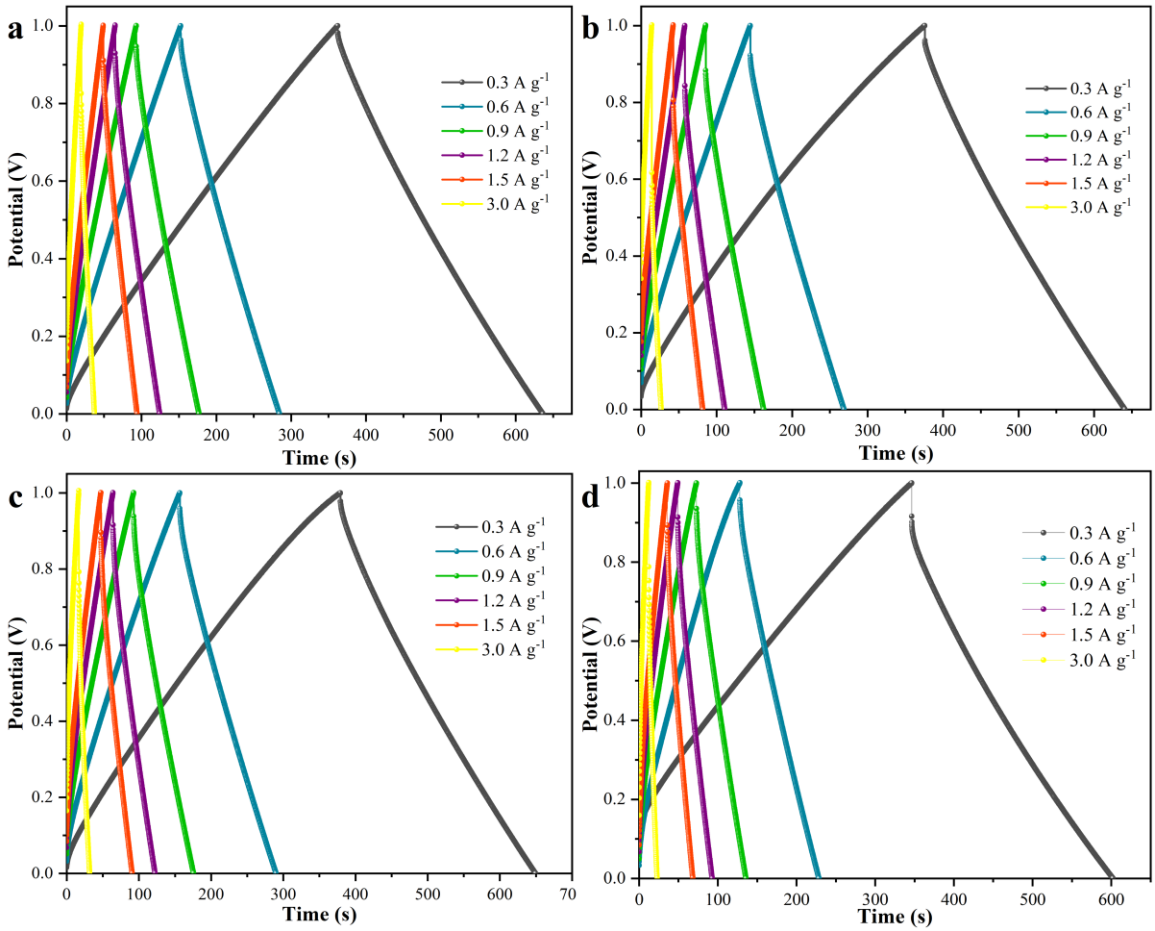


Figure 4.19. Galvanostatic charge/discharge profiles of Ni-MOFs synthesized at different solvothermal times (a, 8h; b, 16h; c, 24h and d, 32h) with different current densities ranging from 0.3 to 3.0 A g^{-1}.

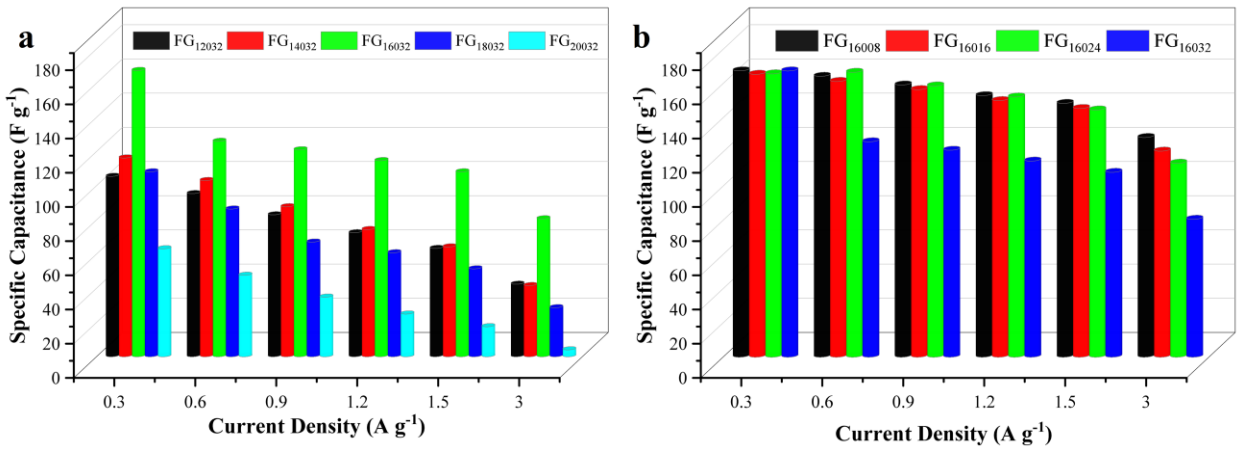


Figure 4.20. Rate performance of Ni-MOFs synthesized at different solvothermal temperatures (a) and times (b).

4.2.3.3 Cyclic stability

The cyclic stability of FG_{16032} was examined at a current density of 1.5 A g^{-1} in 2M NaCl aqueous electrolyte. As demonstrated in **Fig. 4.18c**, the capacitance retention as a function of cycles was plotted. Surprisingly, the as-fabricated electrode was able to retain 117.78% of its initial capacitance (108.17 F g^{-1}) after 10,000 cycles, which evidently annotated the extraordinary long-term electrochemical stability of the as-fabricated Ni-MOF SC electrode. Meanwhile, it was worth noting that the capacitance retention started to raise after 3,000th cycle, which could be caused by the gradual activation of the Ni-MOF crystalline materials on the electrode surface [284]. During the activation process, more channels were opened and the accessibility of electrolyte ions to micropores was further enhanced.

Besides, coulombic efficiency is also an important parameter evaluating the stability of electrode active materials through the constant current charging and discharging process. The retained coulombic efficiency was 76.79% over 10,000 cycles at a rate of 1.5 A g^{-1}. The gradual reduction in the coulombic efficiency could be due to the evolution of oxygen (O_2) and hydrogen (H_2) gases of the aqueous electrolyte. Some defect sites could be produced on the electrode surface during long-term cycling, which might function as the source points to evolve O_2 and H_2 [285]. Moreover, it was found that there was a faint rise in the charging time after 3200th cycle, which further confirmed the decrease in coulombic efficiency.

To better understand the ionic conductivity and electrochemical resistance of the as-fabricated Ni-MOF_{16032} electrode, EIS measurement was carried out before and after performing the cyclic stability measurement at 1.5 A g^{-1} (**Fig. 4.18d**). Meanwhile, the corresponding fitted equivalent circuit was recorded in the inset of **Fig. 4.18d**. A shift of R_s from 0.53 to 1.64 Ω was observed owing to the slight change of the material structure during the repetitive charging and discharging [286]. Nevertheless, a significant decrease of R_{ct} from initial 16.13 Ω to 6.05 Ω after 10,000 cycles was viewed, manifesting the remarkable electrochemical performance and faster charge transport. The obtained lower charge transfer resistance was in good agreement with the GCD cycling

measurement, which could be contributed by the cycling-induced enhancement in wettability as well as the gradual activation of the porous electrodes, leading to an improved accessibility of electrolyte ions [287, 288].

4.2.3.4 Electrochemical impedance spectroscopy (EIS)

Apart from CV and GCD, EIS was carried out to evaluate the electrochemical properties such as ionic conductivity and charge transfer resistance of Ni-MOF nanomaterials synthesized at different solvothermal temperatures and times. **Fig. 4.18** demonstrates the Nyquist plots of Ni-MOF electrode active materials in neutral electrolyte (2M NaCl). Noteworthily, all the EIS plots mainly contained three parts: (i) An intercept at high-frequency regions, correlating to the series resistance (R_s) resulting from the contact resistance, electrolyte resistance and intrinsic resistance of the active materials [289]. (ii) Quasi-semicircles were located in the intermediate frequency regions, which represented charge transfer resistance (R_{ct}) at the interface between electrode and electrolyte. (iii) A linear line at low frequencies with an angle of approximately 45°, also known as Warburg resistance (W), indicating the existence of ideal capacitive characteristics [290].

Fig. 4.18e and **f** depict the Nyquist plots of electrode active materials synthesized at different solvothermal temperatures and times. In general, the obtained Ni-MOFs at different solvothermal time possessed similar R_s and R_{ct} values, and all the samples displayed a straight line with an approximately 60° slope, indicating the excellent capacitive performance and the facile accessibility of electrolyte ions to electrode active materials. Meanwhile, a slightly larger R_{ct} (16.13 Ω) was acquired for Ni-MOFs synthesized for 32 h at 160 ℃, which could be caused by the narrowed hollow architectures. Such structure was unfavorable for the fast diffusion of electrolyte ions and led to an inferior rate performance. Nevertheless, these parameters varied significantly for Ni-MOF nanomaterials synthesized at different temperatures. In particular, series resistance showed a growing trend with increasing temperature (from 0.42 to 1.92 Ω), while the charge transfer resistance decreased gradually until 160 ℃ and then increased again as the solvothermal temperature reached 200 ℃. The variation in electrochemical impedance could be associated with the change in hierarchical hollow structures and surface areas of Ni-MOFs and the electrode/electrolyte interface. All the results were consistent with both CV and GCD analysis.

Time constant (τ) also quoted as dielectric relaxation time is another crucial characteristic to determine the fast-charging function for SC electrodes. To ensure the quick charging and discharging behavior, a low time constant is preferable for electrochemical SCs. The time constant of a SC device can be obtained by **Eq. (13)**:

$$\tau = \frac{1}{2\pi f} \tag{13}$$

where f is the frequency corresponding to the maximum imaginary impedance of the semicircle in the Nyquist plot.

The calculated values of τ were in the range of 0.255 – 0.593 ms for Ni-MOFs synthesized at 160 ℃ for various solvothermal duration times (**Table 4.1**), which was a good indication that fast

electrolyte ions transfer can be achieved. Nonetheless, a slightly larger time constant was obtained when Ni-MOF nanomaterials were treated at different solvothermal temperatures. Evidently, the nanomaterials synthesized at 160 ℃ possessed the lowest time constant (0.448 ms) as compared to those synthesized at different solvothermal temperatures. The low relaxation time constants evidently manifested the fast charging behavior of Ni-MOFs synthesized at a solvothermal temperature of 160 ℃, owing to the large surface area and quick electrolyte ion transfer at the interface between electrolyte and electrode [291]. In contrast, MOFs developed at 200 ℃ exhibited the highest τ (3.221 ms) due to the broken skeleton structures. Additionally, it was worth noting that the τ significantly decreased from 0.448 ms at initial cycle to 0.0622 ms after 10,000 cycles, which evidently indicated the transport of ions was further enhanced because of the gradual activation of the porous electrode in the repeated GCD cycling. All the results are in accordance with both CVs and GCDs analysis.

Table 4.1. EIS parameters for Ni-MOFs synthesized at 160°C for 8, 16, 24 and 32 h after 1 and 10,000 cycles.

Samples		R_s (Ω)	R_{ct} (Ω)	τ (ms)	Samples	R_s (Ω)	R_{ct} (Ω)	τ (ms)
FG_{16008}		0.52	15.01	0.255	**FG_{12032}**	0.58	21.63	1.382
FG_{16016}		0.74	15.72	0.593	**FG_{14032}**	0.42	18.55	2.429
FG_{16024}		0.75	15.53	0.448	**FG_{18032}**	0.60	20.01	1.382
FG_{16032}	1st	0.53	16.13	0.448	**FG_{20032}**	1.92	50.61	3.221
	10,000th	1.64	6.05	0.062				

4.3 Summary

In the present study, the impact of solvothermal reaction temperatures and times on the Ni-MOF nanomaterials synthesized in a solvent mixture (DMF + EG) with high polarity and viscosity was systematically studied. It was found that Ni-MOFs obtained at a high solvothermal temperature (≥ 180 ℃) exhibited small-sized nanosheets, while a relative low isothermal temperature (≤ 120 ℃) was unfavorable for the formation of stable structure. The amount of coordinated DMF solvent molecules tended to decrease with an increasing treatment temperature. In contrast, solvothermal duration had a negligible impact on the overall structures and morphologies of Ni-MOFs. Meanwhile, the electrochemical properties of these Ni-MOF nanomaterials were evaluated in 2M NaCl aqueous electrolyte. It was found that Ni-MOF nanomaterials synthesized at an optimum temperature (160 ℃) possessed excellent electrochemical performance. The delivered specific energy densities of 22.44, 21.23, 22.02 and 19.52 Wh kg^{-1} were observed for FG_{16008}, FG_{16016}, FG_{16024} and FG_{16032}, respectively. Additionally, an extraordinary capacitance retention of 117.78% was recorded after 10,000 cycles. Such excellent electrochemical performance evidently shows its great potential to be applied in electrochemical energy storage systems.

Chapter 5: Probing the Effect of Solvents on the Electrochemical Performance of Graphene Incorporated Nickel-based Metal-Organic Frameworks

5.1 Introduction

In general, MOFs are employed as templates to derive nanomaterials such as TMOs, metal hydroxide, carbonaceous and composite materials. However, it is usually an energy consuming process as elevated treatment temperature is required, and the high treatment temperature is always associated with the structure damage, resulting in the morphology change and decline in the functionality of MOFs. To tackle this issue, various strategies have been employed to synthesize MOFs with high porosity and excellent kinetic performance. Hence, a wide range of MOFs have been synthesized via various approaches (such as solvents conventional solution method, hydro/solvothermal, microwave-assisted and electrochemical synthesis), while the impact of solvent on the electrochemical performance of MOFs was only reported in a few studies. The variation of intrinsic properties of solvents such as polarity, viscosity and solubility for organic ligands could lead to the formation of MOFs with various phases, crystallinities, morphologies and surface areas. Additionally, it is extremely significant to reduce the size of MOFs from micrometers to nanometers for the applications of electrochemical energy storage systems due to two rationalizations: (i) It is beneficial to shorten the diffusion path of molecules and ions. (ii) An electrode with higher surface area will further enhance the charge storage capacity.

In the present study, a systematic study was carried out to investigate the correlation between morphology and electrochemical performance of Ni-MOFs, which were synthesized in various solvent systems via a facile solvothermal method. It was found that Ni-MOFs developed in a binary solvent mixture of DMF and ethylene glycol (EG) exhibited a 3D flower-like morphology, which was formed during the self-assembly of 2D nanosheets. Notably, it possessed the most superior charge storage performance if compared to the electrode materials synthesized in other solvent systems. This was because the unique architecture could facilitate ion transfer and provide abundant exposed surface for the storage of large number of charges. Besides, the unique structure was also beneficial to enhance the capacitive performance by alleviating the intrinsic electrochemical resistance. To further optimize the electrochemical performance of the nanomaterial, graphene nanosheets were incorporated into Ni-MOFs. As a result, a high specific capacitance of 126.21 F g^{-1} was attained in 2M KOH electrolyte, while a remarkable cycling stability over 10,000 cycles without notable capacitance loss was achieved in 2M NaCl neutral electrolyte.

5.2 Experimental

5.2.1 Synthesis of Ni-MOF Nanomaterials

Ni-MOF was synthesized via a solvothermal method reported with a slight modification [292]. In a typical synthesis, 0.030 g of H_2BDC (0.180 mmol) and 0.052 g of $Ni(NO_3)_2 \cdot 6H_2O$ (0.180 mmol) were dissolved in a mixture of 8 mL of DMF and 5 mL of EG under magnetic stirring at room

temperature for 60 min. Subsequently, the light green mixture was transferred into a Teflon-lined stainless-steel autoclave with a capacity of 50 mL. The autoclave was then heated at 160 °C for 6 h. After cooling to room temperature, the products were centrifuged and washed with DMF and ethanol several times. To further remove the extra DMF solvent, the light green powder was immersed in 25 mL of ethanol at 60 ℃ for 96 h, and solvent was changed during aging period. The wet powder was then ultra-sonicated in ethanol for 60 min. Finally, the resultant powder was centrifuged and vacuum dried at 60 ℃ overnight.

Other samples were synthesized through the same procedure by using different solvent systems such as 13 mL of pure DMF, ethanol, D.I. water, mixture of DMF and ethanol, DMF and D.I. water with the same volume ratios, respectively. Hereafter, these samples synthesized in a single solvent system, such as DMF, ethanol and D.I. Water were labelled as F, E and D, respectively. Similarly, the Ni-MOFs prepared in binary solvents, like DMF + EG, DMF + ethanol and DMF + D.I. water were denoted as FG, FE and FD, respectively. The overall synthesis procedure is shown schematically in **Fig. 5.1(i)**. As glycol is able to react with NO_3^- to form explosive mixture [293], pure EG was not used as solvent for the synthesis of Ni-MOFs.

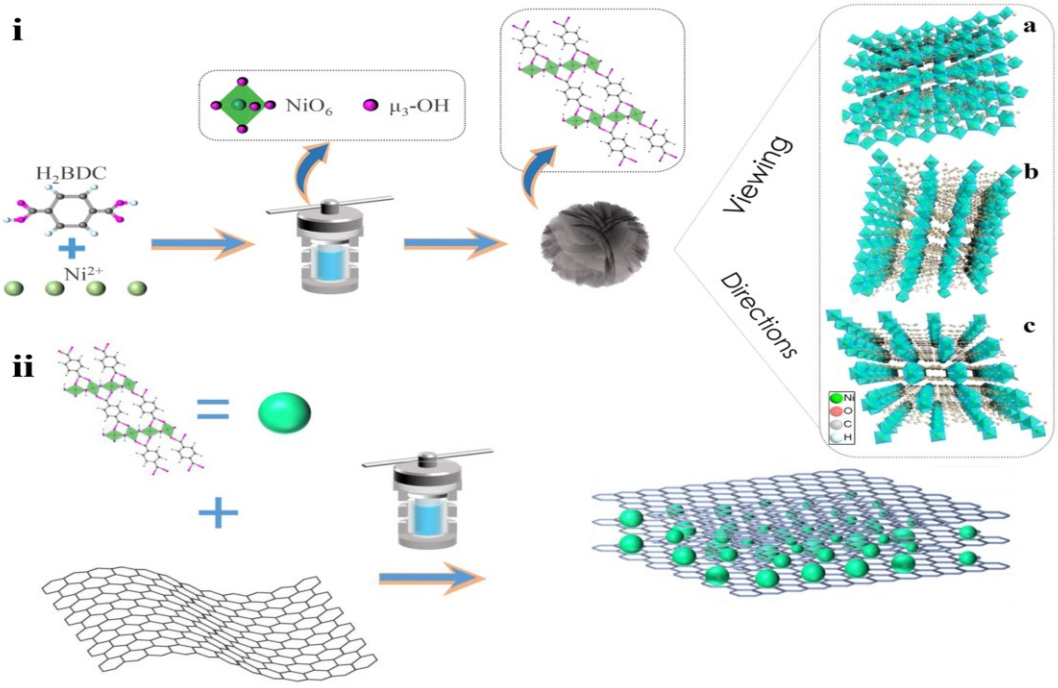


Figure 5.1. Schematic illustration of the fabrication for (i) hierarchical Ni-MOFs and views of the layered structure along different axis, (ii) graphene-incorporated Ni-MOFs via a solvothermal method.

5.2.2 Synthesis of Ni-MOF/graphene Nanocomposite (FG_Gr$_y$)

Following the synthesis procedure as described in section 3.2, the as-synthesized graphene was incorporated into Ni-MOF samples (FG) derived from binary solvent mixture as shown in **Fig.**

5.1(ii). The graphene sample with respective mass ratio was added into the well-mixed solvent under magnetic stirring for 60 min before being heated to 160 ℃ for 6 h. The corresponding concentration of graphene nanosheets was 0.25, 0.5, 0.75, 1.0 and 1.5 mg mL^{-1} (w/v) and denoted as FG_$Gr_{0.25}$, FG_$Gr_{0.5}$, FG_$Gr_{0.75}$, FG_$Gr_{1.0}$ and FG_$Gr_{1.5}$, respectively.

5.3 Results and Discussion

5.3.1 Material Characterization

The crystal structures of Ni-MOFs synthesized in different solvent systems and incorporated with varied concentrations of graphene nanosheets were analyzed with XRD over a 2θ range of 7 - 50°. The results were illustrated in **Fig. 5.2a** and **b**, respectively. The main diffraction 2θ peaks at 9.29, 15.63, 18.34, 23.85 and 29.11° could be indexed into the planes of (100), $(\bar{1}01)$, $(\bar{2}10)$, (020) and $(\bar{1}\bar{2}1)$, respectively. All the diffraction characteristic were consistent with the single crystal $[Ni_3(OH)_2(C_8H_4O_4)_2(H_2O)_4]\cdot 2H_2O$ (CCDC 638866) in simulation. Typically, the unique two-dimensional layered monometallic structure was separated by H_2BDC ligands (**Fig. 5.1**), in which NiO_6 octahedral structures were formed by nickel and oxygen atoms at a molar ratio of 1 : 6 and they were coordinated by edge-corner in the plane of (100) [294]. Meanwhile, the (100) plane was identified to be the largest exposed facet for all as-synthesized MOF nanomaterials. In addition, the results revealed that the incorporated graphene did not affect the crystal structures of Ni-MOFs. More significantly, no other additional diffraction peaks were found, suggesting the high purity of these Ni-MOF nanostructures. Furthermore, the XRD spectra of graphene was also investigated as demonstrated in **Fig. 5.3a**, three sharp characteristic peaks were detected at 2θ = 26.42, 44.03 and 54.54º, corresponding to the (002), (100) and (004) planes of graphene nanosheets [295, 296].

The FT-IR spectra of the Ni-MOFs synthesized in various solvent systems were illustrated in **Fig. 5.2c**, which clearly indicated the presence of stretching vibration of hydroxide (OH^-), carbon-hydrogen (C-H) and carboxyl (-COO-) groups [297, 298]. Two strong peaks at 1375 and 1570 cm^{-1} could be ascribed to the symmetric and asymmetric stretching vibrations of carboxyl groups where the difference between these two bands was attributed to the coordination of two oxygen atoms with nickel cations (Ni^{2+}) [299]. The small peak at around 3600 cm^{-1} could be assigned to OH^- stretching vibration. The stretching vibrations of H_2O molecules at approximately 3425, 3342 and 3053 cm^{-1} were observed, which clearly indicated the presence of water molecules within Ni-MOF nanomaterials [300]. Meanwhile, the band at 1500 cm^{-1} could have resulted from the stretching of para-aromatic C-H groups and the vibration of carbon-oxygen (C-O) bonds could be observed in between 1015 – 1160 cm^{-1} in the IR spectra. The substitution of Ni^{2+} on benzene rings could be indexed in the range of 745 – 755 cm^{-1}. Additionally, the stretching band of O-Ni-O was detected at 430 and 535 cm^{-1} [301]. As compared to IR spectra of H_2BDC (**Fig. 5.2d**), the peak at 1670 cm^{-1} resulting from C=O vibration disappeared, which indicated that carboxyl groups were coordinated to metal cations (Ni^{2+}) successfully. As depicted in **Fig. 5.3b**, the symmetric and asymmetric stretching vibrations of C-H bonding were observed at 2853 and 2922 cm^{-1}. The adsorption peaks viewed at around 3600 cm^{-1} could be assigned to the vibration of ν(OH), originating from physiosorbed water molecules [302]. The peaks at approximately 1575 cm^{-1}

corresponded to the strong aromatic C=C bonds [295, 296]. The result was consistent with that derived from XRD. More significantly, the results have shown that the formation of Ni-MOFs were not affected by the incorporation of graphene (**Fig. 5.2d**). All these observations were in accordance with the results from XRD, which further confirms that Ni-MOF nanomaterials were successfully synthesized.

Fig. 5.4a depicts the thermogravimetric and DTG curves of Ni-MOFs. The results clearly revealed that all Ni-MOFs were thermally stable at a temperature below 450 ℃. Basically, there was a three-stage weight loss detected in all Ni-MOFs. Most Ni-MOF samples shown an initial weight loss from room temperature up to 170 ℃ mainly due to the removal of lattice and coordinated water molecules [303] and other moisture contents adsorbed on the surface of the nanomaterials. This was followed by the loss of other solvated water molecules in the Ni-MOF pores within the temperature range of 170 – 330 ℃, and the decomposition of organic linkers occurred between 330 ℃ and 450 ℃ [299].

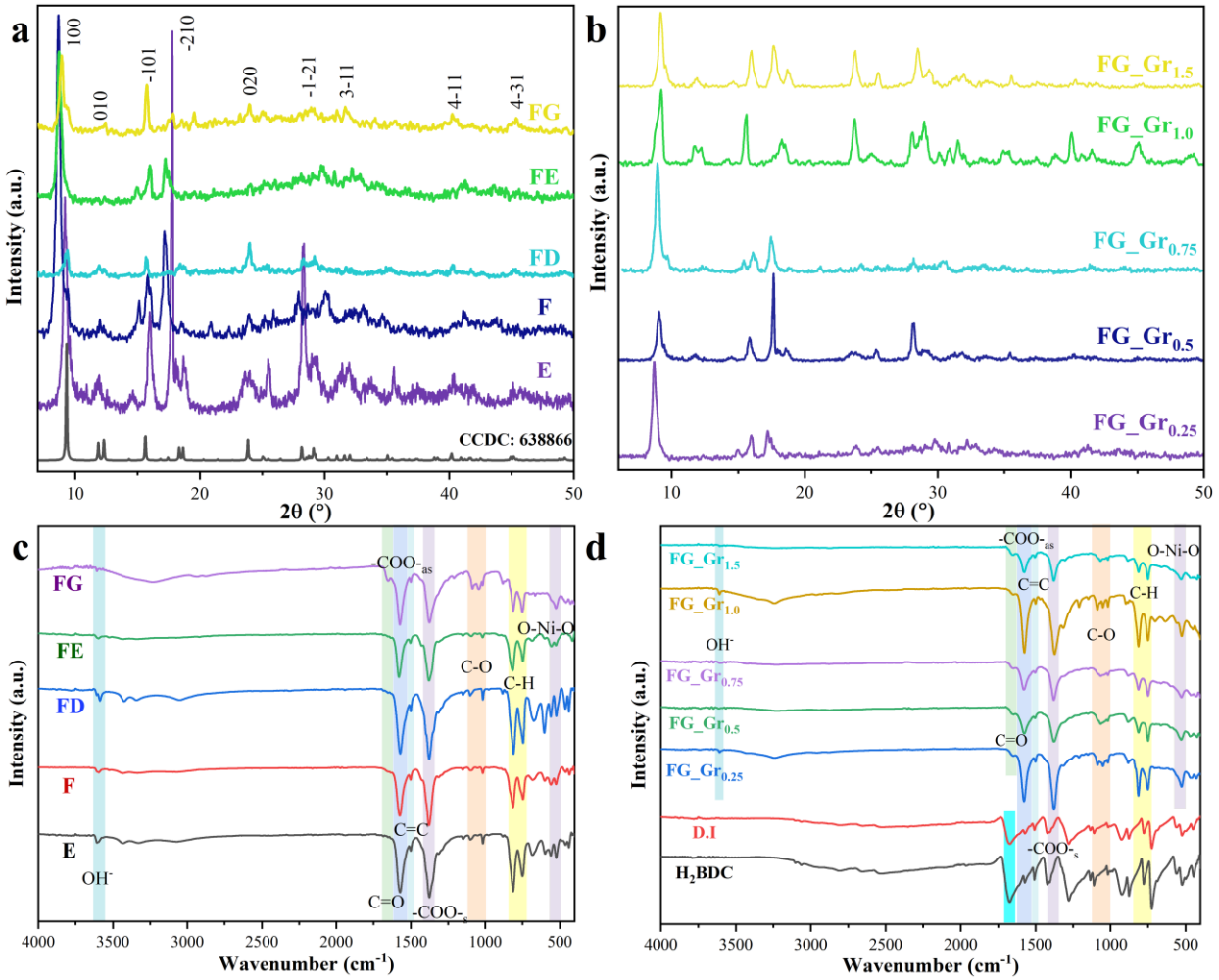


Figure 5.2. (a, b) XRD patterns and (c, d) FT-IR spectra of the as-synthesized Ni-MOF and FG_Gr$_y$ nanomaterials.

Meanwhile, as indicated in the thermo-grams, FG exhibited a slightly different thermal decomposition behavior. The first stage weight loss of 7.66% took place between 30 and 170 °C, while the second weight loss (about 14.84%) was observed to be much higher temperature than other samples. This could be ascribed to the degradation of oxygen-containing and hydroxyl groups [304] originating from the EG compounds (boiling point = 197.3 °C) in addition to the water and moisture evaporation. The weight loss owing to the decomposition of organic linkers was approximately 44.66%, the least value among the Ni-MOFs synthesized using various solvents. This could be caused by the formation of alkoxides such as $Ni(C_2H_4O_2)$ during the synthesis. Therefore, less amount of H_2BDC was coordinated due to the competing reaction [155, 305]. In addition, FG_Gr_y was observed to have similar thermal diagrams as FG (**Fig. 5.4b**), suggesting the incorporation of graphene nanomaterials did not alter the thermal stability of Ni-MOFs.

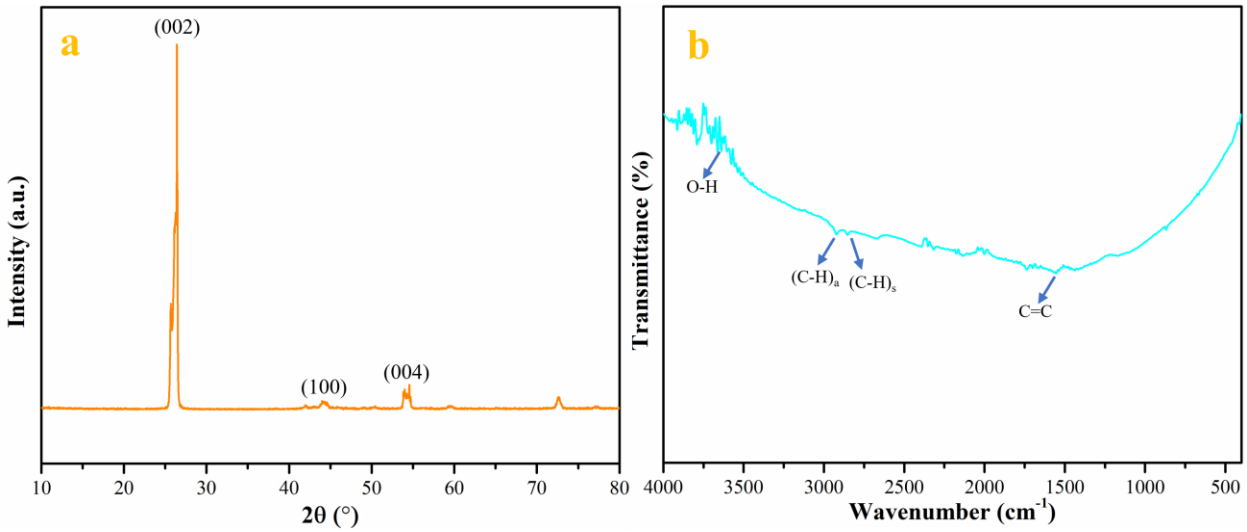


Figure 5.3. (a) XRD pattern and (b) FT-IR spectra of graphene nanosheets.

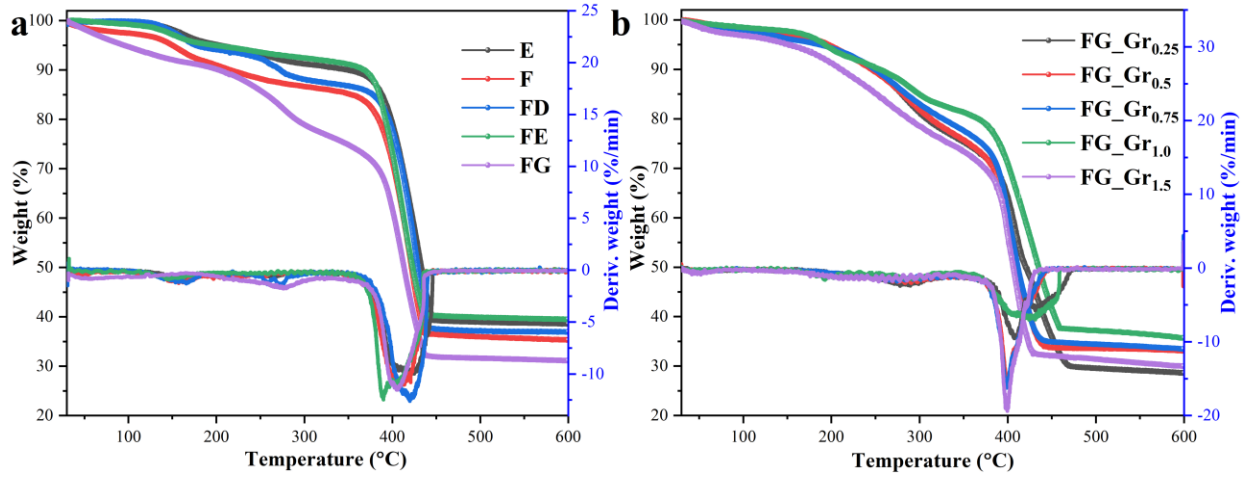


Figure 5.4. TG/DTG curves of (a) the as-synthesized Ni-MOFs and (b) FG_Gr_y nanocomposites.

The morphological study of Ni-MOFs synthesized in different solvent systems was characterized with FESEM (**Fig. 5.5**). Overall, the as-developed Ni-MOFs exhibited hierarchical structures comprising plenty of interconnected nanosheets with various sizes. The Ni-MOFs prepared in both ethanol (E) and the mixture of D.I. water and DMF (FD) possessed a laminar and layered structure, while the average thickness was slightly different. Specifically, E had a higher thickness (~ 70 nm) than that of FD (~ 50 nm). As can be clearly viewed from **Fig. 5.5g** and **h**, the nanosheets of sample FD were parallel stacked, while sample E contained some small-sized and randomly distributed clusters. Similarly, sample F synthesized in DMF also possessed small-sized nano-flakes, which stacked tightly in a disorder manner. **Fig. 5.5j** and **k** reveals that the use of ethanol and DMF solvent mixture was favorable for the formation of nano-bars and large pieces of nanosheets. Unlike the aforementioned morphologies, MOFs with regular microspheres were observed when EG-DMF binary solvent system was used. The flower-like morphology was formed by the self-assembly of nanosheets with an average thickness of 20 nm. Such phenomenon could be caused by the solvents with different viscosity as well as dielectric moment [306, 307]. These observations clearly indicated that the addition of EG was beneficial to stabilize and regulate the formation of nano-architectures in Ni-MOFs.

In addition, the microspheres of the FG sample were found homogeneously and randomly distributed on graphene nanosheets, as indicated in **Fig. 5.6**. These nanocomposites exhibited hierarchical flower-like structure with interconnected 2D nanosheets. In comparison with pristine FG, the average sizes of these 2D nanosheets were enlarged significantly when graphene (1 mg mL^{-1}) was incorporated into FG owing to the strong interaction between Ni-MOF and graphene nanosheets [308]. The vertically deposited nanosheets could offer larger channels for electrolyte transport during electrochemical reactions. The elemental analysis was conducted by energy-dispersive X-ray spectroscopy (EDX, **Fig. 5.5 & 5.6**) and elemental mapping (**Fig. 5.7**), the results presented the expected signals of nickel (Ni), oxygen (O) and carbon (C). Meanwhile, no impurity signals were detected, indicating the high purity of as-synthesized Ni-MOF/graphene nanocomposites. The TEM images of $FG_Gr_{1.0}$ nanostructures were illustrated in **Fig. 5.7a** and **b**. The appearance of slightly darker Ni-MOF nanoparticles on the brighter graphene sheets clearly indicated the successful incorporation of Ni-MOFs on the graphene nanosheets.

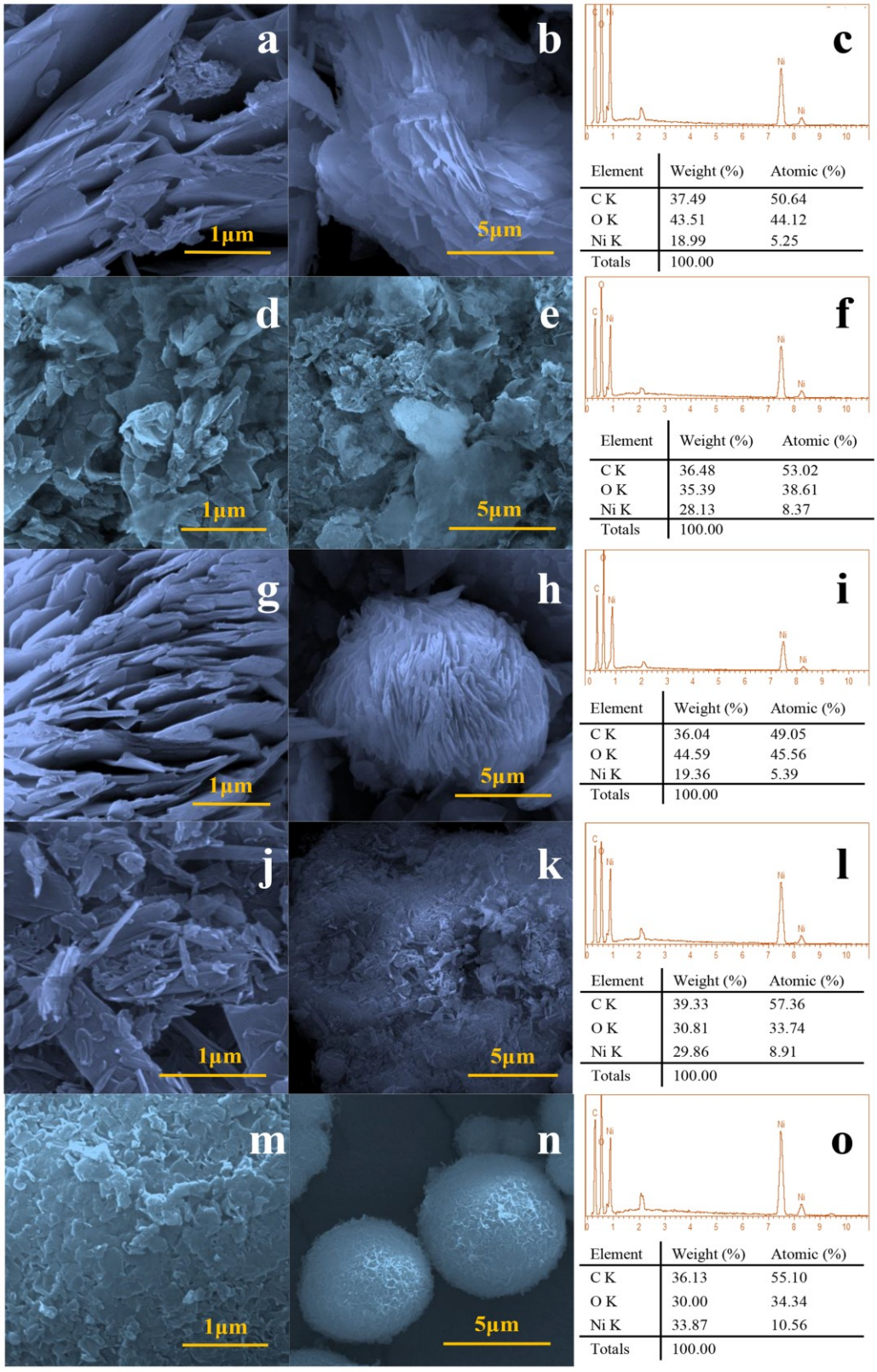


Figure 5.5. FESEM images and EDX of Ni-MOFs synthesized in different solvent systems: (a-c) ethanol, (d-f) DMF, (g-i) DMF + D.I. water, (j-l) DMF + ethanol and (m-o) DMF + EG.

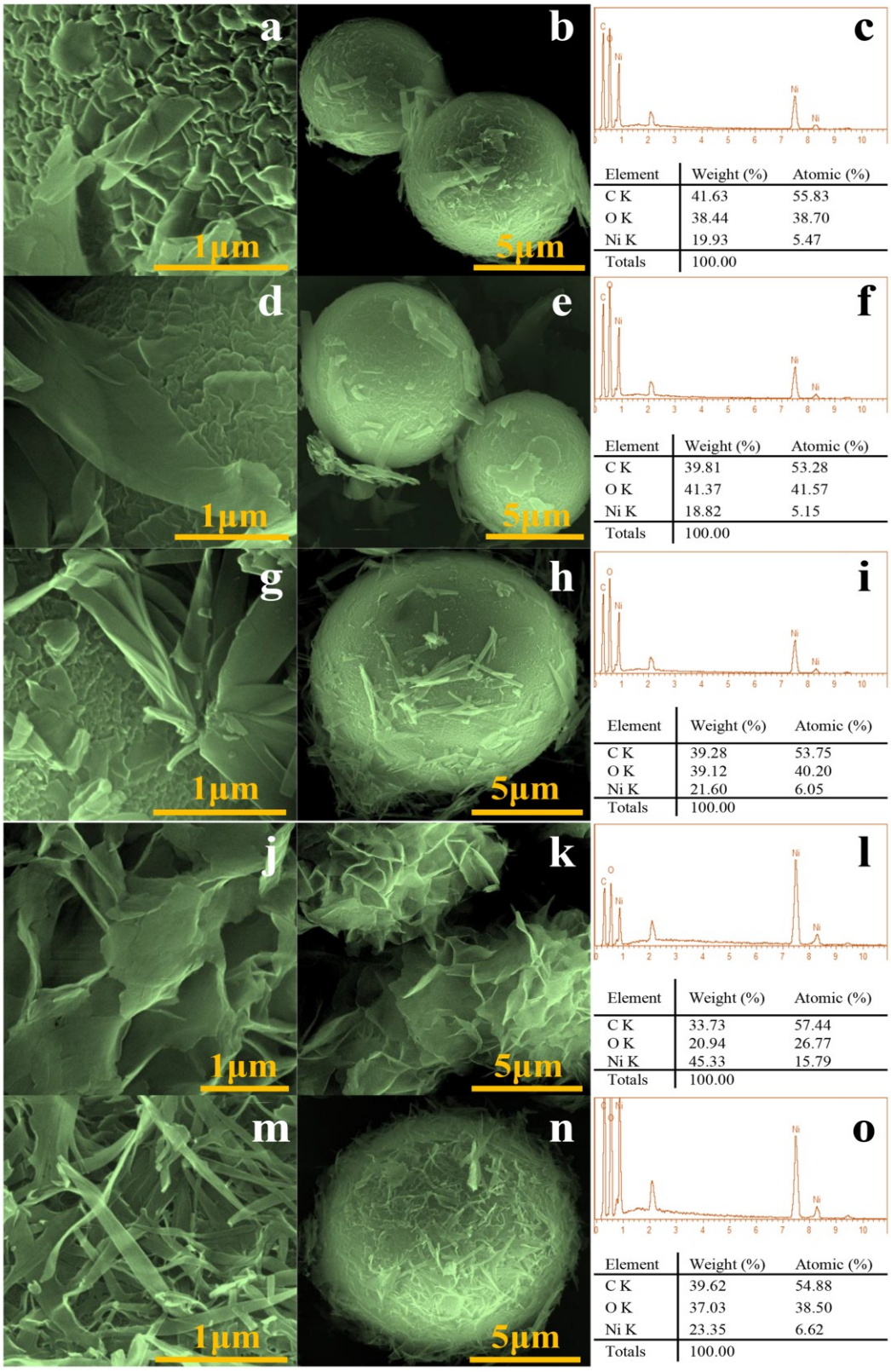


Figure 5.6. FESEM images and EDX of FG_Gr$_y$: (a-c) FG_Gr$_{0.25}$, (d-f) FG_Gr$_{0.5}$, (g-i) FG_Gr$_{0.75}$, (j-l) FG_Gr$_{1.0}$ and (m-o) FG_Gr$_{1.5}$.

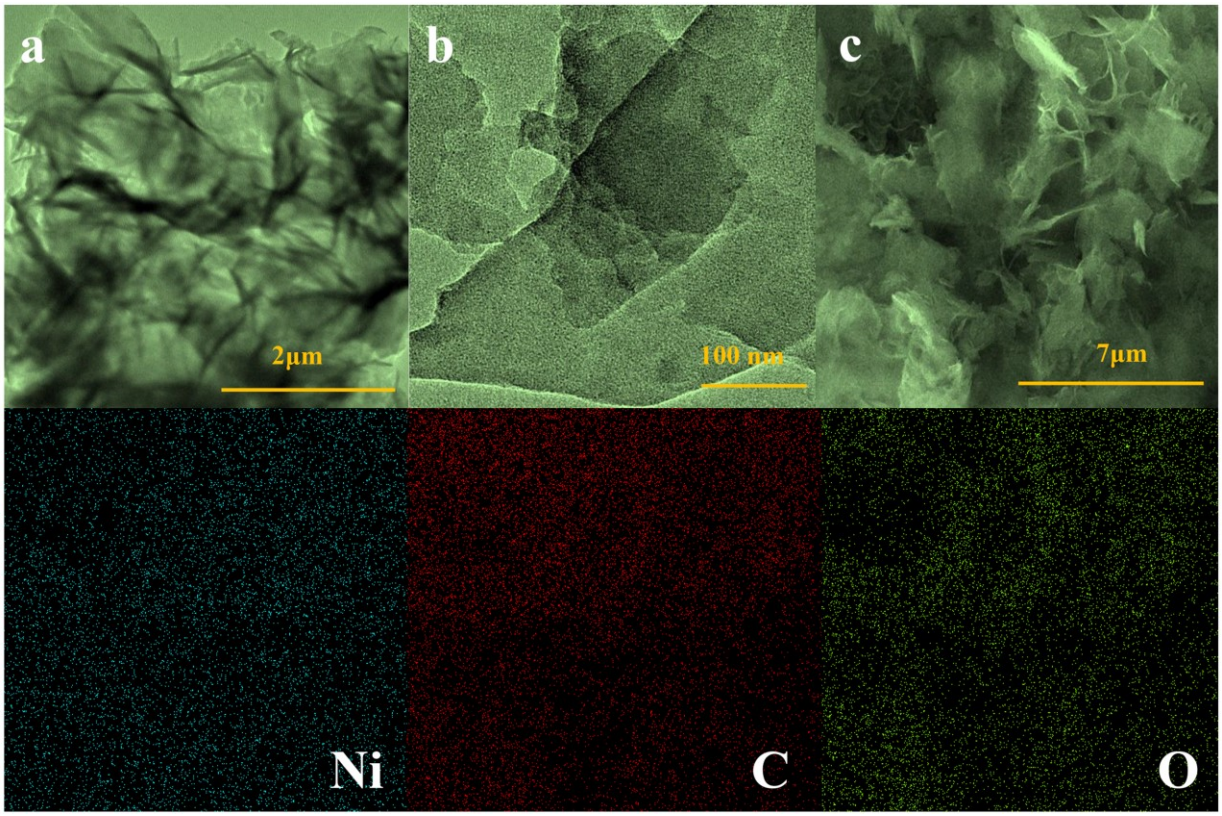


Figure 5.7. (a, b) TEM images and (c) elemental mapping of hierarchical FG_Gr$_{1.0}$.

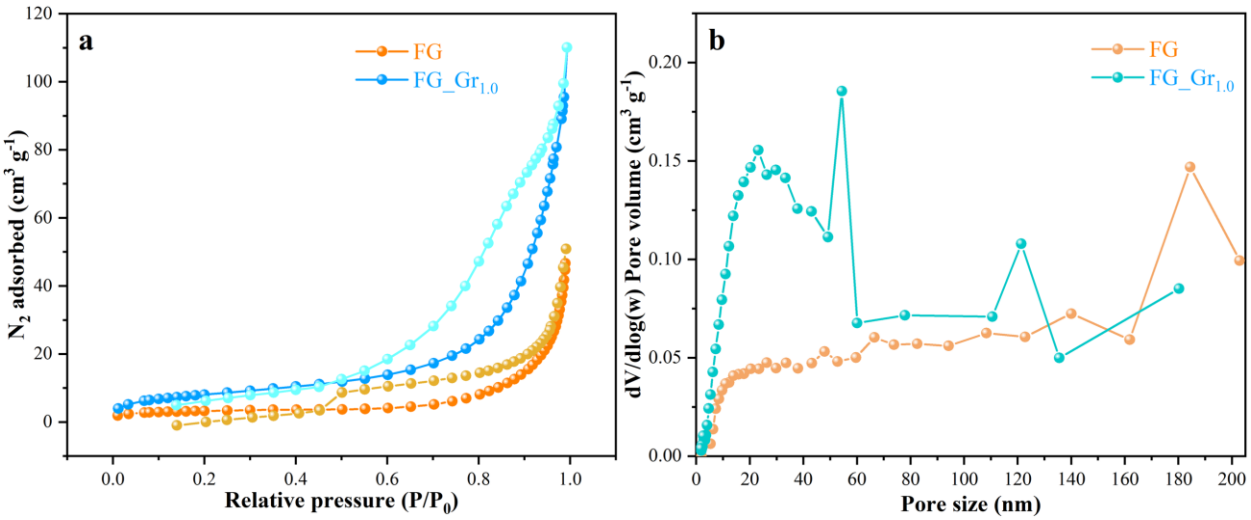


Figure 5.8. (a) N_2 adsorption and desorption isotherms and (b) pore size distributions of FG and FG_Gr$_{1.0}$ samples.

5.3.2 The Impact of Solvent

The coordination behavior between metal and organic precursors can be influenced by the selection of solvents due to different polarity, viscosity and solubility of the solvents. Hence the crystal growth, topology and morphology would vary when different solvents are used. Meanwhile, the morphology and intrinsic interconnected structure can also be affected by the relative coordination capability between solvents and metal cations. Among the various solvents, water molecule exhibited the highest affinity to metal ions (Ni^{2+}) [309], and hence the effective coordination between Ni^{2+} and organic ligand was blocked in pure water. Moreover, water molecules normally possessed a relatively high surface barrier, so the formation of MOF nuclei was further prohibited owing to the high interfacial tension [155]. In addition, the amount of BDC^{2-} formed in water was negligible due to the low solubility of H_2BDC. Although a small number of BDC^{2-} anions were produced through deprotonation, they were surrounded by water molecules through strong hydrogen bonding interactions, and the effective coordination between carboxylate groups and Ni^{2+} was inevitably impeded. As a result, Ni-MOFs could not be formed in water. In contrast, ethanol and DMF were found to have a lower interfacial tension if compared to water, which was beneficial to facilitate the crystallization and growth of nucleus. Therefore, the nucleation of Ni-MOF could be enhanced in the ethanol and DMF solutions, ultimately towards the formation of Ni-MOF crystals with high product yield (**Table 5.1**).

Table 5.1. Chemical properties of solvents used, average width and yield of synthesized Ni-MOFs.

Solvent	***Water***	***Ethanol***	***DMF***	***FD***	***FE***	***FG***	***EG***
Dielectric Constant (ε)	80.1	26.72	36.7	53.39	32.86	36.82	37.0
Dipole Moment (C m)	1.82	1.69	3.86	-	-	-	0
Viscosity (cP)	0.895	1.074	0.802	-	-	-	16.1
Average Sizes (μm)	-	1.5	0.2	1.3	0.7	0.09	-
Yield (%)	-	57.14	47.12	46.82	54.92	57.50	-

* All data was obtained from Ref. [310].

Moreover, the surface energy of these nucleus could be changed when organic solvents (ethanol, DMF and EG) were utilized, as these solvent molecules could cover the outer surface of the crystal nucleus, which significantly prohibited the anisotropic growth of the crystals [311, 312]. Hence, laminated structures were formed due to the equable growth of these crystals in various plane orientations, especially for those solvents containing water molecules. According to **Fig. 5.5**, large-sized lamellar structures were acquired in the binary solvents (i.e., ethanol (96%), FE and FD). The deprotonation of H_2BDC was facilitated upon the dilution of water molecules by organic solvents, leading to the effective coordination between Ni^{2+} and BDC^{2-} ions. Eventually, the crystal growth rate was accelerated, leading to the generation of large-sized crystals by one-face unidirectional growth [313]. It also evidently indicated that the existence of water molecules in the solvent is favorable for the formation of large-sized lamellar structures [314].

In addition, when metal and organic ligand precursors were added into solvents, they firstly would dissolve and deprotonate to free ions. Nonetheless, the amount of deprotonated H_2BDC mainly relies on the polarity of solvent used, as a result of the acid-base equilibrium [315]. In general, the polarity can be indicated by the dielectric constant and dipole moment. As can be observed from **Fig. 5.5**, the average sizes of the nanosheets obtained in ethanol ($\varepsilon = 26.72$) were much larger than that obtained in pure DMF solvent ($\varepsilon = 36.7$). This could be explained by DLVO theory [316], in which the energy barrier for agglomeration is low when the dielectric constant is low. Consequently, the average sizes of these lamellas decreased with increasing dielectric constants. Nonetheless, there was a huge difference on the morphologies between samples F and FG, even though the dielectric constants of the solvents were found to be similar (**Table 5.1**). This could be attributed to the following two reasons. Firstly, EG exhibited the highest viscosity among these solvents and could result in a higher steric hindrance [311], which crucially hindered the agglomeration and transport of crystals. Secondly, alkoxides might be produced owing to strong chelating capability of EG when metal salts and organic ligands were dissolved in EG [305]. As a result, the amount of free Ni^{2+} could be significantly reduced, and the nucleation rate was decreased as well, in which the agglomeration of Ni-MOF nucleus was greatly hampered.

The significance of viscosity in tuning the crystal structure and morphology of the nanomaterials was observed as well. The viscosities of D.I. water, ethanol and EG are 0.895 cP, 1.074 cP and 16.1 cP, respectively. Generally, when highly viscous organic solvent (such as EG) was added to the reaction system, the diffusion of Ni^{2+} and BDC^{2-} could be greatly hampered and hence the nucleation and particle growth rate could be significantly reduced [317]. As illustrated in the FESEM micrographs (**Fig. 5.5**), it was apparent that the Ni-MOFs obtained from the least viscous solvent - deionized water (denoted as sample FD) possessed the largest average size among other samples. Additionally, the viscosity of the solvent is also a crucial factor to limit the mass transfer, and highly viscous solvent is favorable for enhancing the formation of the Ni-MOFs due to the effective interactions between Ni^{2+} and BDC^{2-} ions. This was well corroborated with the product yield from various solvent mixtures, which was in the order of FG (57.5%) > FE (54.92%) > FD (46.82%). In a nutshell, the diffusivity of reactants was greatly influenced by the viscosity of the solvents, which ultimately affected the nucleation rate, particle growth as well as the morphology of the final product [318].

5.3.3 Electrochemical Analysis

5.3.3.1 Cyclic voltammetry

Cyclic voltammetry (CV) was conducted to study the redox reaction behavior of the as-obtained Ni-MOF nanostructures at various scan rates (50, 75, 100, 150, 200, 300 and 500 mV s^{-1}), in which the potential window was manipulatively set as -1.0 – 1.0 V in a two-electrode system. **Fig. 5.9a** depicts the CV profiles at 50 mV s^{-1} for Ni-MOFs synthesized in different solvent systems. It could be observed that the peak current densities as well as enclosed CV areas were different (in an order of FG > FE > E > FD > F), clearly indicating various electrochemical performance for samples synthesized in different solvent systems. In particular, sample FG exhibited the largest CV area,

manifesting the best capacitive performance among other Ni-MOF nanomaterials [319]. This could be ascribed to the hierarchical flower-like morphology, which was favorable for providing a large surface area (11.45 m^2 g^{-1}, **Fig. 5.8**) for charge storage. Meanwhile, the layered architectures were beneficial to shorten the ion diffusion path during electrochemical reactions. Besides, the CV curves of FG_Gr_y at 50 mV s^{-1} were shown in **Fig. 5.9b**.

As compared to pristine FG, an almost perfect rectangular CV curve was observed when graphene was incorporated into Ni-MOFs, implying that the highly conductive single-layered carbonaceous nanomaterial enhanced electric double-layer capacitive behavior in the nanocomposites. Similarly, pseudo-rectangular CV shapes of FG_$Gr_{1.0}$ in different electrolytes (NaCl and KOH, 2M) could be observed in **Fig. 5.10a**. Notably, a larger peak current density and enclosed CV area were obtained in the set up containing alkaline-based electrolyte, indicating a higher specific capacitance. This might be related to two reasons: (i) Higher ionic mobility of K^+ could enhance the specific capacitance ($K^+ = 7.62 > Na^+ = 5.19 \times 10^{-8}$ m^2 s^{-1} V^{-1}), since the capacitive performance of an electrode material was proportional to the electrolyte conductivity [320]. (ii) Extra pseudo-capacitance was contributed by alkaline electrolyte (KOH), as represented by **Eq. (14)**. In comparison, the electrochemical property of FG_$Gr_{1.0}$ was further evaluated with a three-electrode system in a 2M KOH aqueous electrolyte, using Ag/AgCl as the reference electrode. A pair of redox peaks were observed (**Fig. 5.11a**) resulting from the interactions between OH^- and electroactive materials as represented by **Eq. (14)**. Additionally, a maximum specific capacitance of 420.4 F g^{-1} was obtained at 1 A g^{-1} (**Fig. 5.11b**), confirming the excellent electrochemical performance of FG_$Gr_{1.0}$.

$$[Ni_3(OH)_2(C_8H_4O_4)_2(H_2O)_4] \cdot 2H_2O_{(s)} + OH^-_{(aq)} \leftrightarrow [Ni_3O(OH)(C_8H_4O_4)_2(H_2O)_4] \cdot 2H_2O_{(s)} + H_2O_{(l)} + e^- \quad (14)$$

The cyclic voltammograms of FG_$Gr_{1.0}$ at various scan rates were shown in **Fig. 5.12**. Evidently, no redox peaks were observed during the potentiodynamic study, suggesting the dominance of electrical double-layer capacitive response on the as-fabricated FG_$Gr_{1.0}$ electrode. Meanwhile, the areas under CV curves were expanded as the scan rates increased, indicating the fast diffusion kinetics upon the surface of the electrode [321]. Besides, a slight distortion was observed as the rate increased, particularly at high scan rates. The deviation from rectangular shape could be ascribed to the slow diffusion of ions at the interface between electrode and electrolyte, in which the concentration of electrolyte increased rapidly. Hence, the effective diffusion was hindered and there was not enough time for ions to completely access all the internal pores of the active material, leading to a lower specific capacitance [322]. Nonetheless, a fairly rectangular CV profile could be retained, such excellent capacitive behavior could be attributed to the porous structures formed by the self-assembly of ultra-thin 2D nanosheets, which provided sufficient space for the storage of electrolyte and effectively facilitated the charge transfer. The results evidently illustrated the existence of mesopores in FG_$Gr_{1.0}$ nanocomposite, which was beneficial to maintain excellent EDLC behavior at high scan rates.

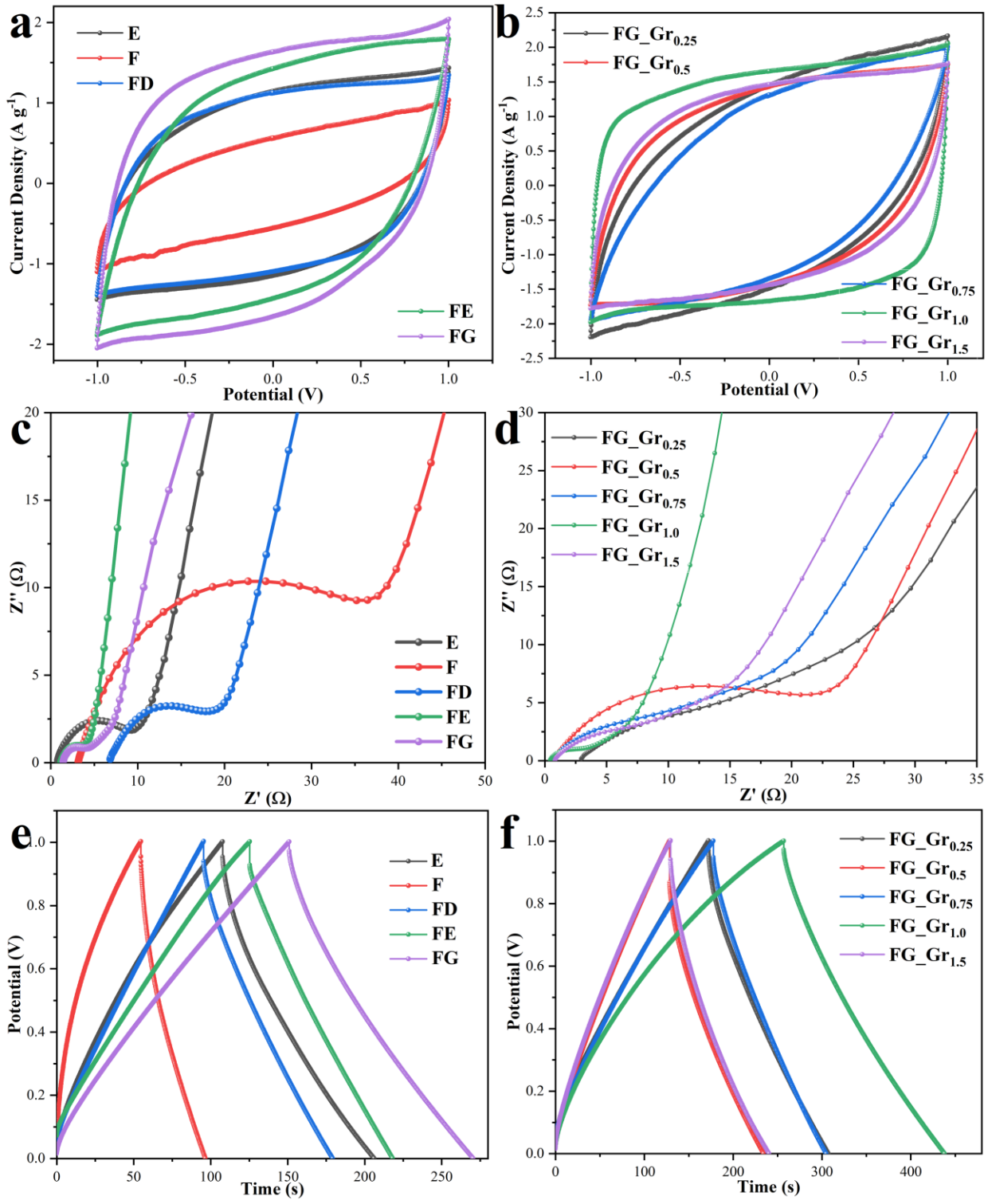


Figure 5.9. (a) Cyclic voltammetry profiles at 50 mV s^{-1}, (c) Nyquist plots and (e) Galvanostatic charge/discharges profiles at a current density of 0.3 A g^{-1} of as-developed Ni-MOFs in different solvent systems. (b) Cyclic voltammetry profiles at 50 mV s^{-1}, (d) Nyquist plots and (f) Galvanostatic charge/discharges profiles at 0.3 A g^{-1} of FG_Gr_y in 2M NaCl electrolyte.

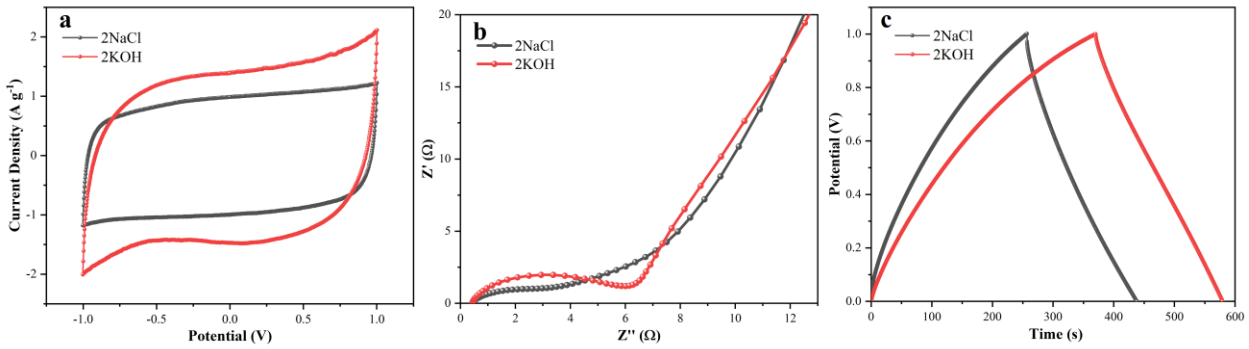


Figure 5.10. (a) Cyclic voltammetry profiles (50 mV s^{-1}), (b) Nyquist plots and (c) Galvanostatic charge/discharges profiles (0.3 A g^{-1}) of FG_Gr1.0 in 2M NaCl and 2M KOH aqueous electrolyte, respectively.

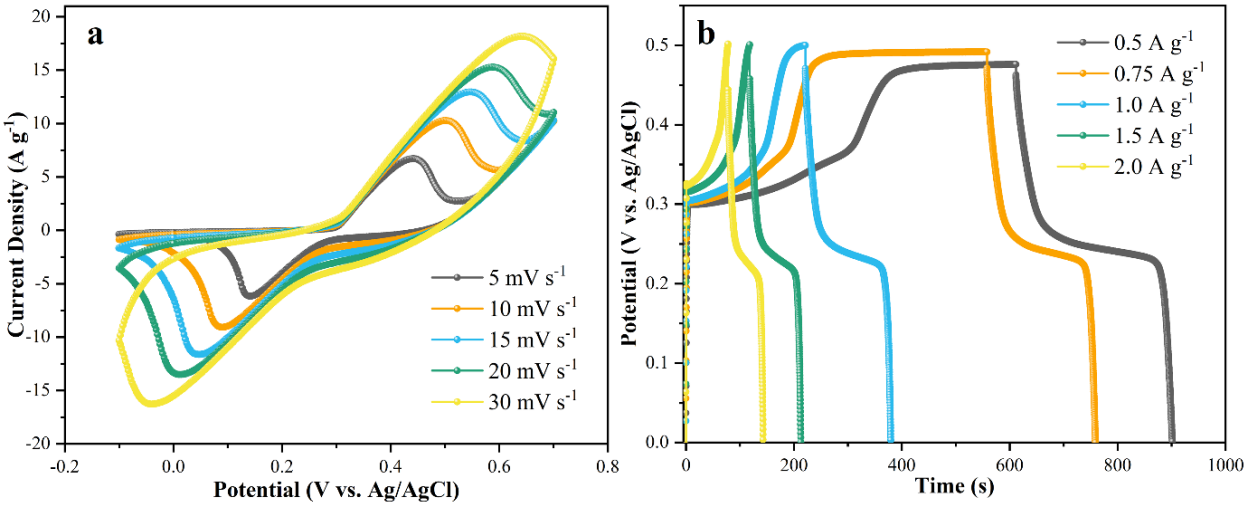


Figure 5.11. (a) Cyclic voltammograms at different scanning rates and (b) Galvanostatic charge/discharges profiles at different current densities of FG_Gr1.0 in a three-electrode system using 2M KOH aqueous electrolytes.

The relationship between peak current density and scan rate is shown in **Fig. 5.12c** and **d**. The linear relationship between peak current density and the corresponding scan rate (I vs. v) implies the charge storage behavior is dominated by EDLC, while if the peak current density is proportional to the square root of scan rate (I vs. $v^{1/2}$), diffusion-controlled process plays a more crucial role in the charge storage process. In **Fig. 5.12c** and **d**, the EDLC (I vs. v) and diffusion-limited process (I vs. $v^{1/2}$) with linear fitting have been plotted for FG_Gr1.0 nanocomposite in both neutral and alkaline electrolytes ranging from 50 to 500 mV s^{-1}. The R^2 values were found in an order of $R^2_{2M\ KOH} > R^2_{2M\ NaCl}$ for the linear fitting plots of I vs. $v^{1/2}$. However, a reverse trend was viewed in the linear fitting plots of I vs. v ($R^2_{2M\ KOH} < R^2_{2M\ NaCl}$). The results indicated that diffusion-controlled process was the reasonable fit mechanism for FG_Gr1.0 in alkaline-based

electrolytes (2M KOH), while in neutral salt-based electrolyte (2M NaCl), surface charge adsorption/desorption processes were dominant for the charge storage. Notably, in comparison, the R^2 values for linear fitting plots of I vs. v were similar to that of I vs. $v^{1/2}$ in 2M KOH electrolyte, which could be interpreted that both of the nondiffusion-controlled and diffusion-controlled processes were responsible for the charge storage. Besides, the CV profiles of a symmetrical SC device in 2M NaCl electrolyte at a high scan rate of 100 mV s^{-1} were shown in **Fig. 5.12b**, in which the highly symmetric CV profiles indicated the symmetric nature of the as-fabricated SC device. Additionally, it also evidently revealed that the wide operation potential window was beneficial to enhance the energy density significantly.

Besides, to estimate the nano-structuring effect on the capacitive performance, a power-law equation was utilized and as given in **Eq. (11)** [323]. In the power-law relationship, the capacitive performance is diffusion-limited if the value of b is approximately 0.5, while it is considered as capacitive process if b ≈ 1.0. The plot of $\log(i_p)$ vs. $\log(v)$ was shown in **Fig. 5.13a**, the obtained b values were 0.893 in 2M NaCl and 0.765 in 2M KOH electrolyte, respectively. These values evidently indicated that the charge storage behavior of the as-fabricated nanocomposite electrode contained both capacitive and diffusion-limited charge storage processes in both alkaline-based and neutral electrolytes [324].

Furthermore, to evaluate the electrochemical performance quantitatively, the percentage contribution of EDLC and diffusion-controlled process can be separated into two components as shown in **Eq. (12)** [325].

It was noteworthy that the capacitance contribution was different in different electrolytes (**Fig. 5.13b**). The energy storage was dominated by capacitive behavior in neutral electrolyte, whereas the charge kinetics in alkaline-based electrolyte was mainly dominated by the diffusion-limited process at a lower scan rate (50 mV s^{-1}). However, the proportion contribution from capacitive behavior increased with increasing scanning rate in both electrolytes, in which the percentage of capacitive charge contribution increased from 49.70% to 75.88% in neutral electrolyte and 18.13% to 40.81% in 2M KOH (**Fig. 5.13c**), indicating the excellent electrolyte surface accessibility of the as-synthesized FG_$Gr_{1.0}$ nanocomposite. The decrease in diffusion-limited capacitance was due to the limited time given at high scan rate, in which electrolyte ions could not access all pores of the electrode active materials.

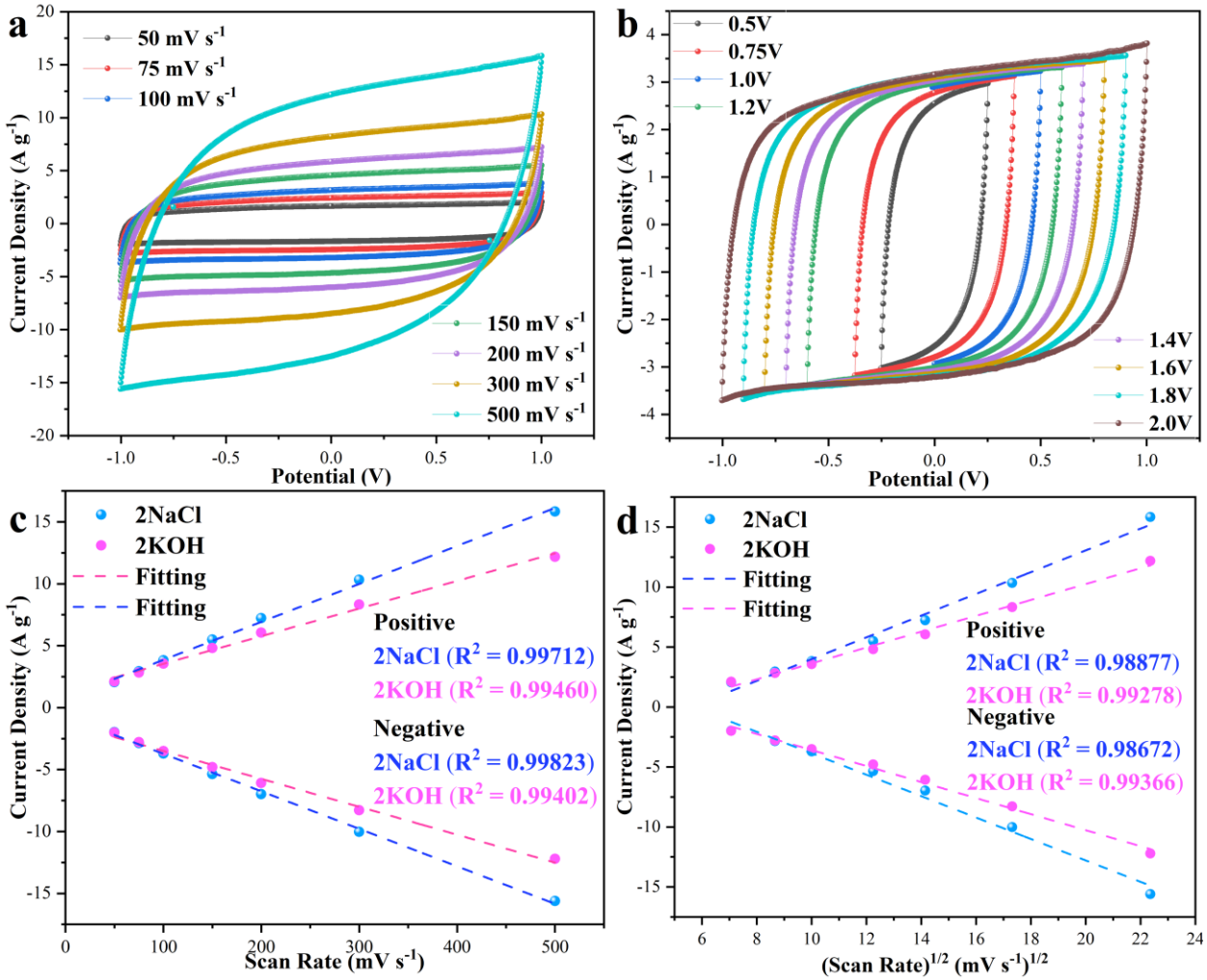


Figure 5.12. The electrochemical performance of FG_Gr$_{1.0}$ nanocomposites: (a) cyclic voltammograms at different scan rates, (b) CV profiles with different potential windows, (c) linear response of peak current density versus scan rate plot, (d) peak current density versus square root of scan rate at 1.0 V.

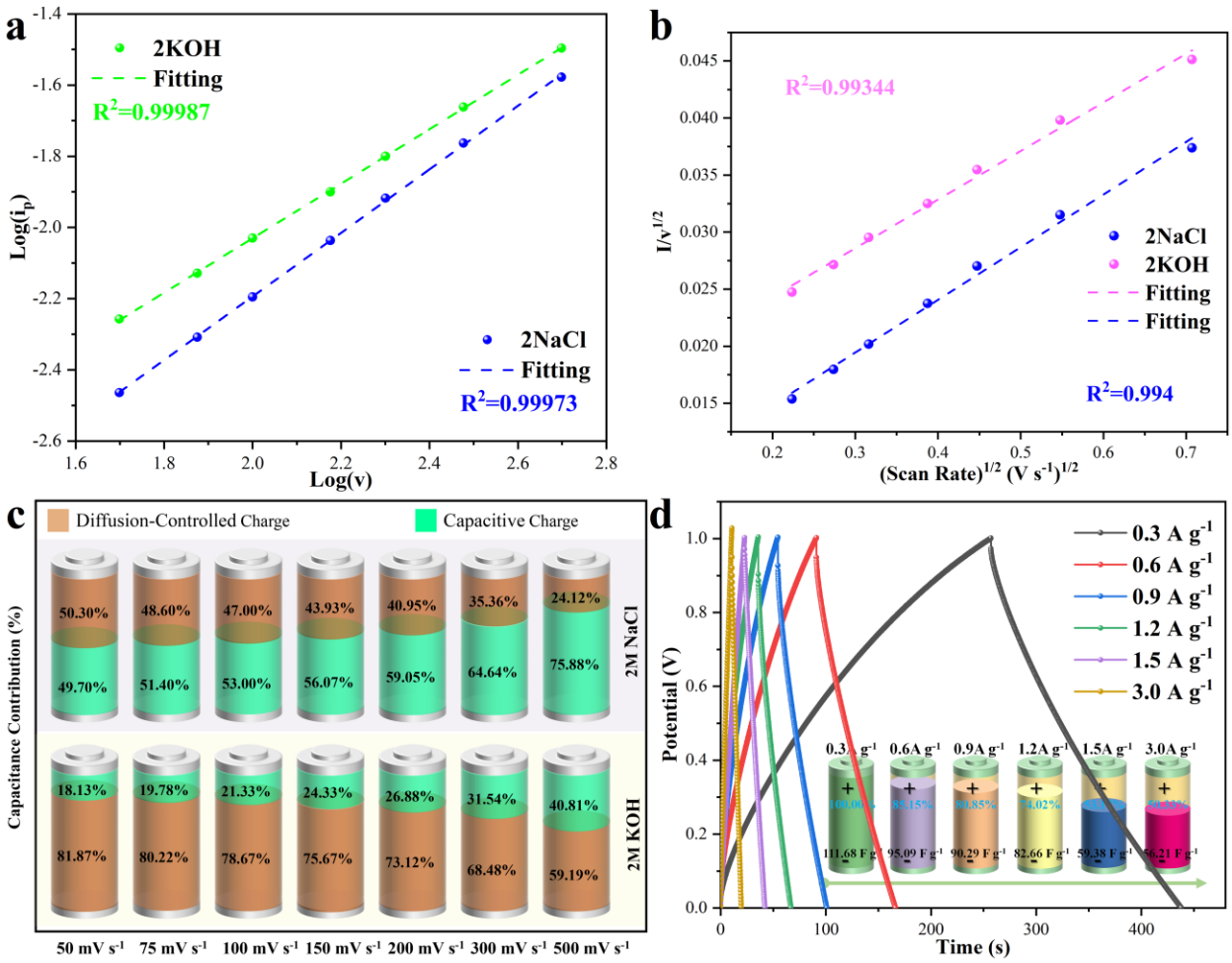


Figure 5.13. (a) The plot of log(i_p) versus log(v) with linear fitting and (b) plot of I/ $v^{1/2}$ vs. $v^{1/2}$ at a potential of 1.0 V, (c) The capacitance contributions of EDLC and nondiffusion-controlled process, (d) GCD at different current densities for FG_$Gr_{1.0}$ electrode in both neutral and alkaline aqueous electrolytes.

5.3.3.2 Galvanostatic charge/discharge

Additionally, GCD measurements were carried out in 2M NaCl within a potential window of 1.0 V (0 – 1.0 V) to study the specific capacitance of the as-fabricated cell (**Fig. 5.9e**). A relatively linear trend of the charge and discharge curves was observed, clearly annotating the EDLC behavior of the system. It was worth noting that sample FG exhibited the longest discharge time, suggesting excellent energy storage performance. According to GCD profiles, the specific capacitance of Ni-MOFs nanomaterials was calculated and found to follow the trend: FG (73.77 F g^{-1}) > E (61.89 F g^{-1}) > FE (60.00 F g^{-1}) > FD (53.49 F g^{-1}) > F (26.32 F g^{-1}). These results were in good agreement with the observations from CV profiles. The variation in capacitive performance could be ascribed to the different morphologies of the electrode materials (**Fig. 5.5**). Generally, the randomly distributed and tightly stacked structure, as can be seen in the sample F, was unfavorable for the transportation of electrolyte ions [326]. As large-sized nanosheets were

formed in the DMF and D.I. water solvent mixture, approximately twice of the specific capacitance was obtained. Additionally, the microspheres were uniformly distributed on the ultra-thin graphene nanosheets to form flower-like structure, which was beneficial for ionic transfer and charge storage, leading to the further enhancement of the electrochemical performance [278].

As depicted in **Fig. 5.9f**, a prolonged discharge time was achieved by FG_$Gr_{1.0}$ nanocomposite in 2M NaCl electrolyte and an improvement of 51.39% in capacitance (111.68 F g^{-1}) was recorded if compared to the FG electrode (73.77 F g^{-1}). The improvement of the capacitance could be attributed to the structurally optimized synergistic effects between hierarchical Ni-MOF and graphene in the nanocomposite electrode [327]. The intrinsic properties of graphene, such as high conductivity, large surface area, excellent mechanical and chemical stability, could enhance ionic conductivity and cyclic stability [328]. In addition, the layered architecture was favorable for providing large exposed active area (29.53 m^2 g^{-1}, **Fig. 5.8**) for the storage of electrolyte ions [329]. Meanwhile, FG_$Gr_{1.0}$ delivered an electrochemical capacitance of 111.68, 95.09, 82.66, 59.38 and 56.21 F g^{-1} at various current densities of 0.3, 0.6, 0.9, 1.2, 1.5 and 3.0 A g^{-1} (**Fig. 5.13d**). It was noticed that the specific capacitance declined with increasing current density. This could be attributed to the limited time given, electrolyte ions were not able to completely contact with electrode active material at a high current density [321]. Similar behavior was viewed in alkaline electrolyte, the capacitive performance declined from 126.21 to 50.11 F g^{-1} as the current density was increased from 0.3 to 3.0 A g^{-1}. Nevertheless, a higher capacitance retention of 50.33% was achieved in neutral electrolyte with a ten-fold increase in current density, whereas the retaining capacitance was merely 39.70% in 2M KOH, suggesting that FG_$Gr_{1.0}$ possessed a better rate performance in neutral electrolyte. This was due to the fact that charges were stored by physical means in neutral electrolyte as discussed above. The adsorption and desorption of electrolyte ions could complete rapidly. Additionally, the energy and power density of FG_$Gr_{1.0}$ was recorded as 14.68 Wh kg^{-1} and 291.82 W kg^{-1} in 2M NaCl, respectively. Profoundly, the as-fabricated electrode could reach a maximum power density of 2851.69 W kg^{-1}.

5.3.3.3 Electrochemical impedance spectroscopy

The electrical conductivity is vital for SC electrode active materials. Hence EIS was adopted to examine the reaction kinetics from 0.01 Hz to 10,000 Hz with a potential amplitude of 10 mV. The Nyquist plots were displayed in **Fig. 5.9c, d** and **5.10b**. Evidently, three distinctive regions were observed: (i) Intercept on the high frequency regions corresponded to the series resistance (R_s), which was the combined resistances of ionic, intrinsic, diffusive, electronic and contact resistance of the electrode. (ii) Semicircle at a mild-frequency region represented the charge transfer resistance (R_{ct}). (iii) A straight line at low frequency region corresponded to Warburg impedance (W) [330, 331]. As can be observed from **Fig. 5.9c** and **Table 5.2**, the R_s of the Ni-MOFs in aqueous-based neutral electrolyte were found to be 0.72, 3.06, 6.60, 1.16 and 1.38 Ω for E, F, FD, FE and FG, respectively. Moreover, the charge transfer resistance (R_{ct}) for FG, FE, E, FD and F were recorded at 3.00, 3.55, 9.08, 13.51 and 42.23 Ω, respectively. The results are in agreement with the CV profiles, which evidently manifested that the electrochemical performance of Ni-MOFs relied upon the morphology of electrode material. For sample F, the high R_{ct} could result from the randomly distributed and tightly stacked morphology where less charge transfer channels

were offered. On the other hand, the low R_{ct} of FG electrode (comparable to other reported MOF-based supercapacitors) [300, 310, 332], demonstrated the excellent electrical conductivity of Ni-MOFs with flower-like morphology, which was able to provide sufficient contact between electrode and electrolyte. Furthermore, Warburg lines with an angle of larger than 45° was observed, indicating the double-layer capacitor behavior and fast ion diffusion of the FG electrode [333].

Additionally, the impedance spectra of different concentrations of graphene and FG_$Gr_{1.0}$ in various electrolytes are shown in **Fig. 5.9d** and **5.10b**. The semicircles at mild frequency and Warburg lines at the low frequency regions indicated the appearance of both capacitive and diffusion-limited processes, which was in perfect agreement with the result from CV profiles. It was viewed that the R_s and R_{ct} of FG_$Gr_{1.0}$ were 0.44 and 2.55 Ω in neutral electrolyte, which were slightly lower than that of pristine FG. In comparison, larger electrochemical resistance (R_s = 0.47 Ω and R_{ct} = 5.0 Ω) were recorded in alkaline-based electrolyte (**Fig. 5.10b**), suggesting that the pH of the electrolyte could substantially influence the internal resistance of the electrochemical capacitor. The slightly larger charge transfer resistance in 2M KOH electrolyte could be caused by the large-sized cations (K^+) [K^+ (1.33 Å) > Na^+ (0.95 Å)] [320].

Table 5.2. Solution and charge transfer resistance of Ni-MOFs synthesized in different solvents.

Samples	***E***	***F***	***FD***	***FE***	***FG***
R_s (Ω)	0.72	3.05	6.60	1.56	1.38
R_{ct} (Ω)	9.08	42.23	13.51	3.55	3.00

5.3.3.4 Cyclic stability

The cyclic stability of the FG_$Gr_{1.0}$ sample was also evaluated, as it is one of the most crucial parameters for practical applications. The as-fabricated SC electrode was studied utilizing a chronopotentiometry measurement in 2M NaCl electrolytes at a high current density of 1.5 A g^{-1} within a potential range from 0 to 1.0 V. As illustrated in **Fig. 5.14b**, an outstanding capacitance retention of 97.70% and coulombic efficiency of 89.05% were acquired after 10,000 cycles (**Fig. 5.14c**), demonstrating a remarkable cycling stability of FG_$Gr_{1.0}$ electrode. The enhanced electrochemical performance of FG_$Gr_{1.0}$ could be ascribed to the architectural and compositional features of the nanocomposite. The high porosity feature offered large surface area for charge storage, while the layered structure was favorable for electrolyte ion transfer. Meanwhile, the electrochemical resistance was found to be significantly reduced with the incorporation of graphene nanosheets, which was highly favorable for effective transportation of the ions. In comparison, the cyclic stability of FG_$Gr_{1.0}$ was also measured in 2M KOH using the identical current density (1.5 A g^{-1}). Though a slightly higher capacitive performance was obtained, the retained specific capacitance was merely 54.27% of its initial value (36.94 F g^{-1} as compared to 68.07 F g^{-1}) after 6.000 cycles (**Fig. 5.14a**). The recession of cycling performance in alkaline electrolyte might be due to insertion of large-sized K^+ cations to the electrode during the long-term

cycling process, in which the K^+ repeatedly penetrated and de-intercalated at the electrolyte and electrode interface, leading to the loss of charge carriers and collapse of the frameworks eventually.

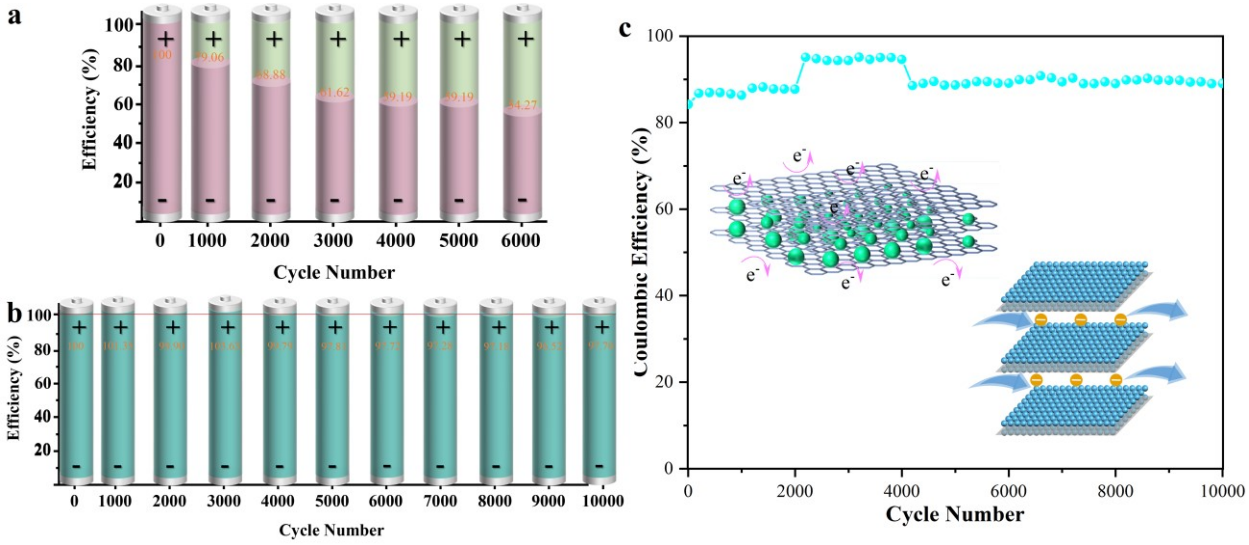


Figure 5.14. Cycling performance of FG_$Gr_{1.0}$ at 1.5 A g^{-1} in (a) 2M NaCl, (b) 2M KOH, and (c) the coulombic efficiency of FG_$Gr_{1.0}$.

The cycling stability of the as-fabricated cells were further investigated by EIS after cyclic measurement. **Fig. 5.15a** and **b** depict the resulting Nyquist plots in 2M NaCl and 2M KOH electrolytes and the equivalent circuit diagrams with fitting data were shown in the inset of **Fig. 5.15a** and **b**, respectively. The slight shift of R_s to higher values after long-term cycling analysis (0.69 Ω for NaCl and 0.61 Ω for KOH) could be caused by the poisoning of electrolytes after repetitive insertion and de-insertion of ions into electrode active materials. Meanwhile, a similar resistance shift for R_{ct} (from 2.55 to 4.47 Ω) was observed in the neutral electrolyte, whereas a significant increase in R_{ct} (from 5.0 to 35.68 Ω) was found in alkaline electrolyte, indicating the crucial impact of the electrolyte on the stability of the device.

In neutral electrolyte, the charge storage mechanism mainly relied on EDLC process, the crystal lattice of hierarchical FG_$Gr_{1.0}$ was saturated with Na^+ cations during the continuous GCD process. The formation of an electric double layer was strongly dependent on the physical adsorption and de-adsorption of the ions along the electrode-electrolyte interface. However, in strong alkaline electrolyte, faradaic redox reactions are more likely to occur, resulting in partial decomposition and loss of the active materials [334]. Consequently, prolonged cyclic stability was observed for the electrode operated in neutral aqueous-based salt electrolyte.

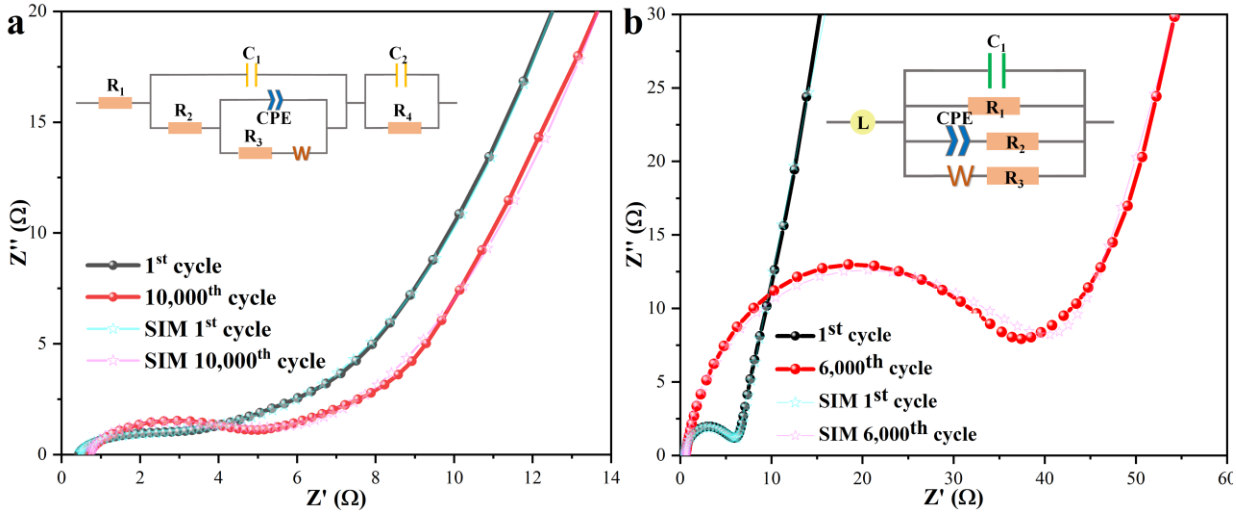


Figure 5.15. Nyquist plots before and after cycling measurement with fitting data and equivalent circuits (inset) in (a) 2M NaCl, (b) 2M KOH.

5.4 Summary

In summary, hierarchical Ni-MOFs with nanosheet structures were successfully synthesized via a facile solvothermal approach in various solvent systems. The morphology and electrochemical performance of the Ni-MOFs nanomaterials were found strongly to be dependent on the solvent system used in the synthesis process. The morphological results indicated that Ni-MOF synthesized in the binary solvent mixture of DMF and EG exhibited 3D flower-like morphology assembled by 2D nanosheets. In addition, the electrochemical performance was further enhanced by incorporating highly conductive graphene nanosheets. The as-fabricated FG_$Gr_{1.0}$ delivered a specific capacitance of 111.68 F g^{-1} in neutral electrolyte. Meanwhile, an excellent rate performance of 50.33% with a ten-fold increase in current density was recorded. At the same time, a preferable capacitance retention of 97.70% was acquired after 10,000 cycles at a high current density of 1.5 A g^{-1} in neutral electrolyte. Furthermore, the specific energy density of the electrode was recorded as 14.68 W h kg^{-1} at a power density of 291.82 W kg^{-1}. The optimized solvent system (DMF + FG) introduced in the current study provides a facile and efficient strategy to synthesize MOFs with excellent electrochemical performance for electrochemical capacitors.

Chapter 6: Facile Synthesis of Nanostructured MoS_2 Incorporated Ni-MOFs With Excellent Cyclic Durability for Symmetric Supercapacitor Application

6.1 Introduction

In general, the excellent functional properties and potential applications of pristine MOF-based supercapacitor electrode active materials have been significantly hindered by the inferior electronic conductivity and chemical stability. In response to these challenges, recent trends in the design and synthesis of MOF-based composite materials normally involve the incorporation of other functional elements, such as quantum dots, metal/metal oxides, carbon-based materials, conductive polymers and others. This strategy could lead to a significant enhancement in physiochemical properties (i.e., electronic conductivity, electrochemical reactivity and stability) due to additive or synergetic effects [335-337]. For instance, the incorporation of graphene into Ni-MOFs has proven to be beneficial in elevating electronic conductivity and widening potential windows. This, in turn, enhances both energy density and cycling stability [241, 282]. Additionally, optimizing effective sites could further facilitate the charge transfer kinetics and elevate energy densities. Consequently, substantial efforts have been devoted to fabricating MOFs with enhanced electronic conductivity and cycling durability for practical applications.

More recently, two-dimensional (2D) transitional metal dichalcogenides have garnered a lot of research attention by virtue of their distinct chemical and physical characteristics. In particular, molybdenum disulfides (MoS_2), with diverse charge storage mechanisms, have attracted tremendous interest in the realm of energy storage. This novel material not only can store charge through physical means via electrical-double layers, but also provides additional capacitance by ionic intercalation and interfacial reversible Faradaic redox reactions. Nonetheless, newly synthesized MoS_2 has a high tendency to aggregate and restack together owing to strong van der Waals force [338], resulting in the reduction of specific surface areas and charge transfer channels. Consequently, this leads to a substantial decrease in specific capacitance and overall electronic conductivity. To tackle this issue, one potential solution lies in the incorporation of other materials to produce nanocomposites with 2D or 3D architectures.

Besides, electrode materials with appropriate structures and pores could provide more Faradic active sites and facilitate fast diffusion of electrolyte ions during electrochemical reactions. This enhancement ultimately leads to enhanced energy density and capacity rate. In recent studies, Ni-MOFs synthesized in a binary solvent system were observed to exhibit a unique 2D nanosheet structure with outstanding cyclability [241]. Such unique architectures could not only offer large surface areas for redox reactions and interfaces for ion adsorption and desorption, but also shorten ion diffusion paths. Hence, they could serve as a promising matrix when coupled with 2D layered MoS_2. Nevertheless, the recorded specific energy was not preferable for practical applications. This limitation could be effectively addressed by pseudocapacitance resulting from the redox active sites of MoS_2. As a result, the resulting composites were expected to exhibit a unique morphology and exceptional electrochemical properties, including electronic conductivity, specific energy and cycling stability. Despite a wide range of studies emphasized the design and synthesis of 2D MoS_2 in the last decade, there have been very few studies on the fabrication of MoS_2 incorporated Ni-MOF nanosheets synthesized in a binary solvent system for supercapacitor

applications. In this study, MoS_2 was successfully incorporated onto Ni-MOF nanocomposites via a facile hydrothermal approach, which is a facile and cost-effective method to produce large-scale MoS_2 and MOF-based hybrid electrodes. Additionally, to enhance the electronic conductivity, sodium ions (Na^+) were introduced to form the nanocomposites. By taking advantage of the synergistic effects, the as-prepared symmetric supercapacitor device was capable of delivering a maximum energy density and power density of 33.33 Wh kg^{-1} and 3390 W kg^{-1}, respectively. Furthermore, the obtained capacitance retention and coulombic efficiency were remarkable and recorded at 97.42% and 97.82% after more than 10,000 cycles, respectively. The result evidently affirmed the potential application of sodium and MoS_2 incorporated Ni-MOF nanocomposites as promising electrode active materials for high efficiency electrochemical energy storage.

6.1.1 Synthesis of Ni-MOF Nanosheets

2D Ni-MOFs were prepared via a hydrothermal method reported previously [241, 339]. Typically, 1.57 g (5.4 mmol) of nickel nitrate hexahydrate ($Ni(NO_3)_2 \cdot 6H_2O$) and 0.299 g (1.8 mmol) of *p*-benzene dicarboxylic acid (H_2BDC) were dissolved in a mixture of 8 mL of N, N-Dimethylformamide (DMF) and 5 mL of ethylene glycol, then magnetically stirred at room temperature for 60 min. When a homogeneous solution was formed, the solution was transferred into a Teflon-lined stainless-steel autoclave (50 mL) and heated at 160 ℃ for 12 h. After cooling to ambient temperature, the light green products were centrifuged at 3000 rpm and washed with DMF and ethanol three times. Finally, the green precipitates were dried in a vacuum oven at 60 ℃ overnight.

6.1.2 Synthesis of Na^+-doped MoS_2@Ni-MOFs Nanocomposites

The as-prepared Ni-MOF nanosheets were dispersed in 30 mL of high-pure water with magnetic stirring for 60 min to form a homogeneous light blue solution. Subsequently, 3 mmol of Na_2MoO_4 and 6 mmol of thiourea were dispersed in the same solution and stirred for another one hour to ensure the precursors are well-mixed in the solution. Then, the homogeneous solution was transferred into a Teflon-line autoclave and heated at 180 ℃ for 24 h. Finally, the obtained dark products were rinsed with water for three times, and final products were obtained by drying at 60 ℃ overnight, which was denoted as MNM_1.

The other samples were prepared through a similar synthesis method, while the molar ratios between Ni^{2+} and Mo^{4+} were varied from 1:2 to 1:3, and the corresponding samples were labelled as MNM_2 and MNM_3, respectively. Meanwhile, MNM_0 is the resultant product of pristine Ni-MOFs after hydrothermal reactions, and the molar ratio between Mo^{4+} and S^{2-} was set as 1:2 for all samples.

6.2 Results and Discussion

6.2.1 Material Characterizations

X-ray diffraction (XRD) was adopted to characterize the crystallographic structures for the as-synthesized samples, as depicted in **Fig. 6.1a**. Two apparent broad diffraction peaks were observed

at 2θ=9.35° and 23.79° in Ni-MOFs (MNM_0), which corresponded to the (100) and (002) planes of Ni-MOFs ($[Ni_3(OH)_2(C_8H_4O_4)_2(H_2O)_4]\cdot 2H_2O$, CCDC 638866) [340]. Meanwhile, other weak peaks of 15.63°, 28.13° and 30.33° were also detected, relating to the planes of $(\bar{1}01)$, (300) and $(\bar{1}\bar{1}2)$, respectively. Notably, the resultant product possessed an inferior crystallinity as compared to pristine Ni-MOFs (**Fig. 6.2**), which could be owing to the hydrothermal reaction. Nevertheless, the hydrothermal reaction could also result in the formation of a large number of defects, facilitating the overall electrochemical performance. **Fig. 6.3** demonstrates the crystal structure of Ni-MOFs with a space group of *p*-1. The XRD patterns of samples incorporated with MoS_2 exhibited similar diffraction peaks of Ni-MOFs, confirming the successful incorporation of Ni-MOF crystal structures. In addition, the simultaneous existence of the reflection peaks of MoS_2 and Ni-MOFs was viewed for sodium ions and MoS_2-incorporated samples (**Fig. 6.1a**), indicating the successful preparation of MoS_2 incorporated Ni-MOFs nanocomposites. In particular, the strong diffraction peaks at 2θ=32.11°, 39.21°, 48.33° and 60.11° in MoS_2-incorporated nanomaterials could be assigned to (010), (013), (015) and (008) planes of MoS_2 (JCPDS No. 37-1492) [341].

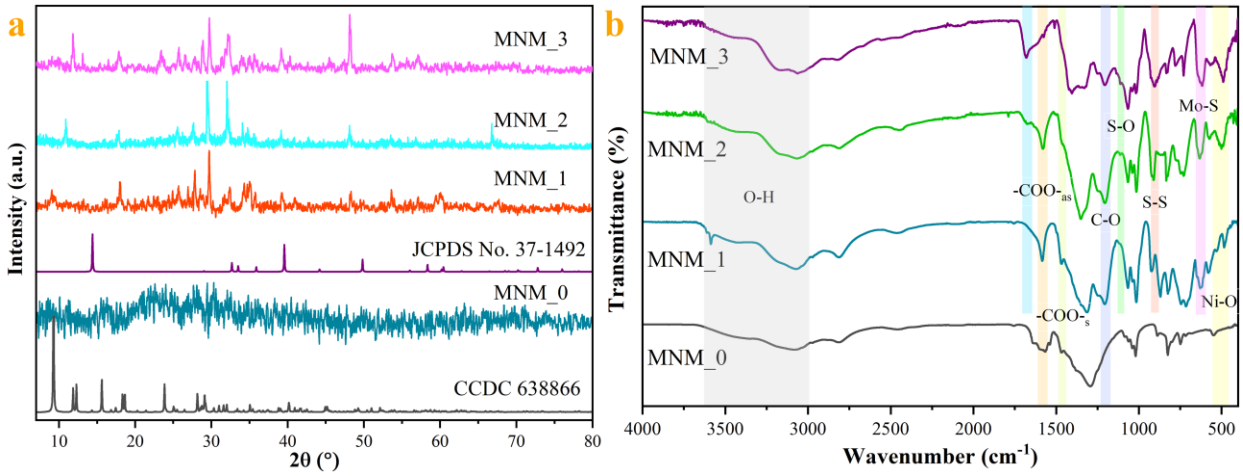


Figure 6.1. (a) XRD pattern and (b) FT-IR spectra of the as-synthesized nanocomposites.

The molecular groups of the as-prepared samples were evaluated by employing Fourier transform infrared spectroscopy (FT-IR) technique, as depicted in **Fig. 6.1b**. The symmetric and asymmetric stretching vibrations at 1387.8 and 1516.7 cm^{-1} could be attributed to C=O (-COOH) of *p*-benzenedicarboxylic anions, indicating the same bidentate mode during the coordination of BDC^{2-} and Ni^{2+} [342]. The vibration frequency of C-O bonding could be viewed at 1198 cm^{-1}, while the vibrations of Ni-O were located at 483 and 525 cm^{-1}, which further confirmed the successful coordination between nickel cations and organic ligands (H_2BDC). Moreover, the bands between 3000 and 3600 cm^{-1} corresponded to the coordinated H_2O molecules [343]. In case of MoS_2 incorporated Ni-MOFs nanomaterials, the appearance of a new strong absorption peak of 1683.5 cm^{-1} was observed in the IR spectra, which could be attributed to the interactions between MoS_2 and Ni-MOFs [344]. The stretching vibrational peak of Mo-S and S-S were found at 629 and 908 cm^{-1}, respectively [345, 346]. Additionally, a relatively weak peak of S-O was detected at 1113.5 cm^{-1}. As a result, the obtained FT-IR spectra was in accord with the XRD results, annotating the successful preparation of Na^+ and MoS_2 incorporated Ni-MOF nanostructures.

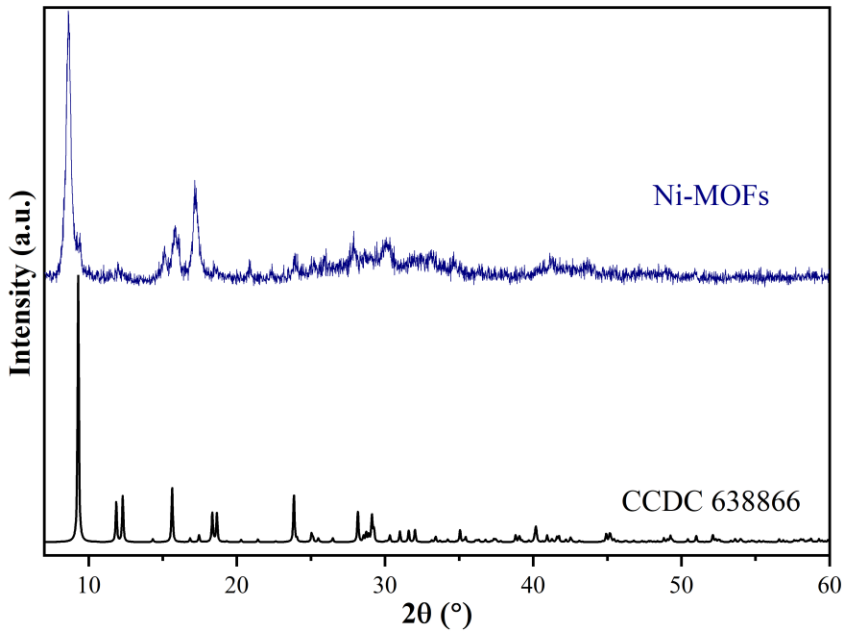


Figure 6.2. XRD patterns of pristine Ni-MOFs synthesized via a solvothermal method.

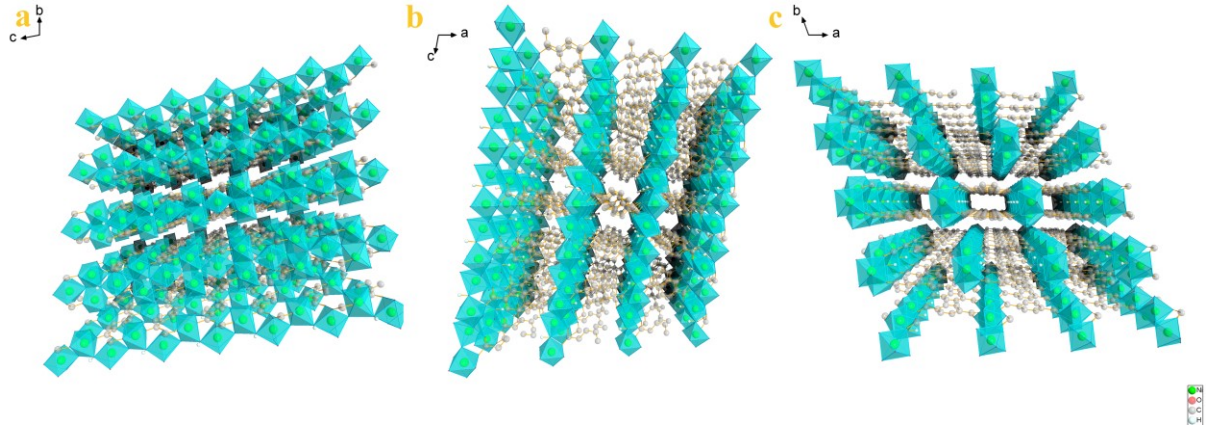


Figure 6.3. The crystal structures of Ni-MOFs viewed along (a) a, (b) b and (c) c directions, respectively.

Fig. 6.4 demonstrates the TG-DTG curves of Na^+ and MoS_2 incorporated Ni-MOF samples. It could be observed that the thermal stability of the pristine Ni-MOFs was inferior. The structure collapse took place at a treatment temperature of 200 ℃ after the removal of physically adsorbed water molecules at 150 ℃. Thermal stability was improved after the introduction of MoS_2 nanomaterials. The initial weight loss between 30 and 150 ℃ was owing to the elimination of adsorbed water on the surface [347]. The second weight loss in the region of 150-215 ℃ could be due to the elimination of chemically adsorbed water as well as solvent molecules. Lastly, the decomposition of overall structures and the formation of MoO_3 occurred at the temperature range of 215-560 ℃ [348]. Meanwhile, it was obvious that the final weights were 50.59, 57.85 and 67.76% for MNM_1, MNM_2 and MNM_3, respectively, confirming the increase in molar ratios between molybdenum and nickel cations.

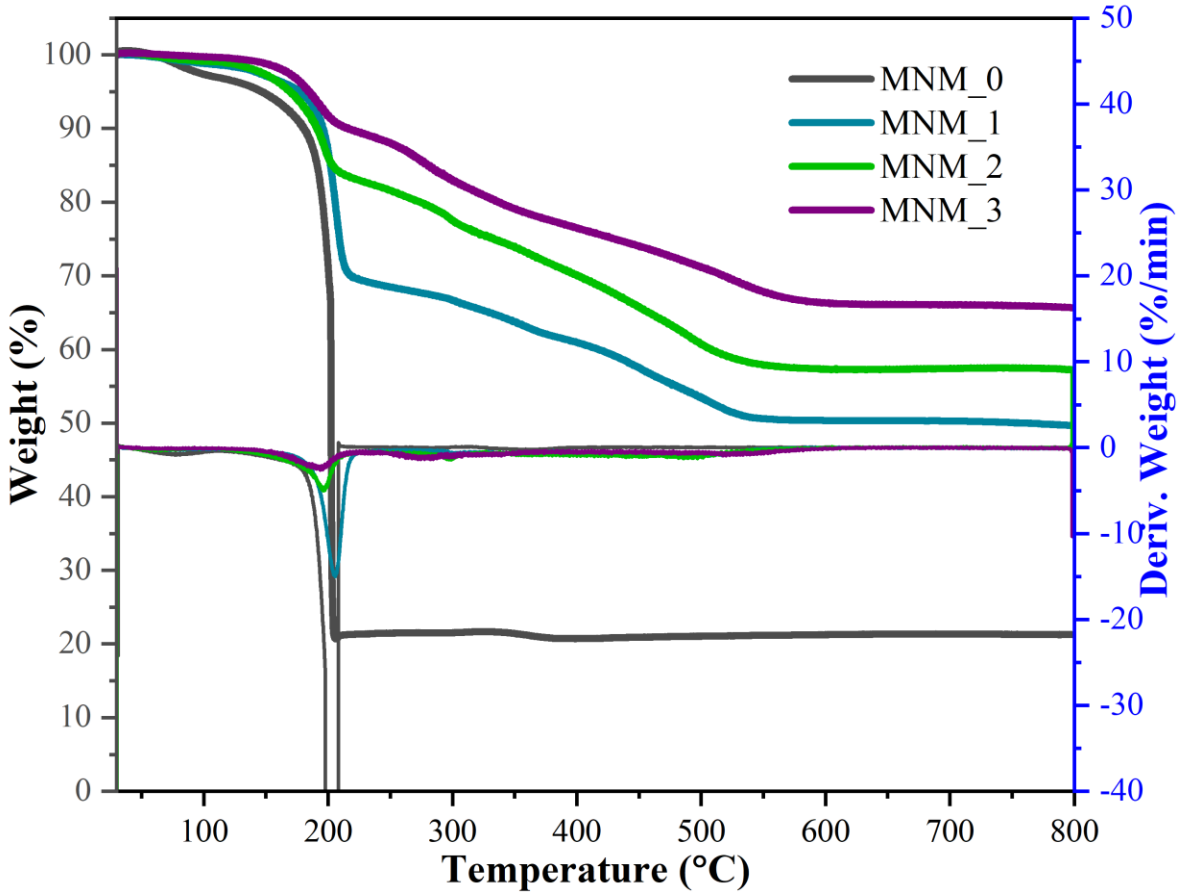


Figure 6.4. TG/DTG curves of Na and MoS_2 incorporated Ni-MOF nanocomposites.

FESEM was carried out to analyze the morphology and microstructures of the as-prepared Na^+ and MoS_2-incorporated Ni-MOF nanocomposites, as demonstrated in **Fig. 6.5**. In particular, the high-resolution images illustrated the surface characteristics while the low-resolution SEM images sufficiently showed the overall shape of the sample. The typical FESEM images of Ni-MOFs were illustrated in **Fig. 6.5a** and **b**, which revealed that Ni-MOFs exhibited hierarchical structure with microspheres morphology. These compactly aggregated microspheres with an average diameter of 3.0 µm were mainly owing to Van der Waal's interactions. When sodium cations and MoS_2 were incorporated, hierarchical porous structures with small-sized nanoparticles were observed (**Fig. 6.5c** and **d**). The reduction in the particle sizes was beneficial to boost the surface area and facilitate the contact between electrode and electrolyte. The obtained BET surface area was approximately 39.0 $m^2\ g^{-1}$ with total pore volume of 0.134 $m^3\ g^{-1}$ and average pore size of 12.67 nm, respectively (**Fig. 6.6**). **Fig. 6.5e** and **f** display the morphology of MNM_2. Interestingly, large clusters and parallel-arranged layered structures were observed, which could be owing to the perfusion of S. By further increasing the amount of incorporated sodium ions and MoS_2, a complicated structure composed of microbars, two-dimensional (2D) thin sheets and small-sized nanoparticles was observed (**Fig. 6.5g** and **h**). Meanwhile, the cracks on the large-sized sheets were detected as well, which could be caused by the large surface tension.

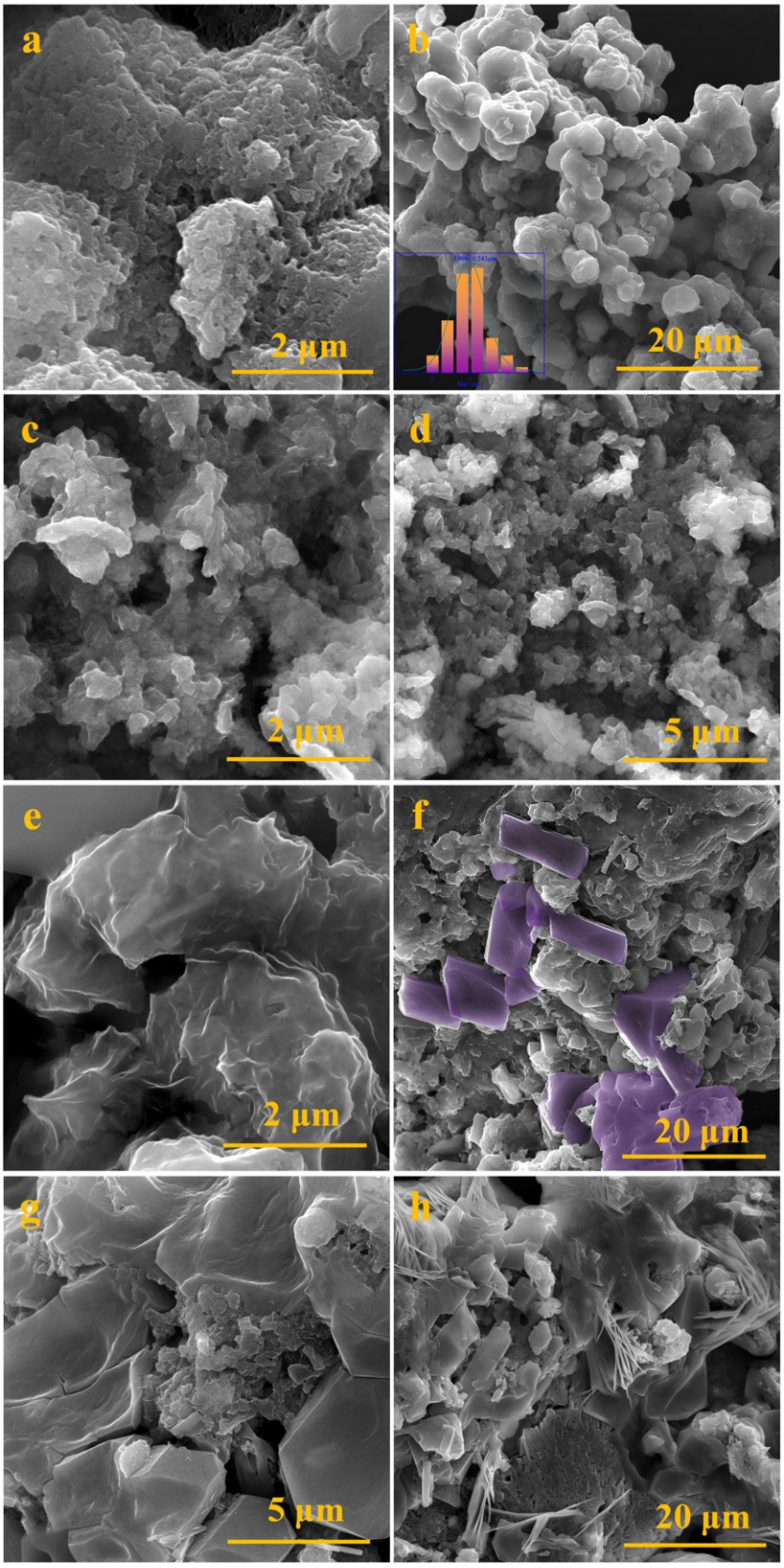


Figure 6.5. FESEM images of (a, b) MNM_0, (c, d) MNM_1, (e, f) MNM_2 and (g, h) MNM_3.

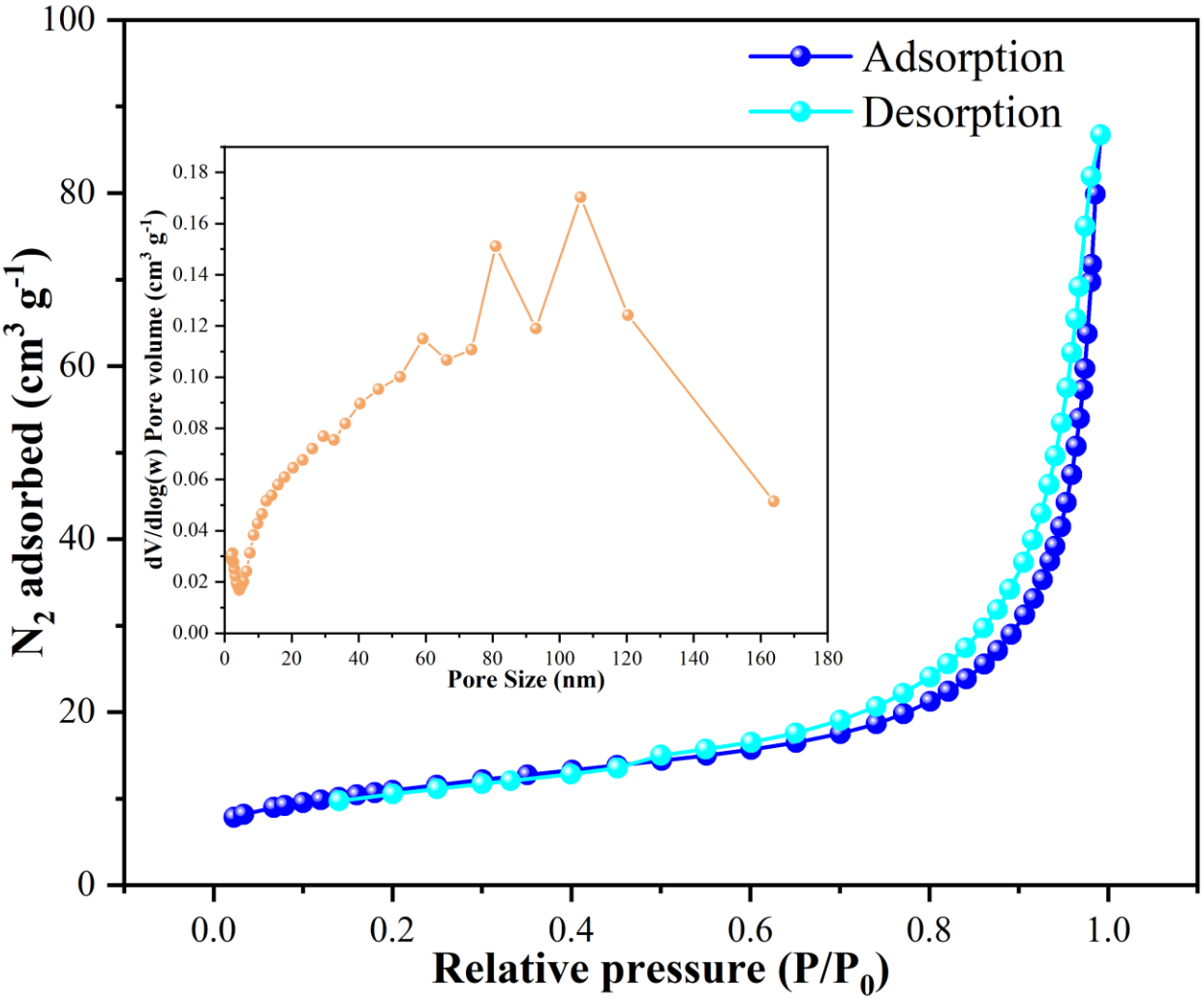


Figure 6.6. N_2 adsorption and desorption isotherms and pore size distribution (inset) of MNM_1.

Moreover, the energy dispersive X-ray spectroscopy (EDX) and elemental mapping diagrams were depicted in **Fig. 6.7 - 6.9**, respectively. These results confirmed the uniform distribution of Ni, C, O, N, Na, Mo and S on the nanocomposites. Specifically, the presence of S, Na and Mo revealed the successful incorporation of sodium ions and MoS_2 into the nanomaterials. Meanwhile, the existence of N was also observed, originating from DMF during the preparation of Ni-MOF nanostructures.

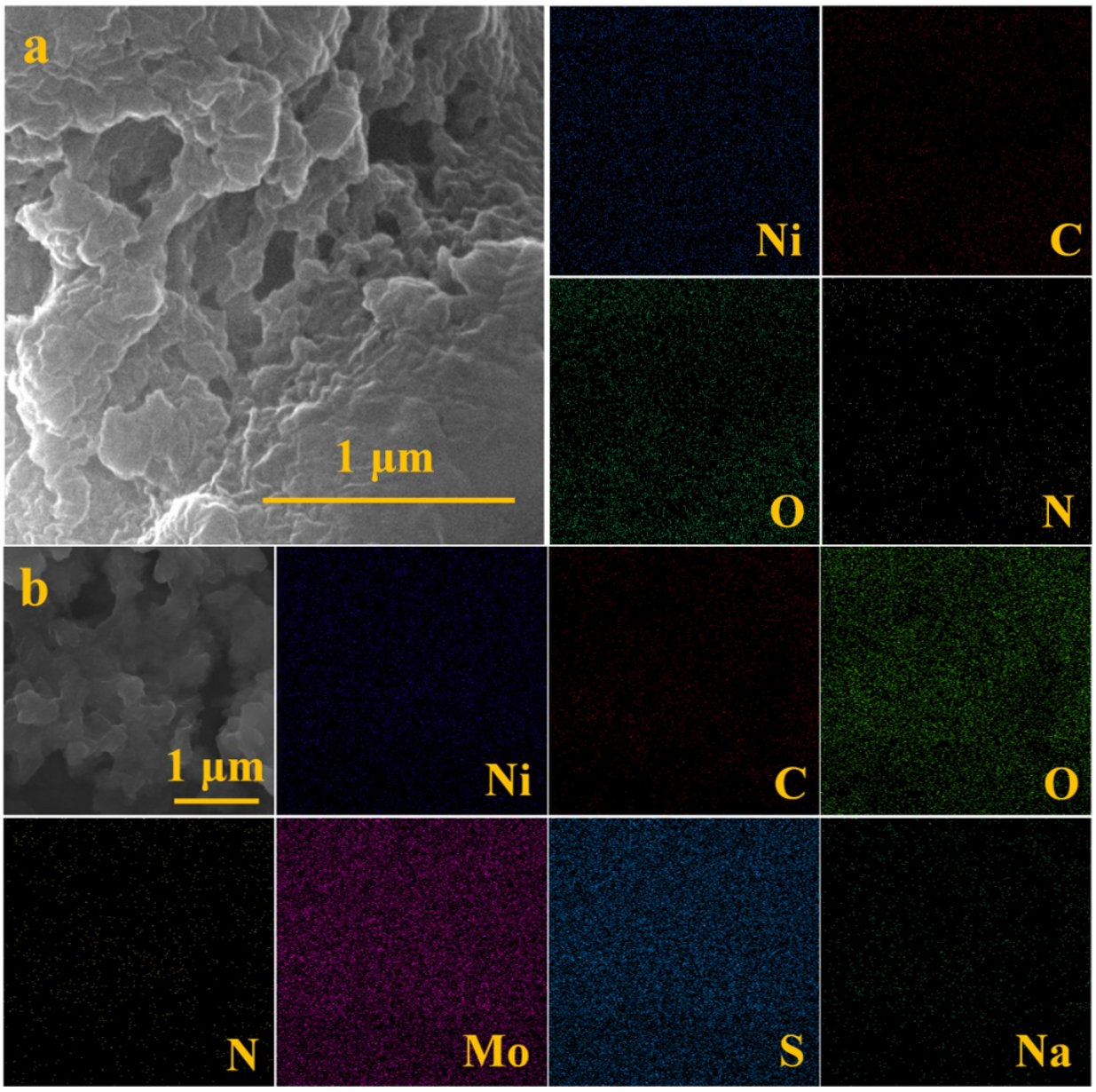


Figure 6.7. Elemental mapping of (a) MNM_0 and (b) MNM_1.

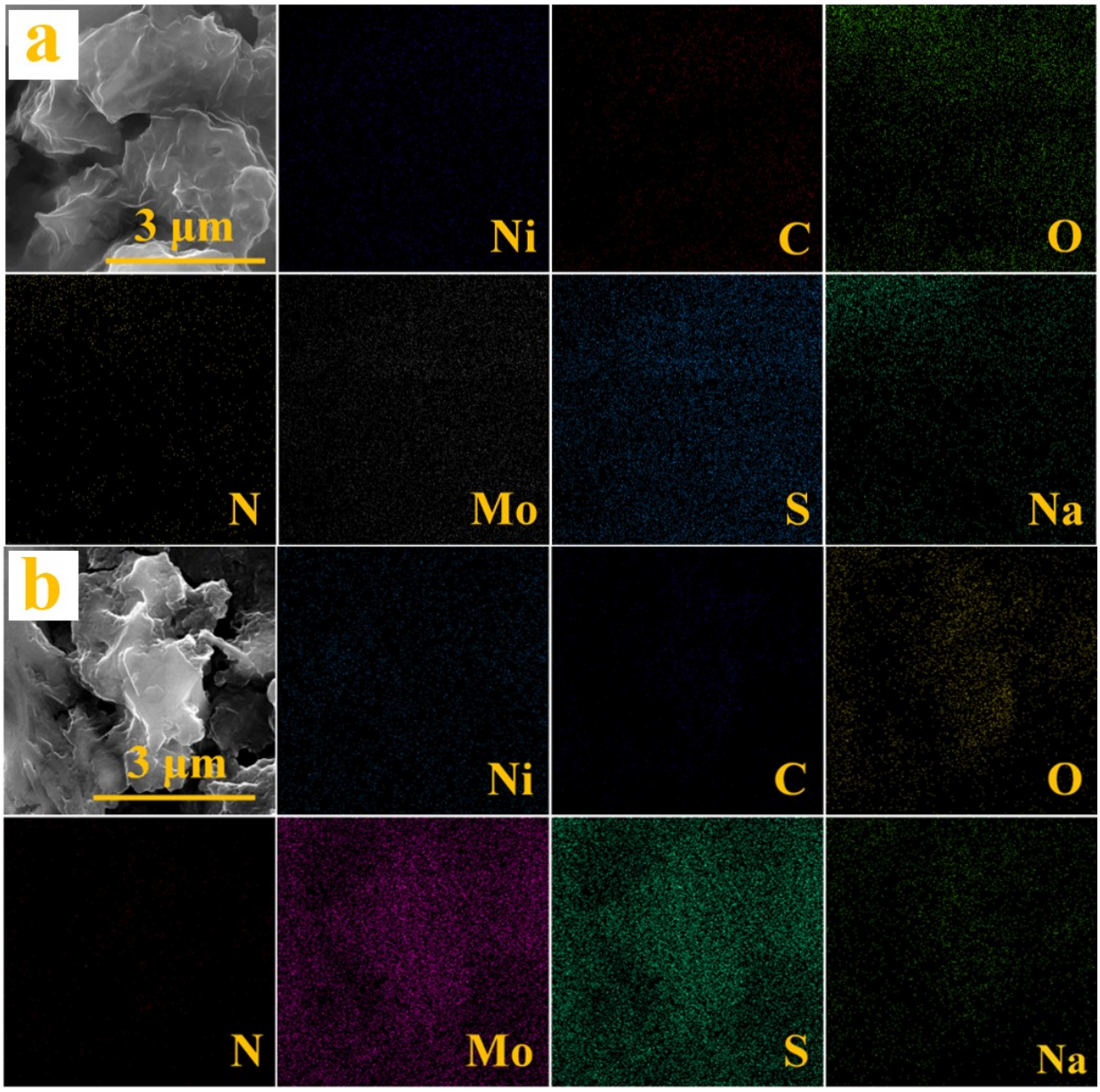


Figure 6.8. Elemental mapping of (a) MNM_2 and (b) MNM_3.

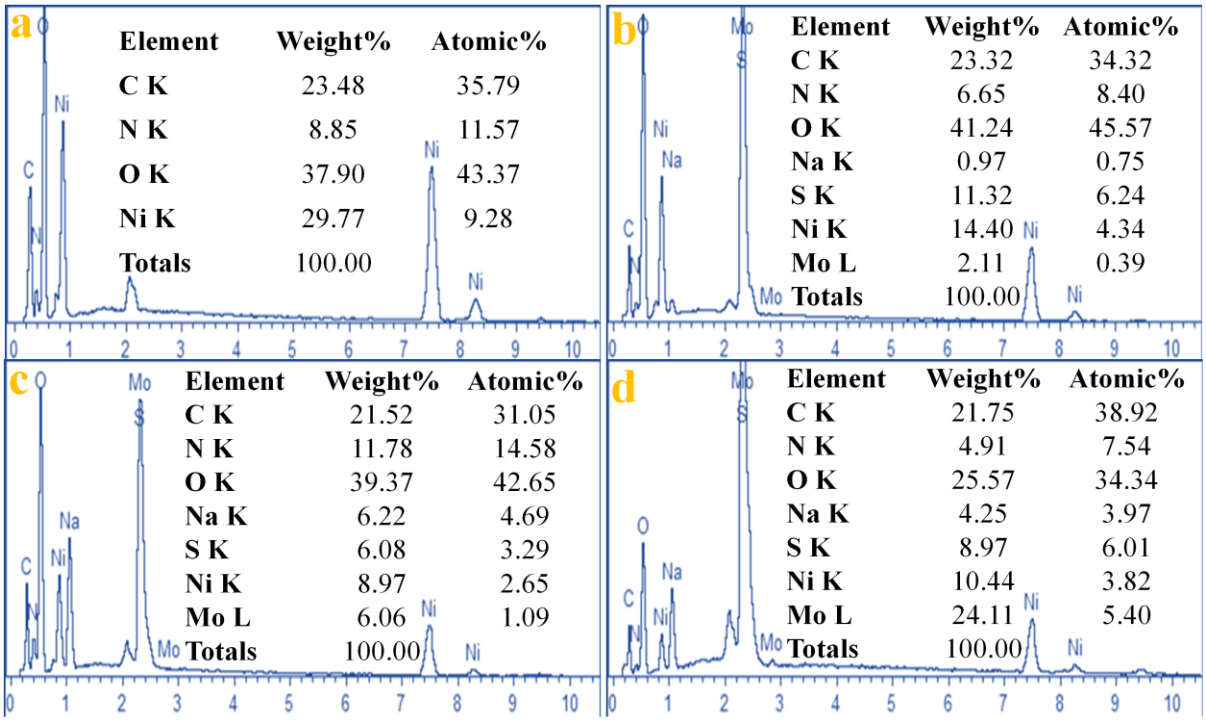


Figure 6.9. EDX and elemental composition of (a) MNM_0, (b) MNM_1, (c) MNM_2 and (d) MNM_3.

To further analyze the detailed morphology and structure of MNM_1as illustrated by **Fig. 6.10**, both low- and high-resolution TEM (HRTEM) were carried out. The low-resolution TEM images revealed the co-existence of nanoparticles and lamellar structures, which were consistent with the FESEM images (**Fig. 6.5**). Meanwhile, The HRTEM images of Na^+ and MoS_2 incorporated Ni-MOFs demonstrated in **Fig. 6.10c** and **d** clearly indicated that the excellent crystalline feature of the as-prepared nanocomposites. In particular, the obvious lattice fringes observed in **Fig. 6.10c** belonged to the (002) spacing of Ni-MOFs [342], in which the lattice spacing was found to be 3.17 Å. Moreover, the crystalline spacing of MoS_2 (062) was also measured to be 2.04 Å (**Fig. 6.10d**) [349]. These results further annotated the successful incorporation of MoS_2 and Ni-MOF hierarchical structures.

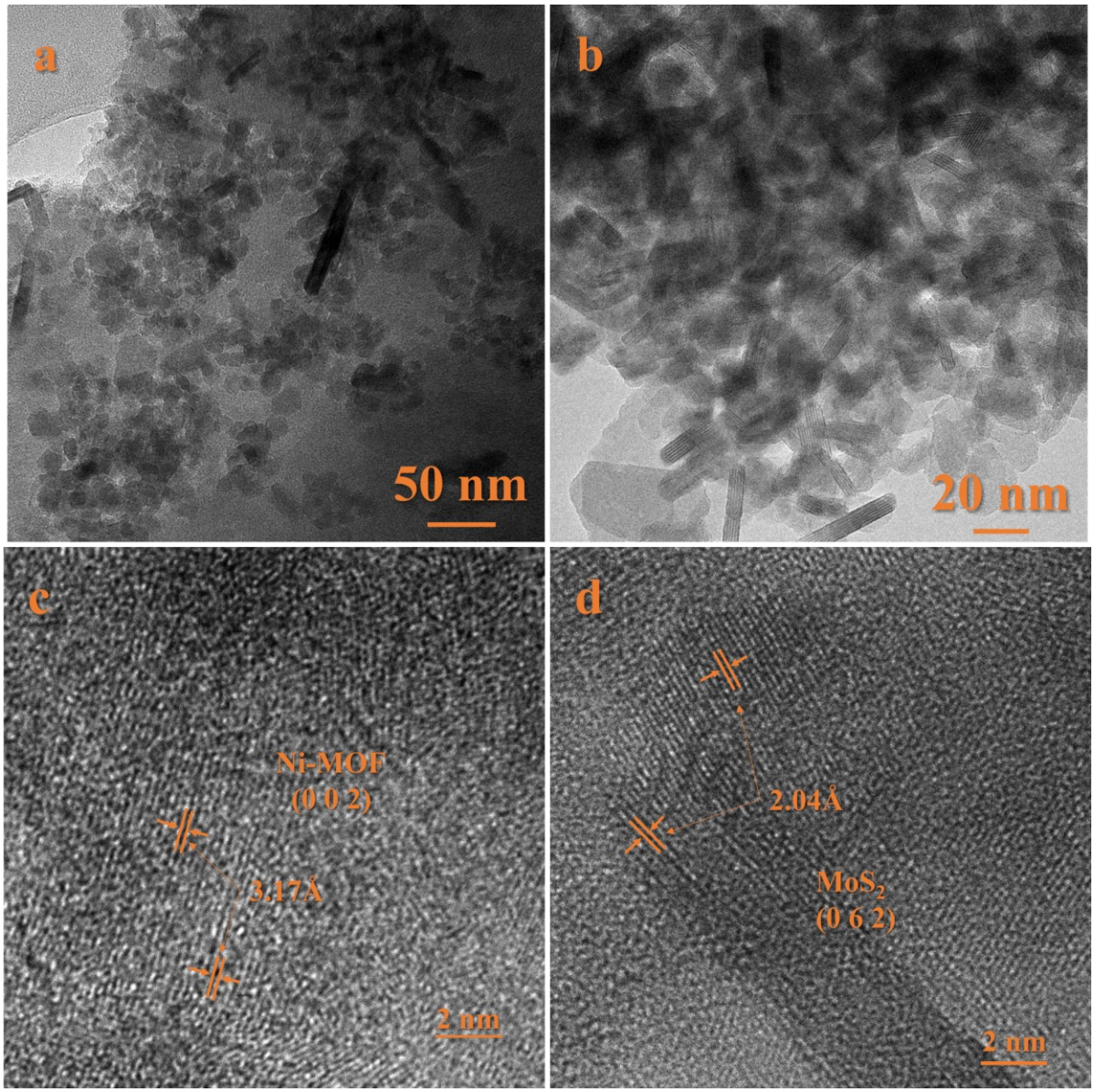


Figure 6.10. (a, b) Low-resolution and (c, d) HRTEM images showing the lattice spacing of the MNM_1 sample.

6.2.2 Electrochemical Performance of Nanocomposites

Cyclic voltammetry (CV) and galvanostatic charge and discharge (GCD) were conducted to investigate the electrochemical properties of Na^+ and MoS_2-incorporated Ni-MOF nanocomposites in a conventional three-electrode system. **Fig. 6.11a** displays the cyclic voltammograms at a scanning rate of 2 mV s^{-1}, and the working potential window was manipulated between 0 and 0.6 V (vs. Ag/AgCl). The appearance of a pair of redox peaks indicated the predominance of pseudocapacitance, resulting from the reversible redox reactions between KOH aqueous electrolyte and Ni-MOF nanostructures, as represented by **Eq. (14)** [241]. Moreover, the interactions between MoS_2 and cations (K^+) could also significantly contribute to the

electrochemical capacitance (**Eq. (15)**). When the molar ratio between Mo^{4+} and Ni^{2+} was increased from 0 : 1 to 1 : 1, it was noteworthy that the enclosed CV area enlarged. However, further increase in the molar ratio of Mo^{4+} (i.e., MNM_2 and MNM_3) led to a minification in the enclosed CV areas. These results revealed that MNM_1 exhibited the highest specific capacitance among other samples and the incorporation of higher amount of MoS_2 nanostructures was not beneficial to the electrochemical performance.

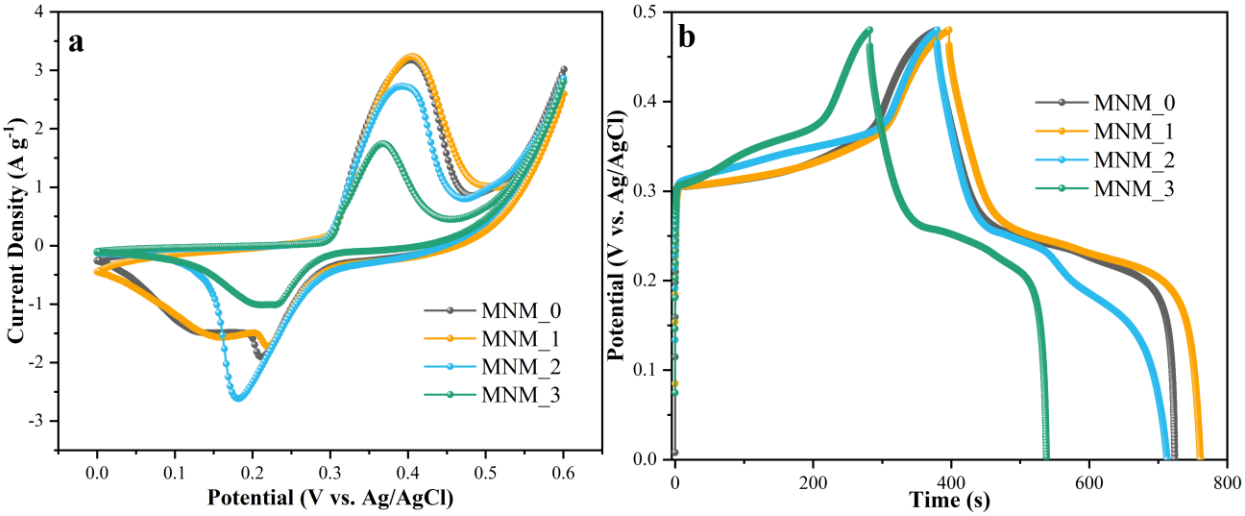


Figure 6.11. (a) CV profiles and (b) GCD curves of the prepared electrodes in 2M KOH electrolyte.

$$MoS_{2\,(s)} + K^{+}_{(aq)} + e^{-} \leftrightarrow MoS - SK_{(s)} \qquad (15)$$

Additionally, the CV profiles at various scanning rates ranging from 2 – 20 mV s^{-1} were demonstrated in **Fig. 6.12**. With an increasing scanning rate, it was observed that the oxidation peaks shifted positively and reduction peaks shifted negatively. This revealed the existence of internal resistance in the nanocomposites [350]. The overall shapes of CVs could be maintained, although there was a significant increase in scan rate. This was mainly owing to the hierarchical structure of sodium ions and MoS_2-incorporated Ni-MOF nanocomposites, in which the large surface area could buffer electrolytes better and the porous structure could facilitate the mass transfer more effectively.

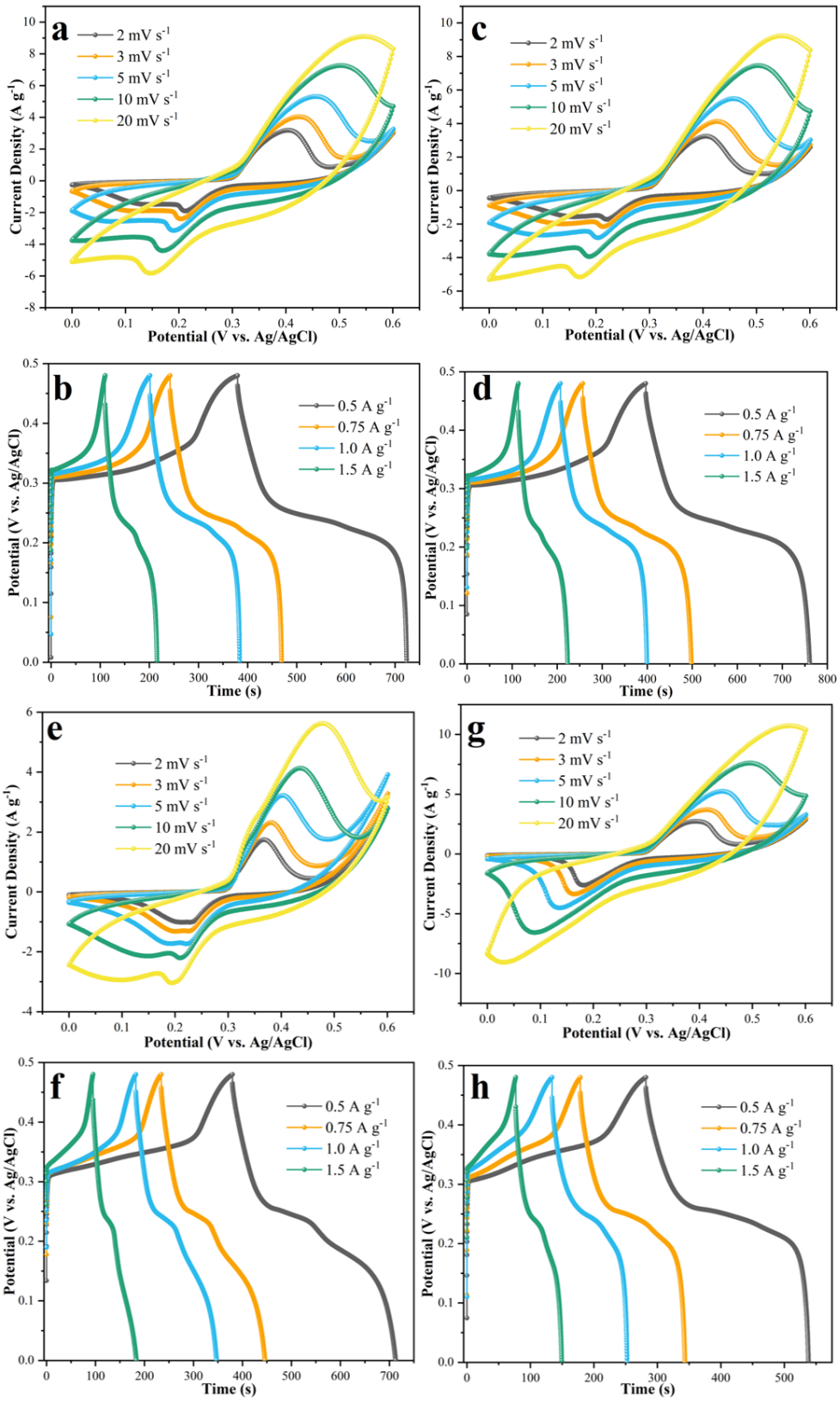


Figure 6.12. Electrochemical properties of the as-prepared electrodes in a three-electrode system in 2M KOH electrolyte: (a, b) MNM_0, (c, d) MNM_1, (e, f) MNM_2 and MNM_3.

Fig. 6.11b depicts the GCD profiles of the nanocomposites at 0.5 A g^{-1} in 2M KOH. The potential could only reach 0.48 V (vs. Ag/AgCl) due to the limitation of the electrode itself. The nonlinear response between potential and time showed that the capacitances were mainly contributed by Faradaic redox behavior [152]. Besides, with the longest discharge time, MNM_1 revealed the highest electrochemical capacitance. These results were congruent with the results from CVs. The calculated specific capacitance of MNM_0, MNM_1, MNM_2 and MNM_3 was 0.5 A g^{-1} were 464.64, 491.63, 447.85 and 345.84 F g^{-1}, respectively. The decrease in specific capacitance was observed in MNM_2 and MNM_3. This could be due to two reasons: (i) The perfusion of sulfur could reduce the porosity and surface areas, leading to a decrease in electrochemical capacitance. (ii) The formation of layered structures might induce shrinkage in gas spacing and dead volume could occur, leading to a reduction in surface area and electroactive sites in MNM_2 and MNM_3. Furthermore, it was noted that a high energy capacity was obtained at a low current density (**Fig. 6.12**), which could be assigned to the limited time given where K^+ and OH^- could only access the outer surface. As a result, the effective use of electrode active materials was reduced, resulting in a low electrochemical capacitance.

The supercapacitive property of the as-synthesized nanocomposites was also studied utilizing a two-electrode system in a freshly prepared 2M Na_2SO_4 aqueous electrolyte. The CV profiles of these samples at a scanning rate of 50 mV s^{-1} were presented in **Fig. 6.13a**. Clearly, all the CV profiles presented a quasi-rectangular shape with a high degree of symmetry between both positive and negative scans, which indicated the co-existence of both electric double layer capacitance (EDLC) and diffusion-limited pseudo-capacitance (intercalation and deintercalation) [323]. The excellent rate performance of the as-prepared Ni-MOF-based nanocomposites was revealed by the fact that such quasi-rectangular geometry could be retained even at a high scanning rate of 500 mV s^{-1} (**Fig. 6.14**). Meanwhile, it annotated an outstanding capacitive performance and fast electrolyte ion transfer as well. Besides, MNM_1 exhibited the largest integrated CV area among other samples, which implied that MNM_1 possessed the highest specific capacitance since the electrochemical capacitance was strongly correlated to the mathematical area of an enclosed CV profile.

As compared to pristine Ni-MOFs, the enclosed CV area increased when MoS_2 was incorporated at a molar ratio of 1:1 between Ni^{2+} and Mo^{4+}, demonstrating that the incorporation of MoS_2 with Ni-MOFs enhanced supercapacitive performance as the result of the synergistic effect between the two components. In contrast, a reduction in CV areas was seen when a higher molar ratio was employed. This could be attributed to change of overall structure after the incorporation of large amount of sodium ions and MoS_2, in which the surface area and porosity were decreased. As observed in **Fig. 6.5**, the formation of large pieces of clusters and folded nanosheets marginally reduced the contact between electrolyte and electrodes, it also had adversely affected the diffusion of electrolyte ions, leading to the reduction in electrochemical capacitance.

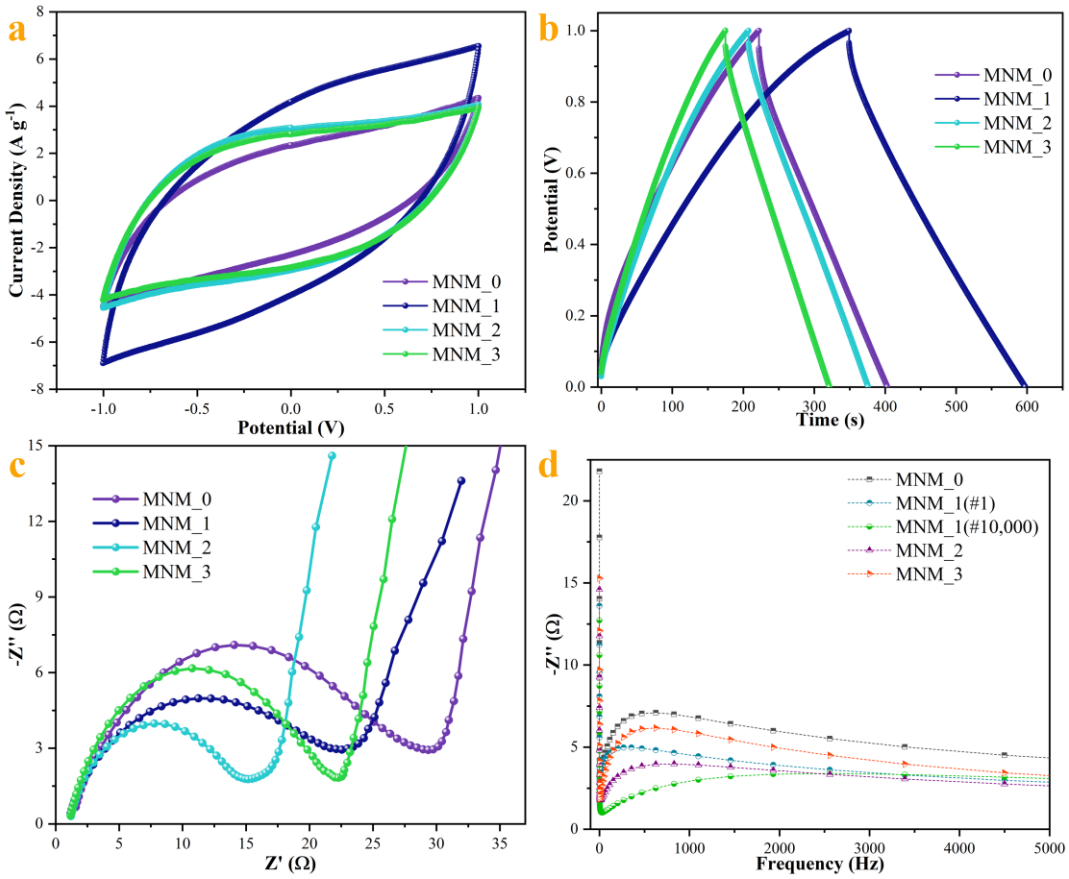


Figure 6.13. (a) CV profiles, (b) GCD curves, (c) Nyquist plots and (d) the plot of resistance versus frequency.

The GCD curves of different samples at a current density of 0.5 A g^{-1} were shown in **Fig. 6.13b**. Evidently, all the GCD profiles illustrated an isosceles triangular shape, suggesting that these nanomaterials exhibited a typical electric double-layer capacitive behavior and excellent rate performance [351]. Moreover, a slight voltage drop, also called IR drop, was viewed at the initial stage of discharge for all samples, which could be resulted from the relatively higher internal resistance. The calculated specific capacitances of MNM_0, MNM_1, MNM_2 and MNM_3 were 190.53, 257.14, 174.72 and 153.14 F g^{-1}, respectively. These findings agreed with the results derived from CV profiles. **Fig. 6.15** depicts the GCD profiles at different current densities. When there was a four-fold increase in current density, the delivered specific capacities of MNM_0, MNM_1, MNM_2 and MNM_3 were 114.50 F g^{-1} (60.10%), 191.48 F g^{-1} (74.47%), 159.63 F g^{-1} (91.36%) and 128.71 F g^{-1} (84.05%), respectively, indicating the excellent rate performance of the as-synthesized MOF-based SC electrode active materials. In comparison to pristine Ni-MOFs, the rate performance of samples containing Na^+ and MoS_2 were much higher. Hence, it could be concluded that the introduction of Na ions and MoS_2 was advantageous to enhance the rate performance. In particular, the introduction of Na cations was beneficial to improve specific capacitance and electric conductivity. Nevertheless, the incorporation of large amount of Na ions could lead to destructions of hierarchical structures [352]. Additionally, the incorporation of MoS_2 could offer more porous structures for the quick diffusion of electrolyte ions.

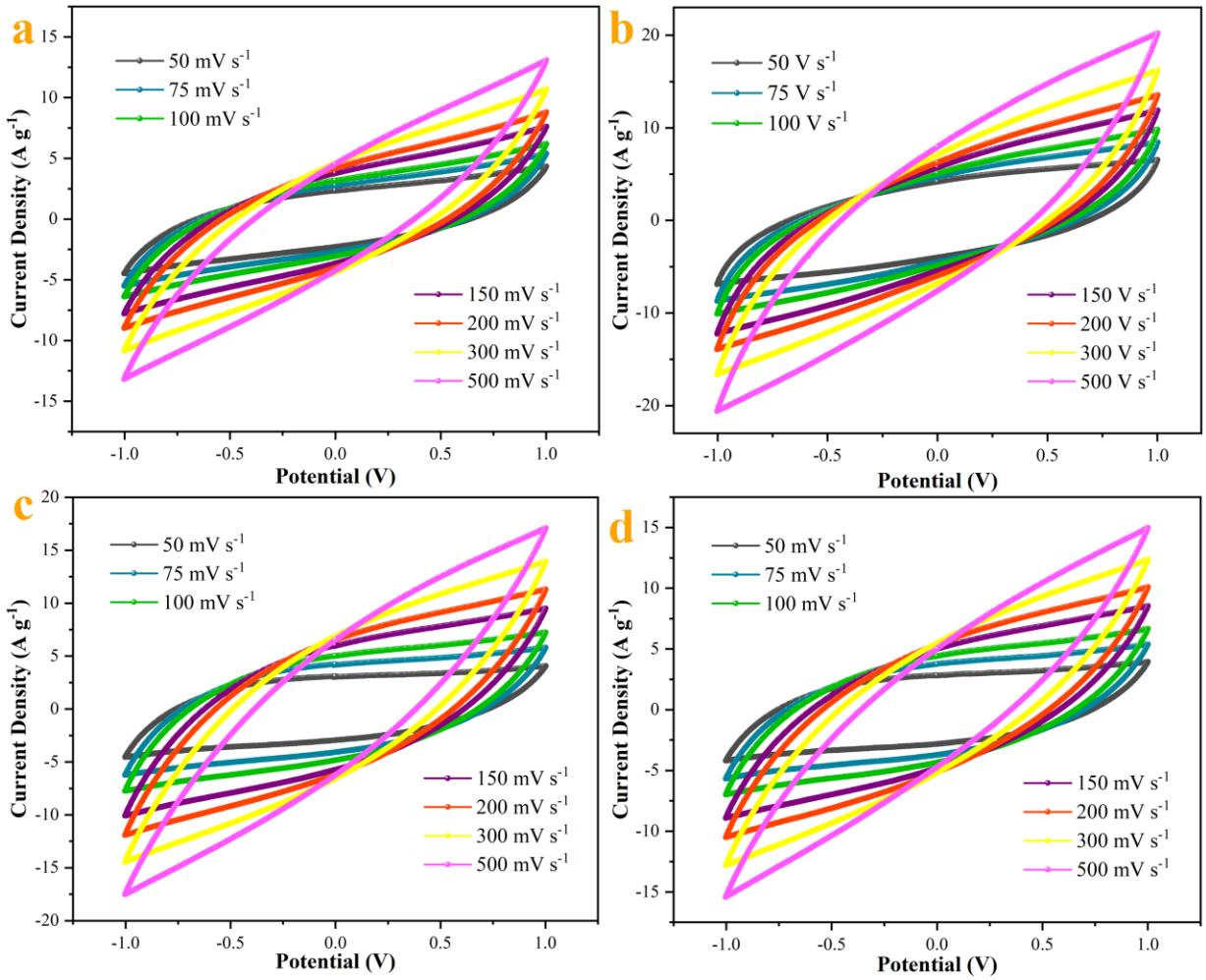


Figure 6.14. CV curves of the as-prepared electrodes in a two-electrode system at different scan rates: (a) MNM_0, (b) MNM_1, (c) MNM_2 and (d) MNM_3.

Furthermore, the as-fabricated symmetric SC device possessed a maximum energy density of 33.33 Wh kg^{-1} at 483 W kg^{-1} for MNM_1, as depicted in **Fig. 6.15**, and the delivered energy density was 6.4 Wh kg^{-1} at a high-power density of 3390 W kg^{-1}. Such value was better than previously reported studies (**Table 6.1**) such as nickel-based metal-organic framework/graphene oxide incorporated graphene nanoplatelet (14.02 Wh kg^{-1} at 933.54 W kg^{-1}) [282], Sm and La-based based 1D-MOFs (18 Wh kg^{-1} at 750 W kg^{-1}) [353], N-doped graphitic carbon derived from MOF (17.08 Wh kg^{-1} at 500 W kg^{-1}) [354], N-decorated porous carbon derived from MOF (5.36 Wh kg^{-1} at 49.7 W kg^{-1}) [355], MIL-53(Al)@rGO (6.66 Wh kg^{-1} at 200 W kg^{-1} and 2.75 Wh kg^{-1} at 3655 W kg^{-1}) [356], graphene/carbonized metal-organic frameworks (21.1 Wh kg^{-1} at 304 W kg^{-1}) [357], N/O co-doped carbon derived from MOF (6.25 Wh kg^{-1} at 100 W kg^{-1} and 5.07 Wh kg^{-1} at 1,000 W kg^{-1}) [332], N-doped porous carbon (24.8 Wh kg^{-1} at 700 W kg^{-1}) [332]. Additionally, the delivered energies were 23.88 Wh kg^{-1} at 475 W kg^{-1}, 22.60 Wh kg^{-1} at 482.5 W kg^{-1}, 19.44 Wh kg^{-1} at 478 W kg^{-1} for MNM_0, MNM_2 and MNM_3, respectively. Even at high power densities of 2175, 2409 and 2277 W kg^{-1}, the attained energies of MNM_0, MNM_2 and MNM_3 were 6.53, 13.12 and 9.23 Wh kg^{-1}, respectively.

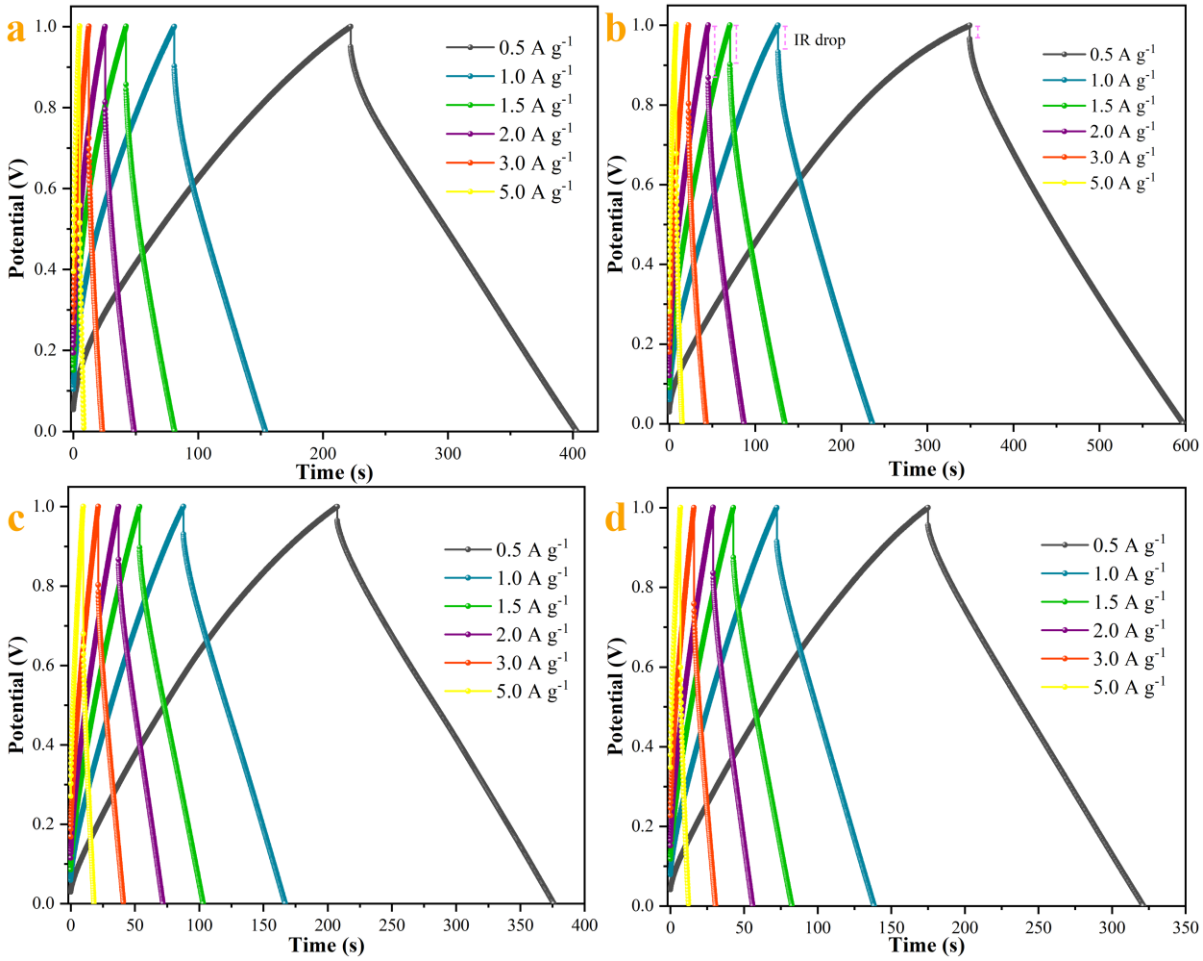


Figure 6.15. GCD curves of the as-prepared electrodes in a two-electrode system at different scan rates: (a) MNM_0, (b) MNM_1, (c) MNM_2 and (d) MNM_3.

Table 6.1. Comparison of electrochemical performance of various carbon- and MOF-based electrode for supercapacitor applications.

Materials	Electrolyte	Specific Capacitance ($F\ g^{-1}$)	Energy Density ($Wh\ kg^{-1}$)	Power Density ($W\ kg^{-1}$)	Efficiency (%)	Cycles	Ref.
Ni-MOF/GO/GNP	2M CH_3COOK	102.24F/g	14.02	933.54	85.6	20,000	[282]
Sm-H_2PDA	2M KOH	1580F/g	18	750	87	2,000	[353]
N-doped graphite carbon	6M KOH	244F/g	17.08	500	93	5,000	[354]
N-doped porous carbon	6M KOH	272F/g	5.36	49.7	100	10,000	[355]
MIL-53(Al)@rGO	1M KOH	212F/g	6.66 2.75	200 3,655	50	5,000	[356]
Graphene/carbonized MOF	1M H_2SO_4	420F/g	21.1	304	85	60,000	[357]
N/O-doped carbon	6M KOH	220F/g	24.8	700	99.1	10,000	[332]
MNM-1	2M KOH	492.63	33.33 6.4	483 3,390	97.42	10,200	This work
Porous carbon nanotubes	6M KOH	300.1F/g	7.38	-	83.7	10,000	[358]
3D LCAC	6M KOH	223	6.7	500	92.5	10,000	[359]
Porous carbon	3M KOH	274.9F/g	20.51	1,031	95.6	5,000	[360]
N-doped carbon	6M KOH	473.5F/g	15.99	500	95.74	10,000	[361]
3D AC	6M KOH	320	8.6 6.9	250 1,000	98	10,000	[362]

To study the charge transfer kinetics for the as-prepared samples, the EIS was conducted with an alternative current amplitude of 10 mV between 100,000 and 0.01 Hz. **Fig. 6.13c** depicts the EIS plots of all samples in 2M Na_2SO_4 electrolyte. The Nyquist plot could be divided into three regions, high-frequency region, medium-frequency region and low-frequency region: (i) The intercept with real axis (Z') at high-frequency regions represents the internal resistance (R_s) resulting from the bulk resistance at the interface between electrode and electrolyte [363]. (ii) The diameter of a semicircle in the mild-frequency region represented the charge transfer resistance (R_{ct}), which mainly resulted from the contact resistance, intrinsic resistance of the electrode active materials and ionic resistance from electrolyte [364]. (iii) A linear line at low-frequency region stands for the electrolyte diffusion resistance, also quoted as Warburg impedance (W). The Warburg impedance, originating from the diffusion of electrolyte ions within the electrode, measures the degree of difficulty for electrolyte penetrating the pores of electrodes [365]. The R_s values for MNM_0, MNM_1, MNM_2 and MNM_3 were 0.83 Ω, 0.30 Ω, 2.78 Ω and 0.79 Ω, respectively (**Table 6.2**). Meanwhile, the obtained R_{ct} were 27.50 Ω, 22.77 Ω, 14.40 Ω and 20.63 Ω for MNM_0, MNM_1, MNM_2 and MNM_3, respectively. Clearly, Na^+ doping and incorporation of MoS_2 nanosheets could reduce both internal and solution resistance. This was mainly owing to the enhanced hydrophilicity of electrode surface and affinity with electrolyte ions, which was favorable for the accumulation of electrolyte ions and the decrease of mass transfer resistance [366]. In addition, the recorded higher capacitance of MNM_1 was associated with the reduction in both charge transfer resistance and Warburg impedance. Nonetheless, MNM_2 and MNM_3 possessed a relatively lower R_{ct} value as compared to MNM_1 due to the perfusion, which could block the porosity and offer smooth surface to facilitate the diffusion of electrolyte ions. All the EIS plots displayed a linear region with a fitting angle of approximately 75°, which evidently annotated the effective diffusion of electrolyte ions.

Table 6.2. The electrochemical impedance of MoS_2-incorporated nanocomposites.

Samples		R_s (Ω)	R_{ct} (Ω)	Warburg Angle (°)	τ (ms)
MNM_0		0.83	27.50	79	0.255
MNM_1	**1st**	0.30	22.77	71	0.448
	10,000th	1.19	10.18	75	0.062
MNM_2		0.78	14.40	80	0.192
MNM_3		0.79	20.63	80	0.255

Cycling stability was one of the most crucial parameters for electrode active materials. As shown in **Fig. 6.16a**, MNM_1 possessed a promising cycling stability at 1.5 A g^{-1} in an aqueous-based neutral electrolyte (2M Na_2SO_4). After 10,200 continuous GCD cycles, more than 97.42% of its original capacitance was recorded. More significantly, it was worth noting that an outstanding coulombic efficiency of 97.82% was achieved, manifesting the remarkable reversibility and long-term durability of Na^+ and MoS_2-incorporated Ni-MOF electrode active materials. Furthermore, it could be observed that the supercapacitive performance gradually increased from 212.76 to 265.86 F g^{-1} after 800 cycles (**Fig. 6.16a,** inset), which could be caused by the gradual activation of more electroactive sites during the repetitive penetration of electrolyte ions [367, 368].

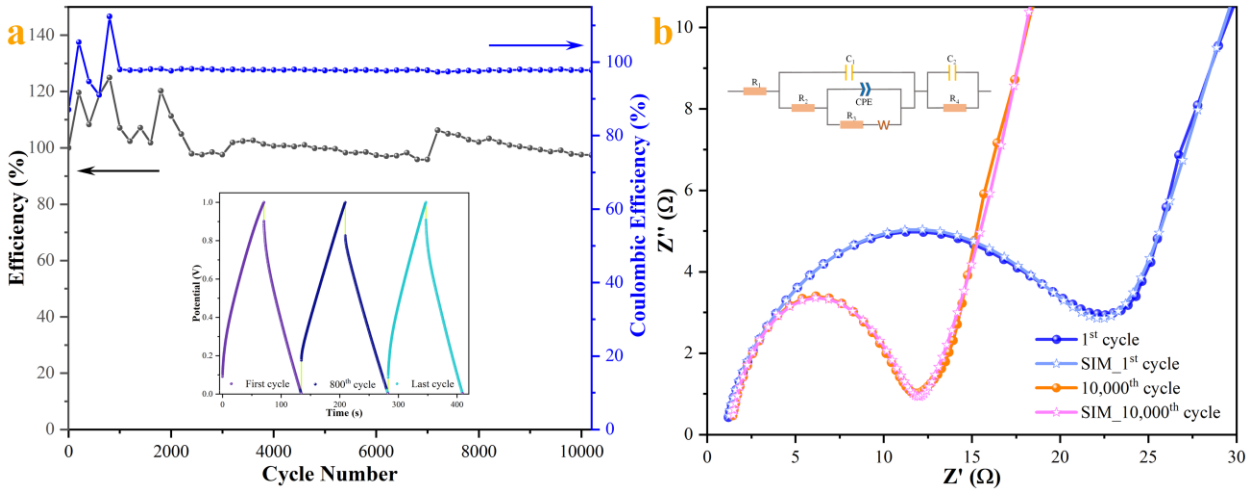


Figure 6.16. (a) Cycling stability and (b) Nyquist plots before and after performing cyclic stability study with equivalent circuit and fitting (inset) of MNM_1 in 2M Na_2SO_4 electrolyte.

Besides, the electrochemical impedance of MNM_1 before and after performing cyclic stability test was measured as well. The Nyquist plots with electrochemical circuit fitting were illustrated in **Fig. 6.16b**. A slight increase in R_s was detected, which shifted from 0.30 to 1.19 Ω. The marginal increase in R_s could be assigned to the partial detaching of electrode active materials from current collector after a long-term and repetitive intercalation and de-intercalation of Na^+ [369]. In contrast, the reduction of R_{ct} from 22.77 to 10.18 Ω could be mainly due to the activation of electroactive sites, in which more charge transfer channels were provided. In addition, the slight increase in Warburg angle at low-frequency region after 10,200 cycles annotated the enhancement in capacitive performance (**Table 6.2**), which further confirmed the activation of electrode active materials [370].

Additionally, the as-obtained EIS data was also used to calculate the relaxation time constant (τ, **Eq. (13)**), which is an important parameter to determine the fast-charging function of SC devices [371]. In general, a low time constant is favorable for SC devices to achieve quick response and fast energy storage.

The plot of resistance versus frequency was shown in **Fig. 6.13d** and the calculated τ values for Ni-MOF-based nanocomposites were less than 0.5 ms, as summarized in **Table 6.2**, elucidating the quick response of the SC devices and the fast mobility of electrolyte ions [372]. Meanwhile, it could be observed that MNM_1 possessed a time constant of 0.448 ms, which was slightly higher than other samples. The result suggested that a longer duration was required for the movements of electrolyte ions and charges, which could be caused by the cross-linked networks which prolonged the diffusion distance of electrolyte ions. Furthermore, the time constant was reduced after performing cyclability for MNM_1 sample, in which the value of τ decreased from 0.448 ms to 0.062 ms, which suggested this device could be charged faster after cycling.

6.2.3 Sodium Storage Mechanism

To evaluate the sodium storage mechanism for the as-synthesized samples, the CV profiles of MNM_1 were further studied in-depth due to its best performance among other samples. **Fig. 6.17**

demonstrates the relationship between current densities and scanning rates. In general, the corresponding current density should be linearly dependent on the applied scan rate if the charge storage was dominant by nondiffusion-controlled behavior, in which charges were stored through physical adsorption and desorption on the electrode surface (capacitive feature) [373]. In contrast, the dominance of charge storage was associated with diffusion-limited process if the current response shown a linear relationship with square root of applied scan rate [374]. **Fig. 6.17a** and **b** depict the relationship plots of current densities versus scan rates (I vs. v) and square root of scan rates (I vs. $v^{1/2}$), respectively. According to the resultant plots, the coefficient of determination of I vs. $v^{1/2}$ (>0.99) was much higher than that of I vs. v (~0.95), which could be interpreted that the storage of Na^+ ions was mainly restricted by diffusion-limited process.

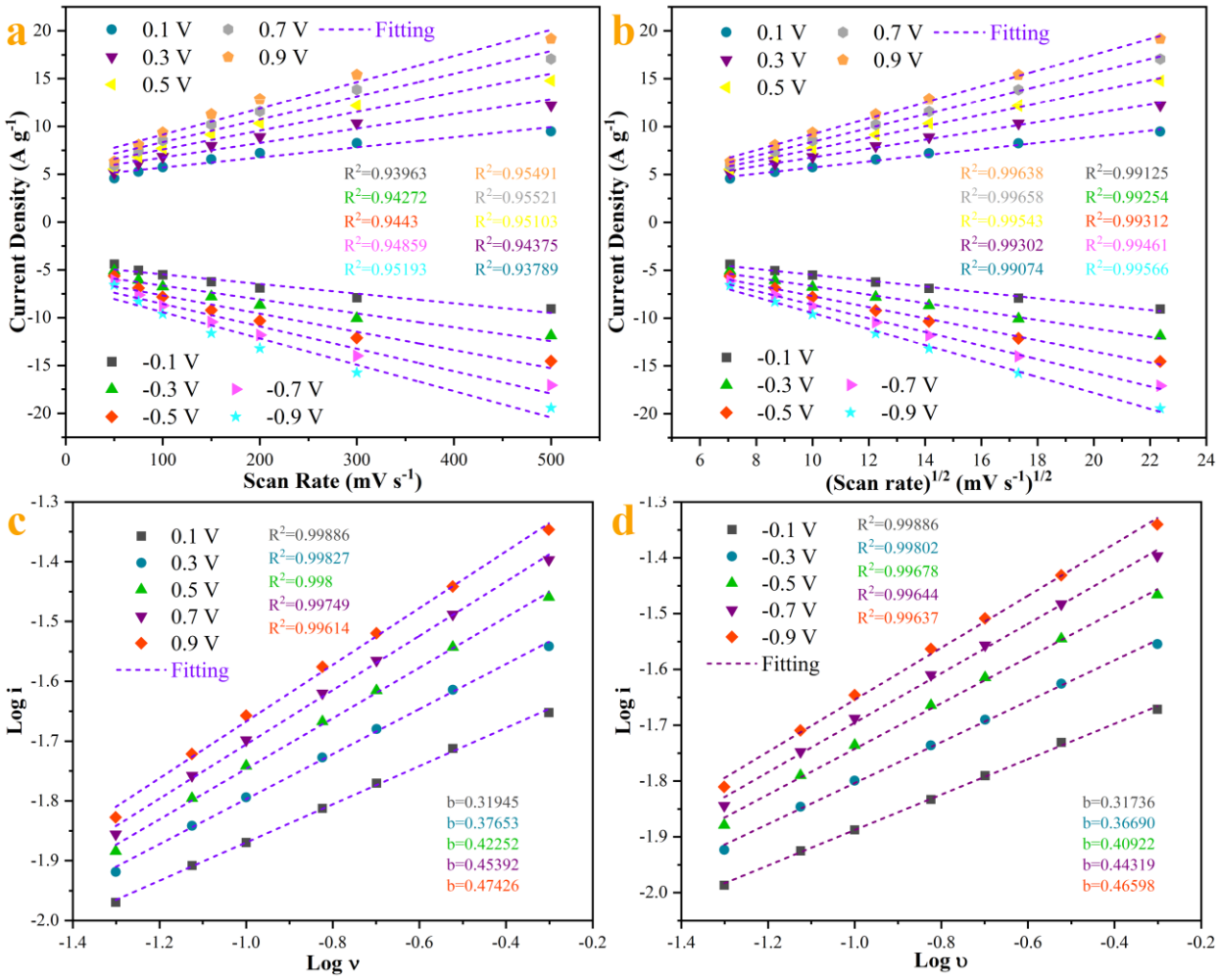


Figure 6.17. The plot of current densities versus (a) scanning rates and (b) square root of scanning rates. The linear relationship between log(i) and log(*v*) at (c) positive and (d) negative potentials, respectively.

Moreover, Dunn's power-law method [351, 375] was adopted to further confirm the sodium storage kinetics. In this relationship, the corresponding current (i) of a SC electrode and scan rates (*v*) should follow **Eq. (11)**.

In the equation, a and b are two constants, and b is a critical indicator for evaluating the charge storage behavior. Usually, the storage of sodium cations was surface-limited process if the value of b approaches 1.0. While charge storage is dominated by diffusion-limited process if b approaches 0.5. To find the value b, the plots of logarithm of current (log i) versus the logarithm of scan rate (log *v*) at various potentials are shown in **Fig. 6.17c** and **d**. Clearly, the values of b were found to be approximately 0.5, manifesting the storage of Na^+ was controlled by diffusion-limited Faradic behavior.

Furthermore, the current response at a particular potential and scanning rate could be further divided into surface- (i_s) and diffusion-limited currents (i_d) as given below:

$$i_s = k_1 v \tag{16}$$

$$i_d = k_2 v^{1/2} \tag{17}$$

Here, k_1 and k_2 are two constant coefficients. Hence, the total current (i_t) response could be rewritten as **Eq. (12)**.

Consequently, the percentage of capacitance contribution could be quantified by determining both values of k_1 and k_2. An example of differentiated CV profile of MNM_1 was demonstrated in **Fig. 6.18a**, and the proportion of surface charge contribution (EDLC, brown region) was calculated at 50 mV s^{-1}, and it was apparent that 19.14% of the overall capacitance was contributed by rapid physical adsorption and desorption. The calculated CV area lied beyond the original CV profile, originating from the polarization of electrode [267]. Moreover, the percentage contribution at different scanning rates was demonstrated in **Fig. 6.18** as well. The capacitance contribution from EDLC was increased up to 94.27% at a high sweeping rate of 500 mV s^{-1}. This could be explained as follows: at a low scan rate, the sodium storage was limited by diffusion-limited process owing to slow electrolyte ion migration, and the overall sodium storage behavior was dominated by pseudocapacitance due to the intercalation and deintercalation of Na^+ into bulk electrode materials. When the scanning rate was increased, a gradual transition from diffusion-limited process to nondiffusion-limited process could occur because of the limited time given, electrolyte ions didn't have sufficient time to completely access all the active sites (**Fig. 6.18b)** [376], resulting in a reduction of effective interactions between electrolyte and electrode active materials. Hence, the storage of sodium cations was mainly attributed to the rapid adsorption and desorption capability to electrolyte ions at high scan rates, which was also favorable for providing high-rate performance.

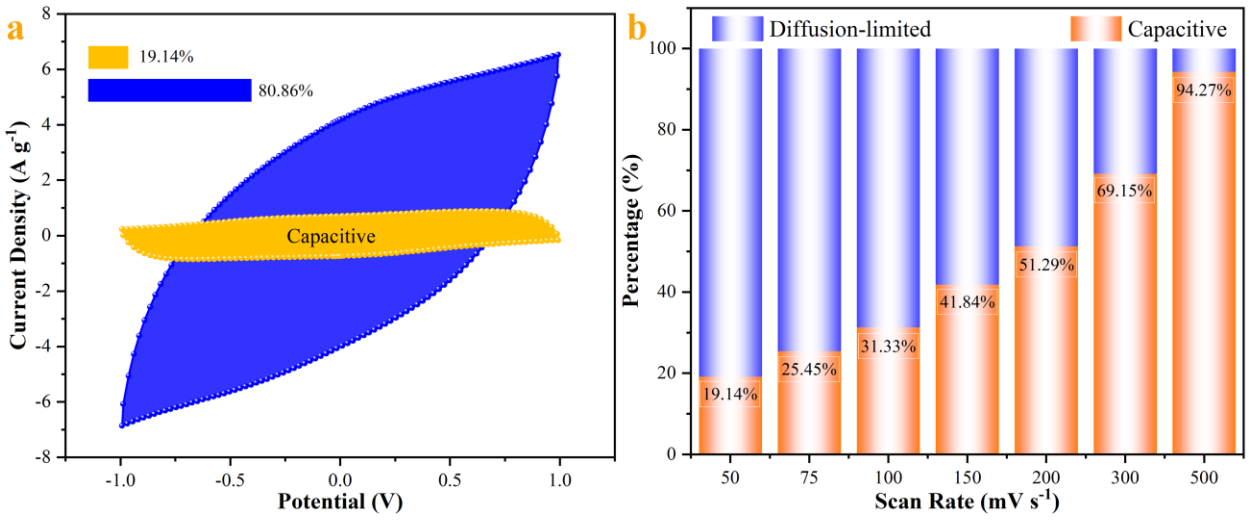


Figure 6.18. (a) Capacitance contribution at 50 mV s^{-1} and (b) the proportion contribution of capacitive and diffusion-limited capacitances at various scan rates for MNM_1.

6.3 Summary

In summary, hierarchical Na^+ and MoS_2-incorporated Ni-MOFs were successfully synthesized via a simple and low-cost hydrothermal approach. Benefiting from the hierarchical porous structures, the as-synthesized Na^+ and MoS_2 incorporated Ni-MOF nanocomposite exhibited excellent electrochemical performance. In particular, the hierarchical porous structure formed by nanoplatelets offered a large surface area for electrolyte ion storage. The highly porous structure could facilitate the charge transfer during electrochemical measurement. Moreover, the optimum MoS_2-incorporated Ni-MOF nanostructure exhibited a maximum energy density of 33.33 Wh kg^{-1} at 483 W kg^{-1}, and the retained energy density was 6.4 Wh kg^{-1} at a high-power density of 3390 W kg^{-1}. In addition, an outstanding capacitance of 97.42% was recorded after more than 10,000 GCD cycles, and the acquired remarkable coulombic efficiency was as high as 97.82% in an aqueous-based neutral electrolyte. Hence, this work indicates the potential of application of Ni-MOF-based nanocomposites as high-performance supercapacitor in an aqueous neutral electrolyte, which is environmental-friendly, relatively inexpensive and thermally stable.

Chapter 7: Fabrication of Sodium and MoS_2 Incorporated NiO and Carbon Nanostructures for Advanced Supercapacitor Application

7.1 Introduction

The applications of MOFs in SCs are generally categorized into three main areas: (a) Pristine MOF nanomaterials directly serving as electrode active materials. (b) MOFs employed as precursors for deriving metal oxides and carbons. (c) MOFs incorporated with other nanomaterials to form innovative nanocomposites. Nonetheless, the application of pristine MOFs as SC electrodes suffers from limited energy density due to their inferior intrinsic properties. To enhance the specific capacitance, pseudocapatance-rich materials such as conductive polymers, transition chalcogenides and metal oxides facilitating surface Faradaic redox reaction have been rapidly emerging as potential electrode active materials for supercapacitors [377]. Meanwhile, it is significant to design and synthesize heterostructures composed of various nanostructured materials with unexpected physical and chemical properties for high-performance supercapacitors.

To maximize the specific capacitance and energy density, it is crucial to develop transition metal oxide-based nanocomposites due to their tempting theoretical capacitance and electrochemical activities. Nonetheless, metal oxides normally suffer from inferior electronic conductivity and unpredictable volume expansion, leading to relatively poor coulombic efficiency. This issue could be efficiently tackled through the introduction of carbonaceous and conductive agents. Hence, carbon nanostructures derived from highly porous MOF and Na were incorporated, in which the highly conductive and porous structure could not only able to promote the electronic conductivity, but also provide abundant space to tolerate the volume change and enhance the accessibility of electroactive sites. Besides, the introduction of MoS_2, a representative of transition metal dichalcogenide with a unique 2D layered architecture and excellent electronic conductivity, was expected to offer a unique morphology which simultaneously exhibits superior electrochemical properties. In this study, nickel-based MOF-derived transition metal oxide and carbon (NiO/C) incorporated with sodium and MoS_2 (Na-doped MoS_2@NiO/C) hierarchical porous structures were successfully prepared via a facial hydrothermal route. The morphology, thermal stability, crystalline structure and element composition of the as-synthesized nanocomposites were characterized by using FESEM, TGA, XRD and XPS, respectively. The obtained specific capacitance of MOF-derived NiO/C yolk-shell structure was 1779.50 F g^{-1} in 2M KOH, and the electrochemical capacitance was further facilitated by incorporating sodium ions and MoS_2, which ultimately could reach 2540.63 F g^{-1}. Meanwhile, it was worth noting that the delivered optimum energy density for the fabricated symmetrical device was 36.93 Wh kg^{-1} at 477 W kg^{-1}. Besides, a remarkable cycling durability of 111.92% and coulombic efficiency of 97.6% were retained over 4,000 cycles. These results evidently revealed the sodium-doped MoS_2@NiO/C hierarchical porous nanocomposites can be employed as promising electrode active materials for future energy storage/conversion technologies.

7.1.1 Synthesis of Ni-MOF-derived NiO/C

Nickel-based MOFs were synthesized via a solvothermal approach as reported [241], and the overall synthesis was schematically illustrated in **Fig. 7.1**. Typically, 0.030 gram of H_2BDC and 0.314 gram of $Ni(NO_3)_2 \cdot 6H_2O$ were weighed and dissolved in a solvent mixture containing DMF and EG at a volume ratio of 8 : 5. The mixture was then stirred for approximately one hour, and the homogeneous green solution was transferred into a stainless-steel autoclave (capacity of 50 mL). Subsequently, the reactor was maintained at 160 ℃ for 12 h. The green precipitates were then centrifuged and rinsed with ethanol and DMF three times until it cooled down. A light-green product was obtained after drying at 60 ℃ in a vacuum oven overnight. Lastly, the resultant powder was put in a high alumina combustion boat and calcined in air at 400 ℃ for 4 h at a ramping rate of 5 ℃ min^{-1}. The as-obtained NiO/C was labelled as MNC_0.

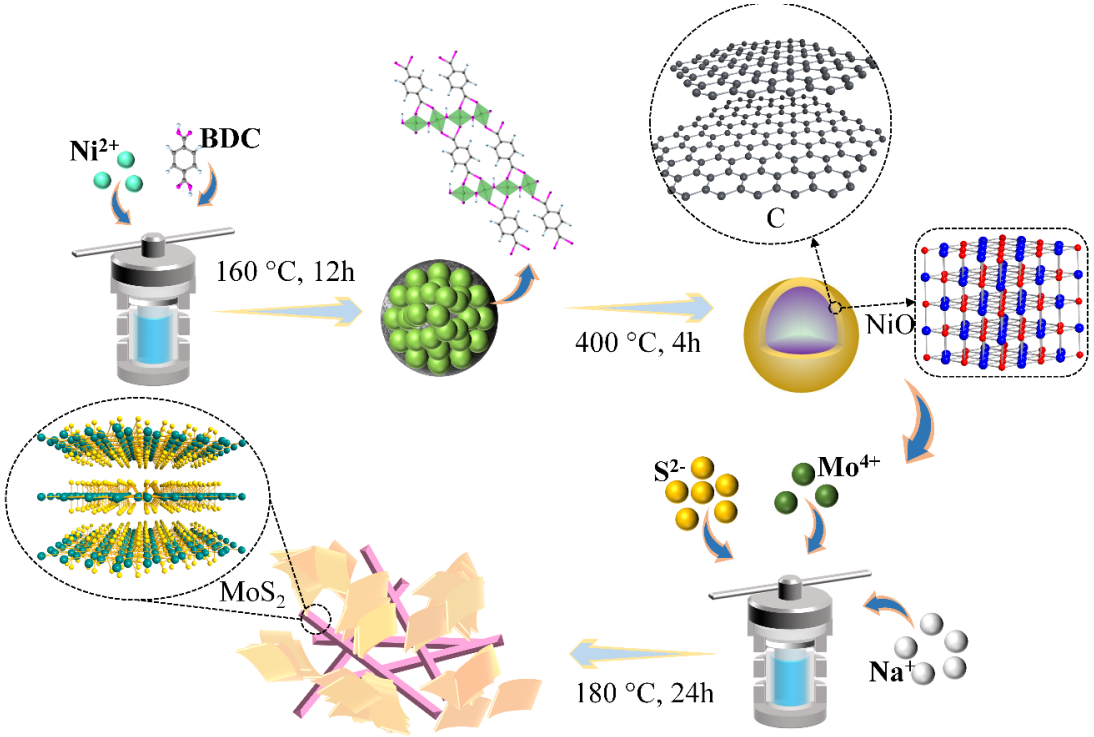


Figure 7.1. A schematic illustration for the synthesis of Na-doped MoS_2@NiO/C nanocomposites.

7.1.2 Synthesis of Na-doped MoS_2@NiO/C

The Na-doped MoS_2@NiO/C nanocomposites were synthesized through a one-pot hydrothermal route. Typically,150 mg of as-synthesized NiO/C was firstly dissolved into deionized water (30 mL) under magnetic stirring for 30 min. Subsequently, 2 mmol sodium molybdate and 4 mmol thiourea (Mo : S = 1 : 2) were added into as-prepared NiO/C solution, under magnetic stirring for another 60 min. Then, the homogeneous deep dark solution was transferred into a Teflon-lined stainless-steel autoclave (capacity of 50 mL), and it was heated at 180 °C for 24 h. After the mixture was cooled down to room temperature, it was then washed with excessive deionized water

several times. The resultant nanocomposites were obtained after drying at 80 °C for 24 h. The as-synthesized sample was denoted as MNC_1. Similarly, other samples were developed through the same method by varying molar ratio of Mo^{4+} to Ni^{2+} from 2 : 1 and 3 : 1. These products were named as MNC_2 and MNC_3, respectively. The schematic diagram of the synthesis procedure is depicted in **Fig. 7.1**.

7.2 Results and Discussion

7.2.1 Material Characterizations

The crystal structures of the as-synthesized nanocomposites were characterized by XRD. **Fig. 7.2a** illustrates the XRD spectra of NiO/C derived from Ni-MOFs. The diffraction peaks observed at 37.45, 43.39, 63.03, 75.59 and 79.51° could be attributed to the (111), (200), (220), (311) and (222) lattice planes of NiO [378, 379]. These reflections were in good agreement with the standard XRD patterns of NiO crystal structure in JCPDS card (47-1049). Meanwhile, three peaks were also detected at 44.61, 52.05 and 76.57°, corresponding to the planes of (111), (200) and (220) due to the diffraction of Ni (JCPDS card 75-1097). The existence of Ni might be ascribed to partial oxidation of Ni at a low calcination temperature (400 °C) [380]. Additionally, no obvious diffraction peaks of carbon were viewed, indicating the amorphous nature of MOF-derived carbon. Hence, these results evidently confirmed the successful synthesis of MOF-derived NiO/C nanocomposites. Besides, Na-doped MoS_2@NiO/C nanocomposites exhibited analogous peaks of NiO/C nanomaterials (**Fig. 7.2b**), and the rest of the peaks at 2θ = 14.75, 32.19, 39.65, 49.25 and 72.27° corresponded to (002), (010), (013), (015) and (023) planes of MoS_2, respectively (JCPDS card 37-1492) [381]. In addition, some small diffraction peaks were detected as well, suggesting minor impurities were possibly formed during the hydrothermal process.

FT-IR was studied to confirm the chemical compounds, as illustrated in **Fig. 7.2c**. The bending vibration of Ni-O-H was detected in the range of 663 - 701 cm^{-1} for pristine MOF-derived NiO/C and Na-doped MoS_2@NiO/C nanocomposites [379]. The stretching vibration of Ni-O was observed between 412 and 416 cm^{-1}. Meanwhile, the absorption peaks at 1662 and 2356 cm^{-1} were ascribed to the O-H bending vibrations. The absorption peaks were observed approximately between 3373 and 3660 cm^{-1}, which was also attributed to the vibrations of O-H [378]. The appearance of O-H stretching vibrations was detected owing to the physically adsorbed water molecules on the surface of NiO/C nanoparticles [378, 382]. The peaks at 2827 – 2881 cm^{-1} and 2920 – 2994 cm^{-1} originated from the symmetric and asymmetric vibrations of C-H bonds respectively, suggesting the existence of Ni-MOFs residues due to the incomplete transformation. Besides, a band appeared at 472 and 921 cm^{-1} was indicative of the stretching vibrations of the S-S bond [383]. A sharp peak at 1407 cm^{-1} could be assigned to the vibration of S-Mo-S [384], and the vibration of S-O was observed at 1113 cm^{-1} [348]. In addition, the existence of multiple bands in the range from 695 to 1200 cm^{-1} could be related to the vibration of sulfur groups [385]. The FTIR result was in good agreement with XRD, indicating the successful synthesis of Na-doped MoS_2@NiO/C nanocomposites.

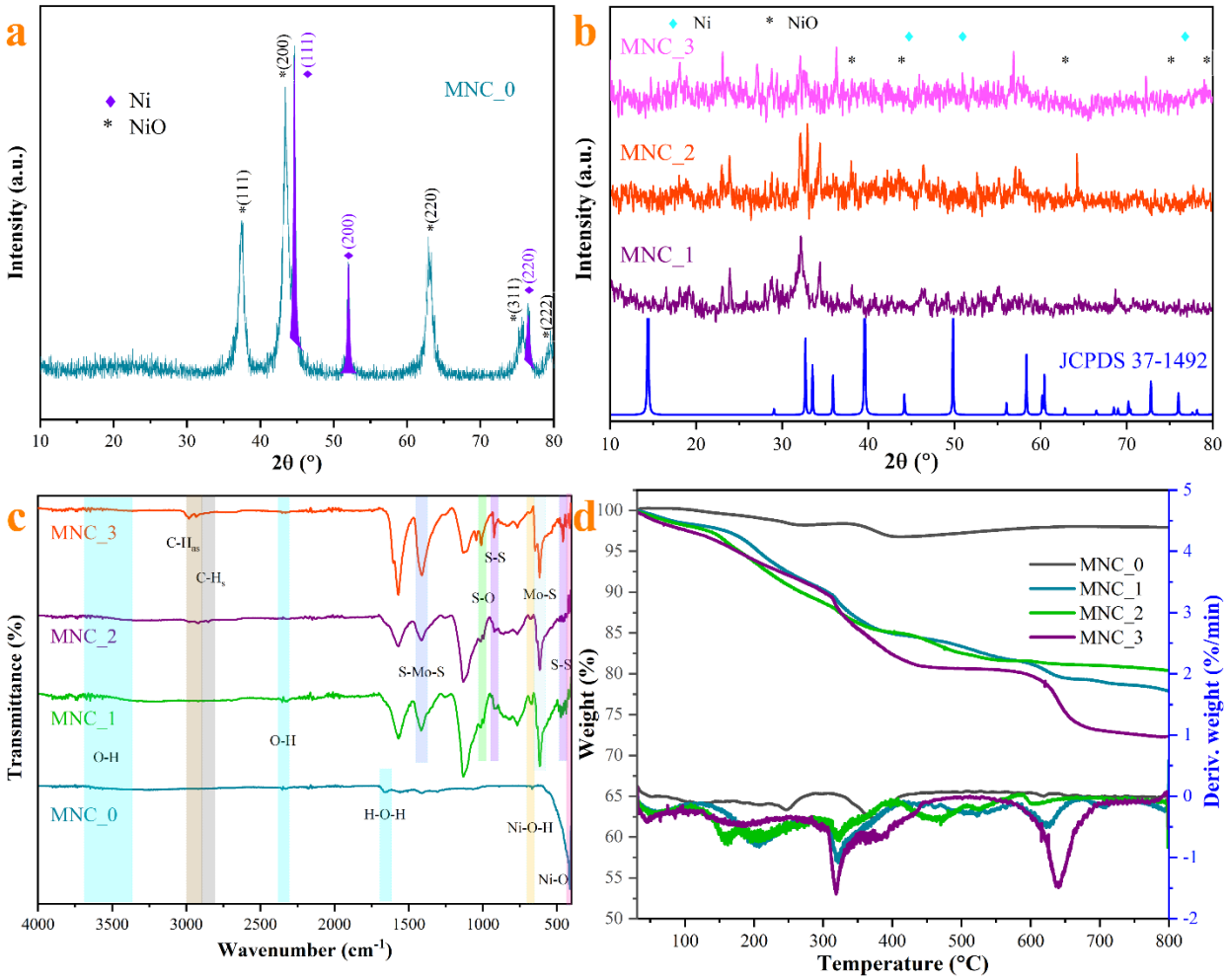


Figure 7.2. XRD patterns of (a) NiO/C nanocomposites derived from Ni-MOFs, (b) Na-doped MoS_2@NiO/C nanocomposites prepared at different molar ratio of Ni^{2+} to Mo^{4+}. FT-IR (c) and TG/DTG (d) curves of the as-synthesized Na-doped MoS_2@NiO/C nanocomposites.

Fig. 7.2d displays the TG/DTG profiles of the as-synthesized nanocomposites. Clearly, negligible amount of weight loss was observed in NiO/C, indicating the outstanding thermal stability of MOF-derived porous structures. Two slightly obvious weight variations were observed at 245 and 370 °C, respectively, which could be the oxidation of carbon [386]. However, it was noted that there were three-stage weight loss for MoS_2 incorporated NiO/C nanocomposites. Firstly, the marginal decrease in weight below 100 °C could be assigned to the removal of physically adsorbed moisture. Subsequently, a significant descending trend was observed due to the removal of carbon and sulfur compounds. Lastly, a decline in weight from 550 to 700 °C could be caused by the degradation and decomposition of MoS_2 [387].

To further confirm the existence of Ni in MOF-derived NiO/C nanocomposites, the thermal gravimetric measurement of sample NiO/C was also carried out at an air flow of 10 mL min^{-1} (**Fig. 7.3**). The weight changes were observed within the range of 230 – 410 °C, which could be assigned

to the oxidation of amorphous carbon since NiO remained stable over this temperature range. The slight increase in weight after 535 °C evidently revealed the oxidation of Ni, and the final weight reached 102.02% at 800 °C.

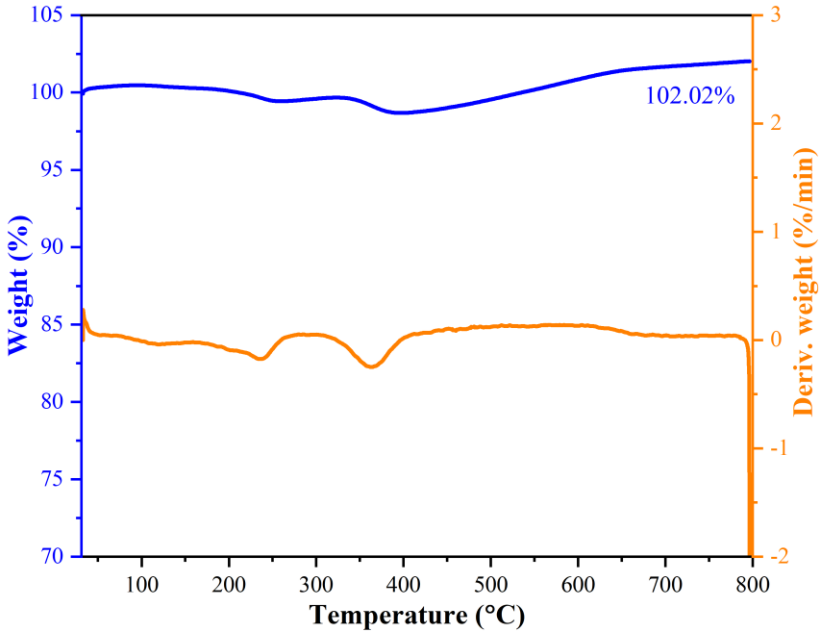


Figure 7.3. TG/DTG curves of MOF-derived NiO/C yolk-shell structures under air flow.

The morphology and structure of the as-synthesized nanostructures were studied by using FESEM and TEM, respectively (**Fig. 7.4** and **7.5**). Ni-MOF-derived NiO/C exhibited a yolk-shell structure with rough surface (**Fig. 7.4a**). The average size of the yolk-shell microsphere was approximately 7 µm, and the agglomeration of these microspheres was caused by the van der Waals interactions. Meanwhile, a broken structure was observed in **Fig. 7.4c**, revealing the three-dimensional MOF-derived NiO/C yolk-shell structures. Interestingly, nanobars with hollow porous structures and nanoparticles appeared when Na and MoS_2 were incorporated (**Fig. 7.4**), and the well agglomerated NiO/C yolk-shell structures disappeared. This could be attributed to redistribution of NiO/C microspheres during high-temperature hydrothermal treatment, and such distribution could result in more exposed active sites for electrochemical reactions as well. The distribution of these nanoparticles was further enhanced when the molar ratio of Ni^{2+} to Mo^{4+} was set at 1 : 2, as shown in **Fig. 7.5(a-c)**. As confirmed by nitrogen physisorption measurement (**Fig. 7.6**), the calculated Langmuir surface area of MNC_2 was approximately 17.24 $m^2\ g^{-1}$, and a large pore volume of 0.036 $m^3\ g^{-1}$ was obtained. The formation of hierarchical porous structures provided large space for the storage of electrolyte ions during charge storage process. Nonetheless, the hierarchical porous structures completely disappeared due to the perfusion of sulfur when the ratio of Ni^{2+} to Mo^{4+} was further increased to 1 : 3. Hence, it evidently indicated that coating of sulfur molecules could take place as the ratio of S was too high. The shapes of nanoparticles and nanobars were still observed, even though the overall structure was wrapped by S, revealing the overall structure remained intact after the perfusion of S.

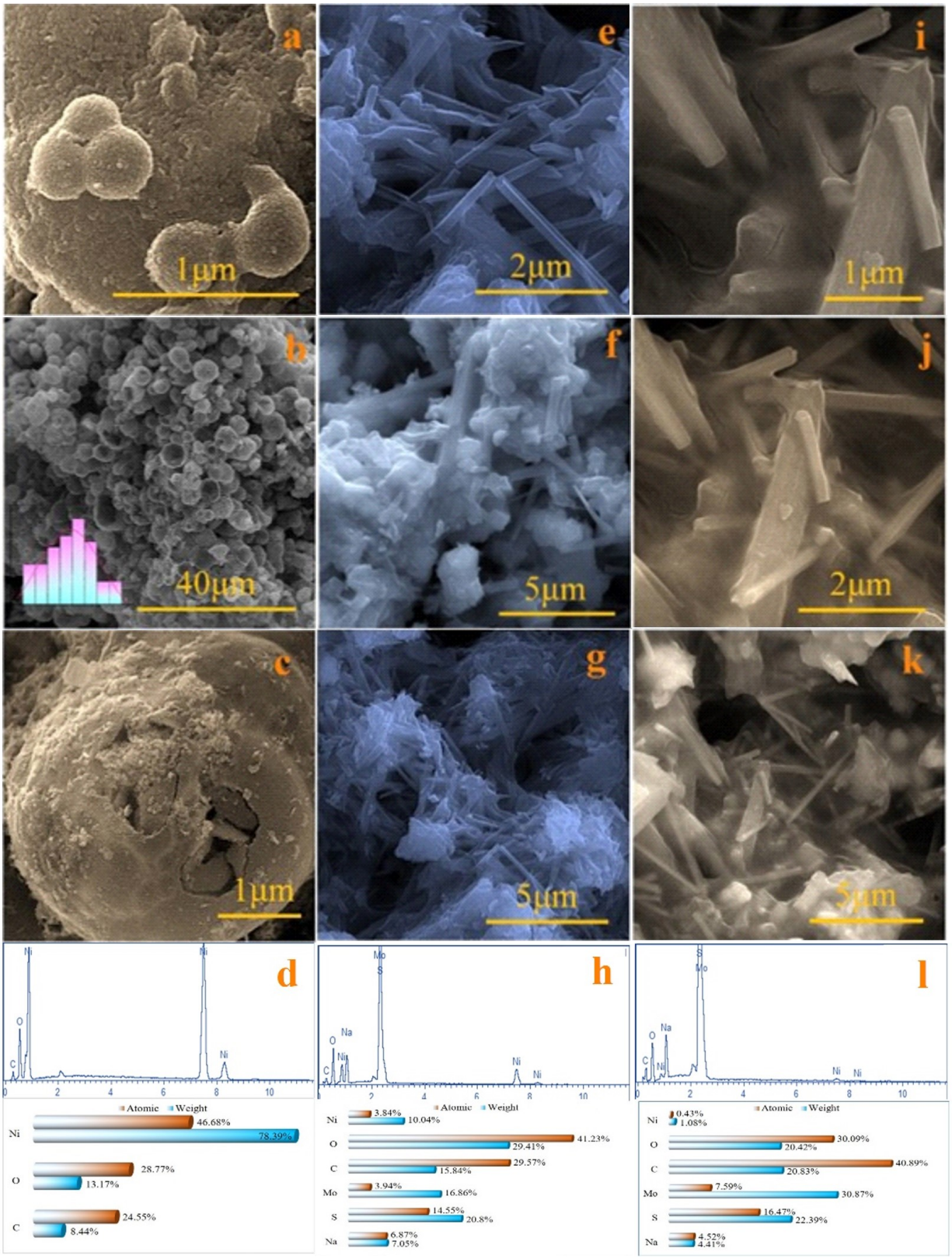


Figure 7.4. FESEM and EDX images of (a-d) NiO/C yolk-shell derived from Ni-MOFs (MNC_0), (e-h) MNC_1 and (i-l) MNC_3.

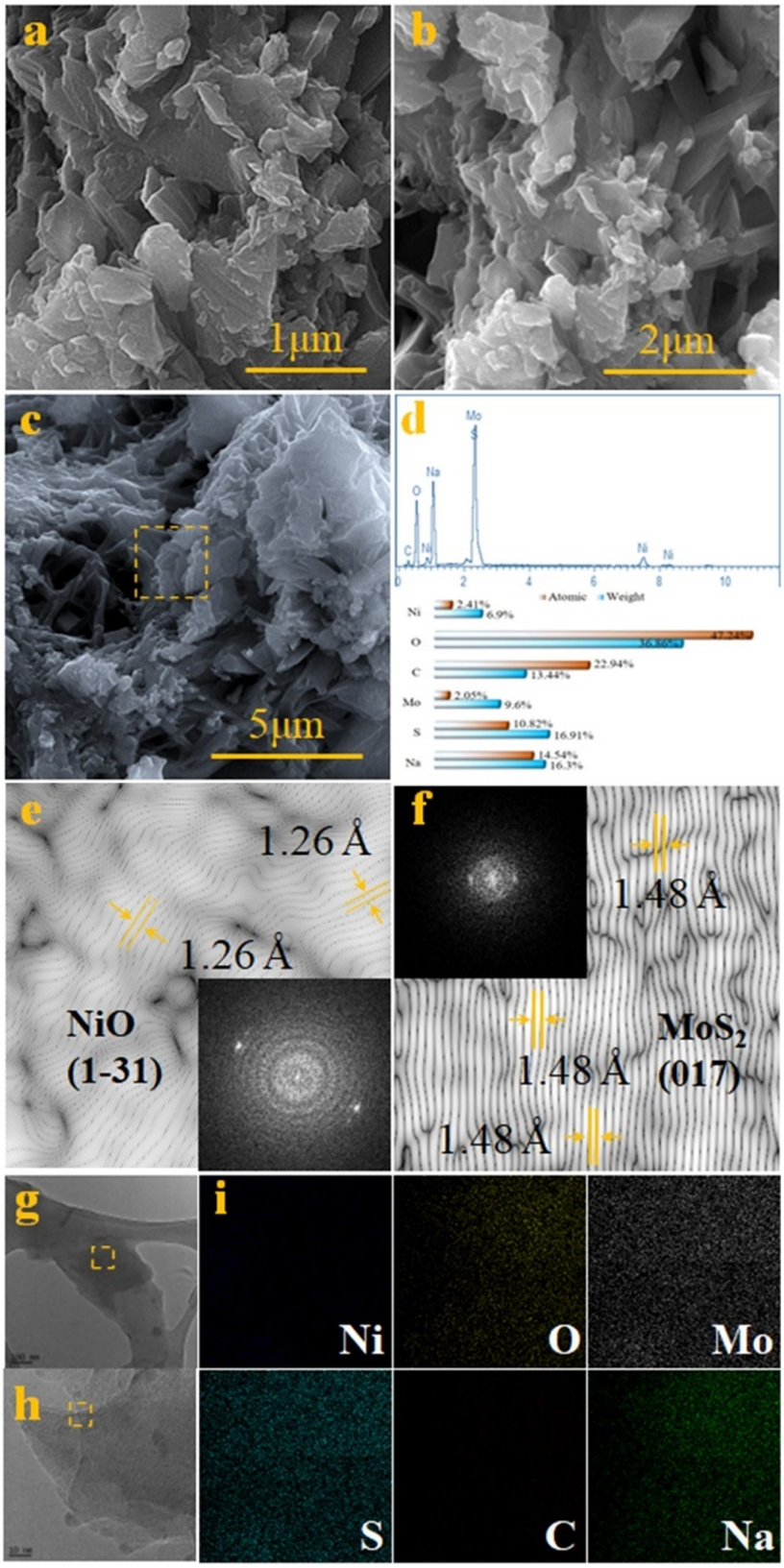


Figure 7.5. FESEM and EDX images (a-d), (e, f) lattice fringes and FFT results (inset), (g, h) TEM images and (i) corresponding elemental mapping of MNC_2 nanocomposites.

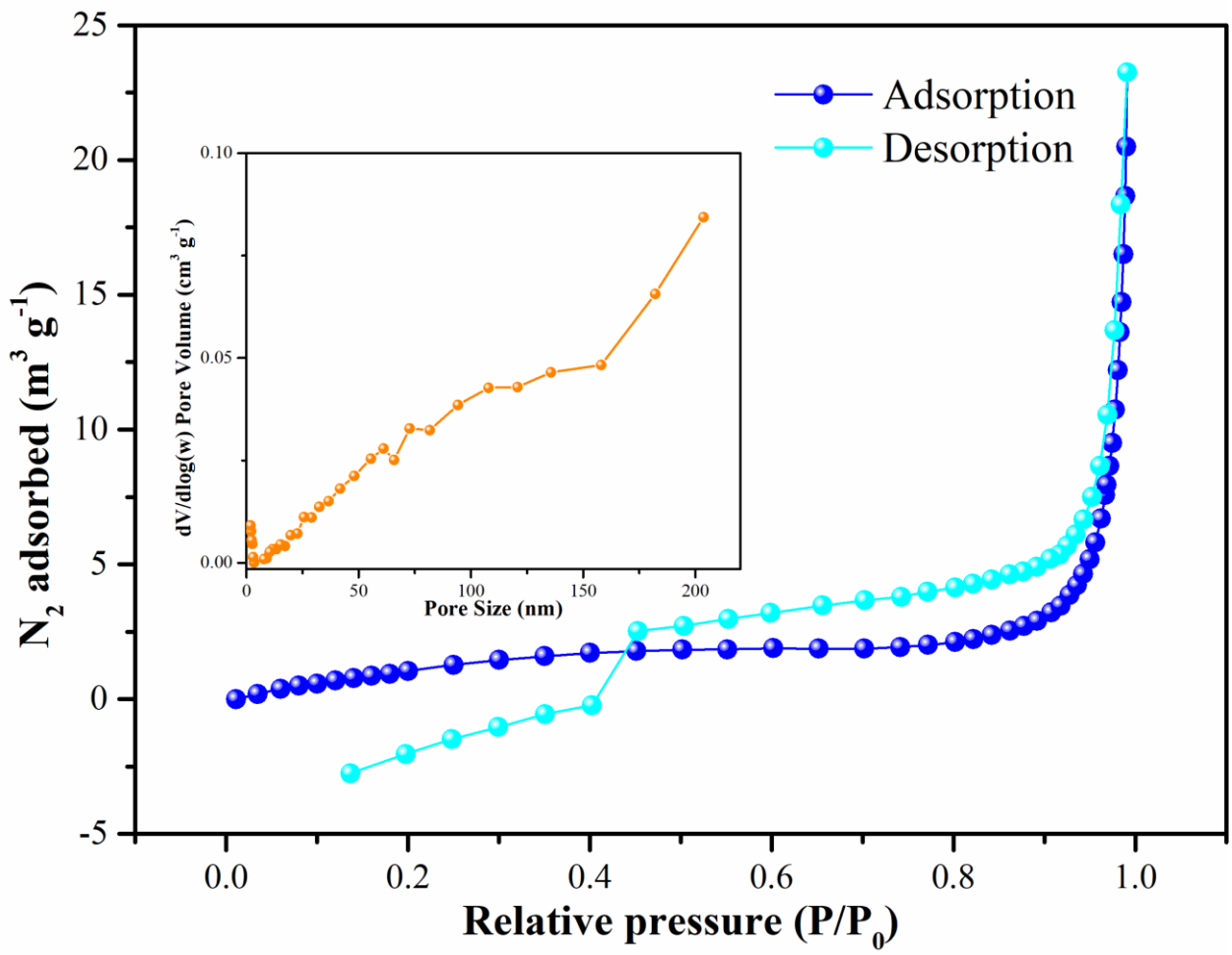


Figure 7.6. N_2 adsorption and desorption isotherms and pore size distributions (inset) of MNC_2.

TEM was utilized to further characterize the MOF-derived NiO/C-based nanostructures. **Fig. 7.5g** and **h** depict the low-resolution TEM micrograph of MNC_2, which evidently revealed the nanoflakes on the nanobars structures. Meanwhile, the existence of nanoparticles was also observed, which could be ascribed to the redistribution of NiO/C nanoparticles. To further study the lattice compression, fast Fourier transform (FFT) analysis was conducted, and the selected areas were indicated in **Fig. 7.5g** and **h**, respectively. The corresponding results were demonstrated in **Fig. 7.5e** and **f**. The nonuniform distributions of the lattice fringes annotated the polycrystalline nature of the nanocomposites. The amorphous structure was also detected around the edges. Additionally, the obvious lattice spacings were 1.26 and 1.48 Å, corresponding to the planes of (1-31) of NiO and (017) of MoS_2, respectively. These results revealed that MoS_2 was successfully incorporated into NiO/C nanocomposites.

Besides, the EDX and elemental mapping were also performed on the nanocomposites. As shown in **Fig. 7.4, 7.5** and **7.7**, these figures clearly indicated the appearance of Ni, O and C for MOF-derived NiO/C yolk-shell nanomaterials. Moreover, the existence of S and Mo in MoS_2@NiO/C

nanocomposites annotated the successful incorporation of MoS_2. Lastly, the appearance of Na in MNC_1, MNC_2 and MNC_3 samples revealed the successful doping of Na ions onto the nanocomposite material.

The XPS technique was carried out to further study the elemental composition and valence states of the as-synthesized nanocomposites. The appearance of C, Na, O, Mo and S was observed in the wide-scanning spectrum (**Fig. 7.8**), revealing the successful integration of Na and MoS_2 on MOF-derived NiO/C. The typical high-resolution XPS spectrum of Ni 2p was illustrated in **Fig. 7.8b**, it shows that the binding energies of Ni 2p displayed symbolic peaks at 859.06 and 876.36 eV, corresponding to Ni 2p3 and Ni 2p1 of NiO, respectively. The satellite peaks, originating from the electron transfer from ligands to nickel during irradiation, were detected at 879.43 and 881.76 eV (Ni 2p1), 861.68 and 864.48 eV (Ni 2p3) [350]. Meanwhile, the peaks at binding energies of 853.23 and 870.53 eV were ascribed to the Ni 2p3 and Ni 2p1 of Ni, respectively. The peaks resulting from $Ni(OH)_2$ were observed at 856.15 and 873.45 eV, which could be formed during the hydrothermal process. Additionally, the lattice oxygen of NiO and the adsorbed hydroxyl group on the surface of nanocomposites were observed at peaks 530.18 eV and 532.07 eV, respectively in **Fig. 7.8c** [388]. The existence of Mo 3d/S 2s and S 2p regions confirmed the successful synthesis of MoS_2 nanostructures [344]. The typical peaks of S 2p at 161.25 and 162.41 eV, Mo 3d at 228.51 and 231.66 eV and S 2s at 226.65 eV belonged to MoS_2. Moreover, the presence of S was detected at 163.50 eV (S 2p3) and165.26 eV (S 2p1), which was consistent with the EDX result. A pair of peaks at 169.01 and 170.27 eV revealed the formation of SO_4^{2-}, which was formed by the oxidation of sulfur throughout the hydrothermal process [389]. Furthermore, as demonstrated in **Fig. 7.8d**, the high-resolution XPS spectrum of Mo 3d demonstrates the existence of Mo(IV)/Mo(VI) in Mo-O, in which the formation of Mo(VI) could be owing to the partial oxidation of Mo(IV).

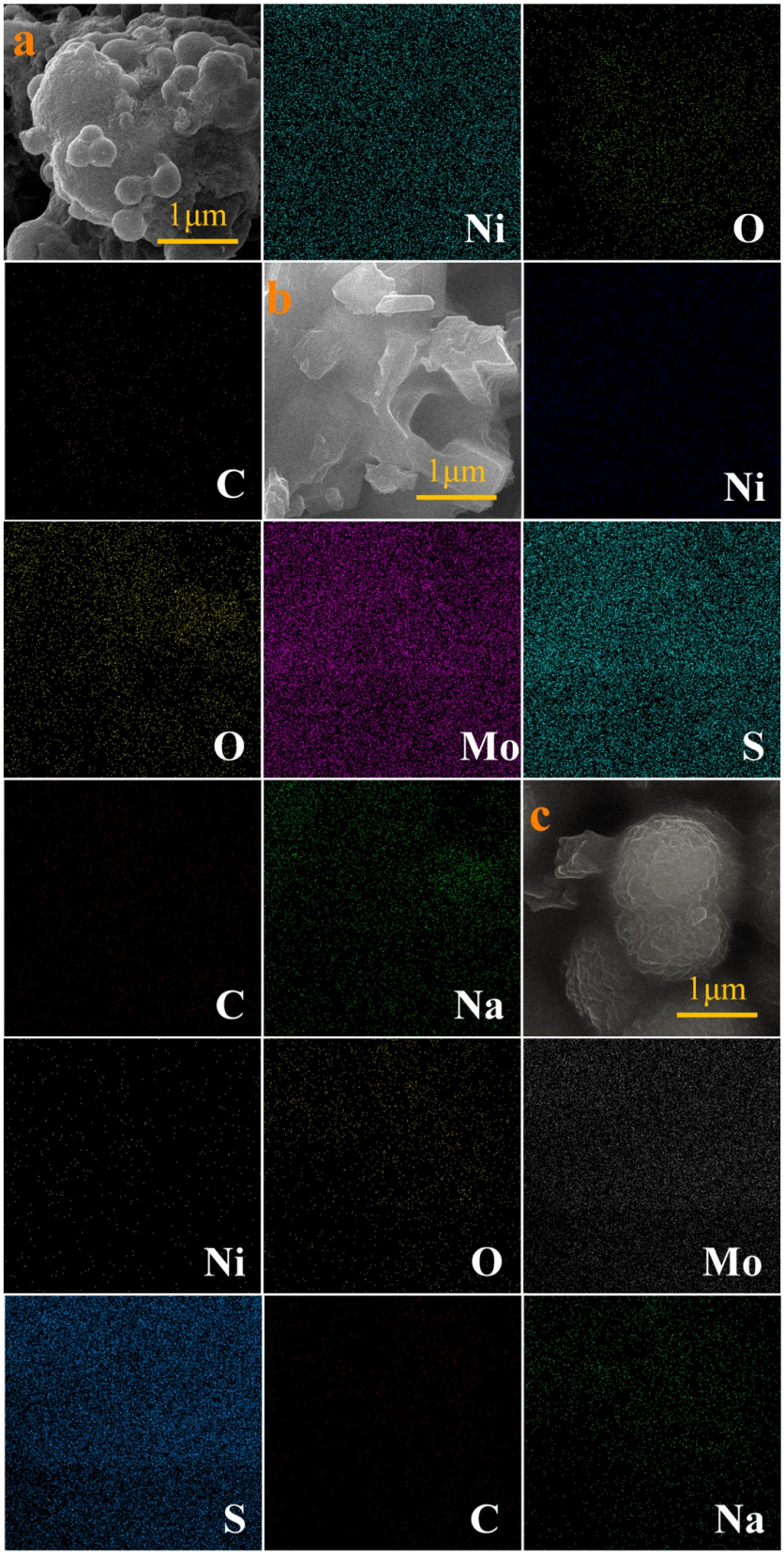


Figure 7.7. Elemental mapping of MNC_0, MNC_1 and MNC_3, respectively.

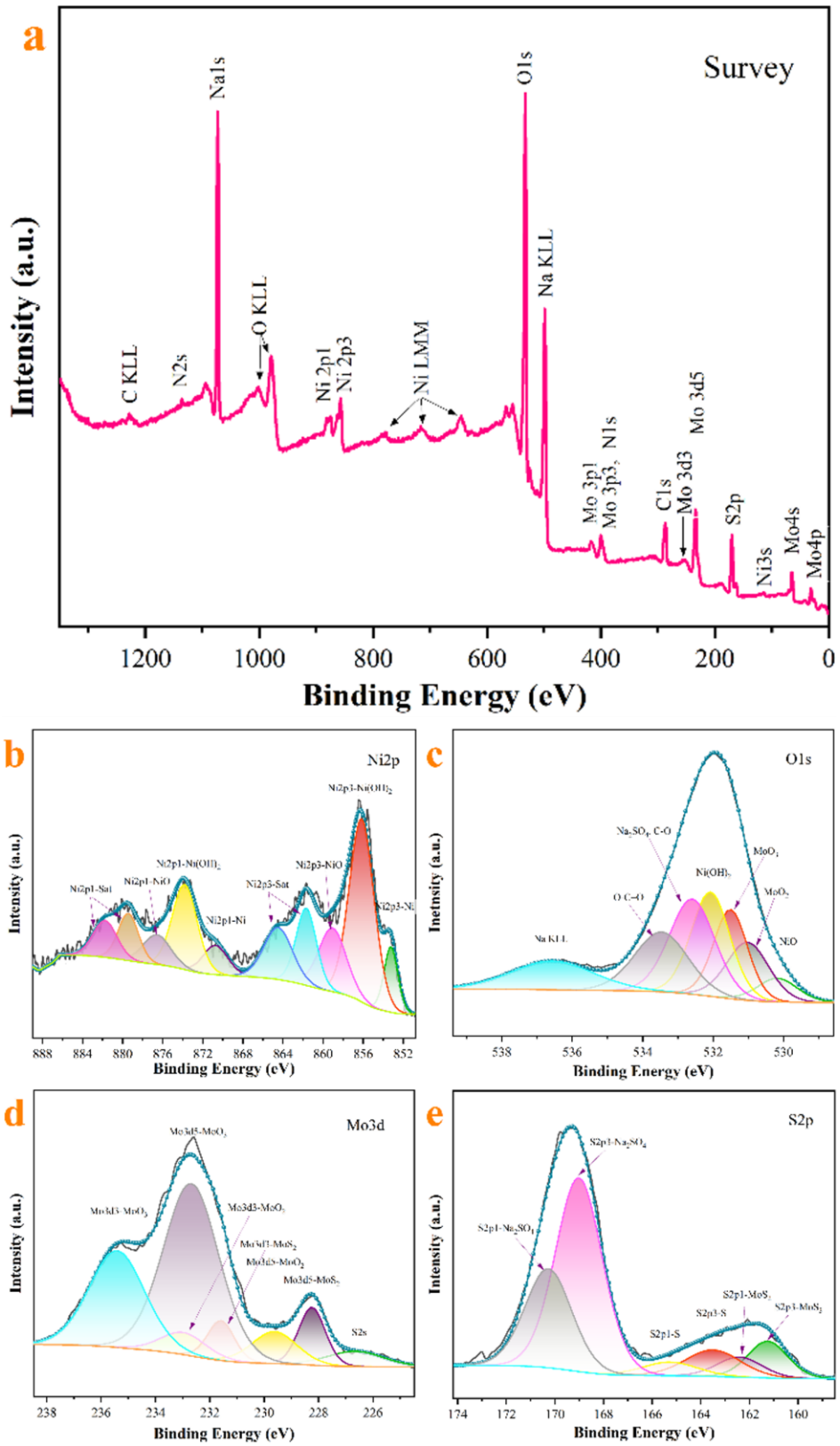


Figure 7.8. XPS spectra of MNC_2: (a) full scanning survey, narrow scan of (b) Ni 2p, (c) O 1s, (d) Mo 3d and (d) S 2p.

7.2.2 Electrochemical Analysis

To evaluate the electrochemical properties of the as-prepared nanocomposites, both CV and GCD were carried out by utilizing a three-electrode system in 2M KOH electrolyte. The average mass load was about 10 mg to access real applications. The CV profiles at different sweeping rates were displayed in **Fig. 7.9a-d**. Clearly, a pair of redox peaks was observed within 0 ~ 0.5 V (vs. Ag/AgCl), resulting from the oxidation of NiO to NiOOH (anodic peaks) and the reduction of NiOOH to NiO (cathodic peaks) [390]. Meanwhile, the interactions between cations (K^+) and MoS_2 could provide extra pseudocapacitance as well [335], as given in **Eq. (15)** and **(18)**:

$$NiO_{(s)} + OH^-_{(aq)} \leftrightarrow NiOOH_{(s)} + e^- \quad (18)$$

A shift of redox peaks, in which anodic peaks shifted to more negative and cathodic peaks shifted to more positive. An increase in current densities were viewed, while the intensity of redox peaks tended to decrease from scanning rate of 2 to 50 mV s^{-1}. The shift of redox peaks could be attributed to the internal resistance (IR) and polarization effect of electrodes and the increasing current densities could be ascribed to the high mobility of K^+ [391]. Insufficient duration given could lead to a reduction of peak intensity. This possibly caused electrolyte ions (K^+ and OH^-) to partially access the active sites [392]. For comparison, the CV diagram of bare nickel foam at a scanning rate of 5 mV s^{-1} was also presented in **Fig. 7.10**, it was evident that negligible amount of capacitance was contributed by nickel foam. This emphasized that the as-synthesized MNC nanocomposites contributed the most to the overall electrochemical capacitance.

Fig. 7.9e-h presents the charge storage behavior of these nanomaterials at different current densities. Evidently, all as-synthesized samples exhibited asymmetric charging and discharging curves, indicating the pseudocapacitance was mainly from Faradaic redox reactions. Meanwhile, a potential drop was also observed in all MOF-derived NiO/C-based nanomaterials, which suggested the existence of slight high internal series resistance due to the low conductivity of NiO [393]. This result was in line with the result from CV measurement. The operating potential window of NiO/C derived from Ni-MOFs could reach 0.45 V (vs. Ag/AgCl), while the potential was reduced to approximately 0.4 V (vs. Ag/AgCl) after the introduction of sodium and MoS_2. The obtained specific capacitances were 1648.72, 2540.63 and 2102.31 F g^{-1} at a current density of 0.5 A g^{-1} for MNC_1, MNC_2 and MNC_3, respectively. Such high electrochemical capacitance was comparable to those studies involving NiO-based supercapacitor electrode active materials, as summarized in **Table 7.1**. Besides, the rate performance was shown in **Fig. 7.10b**, as expected, MNC_3 exhibited a slightly higher rate performance than other MoS_2-incorporated samples due to its smooth surface. Hence, it evidently revealed the high electrochemical performance of Na-doped MoS_2@NiO/C nanocomposites, and a symmetric supercapacitor device was fabricated to gain further insights on its potential for practical application.

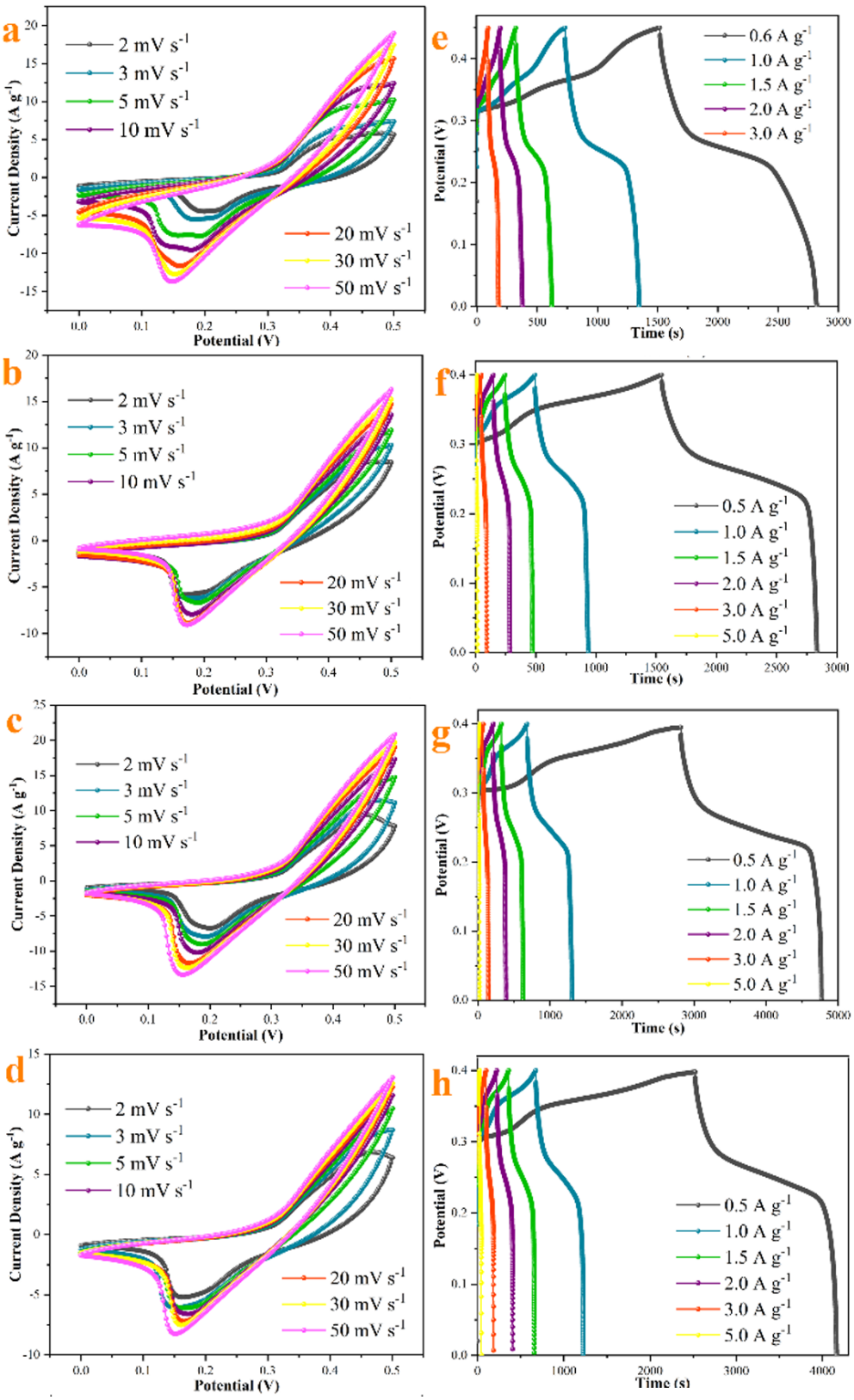


Figure 7.9. Cyclic voltammograms at various scan rates (a-d) and galvanostatic charge/discharge curves (e-f) of Na-doped MoS_2@NiO/C nanocomposites on nickel foam at 2M KOH electrolyte.

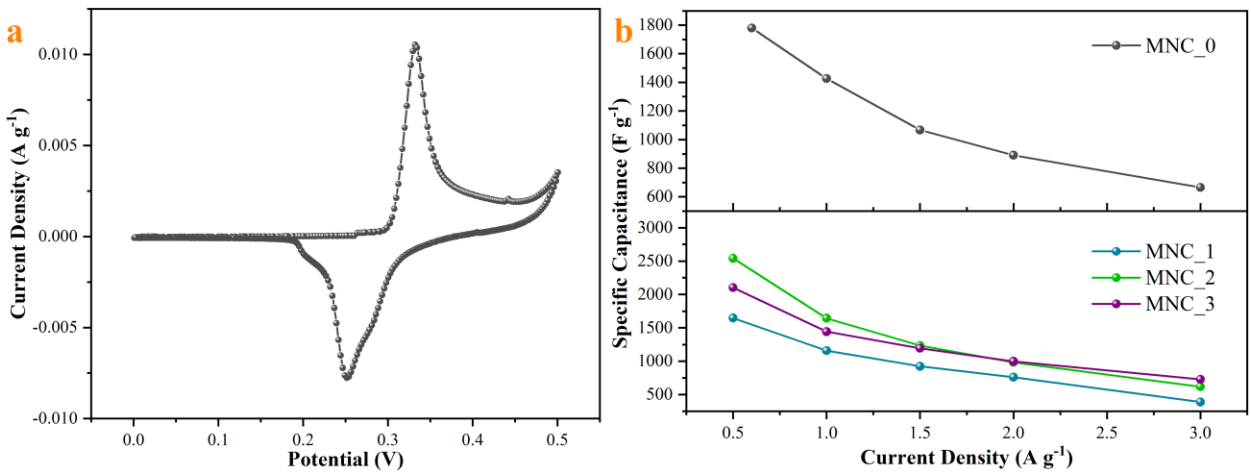


Figure 7.10. (a) CV profile of nickel foam at a scan rate of 5 mV s^{-1} and (b) the specific capacitance obtained for Na-doped MoS_2@NiO/C nanocomposites at various current densities in 2M KOH electrolyte.

Table 7.1. The electrochemical performance of NiO-based SC electrode active materials.

Name	*Electrolyte*	*SC*	*CD*	*ED*	*PD*	*η (%)*	*# of Cycles*	*Ref.*
NiO/NC//AC	6M KOH	1026 F g^{-1}	1	40.2	750.2	80.2	8,000	[386]
$NiCo_2O_4$/NiO //AC	3M KOH	726 F g^{-1}	1	32.9	912.4	91.4	5,000	[394]
N400//AC	3M KOH	473 F g^{-1}	0.5	21.4	375.8	94	3,000	[395]
La_2O_3-NiO//AC	1M KOH	564 F g^{-1}	1	4.3	200	93.4	2,000	[396]
NiO/NiS@CNT //AC	6M KOH	809.7 F g^{-1}	1	29.87	800	82.9	10,000	[397]
NiO/CNT	6M KOH	491.9 F g^{-1}	1	23.36	799	81.2	10,000	[397]
NiO/C/rGO //SCC	6M KOH	496 C g^{-1}	1	35.9	749.1	120	3,000	[398]
MnO_2@NiO //MEGO	1M KOH	374.6 F g^{-1}	0.25	15.4	200	92.7	5,000	[399]
NiO@Co_3O_4@ GQDs//AC	6M KOH	1361 F g^{-1}	1	38.44	750	76.4	3,000	[400]
MNC_2	2M KOH	2541 F g^{-1}	0.5	36.9	477	111.92	4,000	this

* SC: Specific Capacitance; CD: Current Density (A g^{-1}); ED: Energy Density (Wh kg^{-1}); PD: Power density (W kg^{-1}); η: Efficiency.

To study the charge storage mechanism of Na-doped MoS_2@NiO/C nanocomposites, cyclic voltammetry (CV) was conducted at an operating potential window of 0 – 1.0 V in a two-electrode configuration. As depicted in **Fig. 7.11a**, the CV profiles as a function of scan rates were plotted at a scan rate of 50 mV s^{-1} in 2M Na_2SO_4 aqueous electrolyte. As expected, the closed CV curves illustrated a weak and broad pair of redox peaks corresponding to the intercalation and de-intercalation of Na^+ cations, which evidently proved the charge and energy storage mechanism was dominated by pseudo-capacitive behaviors [350, 401]. Notably, all the CV curves possessed highly symmetrical shapes, clearly indicating the high reversibility of Na-doped MoS_2@NiO/C electrode. Besides, MNC_2 electrode showed a larger CV loop area than other samples at the same scan rate, demonstrating a better capacitive performance. Additionally, the comparative study also illustrated that the hierarchical porous structures were beneficial to enhance the electrochemical performance. The synergetic effect of Na and MoS_2 nanomaterials incorporated into MOF-derived NiO/C further enhanced the electrochemical performance.

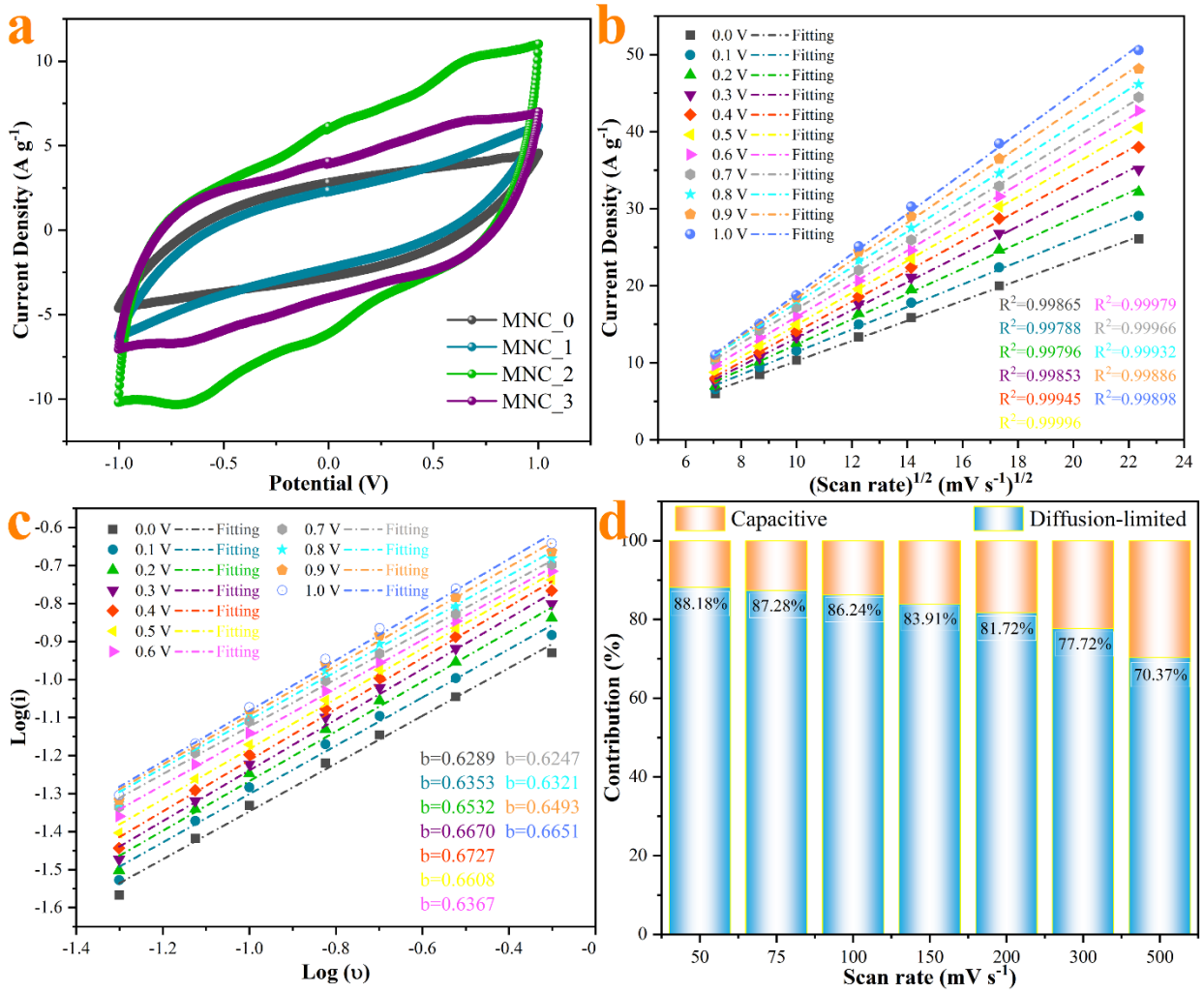


Figure 7.11. (a) CV profiles of Na-doped MoS_2@NiO/C nanocomposites at 50 mV s^{-1}. (b) Linear response between current densities and square root of scan rates, (c) calculation of b values at various potentials and (d) capacitance contributions at different scan rates of MNC_2.

The CV profiles of Na-doped MoS_2@NiO/C electrodes at different scanning rates ranging from 50 to 500 mV s^{-1} were demonstrated in **Fig. 7.12**. Clearly, all the CV loop areas increased with a rising scan rate up to 500 mV s^{-1}, as well as the raising of current densities. This suggested the excellent rate performance of the electrode, owing to the hierarchical structures with high porosity, which have facilitated the rapid electron transfer and electrolyte ion diffusion. Meanwhile, it was observed that oxidation peaks shifted positively and reduction peaks shifted negatively as the scan rate increased, which was primarily caused by the internal resistance and polarization effect. Additionally, **Fig. 7.13a** displays CV curves of MNC_2 at various potential windows at 50 mV s^{-1}. The appearance of polarization peaks was observed when the working potential exceeded 1.0 V (0 – 1.0 V), which could be due to the hydrogen/oxygen evolution reaction. Hence, all the electrochemical analysis was conducted at the same operation potential window.

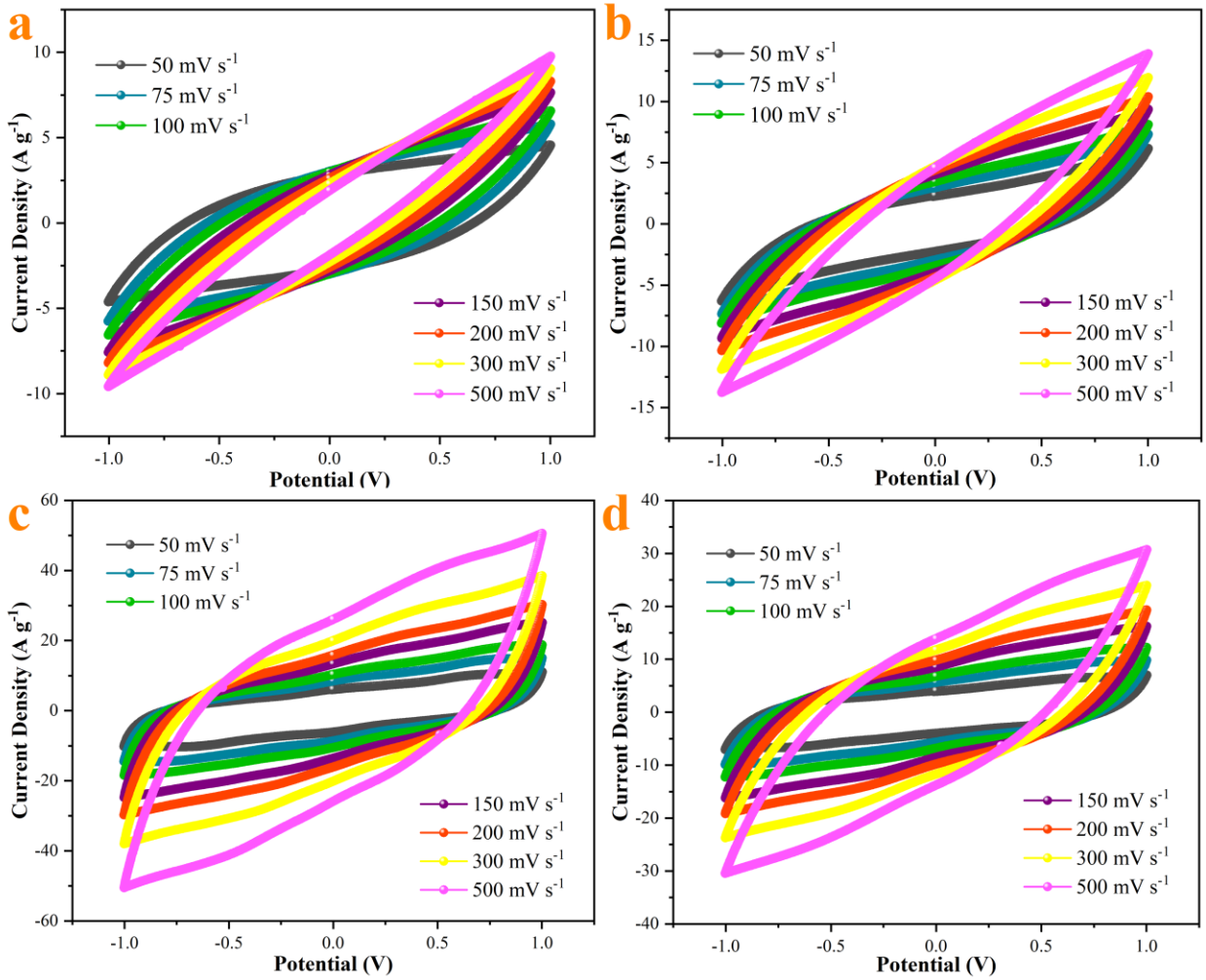


Figure 7.12. CV curves of (a) MNC_0, (b) MNC_1, (c) MNC_2 and (d) MNC_3 at different scan rates ranging from 50 to 500 mV s^{-1} in 2M Na_2SO_4 aqueous electrolyte.

As MNC_2 performed the best among other samples, it was studied further to gain insight on the kinetics of sodium ion storage. As depicted in **Fig. 7.11b** and **7.13b**, the relationship between current density and scan rates, as well as square root of scan rates was plotted. According to the linear fitting plots, the regression values for I vs. v was much lower than that of I vs. $v^{1/2}$ at various potentials, which could be interpreted that diffusion-limited process was the best fitting charge and energy storage mechanism for MNC_2. Moreover, to supplementary prove the diffusion-limited and non-diffusion-limited charge storage characteristics, power-law relationship was evaluated employing **Eq. (11)** [351, 402].

The value of b is a significant indicator to evaluate the sodium storage kinetics which can be obtained from the fitting slope of log (*i*) vs. log (*v*). In particular, the non-diffusion process is dominant in sodium ion storage process if b approaches 1, while the value of b is 0.5 for diffusion-limited capacitive process. **Fig. 7.11c** displays the plots of log (*i*) vs. log (*v*) with linear fittings. Clearly, it could be noted that b values were located between 0.62 and 0.67, revealing the existence of both diffusion- and non-diffusion-limited processes [403]. To quantitatively study the Na^+ ion storage behavior, the proportion contribution of diffusion- and surface-limited capacitance was investigated by Dunn's method [404]. Based on this model, current response at a particular potential in CV can be separated into terms related to the scanning rate, as given in **Eq. (12)**:

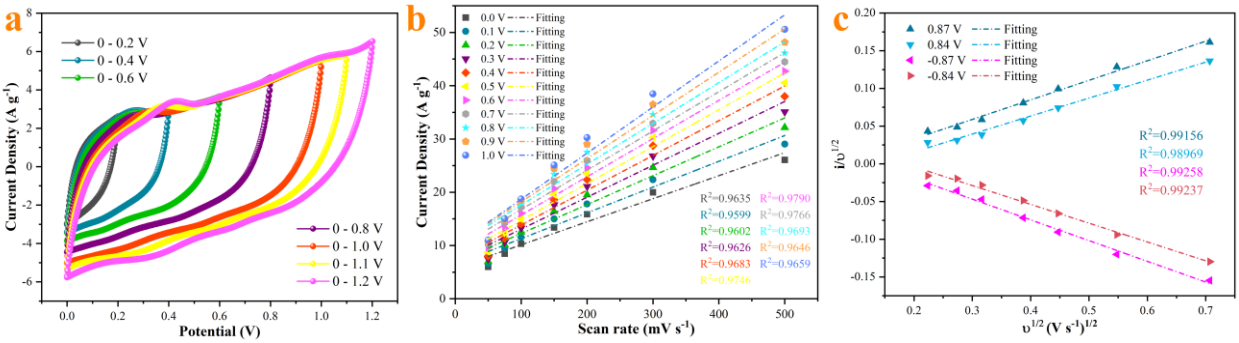


Figure 7.13. (a) Different potential windows at 50 mV s^{-1}, (b) plots of current density versus scan rate, and (c) plots of $iv^{-0.5}$ versus $v^{0.5}$ at both positive and negative 0.84 and 0.87 V for MNC_2.

Fig. 7.13c presents a plot of $iv^{-0.5}$ against $v^{0.5}$ at positive 0.84 V and negative 0.87 V, respectively. Based on calculations, the percentage contribution was only 11.82% for surface-limited process (**Fig. 7.11d**, brown region) at a low scan rate of 50 mV s^{-1}. Meanwhile, the percentage of EDLC behavior increased gradually with increasing sweeping rates, which eventually reached 29.63% at a high rate of 500 mV s^{-1} (**Fig. 7.11d**, brown region). Nevertheless, as presented in **Fig. 7.11d**, the dominance of diffusion-limited process was observed at all scan rates and potentials owing to the involvement of Na^+ insertion/deinsertion. A schematic diagram for sodium storage was demonstrated in **Fig. 7.14.** Hence, it confirmed that the sodium storage process was controlled by both non-diffusion and diffusion processes. Furthermore, the proportion contribution of diffusion-limited capacitance decreased as the scan rate increased, which could be attributed to fact that electrolyte ions did not have adequate time to penetrate into all the pores on the electrode at high scan rate [405]. High scanning rate was unfavorable for the insertion and deinsertion of sodium ions, leading to partial Faradaic redox reactions on the surface of electrode.

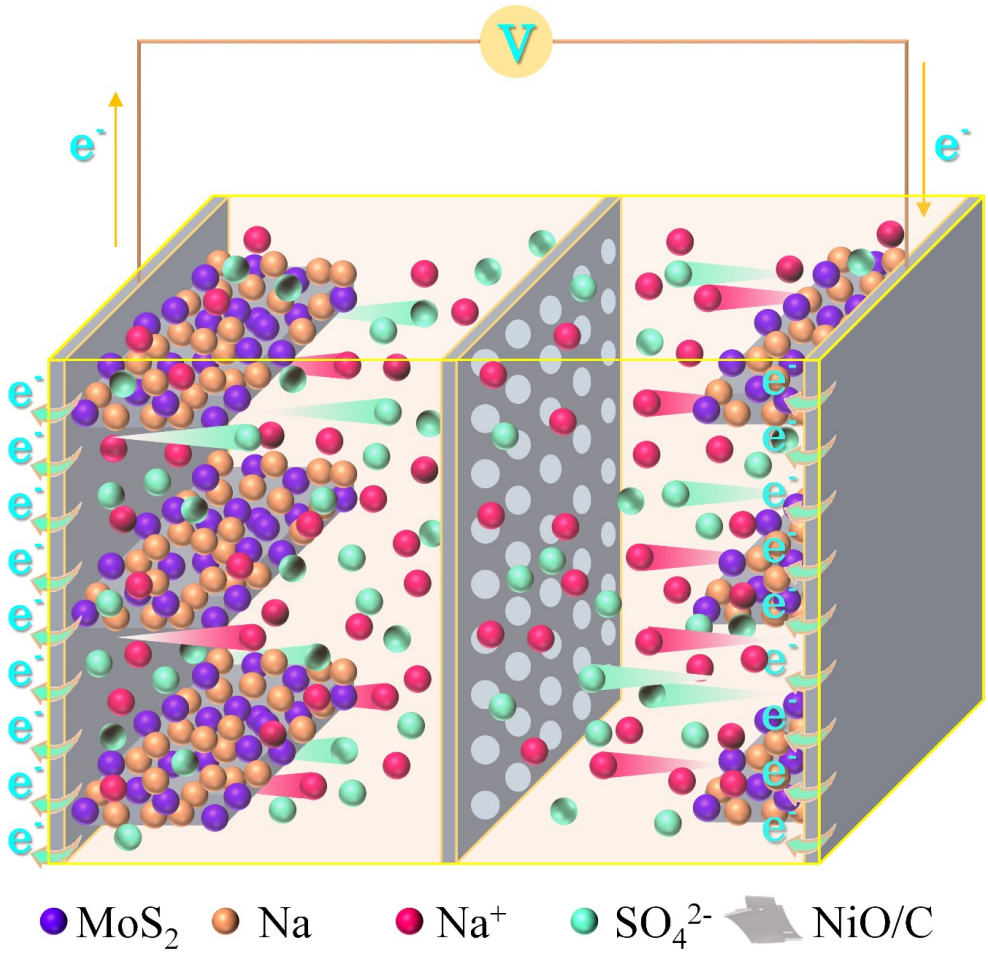


Figure 7.14. Schematic illustration of the sodium storage behavior in hierarchical porous Na-doped MoS_2@NiO/C nanocomposites.

To investigate the specific capacitance of Na-doped MoS_2@NiO/C electrode active materials, galvanostatic charge/discharge (GCD) was performed over an operation potential window of 0 – 1.0 V at various current densities (0.5 to 5.0 A g^{-1}), as shown in **Fig. 7.15**. The almost symmetrical GCD profiles indicated that the symmetrical supercapacitor device exhibited excellent capacitive performance and electrochemical reversibility. The NiO/C derived from Ni-MOFs yielded an electrochemical capacitance of 186.39 F g^{-1} at 0.5 A g^{-1} (**Fig. 7.16a**). Moreover, the electrochemical capacitances were found to be 159.51, 292.14 and 224.85 F g^{-1} at 0.5 A g^{-1} for MNC_1, MNC_2 and MNC_3 electrode, respectively. The result was consistent with that of CV data. The enhancement in electrochemical properties could be caused by the hierarchical porous structures of Na-doped MoS_2@NiO/C nanocomposites with compatible channels, leading to the enhancement in surface areas for charge storage and providing sufficient paths for electrolyte ion transfer. Besides, the rate performance of these nanocomposites was depicted in **Fig. 7.16b**, and the corresponding GCDs were shown in **Fig. 7.15**. It could be noted that inferior rate performance was seen for MNC_0, in which the capacitance retention was only 17.18% as the applied current

density was increased by 10 folds, and a significant potential drop (67 mV) was observed, in particular at a high discharging current density. This could be assigned to the non-conductive nature of most transition metal oxides [406-408]. The capacitive performance was substantially enhanced when layered MoS_2 nanosheets were incorporated, and the potential drops were 17, 46 and 10 mV for MNC_1, MNC_2 and MNC_3, respectively. Additionally, the reduction in the capacitance retention of the electrode active materials at a high current density could be rationalized. As the diffusion limitation was dominant for overall sodium storage, the capacitance could be reduced by the slow migration of electrolyte ions.

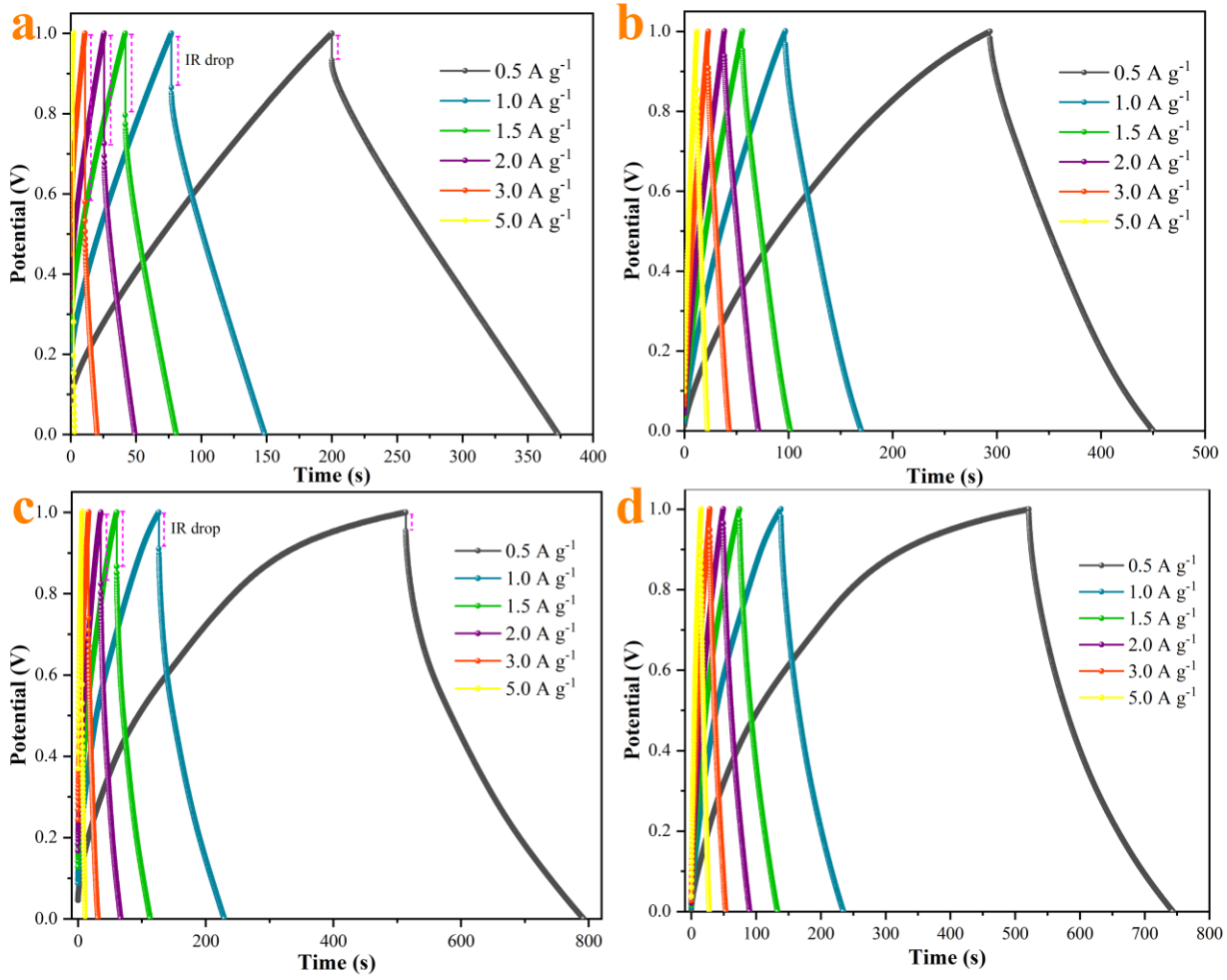


Figure 7.15. GCDs at different current densities (0.5 – 5.0 A g^{-1}) for (a) MNC_0, (b) MNC_1, (c) MNC_2 and (d) MNC_3.

Notably, a Ragone plot was illustrated in **Fig. 7.16c**, the hierarchical porous Na-doped MoS_2@NiO/C nanomaterials possessed excellent energy and power densities. The delivered energy densities of MNC_1, MNC_2 and MNC_3 were 21.41, 36.93 and 30.61 Wh kg^{-1} at power densities of 491.5, 477 and 495 W kg^{-1} respectively. Meanwhile, the retained energy density at 16.10 Wh kg^{-1} was achieved by MNC_3 at a maximum power density of 4,600 W kg^{-1}. Such

excellent energy density was comparable to those supercapacitor devices reported in other studies [282, 409, 410].

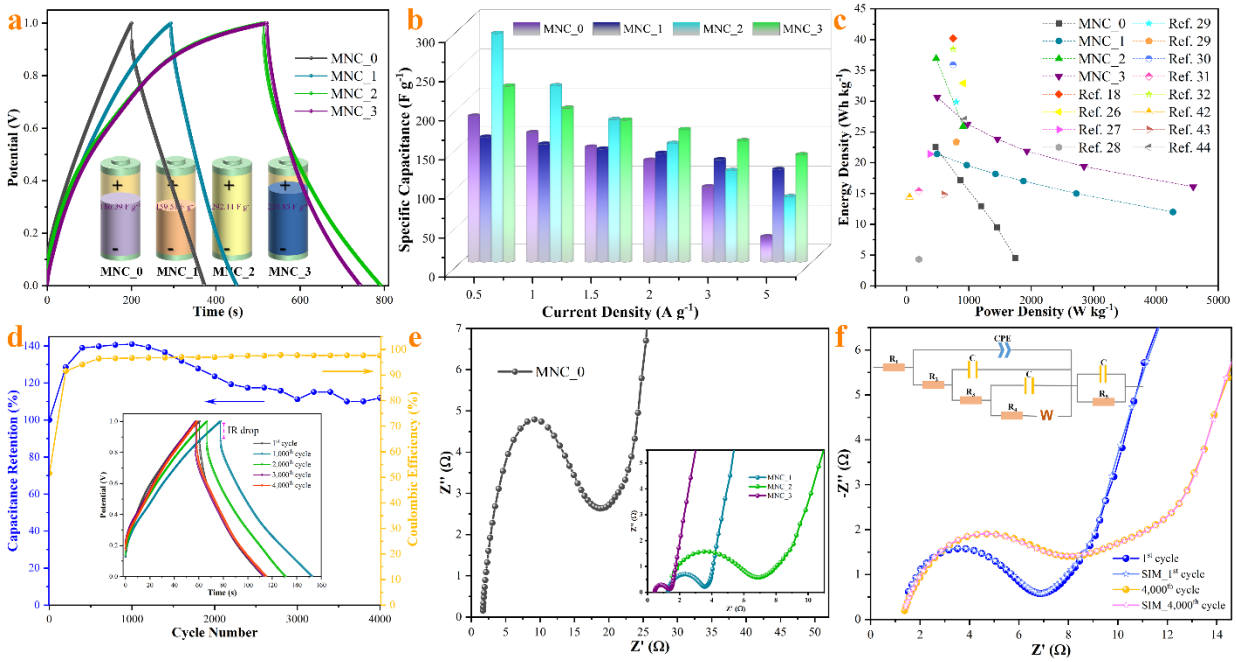


Figure 7.16. (a) GCD profiles at 0.5 A g^{-1}, (b) rate performance of Na-doped MoS_2@NiO/C nanomaterials and (c) Ragone plot of the as-fabricated symmetric SC devices and other references. (d) Cyclic performance, (e) Nyquist plot and (f) EIS spectra before and after cycling performance measurement of Na-doped MoS_2@NiO/C nanocomposites.

Furthermore, recyclability is one of the critical parameters to define the stability of an electrode active material. Hence, the cycling performance of the as-assembled MNC_2 supercapacitor device was evaluated at a constant current density of 1.5 A g^{-1} for 4,000 cycles. An outstanding capacitance retention of 111.92% was obtained after 4,000 GCD cycles (**Fig. 7.16d**), highlighting the superior cyclic stability. The highly porous structure was possibly responsible for tolerating the volume change of NiO during long-term charging and discharging. Moreover, the perfusion of sulfur could prohibit the dissolution of active materials during continuous GCD cycles. It is worth noting that the retained capacitance was 140.99% at 1,000th cycle (**Fig. 7.16d**, inset), which resulted from the activation of MNC_2 electrode active materials during long-term cycling [411]. Moreover, the delivered coulombic efficiency was also as high as 97.6% over 4,000 continuous cycles (**Fig. 7.16d**).

Additionally, charge transfer kinetics were analyzed via the electrochemical impedance spectroscopy (EIS) method. The impedance of the as-fabricated symmetrical supercapacitor devices was evaluated by applying a low-amplitude alternative voltage of 10 mV from 100,000 to 0.01 Hz. **Fig. 7.16e** demonstrates the Nyquist plots of the as-synthesized nanocomposites. These plots mainly consisted of three parts. Intrinsic resistance (R_s), also known as solution resistance, was located at high-frequency regions, interfacial charge transfer resistance (R_{ct}) was at mild-

frequency regions, which was originated from the interfacial charge transfer, and a capacitive line was viewed at low-frequency regions. As shown in **Table 7.2**, both the R_s and R_{ct} were reduced by sodium doping and the incorporation of MoS_2 nanomaterials, suggesting the hierarchical porous structures helped to decrease internal and charge transfer resistance. Nonetheless, MNC_0 electrode exhibited both high R_s and R_{ct}, which implied the inferior electronic conductivity of transition metal oxides. Additionally, the Nyquist plots of the Na-doped MoS_2@NiO/C nanostructures exhibited an oblique line (~45 °) instead of a perfectly vertical line, which could be assigned to the diffusion impedance, also called as Warburg impedance (W) [412]. The frequency-dependent Warburg impedance is always being utilized to model the semi-infinite diffusion process at the interface between electrolyte and electrode, especially the unrestricted diffusion to large planar of electrode. At the low frequency region, normally the ideal diffusion behavior can be observed, represented by a vertical line that is closely parallel to the imaginary impedance axis of the Nyquist plot.

The EIS technique was used to evaluate the MNC_2 electrode before and after performing the cyclic analysis, as demonstrated in **Fig. 7.16f**. Moreover, the Nyquist plots were fitted to an equivalent circuit (**Fig. 7.16f**, inset) as well. Evidently, a slight shift of R_s from 1.11 to 1.19 Ω and similar shift of R_{ct} from 5.08 to 6.97 Ω were observed. The tiny enlargement in R_s could be ascribed to the repetitive insertion and deinsertion of sodium ions, resulting in electrode active materials partially detached from current collectors [413]. The minor shift of R_{ct} to a higher value was mainly attributed to the slight loss of electrode active materials. These results were consistent with the reduction in coulombic efficiency of the electrode.

Table 7.2. EIS data of Na-doped MoS_2@NiO/C nanocomposites in 2M Na_2SO_4 aqueous electrolyte.

Samples		***R_s (Ω)***	***R_{ct} (Ω)***
MNC_0		1.58	14.87
MNC_1		1.25	2.18
MNC_2	**1st**	1.11	5.08
	4,000th	1.19	6.97
MNC_3		0.45	0.78

In principle, the remarkable electrochemical performance of hierarchical porous MOF-derived NiO/C incorporated MoS_2 nanocomposites could be assigned to several reasons. Firstly, the existence of abundant pores of NiO/C yolk-shell structures not only offered sufficient channels for electrolyte ion transport, but also enlarged the surface area for sodium storage. Secondly, the doped Na cations and the amorphous carbon derived from Ni-MOFs were able to facilitate charge transfer by reducing electronic resistance. Besides, the abundance of NiO could offer additional pseudocapacitance resulting from Faradaic redox reactions. These phenomena significantly alleviate the specific capacitance and energy density of the electrode. Furthermore, the

incorporation of MoS_2 nanomaterials with hierarchical structure was not only favorable for reducing electronic resistivity, but also provided extra pseudocapacitance and surface area for EDLC. Therefore, an outstanding electrochemical performance was achieved due to the synergistic effect of the nanocomposites and MOF [414-416].

7.3 Summary

In conclusion, a novel hierarchical porous Na-doped NiO/C (derived from Ni-MOFs) incorporated into MoS_2 nanocomposites were propitiously prepared via a simple hydrothermal approach. The as-synthesized nanostructures showed an excellent specific capacitance in aqueous based electrolyte system, when a symmetric supercapacitor was fabricated. Meanwhile, the delivered energy density was remarkable at 36.93 Wh kg^{-1}, and this value was much higher than simple carbonaceous nanomaterials reported elsewhere. Additionally, a remarkable cyclability was achieved over 4,000 cycles, in which the capacitance retention was 111.92% with a coulombic efficiency of 97.6%. The exceptional electrochemical performance of the nanocomposites could be assigned to the highly pseudocapacitance-rich transition metal oxides and hierarchical MoS_2 nanostructures, which could significantly enhance the energy density. Besides, the MOF-derived carbon nanomaterials and the incorporated Na could facilitate charge transfer. Additionally, the perfusion of S could substantially reduce the loss of active materials and enhance the transfer of electrolyte ions. Hence, this study provided a novel approach on structure design of novel electrodes for high-performance supercapacitor applications.

Chapter 8: Conclusion and Future Perspectives

8.1 Conclusion

In conclusion, this study firstly systematically investigated the impact of critical parameters, including different solvent systems, solvothermal temperature and time, on the morphological and electrochemical properties of Ni-MOFs, which were synthesized via a solvothermal approach. The results indicated that: (a) Binary solvents (DMF + Ethylene glycol) with high polarity and viscosity were beneficial to produce Ni-MOF with high surface area and porosity. (b) The incorporation of highly conductive graphene nanosheets with Ni-MOF nanostructures could further enhance electrochemical performance. (c) The solvothermal reaction temperature had a significant influence on the morphologies, crystallinity and electrochemical capacitive performance of Ni-MOF nanomaterials, whereas solvothermal time only had a slight impact on the resultant morphologies and electrochemical properties. Apart from that, the incorporation of molybdenum disulfide and sodium cations onto Ni-MOF nanostructures was also studied. The findings showed that the as-synthesized nanocomposites could significantly enhance the energy density without compromising the cycling durability. Additionally, transition metal oxides/carbon nanocomposites derived from Ni-MOFs were investigated in detail as well. In particular, highly porous Na^+ and MoS_2 incorporated MOF-derived NiO/C yolk-shell nanocomposites were prepared via a simple hydrothermal approach, followed by the calcination process, which exhibited superior electrochemical capacitance and cyclic stability. It was worth noting that perfusion of sulfur could occur when a large amount of MoS_2 was incorporated. This could reduce the porosity and surface areas, leading to a decrease in electrochemical capacitance. Nevertheless, it was possible to offer smooth surface to facilitate the diffusion of electrolyte ions and prohibit the dissolution of active materials during continuous GCD cycles. Their electrochemical performance was summarized in **Table 8.1**. According to the abovementioned works, all the objectives were achieved, and the following conclusions can be drawn:

i. The average size of Ni-MOF nanosheets tended to decrease as the reaction temperature was increased, whereas the crystallinity of these nanostructures showed a direct correlation with solvothermal temperature.
ii. The nanostructures synthesized at 160°C exhibited extraordinary electrochemical performance.
iii. Binary solvents (DMF + Ethylene glycol) with high polarity and viscosity were favorable for the formation of microspheres.
iv. The electrochemical performance of Ni-MOFs could be further enhanced via the incorporation of highly conductive graphene nanosheets (Ni-MOF/graphene).
v. The porosity and electrochemical property of MOF-derived NiO/C nanocomposites were further enhanced by incorporating Na^+ and hierarchical MoS_2 nanostructures.
vi. The perfusion of sulfur could block the porous structures of the as-synthesized nanomaterials, leading to a decrease in porosity and electrochemical capacitance, but it is beneficial to facilitate electronic conductivity and cyclability.

Table 8.1. Electrochemical performance of MOF-based nanostructures used in SCs.

Nanomaterials	Specific Capacitance	Energy Density (Wh kg^{-1})	Power Density (W kg^{-1})	Cyclic Stability	References
NiCo-MOF	1126.7 F g^{-1} @ 0.5 A g^{-1}	20.94	750.84	90% /5,000	[417]
Co-MOF	300 F g^{-1} @ 1 A g^{-1}	26	400	94%/ 1,000	[418]
NiO/Ni-MOF	1176.6 F g^{-1} @ 1 A g^{-1}	31.3	374.2	88.7% /2,000	[419]
Ni-MOF/rGO	954 F g^{-1} @ 1 A g^{-1}	17.13	750	81.63% /4,000	[420]
H_3TATB	213 C g^{-1} @ 0.5 A g^{-1}	16.0	749	88% /3,000	[283]
Co-BTC	657 F g^{-1} @ 0.5 A g^{-1}	34.4	375.3	81.4% /3,000	[205]
Co-MOF/Gr	549.96 F g^{-1} @ 10 mV s^{-1}	8.1	850	78.85% /1,000	[421]
Ni-MOF/NiS_2	1128 F g^{-1} @ 2 A g^{-1}	23.5	1400	95.2% /10,000	[422]
NiCo-MOF	927.1 F g^{-1} @ 1 A g^{-1}	28.5	400.5	95.4% /5,000	[423]
FG_$Gr_{1.0}$	420.4 F g^{-1} @ 1 A g^{-1}	14.68	291.82	97.7% /10,000	this work
FG_{16032}	619.62 F g^{-1} @ 0.5 A g^{-1}	22.44	294.6	117.78% /10,000	this work
MoS_2@ Ni-MOFs	491.63 F g^{-1} @ 0.5 A g^{-1}	33.33	483	97.42% /10,200	this work
MoS_2@NiO/C	2540.63 F g^{-1} @ 0.5 A g^{-1}	36.9	477	111.92% /4,000	this work

8.2 Future Perspectives

Currently, the design and synthesis of highly porous micro/nanostructured materials with outstanding electrochemical properties have been widely studied for high-performance electrochemical energy devices. A large number of studies have proved that MOFs can be utilized as promising electrode active materials for SCs by virtue of the natural advantages of high porosity, ultra-large specific surface area and easily controllable structures. Moreover, MOFs not only could be directly employed as functional materials, but they have also been utilized as precursors/templates for the synthesis of metal oxides, nanoporous carbon and metal oxide/carbon nanocomposites. Besides, their derivatives show inherent morphology and structures of their parent precursors. Such unique characteristics facilitate large electroactive sites and suitable channels for ion diffusion during electrochemical reactions. Correspondingly, the energy density and cycling performance could be further enhanced. Though MOF-based electrode active materials are attractive, there are still issues which need to be tackled.

Firstly, some pristine MOFs possess intrinsic inferior stability and high electronic resistivity, which could seriously limit electrochemical performance. Recent studies demonstrated that free-standing of 2D MOF structures on a conductive substrate (i.e., gold, silver and graphene) could be an effective route to deal with this problem. On the other hand, the incorporation of other conductive materials with MOF is an alternative strategy. Nonetheless, only a few organic ligands can be used to synthesize conductive MOFs, it is crucial to design and construct conductive MOF structures with excellent conductivity and stability.

Secondly, despite the electrochemical performance could be significantly enhanced through the introduction of transition metal oxides, especially multiple metal oxides, the interactions between these metal oxides and the charge storage mechanism still remain unclear. Hence, more studies are required to be conducted and more advanced technologies in this context are urgently to be addressed.

Lastly, electrolytes also have a significant role to play in electrochemical performance (such as cycling stability, rate performance, energy and power density) as well as safety. The design of efficient electrolytes is still challenging in the application of MOF-materials in SCs. Thus, more studies need to be carried out to understand the interactions in the interface between electrolyte and electrode.

References:

1. Xiao, L., L. Lin, and Y. Liu, *Discussions on the Architecture and Operation Mode of Future Power Grids.* Energies, 2011. **4**(7): p. 1025-1035.
2. Kiani, M.A., et al., *Fabrication of high power $LiNi_{0.5}Mn_{1.5}O_4$ battery cathodes by nanostructuring of electrode materials.* Rsc Advances, 2015. **5**(62): p. 50433-50439.
3. Zheng, J., et al., *Lewis Acid–Base Interactions between Polysulfides and Metal Organic Framework in Lithium Sulfur Batteries.* Nano Lett, 2014. **14**(5): p. 2345-2352.
4. Ko, M., L. Mendecki, and K.A. Mirica, *Conductive two-dimensional metal-organic frameworks as multifunctional materials.* Chem Commun (Camb), 2018. **54**(57): p. 7873-7891.
5. Sezginel, K.B., et al., *Thermal Transport in Interpenetrated Metal–Organic Frameworks.* Chemistry of Materials, 2018. **30**(7): p. 2281-2286.
6. Dalstein, O., et al., *Nanoimprinted, Submicrometric, MOF-Based 2D Photonic Structures: Toward Easy Selective Vapors Sensing by a Smartphone Camera.* Advanced functional materials, 2016. **26**(1): p. 81-90.
7. Chocarro Ruiz, B., et al., *A CO_2 optical sensor based on self-assembled metal–organic framework nanoparticles.* Journal of Materials Chemistry A, 2018. **6**(27): p. 13171-13177.
8. Partridge, J. and D.I. Abouelamaimen, *The Role of Supercapacitors in Regenerative Braking Systems.* Energies (Basel), 2019. **12**(14): p. 2683.
9. Jin, L.-q., et al., *A study of novel regenerative braking system based on supercapacitor for electric vehicle driven by in-wheel motors.* Advances in Mechanical Engineering, 2015. **7**(3): p. 168781401557376.
10. Wang, Y., Y. Song, and Y. Xia, *Electrochemical capacitors: mechanism, materials, systems, characterization and applications.* Chem Soc Rev, 2016. **45**(21): p. 5925-5950.
11. Gautham Prasad G, et al., *Supercapacitor technology and its applications: a review.* 2019.
12. Kim, B.K., et al., *Electrochemical Supercapacitors for Energy Storage and Conversion.* Handbook of Clean Energy Systems, 2015: p. 1-25.
13. Pavaskar, G., et al., *Modeling Electric Double-Layer Capacitors Using Charge Variation Methodology in Gibbs Ensemble.* Frontiers in Energy Research, 2018. **5**.
14. Costentin, C., T.R. Porter, and J.M. Saveant, *How Do Pseudocapacitors Store Energy? Theoretical Analysis and Experimental Illustration.* ACS Appl Mater Interfaces, 2017. **9**(10): p. 8649-8658.
15. El-Kady, M.F., et al., *Engineering three-dimensional hybrid supercapacitors and microsupercapacitors for high-performance integrated energy storage.* Proc Natl Acad Sci U S A, 2015. **112**(14): p. 4233-8.
16. Zeng, L., et al., *Carbonaceous mudstone and lignin-derived activated carbon and its application for supercapacitor electrode.* Surface & coatings technology, 2019. **357**: p. 580-586.
17. Jiang, Y. and J. Liu, *Definitions of Pseudocapacitive Materials: A Brief Review.* Energy & Environmental Materials, 2019. **2**(1): p. 30-37.
18. Salunkhe, R.R., Y.V. Kaneti, and Y. Yamauchi, *Metal-Organic Framework-Derived Nanoporous Metal Oxides toward Supercapacitor Applications: Progress and Prospects.* ACS Nano, 2017. **11**(6): p. 5293-5308.
19. Jiang, H., P.S. Lee, and C. Li, *3D carbon based nanostructures for advanced supercapacitors.* Energy & environmental science, 2013. **6**(1): p. 41-53.

20. Rakhi, R.B., et al., *Nanostructured Ternary Electrodes for Energy‐Storage Applications.* Advanced energy materials, 2012. **2**(3): p. 381-389.
21. Xia, W., et al., *High-Performance Energy Storage and Conversion Materials Derived from a Single Metal–Organic Framework/Graphene Aerogel Composite.* Nano Lett, 2017. **17**(5): p. 2788-2795.
22. Boota, M. and Y. Gogotsi, *MXene-Conducting Polymer Asymmetric Pseudocapacitors.* Advanced energy materials, 2019. **9**(7): p. 1802917-n/a.
23. Zheng, S., et al., *Transition-Metal (Fe, Co, Ni) Based Metal-Organic Frameworks for Electrochemical Energy Storage.* Advanced energy materials, 2017. **7**(18): p. 1602733-n/a.
24. Chen, Y., et al., *An Ultramicroporous Nickel-Based Metal–Organic Framework for Adsorption Separation of CO2 over N2 or CH4.* Energy & Fuels, 2018. **32**(8): p. 8676-8682.
25. Javanbakht, S., M. Pooresmaeil, and H. Namazi, *Green one-pot synthesis of carboxymethylcellulose/Zn-based metal-organic framework/graphene oxide bio-nanocomposite as a nanocarrier for drug delivery system.* Carbohydr Polym, 2019. **208**: p. 294-301.
26. Nadar, S.S. and V.K. Rathod, *Magnetic-metal organic framework (magnetic-MOF): A novel platform for enzyme immobilization and nanozyme applications.* Int J Biol Macromol, 2018. **120**(Pt B): p. 2293-2302.
27. Kang, Z., L. Fan, and D. Sun, *Recent advances and challenges of metal–organic framework membranes for gas separation.* Journal of materials chemistry. A, Materials for energy and sustainability, 2017. **5**(21): p. 10073-10091.
28. Li, B., et al., *Porous Metal-Organic Frameworks for Gas Storage and Separation: What, How, and Why?* J Phys Chem Lett, 2014. **5**(20): p. 3468-79.
29. Chocarro-Ruiz, B., et al., *A CO_2 optical sensor based on self-assembled metal–organic framework nanoparticles.* Journal of Materials Chemistry A, 2018. **6**(27): p. 13171-13177.
30. Schoenecker, P.M., et al., *Effect of Water Adsorption on Retention of Structure and Surface Area of Metal–Organic Frameworks.* Ind. Eng. Chem. Res, 2012. **51**(18): p. 6513-6519.
31. Genesio, G., et al., *Recent status on MOF thin films on transparent conductive oxides substrates (ITO or FTO).* 2018. **42**(4): p. 2351-2363.
32. Senkovska, I. and S. Kaskel, *Ultrahigh porosity in mesoporous MOFs: promises and limitations.* Chem Commun (Camb), 2014. **5**(54): p. 789-798.
33. Ding, M., X. Cai, and H.L. Jiang, *Improving MOF stability: approaches and applications.* Chem Sci, 2019. **10**(44): p. 10209-10230.
34. Xia, W., et al., *Metal–organic frameworks and their derived nanostructures for electrochemical energy storage and conversion.* Energy & Environmental Science, 2015. **8**(7): p. 1837-1866.
35. Zeng, M.-H., *Short-range disorder in MOF glasses.* National Science Review, 2021. **8**(5): p. nwaa207.
36. Yang, C., et al., *Fluorous Metal–Organic Frameworks with Superior Adsorption and Hydrophobic Properties toward Oil Spill Cleanup and Hydrocarbon Storage.* Journal of the American Chemical Society, 2011. **133**(45): p. 18094-18097.
37. Yang, Y., et al., *A water-stable 3D Eu-MOF based on a metallacyclodimeric secondary building unit for sensitive fluorescent detection of acetone molecules.* CrystEngComm, 2019. **21**(2): p. 321-328.

38. Yang, S.J. and C.R. Park, *Preparation of Highly Moisture-Resistant Black-Colored Metal Organic Frameworks.* Advanced Materials, 2012. **24**(29): p. 4010-4013.
39. Shih, Y.H., et al., *A Simple Approach to Enhance the Water Stability of a Metal-Organic Framework.* Chemistry, 2017. **23**(1): p. 42-46.
40. He, H., et al., *A Stable Metal-Organic Framework Featuring a Local Buffer Environment for Carbon Dioxide Fixation.* Angew Chem Int Ed Engl, 2018. **57**(17): p. 4657-4662.
41. Gong, Y.N., et al., *Photoinduced water oxidation by an organic ligand incorporated into the framework of a stable metal-organic framework.* Chem Sci, 2016. **7**(2): p. 1070-1075.
42. Yang, J., et al., *Layered Structural Co-Based MOF with Conductive Network Frames as a New Supercapacitor Electrode.* Chemistry, 2017. **23**(3): p. 631-636.
43. Li, P. and B. Wang, *Recent Development and Application of Conductive MOFs.* Israel Journal of Chemistry, 2018. **58**(9-10): p. 1010-1018.
44. Zong, Z.-a., et al., *Synthesis, crystal structures and dye removal properties of a series of metal-organic frameworks based on N-heterocyclic carboxylic acid ligands.* Microporous and Mesoporous Materials, 2019. **282**: p. 82-90.
45. Yang, C., et al., *A new promising Ni-MOF superstructure for high-performance supercapacitors.* Chem Commun (Camb), 2020. **56**(12): p. 1803-1806.
46. Nguyen, D.K., I.M. Schepisi, and F.Z. Amir, *Extraordinary cycling stability of $Ni_3(HITP)_2$ supercapacitors fabricated by electrophoretic deposition: Cycling at 100,000 cycles.* Chemical Engineering Journal, 2019. **378**.
47. *GM Auto Engine Stop/Start Systems*. 2017 [cited 2022 06.01]; Available from: https://gm-techlink.com/?p=8495.
48. *Mazda 'i-ELOOP' Capacitor-Based Brake Energy Regeneration System*. 2011 [cited 2022 06.01]; Available from: https://newsroom.mazda.com/en/publicity/release/2011/201111/111125a.html.
49. *Supercapacitor light metro train unveiled*. 2012 [cited 2022 06.01]; Available from: https://www.railwaygazette.com/supercapacitor-light-metro-train-unveiled/37218.article.
50. *Maxwell and the Promise of Ultracapacitors*. 2010 [cited 2022 06.01]; Available from: https://www.greentechmedia.com/articles/read/maxwell-and-the-promise-of-ultracapacitors.
51. *Opening doors to space*. 2014 [cited 2022 06.01]; Available from: https://www.esa.int/Applications/Telecommunications_Integrated_Applications/Opening_doors_to_space.
52. Gou, L., et al., *Isostructural metal organic frameworks based on 1,4-naphthalene dicarboxylate as anodes for lithium ion battery.* Materials Technology, 2017. **32**(10): p. 630-637.
53. Hu, X., et al., *Green and Rational Design of 3D Layer-by-Layer MnO_x Hierarchically Mesoporous Microcuboids from MOF Templates for High-Rate and Long-Life Li-Ion Batteries.* ACS Appl Mater Interfaces, 2018. **10**(17): p. 14684-14697.
54. Lim, D.W., M. Sadakiyo, and H. Kitagawa, *Proton transfer in hydrogen-bonded degenerate systems of water and ammonia in metal-organic frameworks.* Chem Sci, 2019. **10**(1): p. 16-33.
55. Liang, Z., et al., *Non-noble trimetallic Cu-Ni-Co nanoparticles supported on metal-organic frameworks as highly efficient catalysts for hydrolysis of ammonia borane.* Journal of alloys and compounds, 2018. **741**: p. 501-508.

56. Liu, S., et al., *Synthesis and properties of ferrocene confined within UiO-67 MOFs.* Microporous and mesoporous materials, 2018. **264**: p. 133-138.
57. Rani, R., et al., *Enhanced hydrothermal stability of Cu MOF by post synthetic modification with amino acids.* Vacuum, 2019. **164**: p. 449-457.
58. Zito, C.A., M.O. Orlandi, and D.P. Volanti, *Accelerated microwave-assisted hydrothermal/solvothermal processing: Fundamentals, morphologies, and applications.* Journal of electroceramics, 2018. **40**(4): p. 271-292.
59. Fu, C., et al., *Microwave-Activated Mn-Doped Zirconium Metal–Organic Framework Nanocubes for Highly Effective Combination of Microwave Dynamic and Thermal Therapies Against Cancer.* ACS Nano, 2018. **12**(3): p. 2201-2210.
60. Buchan, I., M.R. Ryder, and J.-C. Tan, *Micromechanical Behavior of Polycrystalline Metal–Organic Framework Thin Films Synthesized by Electrochemical Reaction.* Cryst. Growth Des, 2015. **15**(4): p. 1991-1999.
61. Lu, M., et al., *Graphene Aerogel–Metal–Organic Framework-Based Electrochemical Method for Simultaneous Detection of Multiple Heavy-Metal Ions.* Anal. Chem, 2019. **91**(1): p. 888-895.
62. Chen, Y., et al., *Highly efficient mechanochemical synthesis of an indium based metal-organic framework with excellent water stability.* Chemical engineering science, 2017. **158**: p. 539-544.
63. Panda, T., et al., *Mechanical Alloying of Metal–Organic Frameworks.* Angew Chem Int Ed Engl, 2017. **56**(9): p. 2413-2417.
64. Bayliss, P.A., et al., *Synthesis of metal-organic frameworks by continuous flow.* 2014.
65. Fan, Z., et al., *Hydrothermal Synthesis and Characterization of a Novel 3D Chiral Inorganic-Organic Hybrid Cadmium(II) Framework With Achiral 1,4-Naphthalenedicarboxylic Acid Ligand.* Synthesis and Reactivity in Inorganic, Metal-Organic, and Nano-Metal Chemistry, 2013. **44**(3): p. 371-375.
66. Zhang, S., et al., *Mixed-metal–organic frameworks (M′ MOFs) from 1D to 3D based on the "organic" connectivity and the inorganic connectivity: syntheses, structures and magnetic properties.* CrystEngComm, 2015. **17**(17): p. 3312-3324.
67. Gao, G.K., et al., *Rapid Production of Metal-Organic Frameworks Based Separators in Industrial-Level Efficiency.* Adv Sci (Weinh), 2020. **7**(24): p. 2002190.
68. Ye, J.-W., et al., *Room-temperature sintered metal-organic framework nanocrystals: A new type of optical ceramics.* Science China Materials, 2018. **61**(3): p. 424-428.
69. Basu, S., A. Cano-Odena, and I.F.J. Vankelecom, *MOF-containing mixed-matrix membranes for CO2/CH4 and CO2/N2 binary gas mixture separations.* Separation and Purification Technology, 2011. **81**(1): p. 31-40.
70. Wu, C., et al., *Palladium nanoclusters decorated partially decomposed porous ZIF-67 polyhedron with ultrahigh catalytic activity and stability on hydrogen generation.* Renewable Energy, 2019. **136**: p. 1064-1070.
71. Chen, C., et al., *Structuring Metal-Organic Framework Materials into Hierarchically Porous Composites through One-Pot Fabrication Strategy.* Chemistry, 2020. **26**(15): p. 3358-3363.
72. Yang, S.J., et al., *Solvent evaporation mediated preparation of hierarchically porous metal organic framework-derived carbon with controllable and accessible large-scale porosity.* Carbon, 2014. **71**: p. 294-302.

73. Ding, M., et al., *Orderly MOF-Assembled Hybrid Monolithic Stationary Phases for Nano-Flow HPLC.* Analytical Chemistry, 2020. **92**(24): p. 15757-15765.
74. Wu, W., et al., *Surface-functionalized nanoMOFs in oil for friction and wear reduction and antioxidation.* Chemical Engineering Journal, 2021. **410**: p. 128306.
75. Tsuruoka, T., et al., *Nanoporous Nanorods Fabricated by Coordination Modulation and Oriented Attachment Growth.* Angewandte Chemie International Edition, 2009. **48**(26): p. 4739-4743.
76. Albuquerque, G.H. and G.S. Herman, *Chemically Modulated Microwave-Assisted Synthesis of MOF-74(Ni) and Preparation of Metal–Organic Framework-Matrix Based Membranes for Removal of Metal Ions from Aqueous Media.* Crystal Growth & Design, 2017. **17**(1): p. 156-162.
77. Hu, Z., et al., *Modulated Hydrothermal Synthesis of Highly Stable MOF-808(Hf) for Methane Storage.* ACS Sustainable Chemistry & Engineering, 2020. **8**(46): p. 17042-17053.
78. Hu, S., et al., *Effects of Monocarboxylic Acid Additives on Synthesizing Metal–Organic Framework NH2-MIL-125 with Controllable Size and Morphology.* Crystal Growth & Design, 2017. **17**(12): p. 6586-6595.
79. Huang, H., et al., *Remarkable promotion effect of lauric acid on Mn-MIL-100 for non-thermal plasma-catalytic decomposition of toluene.* Applied Surface Science, 2020. **503**: p. 144290.
80. Sindoro, M., et al., *Colloidal-Sized Metal–Organic Frameworks: Synthesis and Applications.* Accounts of Chemical Research, 2014. **47**(2): p. 459-469.
81. Wang, X., et al., *Solvothermal synthesis of flower-string-like NiCo-MOF/MWCNT composites as a high-performance supercapacitor electrode material.* Journal of Solid State Chemistry, 2019. **277**: p. 575-586.
82. Zhang, C., L. Ai, and J. Jiang, *Solvothermal synthesis of MIL–53(Fe) hybrid magnetic composites for photoelectrochemical water oxidation and organic pollutant photodegradation under visible light.* Journal of Materials Chemistry A, 2015. **3**(6): p. 3074-3081.
83. Zhang, B., et al., *Facile and template-free solvothermal synthesis of mesoporous/macroporous metal–organic framework nanosheets.* RSC Advances, 2018. **8**(58): p. 33059-33064.
84. McKinstry, C., et al., *Scalable continuous solvothermal synthesis of metal organic framework (MOF-5) crystals.* Chemical Engineering Journal, 2016. **285**: p. 718-725.
85. Lv, Y., et al., *PH-modulated formation of uniform MOF-5 sheets.* Inorganic Chemistry Communications, 2018. **97**: p. 30-33.
86. Wang, S., et al., *Modulated synthesis of monodisperse MOF-5 crystals with tunable sizes and shapes.* Inorganic Chemistry Communications, 2018. **93**: p. 56-60.
87. Ma, M., et al., *A Method for the Preparation of Highly Porous, Nanosized Crystals of Isoreticular Metal−Organic Frameworks.* Cryst. Growth Des, 2011. **11**(1): p. 185-189.
88. Schaate, A., et al., *Modulated synthesis of Zr-based metal-organic frameworks: from nano to single crystals.* Chemistry, 2011. **17**(24): p. 6643-51.
89. Liu, B., et al., *Microwave-Assisted Rapid Synthesis of γ-Cyclodextrin Metal–Organic Frameworks for Size Control and Efficient Drug Loading.* Crystal Growth & Design, 2017. **17**(4): p. 1654-1660.

90. Chen, C., et al., *Microwave-Assisted Rapid Synthesis of Well-Shaped MOF-74 (Ni) for CO_2 Efficient Capture.* Inorganic Chemistry, 2019. **58**(4): p. 2717-2728.
91. Wang, B., et al., *A review on carbon/magnetic metal composites for microwave absorption.* Journal of Materials Science & Technology, 2021. **86**: p. 91-109.
92. He, G.H., et al., *Rational design of mesoporous MnO_2 microwave absorber with tunable microwave frequency response.* Applied Surface Science, 2019. **490**: p. 372-382.
93. Li, J., et al., *High-stable α-phase NiCo double hydroxide microspheres via microwave synthesis for supercapacitor electrode materials.* Chemical Engineering Journal, 2017. **316**: p. 277-287.
94. Taher, A., B.J. Lumbiny, and I.-M. Lee, *A facile microwave-assisted Knoevenagel condensation of various aldehydes and ketones using amine-functionalized metal organic frameworks.* Inorganic Chemistry Communications, 2020. **119**.
95. Wei, F.-h., et al., *Synthesis and characterization of metal–organic frameworks fabricated by microwave-assisted ball milling for adsorptive removal of Congo red from aqueous solutions.* RSC Adv., 2017. **7**(73): p. 46520-46528.
96. Chen, Y., et al., *Microwave-assisted synthesis of honeycomblike hierarchical spherical Zn-doped Ni-MOF as a high-performance battery-type supercapacitor electrode material.* Electrochimica Acta, 2018. **278**: p. 114-123.
97. Tanabe, K.K. and S.M. Cohen, *Postsynthetic modification of metal–organic frameworks—a progress report.* Chemical Society Reviews, 2011. **40**(2): p. 498-519.
98. Gumilar, G., et al., *General synthesis of hierarchical sheet/plate-like M-BDC (M = Cu, Mn, Ni, and Zr) metal–organic frameworks for electrochemical non-enzymatic glucose sensing.* Chemical Science, 2020. **11**(14): p. 3644-3655.
99. Shekhah, O. and M. Eddaoudi, *The liquid phase epitaxy method for the construction of oriented ZIF-8 thin films with controlled growth on functionalized surfaces.* Chemical Communications, 2013. **49**(86): p. 10079-10081.
100. Arslan, H.K., et al., *High-Throughput Fabrication of Uniform and Homogenous MOF Coatings.* Advanced Functional Materials, 2011. **21**(22): p. 4228-4231.
101. Deria, P., et al., *Beyond post-synthesis modification: evolution of metal–organic frameworks via building block replacement.* Chemical Society Reviews, 2014. **43**(16): p. 5896-5912.
102. Wang, L., et al., *Synthesis of a Multinanoparticle-Embedded Core/Mesoporous Silica Shell Structure As a Durable Heterogeneous Catalyst.* Langmuir, 2012. **28**(11): p. 4920-4925.
103. Zhang, W., et al., *Nanowire-directed templating synthesis of metal-organic framework nanofibers and their derived porous doped carbon nanofibers for enhanced electrocatalysis.* J Am Chem Soc, 2014. **136**(41): p. 14385-8.
104. Huang, G., D.M. Yinab, and L.M. Wang, *A general strategy for coating metal–organic frameworks on diverse components and architectures.* Journal of Materials Chemistry A, 2016.
105. Tate, K.L., et al., *Zeolite adsorbent-MOF layered nanovalves for CH4 storage.* Adsorption, 2016. **23**(1): p. 19-24.
106. Wu, Q., et al., *Sandwich structured membrane adsorber with metal organic frameworks for aflatoxin B1 removal.* Separation and Purification Technology, 2020. **246**.
107. Chen, S.Y., et al., *Probing Interactions between Metal-Organic Frameworks and Freestanding Enzymes in a Hollow Structure.* Nano Lett, 2020. **20**(9): p. 6630-6635.

108. Denny, M.S., Jr., et al., *Transmission Electron Microscopy Reveals Deposition of Metal Oxide Coatings onto Metal-Organic Frameworks.* J Am Chem Soc, 2018. **140**(4): p. 1348-1357.
109. Wang, K., et al., *A novel carbon-coated Ga_2S_3 anode material derived from post-synthesis modified MOF for high performance lithium ion and sodium ion batteries.* Electrochimica Acta, 2019. **322**: p. 134790.
110. Martinez Joaristi, A., et al., *Electrochemical Synthesis of Some Archetypical Zn2+, Cu2+, and Al3+Metal Organic Frameworks.* Crystal Growth & Design, 2012. **12**(7): p. 3489-3498.
111. Jabarian, S. and A. Ghaffarinejad, *Electrochemical Synthesis of NiBTC Metal Organic Framework Thin Layer on Nickel Foam: An Efficient Electrocatalyst for the Hydrogen Evolution Reaction.* Journal of Inorganic and Organometallic Polymers and Materials, 2019. **29**(5): p. 1565-1574.
112. Pilloni, M., et al., *Liquid-assisted mechanochemical synthesis of an iron carboxylate Metal Organic Framework and its evaluation in diesel fuel desulfurization.* Microporous and Mesoporous Materials, 2015. **213**: p. 14-21.
113. Shi, Y., et al., *Mechanochemical synthesis of an ethylene sieve UTSA-280.* Journal of Solid State Chemistry, 2020. **287**.
114. Jia, Z., et al., *Electrochemical fabrication of metal–organic frameworks membranes and films: A review.* Microporous and Mesoporous Materials, 2020. **305**: p. 110322.
115. Yang, Q.J., et al., *Self-templated transformation of MOFs into layered double hydroxide nanoarrays with selectively formed Co_9S_8 for high-performance asymmetric supercapacitors.* Chemical Engineering Journal, 2018. **354**: p. 716-726.
116. Ghoorchian, A., et al., *Chapter 9 - Electrochemical synthesis of MOFs*, in *Metal-Organic Frameworks for Biomedical Applications*, M. Mozafari, Editor. 2020, Woodhead Publishing. p. 177-195.
117. Beladona, S.U.M., A. Rochliadi, and A. Patah, *A Facile Synthesis of HKUST-1 MOF through Reductive Electrosynthesis Method.* Key Engineering Materials, 2021. **874**: p. 3-12.
118. Manjunatha, H., et al., *Chapter 4 - Electrochemical aspects of metal-organic frameworks*, in *Metal-Organic Frameworks for Chemical Reactions*, A. Khan, et al., Editors. 2021, Elsevier. p. 65-109.
119. Stassen, I., et al., *Electrochemical Film Deposition of the Zirconium Metal–Organic Framework UiO-66 and Application in a Miniaturized Sorbent Trap.* Chemistry of Materials, 2015. **27**(5): p. 1801-1807.
120. Thorne, M.F., et al., *Mechanochemical synthesis of mixed metal, mixed linker, glass-forming metal–organic frameworks.* Green Chemistry, 2020. **22**(8): p. 2505-2512.
121. Masoomi, M.Y., et al., *Selective CO_2 Capture in Metal-Organic Frameworks with Azine-Functionalized Pores Generated by Mechanosynthesis.* Crystal Growth & Design, 2014. **14**(5): p. 2092-2096.
122. Stolar, T., et al., *In Situ Monitoring of the Mechanosynthesis of the Archetypal Metal–Organic Framework HKUST-1: Effect of Liquid Additives on the Milling Reactivity.* Inorganic Chemistry, 2017. **56**(11): p. 6599-6608.
123. Paseta, L., et al., *Solventless Synthesis of MOFs at High Pressure.* ACS Sustainable Chemistry & Engineering, 2016. **4**(7): p. 3780-3785.

124. Crawford, D., et al., *Synthesis by extrusion: continuous, large-scale preparation of MOFs using little or no solvent.* Chemical Science, 2015. **6**(3): p. 1645-1649.
125. Zhao, X., et al., *A Facile Grinding Method for the Synthesis of 3D Ag Metal-Organic Frameworks (MOFs) Containing $Ag_6Mo_7O_{24}$ for High-Performance Supercapacitors.* Chemistry, 2020. **26**(20): p. 4613-4619.
126. Friscic, T., et al., *Ion- and liquid-assisted grinding: improved mechanochemical synthesis of metal-organic frameworks reveals salt inclusion and anion templating.* Angew Chem Int Ed Engl, 2010. **49**(4): p. 712-5.
127. Crawford, D., et al., *Synthesis by extrusion: continuous, large-scale preparation of MOFs using little or no solvent.* Chem Sci, 2015. **6**(3): p. 1645-1649.
128. Khabzina, Y., et al., *Synthesis and shaping scale-up study of functionalized UiO-66 MOF for ammonia air purification filters.* Industrial & Engineering Chemistry Research, 2018. **57**(24): p. 8200-8208.
129. Laybourn, A., et al., *Combining continuous flow oscillatory baffled reactors and microwave heating: Process intensification and accelerated synthesis of metal-organic frameworks.* Chemical Engineering Journal, 2019. **356**: p. 170-177.
130. Stassin, T., et al., *Aqueous Flow Reactor and Vapour-Assisted Synthesis of Aluminium Dicarboxylate Metal-Organic Frameworks with Tuneable Water Sorption Properties.* Chemistry, 2020.
131. Li, M., et al., *Synthesis of a 2D phosphorus material in a MOF-based 2D nano-reactor.* Chem Sci, 2018. **9**(27): p. 5912-5918.
132. Bayliss, P.A., et al., *Synthesis of metal–organic frameworks by continuous flow.* Green Chem., 2014. **16**(8): p. 3796-3802.
133. Paseta, L., et al., *Accelerating the controlled synthesis of metal-organic frameworks by a microfluidic approach: a nanoliter continuous reactor.* ACS Appl Mater Interfaces, 2013. **5**(19): p. 9405-10.
134. Munn, A.S., et al., *Large-scale continuous hydrothermal production and activation of ZIF-8.* Chem Commun (Camb), 2015. **51**(64): p. 12811-4.
135. Rubio-Martinez, M., et al., *Scalability of Continuous Flow Production of Metal-Organic Frameworks.* ChemSusChem, 2016. **9**(9): p. 938-41.
136. Fatima, R., S. Park, and J.-O. Kim, *Effect of molar ration of Ti/Ligand on the synthesis of MIL-125(Ti) and its adsorption and photocatalytic properties.* Journal of Industrial and Engineering Chemistry, 2020. **90**: p. 166-177.
137. Du, P., et al., *Fabrication of hierarchical porous nickel based metal-organic framework (Ni-MOF) constructed with nanosheets as novel pseudo-capacitive material for asymmetric supercapacitor.* Journal of Colloid and Interface Science, 2018. **518**: p. 57-68.
138. Liu, C., et al., *Establishing Porosity Gradients within Metal–Organic Frameworks Using Partial Postsynthetic Ligand Exchange.* Journal of the American Chemical Society, 2016. **138**(37): p. 12045-12048.
139. Bosch, M., M. Zhang, and H.-C. Zhou, *Increasing the Stability of Metal-Organic Frameworks.* Advances in Chemistry, 2014. **2014**: p. 182327.
140. Liu, Y., et al., *Impact of metal ions and organic ligands on uranium removal properties by zeolitic imidazolate framework materials.* Journal of Cleaner Production, 2021. **278**.
141. Yang, C., et al., *A new promising Ni-MOF superstructure for high-performance supercapacitors.* Chemical Communications, 2020. **56**(12): p. 1803-1806.

142. Han, Y., et al., *Influence of metal ions on the selective catalytic oxidation properties of isostructural MOFs.* Inorganica Chimica Acta, 2018. **471**: p. 176-179.
143. Xu, H.-L., et al., *The impact of metal ions on photoinduced electron-transfer properties: four photochromic metal–organic frameworks based on a naphthalenediimide chromophore.* CrystEngComm, 2018. **20**(17): p. 2430-2439.
144. Yue, M.L., et al., *Six Isomorphous Window-Beam MOFs: Explore the Effects of Metal Ions on MOF-Derived Carbon for Supercapacitors.* Chemistry, 2018. **24**(60): p. 16160-16169.
145. Wang, P. and G.-L. Guo, *Influence of Different Organic Carboxylate Anions On the Crystal Structure of Silver(I) Coordination Polymers.* Chinese Journal of Structural Chemistry, 2012. **31**: p. 1008-1020.
146. Burneo, I., et al., *The influence of the enantiomeric ratio of an organic ligand on the structure and chirality of metal-organic frameworks.* Chem Commun (Camb), 2014. **50**(89): p. 13829-32.
147. Guo, G.S., et al., *Hydrothermal Synthesis and Crystal Structure of Two Novel Lanthanide MOF Compounds with One-Dimensional Water Chains.* Chinese Journal of Inorganic Chemistry, 2010. **26**(9): p. 1583-1589.
148. Strutt, N.L., H. Zhang, and J.F. Stoddart, *Enantiopure pillar[5]arene active domains within a homochiral metal–organic framework.* Chemical Communications, 2014. **50**(56): p. 7455-7458.
149. Ji, Y.J., et al., *Understanding the Effect of Ligands on C_2H_2 Storage and C_2H_2/CH_4, C_2H_2/CO_2 Separation in Metal-Organic Frameworks with Open Cu(II) Sites.* Journal of Physical Chemistry C, 2017. **121**(43): p. 24104-24113.
150. Chang, B., et al., *Chemical blowing strategy synthesis of nitrogen-rich porous graphitized carbon nanosheets: Morphology, pore structure and supercapacitor application.* Chemical Engineering Journal, 2017. **312**: p. 191-203.
151. Choi, K.M., et al., *Supercapacitors of Nanocrystalline MetalOrganic Frameworks.* 2014.
152. Zhang, X., et al., *Shape-controlled synthesis of Ni-based metal-organic frameworks with albizia flower-like spheres@nanosheets structure for high performance supercapacitors.* Journal of Colloid and Interface Science, 2020. **575**: p. 347-355.
153. Liu, Y.Y., et al., *Effect of metal-ligand ratio on the CO_2 adsorption properties of Cu-BTC metal-organic frameworks.* Rsc Advances, 2018. **8**(62): p. 35551-35556.
154. Lin, Z.-J., et al., *Microwave-Assisted Synthesis of a Series of Lanthanide Metal–Organic Frameworks and Gas Sorption Properties.* Inorganic Chemistry, 2012. **51**(3): p. 1813-1820.
155. Tezerjani, A.A., R. Halladj, and S. Askari, *Different view of solvent effect on the synthesis methods of zeolitic imidazolate framework-8 to tuning the crystal structure and properties.* RSC Advances, 2021. **11**(32): p. 19914-19923.
156. Chen, D.M., et al., *Template-directed synthesis of a luminescent Tb-MOF material for highly selective Fe^{3+} and Al^{3+} ion detection and VOC vapor sensing.* Journal of Materials Chemistry C, 2017. **5**(9): p. 2311-2317.
157. Zhang, H., et al., *Hierarchically porous metal–organic frameworks with single-crystal structures and their enhanced catalytic properties.* CrystEngComm, 2018. **20**(38): p. 5754-5759.
158. Yue, D., et al., *Solvent triggering structural changes for two terbium-based metal-organic frameworks and their photoluminescence sensing.* Chem Commun (Camb), 2020. **56**(31): p. 4320-4323.

159. Zhao, M.Y., et al., *Structural variation of transition metal-organic frameworks using deep eutectic solvents with different hydrogen bond donors.* Dalton Trans, 2019. **48**(27): p. 10199-10209.
160. Ramachandran, R., et al., *Morphology-dependent electrochemical properties of cobalt-based metal organic frameworks for supercapacitor electrode materials.* Electrochimica Acta, 2018. **267**: p. 170-180.
161. Aftab, L., et al., *Synthesis, characterization and gas adsorption analysis of solvent dependent Zn-BTC metal organic frameworks.* Separation Science and Technology, 2021. **56**(13): p. 2159-2169.
162. Lee, J.-S., et al., *Microwave Synthesis of a Porous Metal-Organic Framework, Nickel(II) Dihydroxyterephthalate and its Catalytic Properties in Oxidation of Cyclohexene.* Bulletin of the Korean Chemical Society, 2010. **31**(6): p. 1489-1495.
163. Xuan, W., et al., *Influence of synthesis temperature on cobalt metal-organic framework (Co-MOF) formation and its electrochemical performance towards supercapacitor electrodes.* Journal of Solid State Electrochemistry, 2018. **22**(12): p. 3873-3881.
164. Al‐Kutubi, H., et al., *Electrosynthesis of Metal–Organic Frameworks: Challenges and Opportunities.* ChemElectroChem, 2015. **2**(4): p. 447-447.
165. Wang, C.-c., et al., *Series metal–organic frameworks constructed from 1,10-phenanthroline and 3,3′,4,4′-biphenyltetracarboxylic acid: Hydrothermal synthesis, luminescence and photocatalytic properties.* Journal of molecular structure, 2015. **1080**: p. 44-51.
166. Zhang, C.Y., et al., *Hydrothermal Synthesis, Crystal Structure, and Luminescent Properties of Two Zinc(II) and Cadmium(II) 3D Metal‐Organic Frameworks.* Zeitschrift für anorganische und allgemeine Chemie (1950), 2013. **639**(5): p. 826-831.
167. Pu, M., et al., *Synthesis of iron-based metal-organic framework MIL-53 as an efficient catalyst to activate persulfate for the degradation of Orange G in aqueous solution.* Appl Catal A Gen, 2018. **549**: p. 82-92.
168. Jiang, H., et al., *Temperature effect on the morphology and catalytic performance of Co-MOF-74 in low-temperature NH3-SCR process.* Catalysis Communications, 2016. **80**: p. 24-27.
169. Jiao, Y., et al., *Layered nickel metal–organic framework for high performance alkaline battery-supercapacitor hybrid devices.* Journal of materials chemistry A, 2016. **2016 v.4 no.34**(no. 34): p. pp. 13344-13351.
170. Otun, K.O., *Temperature-controlled activation and characterization of iron-based metal-organic frameworks.* Inorganica Chimica Acta, 2020. **507**.
171. Yu, T., et al., *Roles of temperature, solvent, M/L ratios and anion in preparing complexes containing a Himta ligand.* CrystEngComm, 2016. **18**(8): p. 1350-1362.
172. Yuan, F., et al., *Effect of pH/metal ion on the structure of metal–organic frameworks based on novel bifunctionalized ligand 4′-carboxy-4,2′:6′,4′′-terpyridine.* CrystEngComm, 2013. **15**(7).
173. Chi-Duran, I., et al., *pH-Controlled Assembly of 3D and 2D Zinc-Based Metal-Organic Frameworks with Tetrazole Ligands.* ACS Omega, 2018. **3**(1): p. 801-807.
174. Sen, R., et al., *pH-Tuned Modulation of 1D Chain to 3D Metal-Organic Framework: Synthesis, Structure and Their Useful Application in the Heterogeneous Claisen-Schmidt Reaction.* Chempluschem, 2015. **80**(3): p. 591-598.

175. Luo, L., et al., *pH-Dependent cobalt(ii) frameworks with mixed 3,3′,5,5′-tetra(1H-imidazol-1-yl)-1,1′-biphenyl and 1,3,5-benzenetricarboxylate ligands: synthesis, structure and sorption property.* CrystEngComm, 2013. **15**(45).
176. Volkringer, C., et al., *High-throughput aided synthesis of the porous metal-organic framework-type aluminum pyromellitate, MIL-121, with extra carboxylic acid functionalization.* Inorg Chem, 2010. **49**(21): p. 9852-62.
177. Seoane, B., et al., *Metal organic framework synthesis in the presence of surfactants: towards hierarchical MOFs?* CrystEngComm, 2015. **17**(7): p. 1693-1700.
178. Campagnol, N., et al., *A Hybrid Supercapacitor based on Porous Carbon and the Metal-Organic Framework MIL-100(Fe).* ChemElectroChem, 2014. **1**(7): p. 1182-1188.
179. Bao, W., et al., *3D hybrid–porous carbon derived from carbonization of metal organic frameworks for high performance supercapacitors.* Journal of Power Sources, 2016. **325**: p. 286-291.
180. Huang, C.X., et al., *In situ growth of ZIF-8-derived ternary ZnO/$ZnCo_2O_4$/NiO for high performance asymmetric supercapacitors.* Nanoscale, 2019. **11**(20): p. 10114-10128.
181. Liu, X., et al., *Highly Water-Stable Zirconium Metal–Organic Framework UiO-66 Membranes Supported on Alumina Hollow Fibers for Desalination.* Journal of the American Chemical Society, 2015. **137**(22): p. 6999-7002.
182. Goswami, S., et al., *A porous, electrically conductive hexa-zirconium(iv) metal–organic framework.* Chemical Science, 2018. **9**(19): p. 4477-4482.
183. Ray, D., et al., *Tuning the Conductivity of Hexa-Zirconium(IV) Metal–Organic Frameworks by Encapsulating Heterofullerenes.* Chemistry of Materials, 2021. **33**(4): p. 1182-1189.
184. Gao, W., et al., *Fabrication of Hierarchical Porous Metal–Organic Framework Electrode for Aqueous Asymmetric Supercapacitor.* ACS Sustainable Chemistry & Engineering, 2017. **5**(5): p. 4144-4153.
185. Tan, Y., et al., *Facile synthesis and supercapacitive properties of Zr-metal organic frameworks (UiO-66).* RSC Advances, 2015. **5**(23): p. 17601-17605.
186. Liu, L., et al., *Growth‐Oriented Fe‐Based MOFs Synergized with Graphene Aerogels for High‐Performance Supercapacitors.* Advanced Materials Interfaces, 2018. **5**(8).
187. He, L., et al., *Observation of Ion Electrosorption in Metal‐Organic Framework Micropores with In Operando Small‐Angle Neutron Scattering.* Angewandte Chemie International Edition, 2020. **59**(24): p. 9773-9779.
188. Liu, Q., et al., *A copper-based layered coordination polymer: synthesis, magnetic properties and electrochemical performance in supercapacitors.* Dalton Trans, 2015. **44**(44): p. 19175-84.
189. Xiong, X., et al., *Metal–organic frameworks based on halogen-bridged dinuclear-Cu-nodes as promising materials for high performance supercapacitor electrodes.* CrystEngComm, 2017. **19**(47): p. 7177-7184.
190. He, Y., et al., *Electronic Doping of Metal-Organic Frameworks for High-Performance Flexible Micro-Supercapacitors.* Small Structures, 2021. **2**(3): p. 2000095.
191. Linnemann, J., et al., *Electrodeposited films to MOF-derived electrochemical energy storage electrodes: a concept of simplified additive-free electrode processing for self-standing, ready-to-use materials.* Journal of Materials Chemistry A, 2017. **5**(35): p. 18420-18428.

192. Feng, C., et al., *Structural Elucidation and Supercapacitive Performance on a Mn(II)-Based MOF.* Crystal Growth & Design, 2020. **20**(9): p. 5682-5687.
193. Wang, X., et al., *Layered manganese-based metal–organic framework as a high capacity electrode material for supercapacitors.* RSC Advances, 2017. **7**(47): p. 29611-29617.
194. Shinde, P.A., et al., *Layered manganese metal-organic framework with high specific and areal capacitance for hybrid supercapacitors.* Chemical Engineering Journal, 2020. **387**.
195. Xu, J., et al., *Enhanced electrochemical properties of manganese-based metal organic framework materials for supercapacitors.* Journal of Applied Electrochemistry, 2019. **49**(11): p. 1091-1102.
196. Sundriyala, S., S. Mishra, and A. Deep, *Study of Manganese-1,4-Benzenedicarboxylate Metal Organic Framework Electrodes Based Solid State Symmetrical Supercapacitor.* Energy Procedia, 2019.
197. Wang, Z., et al., *A Metal-Organic Framework Host for Highly Reversible Dendrite-free Zinc Metal Anodes.* Joule, 2019. **3**(5): p. 1289-1300.
198. Kannangara, Y.Y., U.A. Rathnayake, and J.-K. Song, *Redox active multi-layered Zn-pPDA MOFs as high-performance supercapacitor electrode material.* Electrochimica Acta, 2019. **297**: p. 145-154.
199. Zhu, G., et al., *A self-supported hierarchical Co-MOF as a supercapacitor electrode with ultrahigh areal capacitance and excellent rate performance.* Chem Commun (Camb), 2018. **54**(74): p. 10499-10502.
200. Dou, J.H., et al., *Signature of Metallic Behavior in the Metal–Organic Frameworks M_3(hexaiminobenzene)$_2$ (M = Ni, Cu).* Journal of the American Chemical Society, 2017. **139**(39): p. 13608-13611.
201. Salunkhe, R.R., et al., *A high-performance supercapacitor cell based on ZIF-8-derived nanoporous carbon using an organic electrolyte.* Chemical Communications, 2016. **52**(26): p. 4764-4767.
202. Wechsler, S.C. and F.Z. Amir, *Superior Electrochemical Performance of Pristine Nickel Hexaaminobenzene MOF Supercapacitors Fabricated by Electrophoretic Deposition.* ChemSusChem, 2020. **13**(6): p. 1491-1495.
203. Cheng, C., et al., *Preparation of flexible supercapacitor with RGO/Ni-MOF film on Ni-coated polyester fabric.* Electrochimica Acta, 2019. **318**: p. 23-31.
204. Rong, H., et al., *A three-dimensional Mn-based MOF as a high-performance supercapacitor electrode.* Dalton Transactions, 2023. **52**(7): p. 1962-1969.
205. Zhang, H., et al., *Wire spherical-shaped Co-MOF electrode materials for high-performance all-solid-state flexible asymmetric supercapacitor device.* Journal of Alloys and Compounds, 2021. **879**: p. 160423.
206. Xiao, G.-B., et al., *Dinuclear cobalt-based pillar-layered-like MOF as an electrode material for supercapacitor and photocatalysis activity.* Polyhedron, 2019. **162**: p. 39-44.
207. Chaturvedi, G., et al., *A systematic approach for selecting suitable morphologies for supercapacitor applications through morphological stability map – A case of Ni-MOF.* Ceramics International, 2023. **49**(6): p. 9382-9394.
208. Pan, Y., et al., *Benzoic acid-modified 2D Ni-MOF for high-performance supercapacitors.* Electrochimica Acta, 2022. **403**: p. 139679.
209. Wang, J.-W., et al., *A novel moss-like 3D Ni-MOF for high performance supercapacitor electrode material.* Journal of Solid State Chemistry, 2022. **309**: p. 122994.

210. Wang, Y., et al., *Application of MOFs-derived mixed metal oxides in energy storage.* Journal of Electroanalytical Chemistry, 2020. **878**.
211. Ouyang, Y., et al., *Hierarchical structure electrodes of NiO ultrathin nanosheets anchored to $NiCo_2O_4$ on carbon cloth with excellent cycle stability for asymmetric supercapacitors.* Chemical Engineering Journal, 2019. **355**: p. 416-427.
212. Zhang, J.J., et al., *Synthesis of 3D porous flower-like NiO/Ni_6MnO_8 composites for supercapacitor with enhanced performance.* Journal of Materials Science-Materials in Electronics, 2018. **29**(9): p. 7510-7518.
213. Yu, J., et al., *Facile fabrication of ZIF-derived graphene-based 2D Zn/Co oxide hybrid for high-performance supercapacitors.* Journal of Energy Storage, 2020. **27**.
214. Chen, S., et al., *Porous $ZnCo_2O_4$ nanoparticles derived from a new mixed-metal organic framework for supercapacitors.* Inorganic Chemistry Frontiers, 2015. **2**(2): p. 177-183.
215. He, D., et al., *Asymmetric Supercapacitors Based on Hierarchically Nanoporous Carbon and ZnCo2O4 From a Single Biometallic Metal-Organic Frameworks (Zn/Co-MOF).* Front Chem, 2020. **8**: p. 719.
216. You, P.Y. and S.K. Kamarudin, *Recent progress of carbonaceous materials in fuel cell applications: An overview.* Chemical Engineering Journal, 2017. **309**: p. 489-502.
217. Yi-Ju, L., Z. Jin-Hui, and G. Shao-Jun, *Advanced Carbon Materials for Non-aqueous Potassium Ion Battery Anodes.* CHINESE JOURNAL OF STRUCTURAL CHEMISTRY, 2019. **38**(12): p. 1993-1998.
218. Chang, T.H., et al., *Synthesis of MOF-525 Derived Nanoporous Carbons with Different Particle Sizes for Supercapacitor Application.* Chem Asian J, 2017. **12**(21): p. 2857-2862.
219. Wang, C., et al., *Electrospun metal–organic framework derived hierarchical carbon nanofibers with high performance for supercapacitors.* Chemical Communications, 2017. **53**(10): p. 1751-1754.
220. Cao, X., et al., *Hybrid micro-/nano-structures derived from metal–organic frameworks: preparation and applications in energy storage and conversion.* Chemical Society Reviews, 2017. **46**(10): p. 2660-2677.
221. Bonaccorso, F., et al., *2D materials. Graphene, related two-dimensional crystals, and hybrid systems for energy conversion and storage.* Science, 2015. **347**(6217): p. 1246501.
222. Salunkhe, R.R., et al., *Fabrication of symmetric supercapacitors based on MOF-derived nanoporous carbons.* J. Mater. Chem. A, 2014. **2**(46): p. 19848-19854.
223. Wang, Y., et al., *A new Cd-based metal organic framework derived nitrogen doped nano-porous carbon for high supercapacitor performance.* Polyhedron, 2020. **189**.
224. Wu, S.-C., et al., *Waffle-Like Carbons Combined with Enriched Mesopores and Highly Heteroatom-Doped Derived from Sandwiched MOF/LDH/MOF for High-Rate Supercapacitor.* Nanomaterials, 2020. **10**(12).
225. Liu, M., et al., *Ultramicroporous carbon nanoparticles derived from metal–organic framework nanoparticles for high-performance supercapacitors.* Materials Chemistry and Physics, 2018. **211**: p. 234-241.
226. Tang, Z., et al., *MOF-derived N-doped carbon bubbles on carbon tube arrays for flexible high-rate supercapacitors.* Energy Storage Materials, 2018. **10**: p. 75-84.
227. Umar, A., et al., *Colloidal synthesis of NiMn2O4 nanodisks decorated reduced graphene oxide for electrochemical applications.* Microchemical Journal, 2021. **160**: p. 105630.
228. An, C., et al., *Novel three-dimensional NiCo2O4 hierarchitectures: solvothermal synthesis and electrochemical properties.* CrystEngComm, 2014. **16**(3): p. 385-392.

229. Qu, C., et al., *Functionalized Bimetallic Hydroxides Derived from Metal–Organic Frameworks for High-Performance Hybrid Supercapacitor with Exceptional Cycling Stability.* ACS Energy Letters, 2017. **2**(6): p. 1263-1269.
230. Dong, Y., et al., *Facile synthesis of hierarchical nanocage MnCo2O4 for high performance supercapacitor.* Electrochimica Acta, 2017. **225**: p. 39-46.
231. Hu, X.-W., et al., *Starfish-shaped Co3O4/ZnFe2O4 Hollow Nanocomposite: Synthesis, Supercapacity, and Magnetic Properties.* ACS Applied Materials & Interfaces, 2015. **7**(18): p. 9972-9981.
232. Biswal, A., et al., *Role of Additives in Electrochemical Deposition of Ternary Metal Oxide Microspheres for Supercapacitor Applications.* ACS Omega, 2020. **5**(7): p. 3405-3417.
233. Raphael Ezeigwe, E., et al., *MOF-deviated zinc-nickel–cobalt ZIF-67 electrode material for high-performance symmetrical coin-shaped supercapacitors.* Journal of Colloid and Interface Science, 2020. **574**: p. 140-151.
234. Yue, M.-L., et al., *Six Isomorphous Window-Beam MOFs: Explore the Effects of Metal Ions on MOF-Derived Carbon for Supercapacitors.* Chemistry – A European Journal, 2018. **24**(60): p. 16160-16169.
235. Cai, J., et al., *MOF-derived conductive carbon nitrides for separator-modified Li–S batteries and flexible supercapacitors.* Journal of Materials Chemistry A, 2020. **8**(4): p. 1757-1766.
236. Chia, J.S.Y., et al., *A novel one step synthesis of graphene via sonochemical-assisted solvent exfoliation approach for electrochemical sensing application.* Chemical Engineering Journal, 2014. **249**: p. 270-278.
237. Brandt, A., et al., *Ionic liquids in supercapacitors.* Mrs Bulletin, 2013. **38**(7): p. 554-559.
238. Gao, S.W., et al., *Facile synthesis of cuboid Ni-MOF for high-performance supercapacitors.* Journal of Materials Science, 2018. **53**(9): p. 6807-6818.
239. Zhao, J. and A.F. Burke, *Review on supercapacitors: Technologies and performance evaluation.* Journal of Energy Chemistry, 2021. **59**: p. 276-291.
240. Cherusseri, J., et al., *Flexible supercapacitor electrodes using metal–organic frameworks.* Nanoscale, 2020. **12**(34): p. 17649-17662.
241. Qiang Zheng, S., et al., *Probing the Effect of Solvents on the Electrochemical Performance of Graphene Incorporated Nickel-Based Metal Organic Frameworks.* Journal of Electroanalytical Chemistry, 2022(925): p. 116860.
242. Ahsan, M.A., et al., *Nanoscale nickel metal organic framework decorated over graphene oxide and carbon nanotubes for water remediation.* Science of The Total Environment, 2020. **698**: p. 134214.
243. Song, K., et al., *Tailoring the crystal forms of the Ni-MOF catalysts for enhanced photocatalytic CO_2-to-CO performance.* Applied Catalysis B: Environmental, 2022. **309**: p. 121232.
244. Wang, H., et al., *Ni_2P nanocrystals embedded Ni-MOF nanosheets supported on nickel foam as bifunctional electrocatalyst for urea electrolysis.* Scientific Reports, 2021. **11**(1): p. 21414.
245. Zhang, Y., et al., *Rock salt type $NiCo_2O_3$ supported on ordered mesoporous carbon as a highly efficient electrocatalyst for oxygen evolution reaction.* Applied Catalysis B: Environmental, 2019. **256**: p. 117852.
246. Yang, J., et al., *Zn-doped Ni-MOF material with a high supercapacitive performance.* Journal of Materials Chemistry A, 2014. **2**(44): p. 19005-19010.

247. Gumilar, G., et al., *General synthesis of hierarchical sheet/plate-like M-BDC (M= Cu, Mn, Ni, and Zr) metal–organic frameworks for electrochemical non-enzymatic glucose sensing.* Chemical science, 2020. **11**(14): p. 3644-3655.
248. Seo, Y.-K., et al., *Microwave synthesis of hybrid inorganic–organic materials including porous $Cu_3(BTC)_2$ from Cu(II)-trimesate mixture.* Microporous and Mesoporous Materials, 2009. **119**(1): p. 331-337.
249. Abd El Salam, H.M., et al., *Antimicrobial Activities of Green Synthesized Ag Nanoparticles @ Ni-MOF Nanosheets.* Journal of Inorganic and Organometallic Polymers and Materials, 2018. **28**(6): p. 2791-2798.
250. Bae, J., et al., *Multiple Coordination Exchanges for Room-Temperature Activation of Open-Metal Sites in Metal–Organic Frameworks.* ACS Applied Materials & Interfaces, 2017. **9**(29): p. 24743-24752.
251. Galli, S., et al., *Fluorous Metal–Organic Frameworks and Nonporous Coordination Polymers as Low-κ Dielectrics.* Advanced Functional Materials, 2019. **29**(40): p. 1904707.
252. Li, J., Q. Wu, and J. Wu, *Synthesis of Nanoparticles via Solvothermal and Hydrothermal Methods 12.* 2016.
253. Khalaf, A.A. and K.J. Takrouri, *Spontaneous nucleation in hypoeutectic Al–Cu system by controlled diffusion solidification process.* SN Applied Sciences, 2020. **2**(8): p. 1337.
254. Hou, J., et al., *Intermarriage of halide perovskites and metal‐organic framework crystals.* Angewandte Chemie, 2020. **132**(44): p. 19602-19617.
255. Celante, D., et al., *Measurement and Correlation of the Solubility of Terephthalic Acid in Six Pure Solvents and Five Binary Mixtures.* Journal of Chemical & Engineering Data, 2021. **66**(9): p. 3512-3519.
256. Tsai, C.-W. and E.H.G. Langner, *The effect of synthesis temperature on the particle size of nano-ZIF-8.* Microporous and Mesoporous Materials, 2016. **221**: p. 8-13.
257. Wu, S., M. Li, and Y. Sun, *In Situ Synchrotron X-ray Characterization Shining Light on the Nucleation and Growth Kinetics of Colloidal Nanoparticles.* Angewandte Chemie International Edition, 2019. **58**(27): p. 8987-8995.
258. Naik, A.N., et al., *Evaluating the mechanism of nucleation and growth of silver nanoparticles in a polymer membrane under continuous precursor supply: tuning of multiple to single nucleation pathway.* Physical Chemistry Chemical Physics, 2019. **21**(8): p. 4193-4199.
259. Szabo, T., P. Maroni, and I. Szilagyi, *Size-dependent aggregation of graphene oxide.* Carbon, 2020. **160**: p. 145-155.
260. Logan, M.W., S. Langevin, and Z. Xia, *Reversible Atmospheric Water Harvesting Using Metal-Organic Frameworks.* Scientific Reports, 2020. **10**(1): p. 1492.
261. Shaddel, S., et al., *Engineering of struvite crystals by regulating supersaturation – Correlation with phosphorus recovery, crystal morphology and process efficiency.* Journal of Environmental Chemical Engineering, 2019. **7**(1): p. 102918.
262. Wang, X., et al., *Rapid construction of TiO_2 aggregates using microwave assisted synthesis and its application for dye-sensitized solar cells.* RSC advances, 2015. **5**(12): p. 8622-8629.
263. Yang, T., et al., *Kinetic enhanced bio-derived porous carbon tile laminate paper for ultrahigh-rate supercapacitors.* Journal of Power Sources, 2022. **525**: p. 231148.
264. Sundriyal, S., et al., *Tetracyanoquinodimethane doped copper-organic framework electrode with excellent electrochemical performance for energy storage applications.* Electrochimica Acta, 2021. **380**: p. 138229.

265. Yamada, H., et al., *Electrochemical Study of High Electrochemical Double Layer Capacitance of Ordered Porous Carbons with Both Meso/Macropores and Micropores.* The Journal of Physical Chemistry C, 2007. **111**(1): p. 227-233.
266. Kirubasankar, B., et al., *2D $MoSe_2$-$Ni(OH)_2$ nanohybrid as an efficient electrode material with high rate capability for asymmetric supercapacitor applications.* Chemical Engineering Journal, 2019. **355**: p. 881-890.
267. Cheng, L., et al., *Two-for-one strategy: Three-dimensional porous Fe-doped Co_3O_4 cathode and N-doped carbon anode derived from a single bimetallic metal-organic framework for enhanced hybrid supercapacitor.* Journal of Colloid and Interface Science, 2021. **583**: p. 299-309.
268. Zhang, X., et al., *Hierarchical Nickel–Cobalt Phosphide/Phosphate/Carbon Nanosheets for High-Performance Supercapacitors.* ACS Applied Nano Materials, 2020. **3**(12): p. 11945-11954.
269. Li, H., et al., *Intertwined carbon networks derived from Polyimide/Cellulose composite as porous electrode for symmetrical supercapacitor.* Journal of Colloid and Interface Science, 2022. **609**: p. 179-187.
270. Cui, Y., et al., *Controlled Design of Well-Dispersed Ultrathin MoS_2 Nanosheets inside Hollow Carbon Skeleton: Toward Fast Potassium Storage by Constructing Spacious "Houses" for K Ions.* Advanced Functional Materials, 2020. **30**(10): p. 1908755.
271. Guo, T., et al., *Flexible $Ti_3C_2T_x$/Graphene Films with Large-Sized Flakes for Supercapacitors.* Small Structures, 2021. **2**(7): p. 2100015.
272. Jiao, Y., et al., *Layered nickel metal–organic framework for high performance alkaline battery-supercapacitor hybrid devices.* Journal of Materials Chemistry A, 2016. **4**(34): p. 13344-13351.
273. Bi, R., et al., *A Hollow Multi-Shelled Structure for Charge Transport and Active Sites in Lithium-Ion Capacitors.* Angewandte Chemie International Edition, 2020. **59**(12): p. 4865-4868.
274. Wu, T., et al., *A Covalent Black Phosphorus/Metal–Organic Framework Hetero-nanostructure for High-Performance Flexible Supercapacitors.* Angewandte Chemie International Edition, 2021. **60**(18): p. 10366-10374.
275. Zhang, X., et al., *A strawsheave-like metal organic framework Ce-BTC derivative containing high specific surface area for improving the catalytic activity of CO oxidation reaction.* Microporous and Mesoporous Materials, 2018. **259**: p. 211-219.
276. Cheng, W., et al., *One-step microwave hydrothermal preparation of Cd/Zr-bimetallic metal–organic frameworks for enhanced photochemical properties.* Advanced Composites and Hybrid Materials, 2021. **4**(1): p. 150-161.
277. Li, P., et al., *Regulation of the Structure of Zirconium-Based Porphyrinic Metal–Organic Framework as Highly Electrochemiluminescence Sensing Platform for Thrombin.* Analytical Chemistry, 2022. **94**(14): p. 5707-5714.
278. Javed, M.S., et al., *High-performance flexible hybrid-supercapacitor enabled by pairing binder-free ultrathin Ni–Co–O nanosheets and metal-organic framework derived N-doped carbon nanosheets.* Electrochimica Acta, 2020. **349**: p. 136384.
279. He, F., et al., *Hydrothermal synthesis of Ni-based metal organic frameworks/graphene oxide composites as supercapacitor electrode materials.* Journal of Materials Research, 2020. **35**(11): p. 1439-1450.

280. Zhao, S., et al., *Core–shell assembly of carbon nanofibers and a 2D conductive metal–organic framework as a flexible free-standing membrane for high-performance supercapacitors.* Inorganic Chemistry Frontiers, 2019. **6**(7): p. 1824-1830.
281. Zhao, X., et al., *A Facile Grinding Method for the Synthesis of 3D Ag Metal–Organic Frameworks (MOFs) Containing $Ag_6Mo_7O_{24}$ for High-Performance Supercapacitors.* Chemistry – A European Journal, 2020. **26**(20): p. 4613-4619.
282. Ibrahim, I., et al., *Hierarchical nickel-based metal-organic framework/graphene oxide incorporated graphene nanoplatelet electrode with exceptional cycling stability for coin cell and pouch cell supercapacitors.* Journal of Energy Storage, 2021. **43**: p. 103304.
283. Wang, K., et al., *Porous Cobalt Metal–Organic Frameworks as Active Elements in Battery–Supercapacitor Hybrid Devices.* Inorganic Chemistry, 2020. **59**(10): p. 6808-6814.
284. Kazemi, S.H., et al., *Facile synthesis of mixed metal–organic frameworks: electrode materials for supercapacitors with excellent areal capacitance and operational stability.* ACS applied materials & interfaces, 2018. **10**(27): p. 23063-23073.
285. Shrivastav, V., et al., *Metal-organic framework derived zirconium oxide/carbon composite as an improved supercapacitor electrode.* Energy, 2021. **235**: p. 121351.
286. Zhang, Y., et al., *Carbon nanotubes@ metal–organic frameworks as Mn-based symmetrical supercapacitor electrodes for enhanced charge storage.* Rsc Advances, 2015. **5**(72): p. 58100-58106.
287. Zhang, H., et al., *Boosting pseudocapacitive charge storage in in situ functionalized carbons with a high surface area for high-energy asymmetric supercapacitors.* Sustainable Energy & Fuels, 2018. **2**(10): p. 2314-2324.
288. Zequine, C., et al., *High per formance and flexible supercapacitors based on carbonized bamboo fibers for wide temperature applications.* Scientific reports, 2016. **6**(1): p. 1-10.
289. Jafari, H., et al., *Terbium metal–organic frameworks as capable electrodes for supercapacitors.* New Journal of Chemistry, 2020. **44**(27): p. 11615-11621.
290. Ghamari, F., et al., *Construction of highly efficient new binder-free bimetallic metal–organic framework symmetric supercapacitors: CONSIDERING surface statistical and morphological analyses.* Journal of Materials Chemistry A, 2021. **9**(27): p. 15381-15393.
291. Dai, S., et al., *MOF-derived Co_3O_4 nanosheets rich in oxygen vacancies for efficient all-solid-state symmetric supercapacitors.* Electrochimica Acta, 2019. **328**: p. 135103.
292. Zheng, S., et al., *Ultrathin nanosheet-assembled $[Ni_3(OH)_2(PTA)_2(H_2O)_4]\cdot 2H_2O$ hierarchical flowers for high-performance electrocatalysis of glucose oxidation reactions.* Nanoscale, 2018. **10**(27): p. 13270-13276.
293. Pohanish, R.P. and S.A. Greene, *Wiley guide to chemical incompatibilities*. 2009: John Wiley & Sons.
294. Han, B., et al., *Nickel metal–organic framework monolayers for photoreduction of diluted CO_2: metal‐node‐dependent activity and selectivity.* Angewandte Chemie International Edition, 2018. **57**(51): p. 16811-16815.
295. Pandey, S., et al., *Bulk synthesis of graphene nanosheets from plastic waste: An invincible method of solid waste management for better tomorrow.* Waste Management, 2019. **88**: p. 48-55.
296. Pandey, S., et al., *Graphene nanosheets derived from plastic waste for the application of DSSCs and supercapacitors.* Scientific Reports, 2021. **11**(1): p. 3916.

297. Li, F.L., et al., *Large‐Scale, Bottom‐Up Synthesis of Binary Metal–Organic Framework Nanosheets for Efficient Water Oxidation.* Angewandte Chemie, 2019. **131**(21): p. 7125-7130.
298. Lou, X., et al., *Capacity control of ferric coordination polymers by zinc nitrate for lithium-ion batteries.* RSC advances, 2016. **6**(89): p. 86126-86130.
299. Mesbah, A., et al., *From hydrated $Ni_3(OH)_2(C_8H_4O_4)_2(H_2O)_4$ to anhydrous $Ni_2(OH)_2(C_8H_4O_4)$: impact of structural transformations on magnetic properties.* Inorganic chemistry, 2014. **53**(2): p. 872-881.
300. Yan, Y., et al., *Facile synthesis of an accordion-like Ni-MOF superstructure for high-performance flexible supercapacitors.* Journal of Materials Chemistry A, 2016. **4**(48): p. 19078-19085.
301. Chang, H., et al., *CO_2‐Induced 2D Ni‐BDC Metal–Organic Frameworks with Enhanced Photocatalytic CO_2 Reduction Activity.* Advanced Materials Interfaces, 2021. **8**(13): p. 2100205.
302. Solgi, M., R. Cheraghali, and M. Aghazadeh, *Self-assembled $Co(OH)_2$/functionalized MWNTs/porous graphene ternary binder-free hybrid for supercapacitors.* Journal of Materials Science: Materials in Electronics, 2021. **32**(1): p. 151-167.
303. Gao, Y., et al., *High proton conductivity in cyanide-bridged metal–organic frameworks: understanding the role of water.* Journal of Materials Chemistry A, 2015. **3**(44): p. 22347-22352.
304. Keshmiri, N., et al., *Designing an eco-friendly lanthanide-based metal organic framework (MOF) assembled graphene-oxide with superior active anti-corrosion performance in epoxy composite.* Journal of Cleaner Production, 2021. **319**: p. 128732.
305. Mi, Y., et al., *Solvent directed fabrication of Bi_2WO_6 nanostructures with different morphologies: Synthesis and their shape-dependent photocatalytic properties.* Materials Research Bulletin, 2012. **47**(9): p. 2623-2630.
306. Israr, F., et al., *High yield synthesis of Ni-BTC metal–organic framework with ultrasonic irradiation: role of polar aprotic DMF solvent.* Ultrasonics sonochemistry, 2016. **31**: p. 93-101.
307. Zhang, B., et al., *Solvent determines the formation and properties of metal–organic frameworks.* RSC Advances, 2015. **5**(47): p. 37691-37696.
308. Liu, L., et al., *Growth‐oriented Fe‐based MOFs synergized with graphene aerogels for high‐performance supercapacitors.* Advanced Materials Interfaces, 2018. **5**(8): p. 1701548.
309. Banerjee, D., et al., *Synthesis and structural characterization of magnesium based coordination networks in different solvents.* Crystal Growth & Design, 2011. **11**(6): p. 2572-2579.
310. Gao, S., et al., *Dandelion-like nickel/cobalt metal-organic framework based electrode materials for high performance supercapacitors.* Journal of colloid and interface science, 2018. **531**: p. 83-90.
311. Hou, Y., et al., *Synthesis, characterization and photocatalytic activity of β-Ga_2O_3 nanostructures.* Powder Technology, 2010. **203**(3): p. 440-446.
312. Bi, J., et al., *Effects of the solvent on the structure, morphology and photocatalytic properties of Bi_2MoO_6 in the solvothermal process.* Materials Research Bulletin, 2013. **48**(6): p. 2071-2075.

313. Sarve, A., et al., *Unidirectional growth of organic single crystals of naphthalene, anthracene and pyrene by isothermal expansion of supercritical CO_2.* RSC Advances, 2020. **10**(38): p. 22480-22486.
314. Yang, C., et al., *Nanostructured morphology control and phase transition of zeolitic imidazolate frameworks as an ultra-high performance adsorbent for water purification.* Inorganic Chemistry Frontiers, 2019. **6**(10): p. 2667-2674.
315. Tao, C.-P., et al., *Single-molecule sensing of interfacial acid–base chemistry.* The Journal of Physical Chemistry Letters, 2020. **11**(23): p. 10023-10028.
316. Kim, Y.J., et al., *Polarity-dependent particle size of zeolitic imidazolate framework synthesized in various solvents.* Materials Chemistry and Physics, 2021. **259**: p. 124021.
317. Baradaran, S., et al., *Synthesis and characterization of monetite prepared using a sonochemical method in a mixed solvent system of water/ethylene glycol/N, N-dimethylformamide.* Metallurgical and Materials Transactions A, 2013. **44**(5): p. 2331-2338.
318. Ejaz, A., J.H. Han, and R. Dahiya, *Influence of solvent molecular geometry on the growth of nanostructures.* Journal of Colloid and Interface Science, 2020. **570**: p. 322-331.
319. Kang, C., et al., *Metal-organic framework derived hollow rod-like NiCoMn ternary metal sulfide for high-performance asymmetric supercapacitors.* Chemical Engineering Journal, 2022. **427**: p. 131003.
320. Sarr, S., et al., *Effect of neutral electrolytes on vanadium dioxide microspheres-based electrode materials for asymmetric supercapacitors.* Journal of Energy Storage, 2021. **43**: p. 103294.
321. Rajak, R., M. Saraf, and S.M. Mobin, *Mixed-ligand architected unique topological heterometallic sodium/cobalt-based metal–organic framework for high-performance supercapacitors.* Inorganic chemistry, 2020. **59**(3): p. 1642-1652.
322. Shrivastav, V., et al., *ZIF-67 derived Co_3S_4 hollow microspheres and WS_2 nanorods as a hybrid electrode material for flexible 2V solid-state supercapacitor.* Electrochimica Acta, 2020. **345**: p. 136194.
323. Kumar, R. and M. Bag, *Quantifying Capacitive and Diffusion-Controlled Charge Storage from 3D Bulk to 2D Layered Halide Perovskite-Based Porous Electrodes for Efficient Supercapacitor Applications.* The Journal of Physical Chemistry C, 2021. **125**(31): p. 16946-16954.
324. Wang, K., et al., *2D Metal–Organic Frameworks (MOFs) for High-Performance BatCap Hybrid Devices.* Small, 2020. **16**(30): p. 2001987.
325. Lu, C. and X. Chen, *Electrospun polyaniline nanofiber networks toward high‐performance flexible supercapacitors.* Advanced Materials Technologies, 2019. **4**(11): p. 1900564.
326. Wu, Y.-y., et al., *Self-assembled activated carbon sandwiched graphene film for symmetrical supercapacitors.* Journal of Central South University, 2020. **27**(12): p. 3603-3614.
327. Azadfalah, M., A. Sedghi, and H. Hosseini, *Synthesis of Nano-Flower Metal–Organic Framework/Graphene Composites As a High-Performance Electrode Material for Supercapacitors.* Journal of Electronic Materials, 2019. **48**(11): p. 7011-7024.
328. Wang, H., et al., *3D graphene‐based macrostructures for water treatment.* Advanced Materials, 2020. **32**(3): p. 1806843.

329. Dubal, D.P., et al., *Metal‐organic framework (MOF) derived electrodes with robust and fast lithium storage for Li‐ion hybrid capacitors.* Advanced Functional Materials, 2019. **29**(19): p. 1900532.
330. Majumdar, D., M. Mandal, and S.K. Bhattacharya, *Journey from supercapacitors to supercapatteries: recent advancements in electrochemical energy storage systems.* Emergent Materials, 2020. **3**: p. 347-367.
331. Sekhar, S.C., et al., *Metal‐Organic Framework‐Derived $Co_3V_2O_8$@ CuV_2O_6 Hybrid Architecture as a Multifunctional Binder‐Free Electrode for Li‐Ion Batteries and Hybrid Supercapacitors.* Small, 2020. **16**(48): p. 2003983.
332. Gu, Y., et al., *Highly N/O co-doped ultramicroporous carbons derived from nonporous metal-organic framework for high performance supercapacitors.* Chinese Chemical Letters, 2021. **32**(4): p. 1491-1496.
333. Abazari, R., et al., *Ultrafast post-synthetic modification of a pillared cobalt (II)-based metal–organic framework via sulfurization of its pores for high-performance supercapacitors.* Journal of Materials Chemistry A, 2019. **7**(19): p. 11953-11966.
334. Yan, Z.S., et al., *One-step synthesis of Mn_S/MoS_2/C through the calcination and sulfurization of a bi-metal–organic framework for a high-performance supercapacitor and its photocurrent investigation.* Dalton Transactions, 2018. **47**(15): p. 5390-5405.
335. Peng, W., et al., *Two-dimensional MoS_2/Mn-MOF/multi-walled carbon nanotubes composite material for high-performance supercapacitors.* Microchemical Journal, 2022. **179**: p. 107506.
336. Liu, C., et al., *In Situ Growth of Three‐Dimensional MXene/Metal‐Organic Framework Composites for High‐Performance Supercapacitors.* Angewandte Chemie, 2022. **134**(11): p. e202116282.
337. Dummert, S.V., et al., *Cyclodextrin metal–organic frameworks and derivatives: recent developments and applications.* Chemical Society Reviews, 2022.
338. Su, Q., et al., *Heterojunction Photocatalysts Based on 2D Materials: The Role of Configuration.* Advanced Sustainable Systems, 2020. **4**(9): p. 2000130.
339. Zheng, S.Q., et al., *Fabrication of sodium and MoS_2 incorporated NiO and carbon nanostructures for advanced supercapacitor application.* Journal of Energy Storage, 2023. **63**: p. 106980.
340. Yue, L., et al., *Ni-MOF coating MoS_2 structures by hydrothermal intercalation as high-performance electrodes for asymmetric supercapacitors.* Chemical Engineering Journal, 2019. **375**: p. 121959.
341. Zhang, L., et al., *High‐Performance Electrochemical NO Reduction into NH_3 by MoS_2 Nanosheet.* Angewandte Chemie, 2021. **133**(48): p. 25467-25472.
342. Chang, H., et al., *CO_2-Induced 2D Ni-BDC Metal–Organic Frameworks with Enhanced Photocatalytic CO_2 Reduction Activity.* Advanced Materials Interfaces, 2021. **8**(13): p. 2100205.
343. Liu, X., et al., *A Simple Ni-based Metal–organic Framework as Catalyst for Dye-sensitized Photocatalytic H_2 Evolution from Water Reduction.* Photochemistry and Photobiology, 2020. **96**(6): p. 1169-1175.
344. Yang, W., et al., *$MoS_2/Ni(OH)_2$ composites derived from in situ grown Ni-MOF coating MoS_2 as electrode materials for supercapacitor and electrochemical sensor.* Colloids and Surfaces A: Physicochemical and Engineering Aspects, 2021. **615**: p. 126178.

345. Dai, J., et al., *Effect of morphology and phase engineering of MoS_2 on electrochemical properties of carbon nanotube/polyaniline@MoS_2 composites.* Journal of Colloid and Interface Science, 2021. **590**: p. 591-600.
346. Gautam, C., et al., *Development of 2D based ZnO–MoS_2 nanocomposite for photodetector with light-induced current study.* Optical Materials, 2022. **123**: p. 111860.
347. Kite, S.V., et al., *Nanostructured TiO_2 Sensitized with MoS_2 Nanoflowers for Enhanced Photodegradation Efficiency toward Methyl Orange.* ACS Omega, 2021. **6**(26): p. 17071-17085.
348. Kanaujiya, N., et al., *Probing the Electrochemical Properties of Flower Like Mesoporous MoS_2 in Different Aqueous Electrolytes.* Journal of Electronic Materials, 2019. **48**(2): p. 904-915.
349. Zhang, S., et al., *Atomically Thin Arsenene and Antimonene: Semimetal–Semiconductor and Indirect–Direct Band-Gap Transitions.* Angewandte Chemie International Edition, 2015. **54**(10): p. 3112-3115.
350. Xu, J., et al., *NiO-rGO composite for supercapacitor electrode.* Surfaces and Interfaces, 2020. **18**: p. 100420.
351. Yao, B., et al., *3D-Printed Structure Boosts the Kinetics and Intrinsic Capacitance of Pseudocapacitive Graphene Aerogels.* Advanced Materials, 2020. **32**(8): p. 1906652.
352. Su, D., et al., *Electrospun Na doped Li_2TiSiO_5/C nanofibers with outstanding lithium-storage performance.* Applied Surface Science, 2021. **541**: p. 148388.
353. Lata Singh, D., et al., *Hydrothermal Synthesis and Symmetrical Supercapacitor Study of 1D Ln-H_2PDA (Ln=La and Sm) Metal-Organic Frameworks.* ChemistrySelect, 2022. **7**(26): p. e202202076.
354. Ping, Y., et al., *N-self-doped graphitic carbon aerogels derived from metal–organic frameworks as supercapacitor electrode materials with high-performance.* Electrochimica Acta, 2021. **380**: p. 138237.
355. Zou, J., et al., *Ultrahigh-content nitrogen-decorated nanoporous carbon derived from metal organic frameworks and its application in supercapacitors.* Electrochimica Acta, 2018. **271**: p. 599-607.
356. Majumder, M., et al., *Aluminum based metal-organic framework integrated with reduced graphene oxide for improved supercapacitive performance.* Electrochimica Acta, 2020. **353**: p. 136609.
357. Shi, X., et al., *Three dimensional graphene/carbonized metal-organic frameworks based high-performance supercapacitor.* Carbon, 2020. **157**: p. 55-63.
358. Lv, S., et al., *One-step copper-catalyzed synthesis of porous carbon nanotubes for high-performance supercapacitors.* Microporous and Mesoporous Materials, 2021. **310**: p. 110670.
359. Dhakal, G., et al., *High-performance supercapacitors fabricated with activated carbon derived from lotus calyx biowaste.* Renewable Energy, 2022. **189**: p. 587-600.
360. Cheng, J., et al., *Green needle coke-derived porous carbon for high-performance symmetric supercapacitor.* Journal of Power Sources, 2021. **494**: p. 229770.
361. Shang, Z., et al., *Houttuynia-derived nitrogen-doped hierarchically porous carbon for high-performance supercapacitor.* Carbon, 2020. **161**: p. 62-70.
362. Dhakal, G., et al., *Litchi seed biowaste-derived activated carbon supporting matrix for efficient symmetric and asymmetric supercapacitors.* Carbon, 2023. **208**: p. 277-289.

363. Dong, X., et al., *Sandwich-like honeycomb Co_2SiO_4/rGO/honeycomb Co_2SiO_4 structures with enhanced electrochemical properties for high-performance hybrid supercapacitor.* Journal of Power Sources, 2021. **492**: p. 229643.
364. Wang, P., et al., *Ammonium vanadium oxide framework with stable NH_4^+ aqueous storage for flexible quasi-solid-state supercapacitor.* Chemical Engineering Journal, 2022. **427**: p. 131548.
365. Majumdar, D., M. Mandal, and S.K. Bhattacharya, *Journey from supercapacitors to supercapatteries: recent advancements in electrochemical energy storage systems.* Emergent Materials, 2020. **3**(3): p. 347-367.
366. He, Y., et al., *Capacitive mechanism of oxygen functional groups on carbon surface in supercapacitors.* Electrochimica Acta, 2018. **282**: p. 618-625.
367. Ansarinejad, H., M. Shabani-Nooshabadi, and S.M. Ghoreishi, *Enhanced Supercapacitor Performance Using a Co_3O_4@Co_3S_4 Nanocomposite on Reduced Graphene Oxide/Ni Foam Electrodes.* Chemistry, an Asian journal, 2021. **16**(10): p. 1258-1270.
368. Tian, Y., et al., *Microwave synthesis of MoS_2/MoO_2@CNT nanocomposites with excellent cycling stability for supercapacitor electrodes.* Journal of Materials Chemistry C, 2019. **7**(31): p. 9545-9555.
369. Manjakkal, L., et al., *A Wearable Supercapacitor Based on Conductive PEDOT:PSS-Coated Cloth and a Sweat Electrolyte.* Advanced Materials, 2020. **32**(24): p. 1907254.
370. Xu, C., et al., *Waste activated carbon transformed to electrode of supercapacitor through combining with $Co(OH)_2$.* Electrochimica Acta, 2021. **367**: p. 137475.
371. Galimzyanov, R.R., et al., *Electrolyte mixture based on acetonitrile and ethyl acetate for a wide temperature range performance of the supercapacitors.* Journal of Power Sources, 2021. **495**: p. 229442.
372. Ali, G.A.M., et al., *Ferrocene functionalized multi-walled carbon nanotubes as supercapacitor electrodes.* Journal of Molecular Liquids, 2020. **318**: p. 114064.
373. Zhang, C., et al., *Ultrahigh-Rate Supercapacitor Based on Carbon Nano-Onion/Graphene Hybrid Structure toward Compact Alternating Current Filter.* Advanced Energy Materials, 2020. **10**(43): p. 2002132.
374. Sundriyal, S., et al., *Surface and diffusion charge contribution study of neem leaves derived porous carbon electrode for supercapacitor applications using acidic, basic, and neutral electrolytes.* Journal of Energy Storage, 2021. **41**: p. 103000.
375. Kumar, R. and M. Bag, *Hybrid Halide Perovskite-Based Electrochemical Supercapacitors: Recent Progress and Perspective.* Energy Technology, 2022. **10**(3): p. 2100889.
376. Manikandan, M., et al., *Hydrothermal synthesis of cobalt telluride nanorods for a high performance hybrid asymmetric supercapacitor.* RSC Advances, 2020. **10**(23): p. 13632-13641.
377. Sun, J., et al., *One-Dimensional Nanostructured Pseudocapacitive Materials: Design, Synthesis and Applications in Supercapacitors.* Batteries & Supercaps, 2019. **2**(10): p. 820-841.
378. Dhas, S.D., et al., *Synthesis of NiO nanoparticles for supercapacitor application as an efficient electrode material.* Vacuum, 2020. **181**: p. 109646.
379. Rahman, M.A., R. Radhakrishnan, and R. Gopalakrishnan, *Structural, optical, magnetic and antibacterial properties of Nd doped NiO nanoparticles prepared by co-precipitation method.* Journal of Alloys and Compounds, 2018. **742**: p. 421-429.

380. Li, N., et al., *NiO nanoparticles decorated hexagonal Nickel-based metal-organic framework: Self-template synthesis and its application in electrochemical energy storage.* Journal of Colloid and Interface Science, 2021. **581**: p. 709-718.
381. Mao, H., et al., *Structure-activity relationship toward electrocatalytic nitrogen reduction of MoS_2 growing on polypyrrole/graphene oxide affected by pyridinium-type ionic liquids.* Chemical Engineering Journal, 2021. **425**: p. 131769.
382. Patel, K.N., et al., *Effect of Mn doping concentration on structural, vibrational and magnetic properties of NiO nanoparticles.* Advanced Powder Technology, 2018. **29**(10): p. 2394-2403.
383. Lalithambika, K.C., K. Shanmugapriya, and S. Sriram, *Photocatalytic activity of MoS_2 nanoparticles: an experimental and DFT analysis.* Applied Physics A, 2019. **125**(12): p. 817.
384. Koventhan, C., et al., *Efficient hydrothermal synthesis of flake-like molybdenum disulfide for selective electrochemical detection of metol in water real samples.* International Journal of Electrochemical Science, 2020. **15**: p. 7390-7406.
385. Ali, G.A.M., et al., *One-step electrochemical synthesis of MoS_2/graphene composite for supercapacitor application.* Journal of Solid State Electrochemistry, 2020. **24**(1): p. 25-34.
386. Huang, C., et al., *Boosting the energy density of supercapacitors by designing both hollow NiO nanoparticles/nitrogen-doped carbon cathode and nitrogen-doped carbon anode from the same precursor.* Chemical Engineering Journal, 2022. **431**: p. 134083.
387. Xu, X., et al., *Synergistic lubrication of a porous MoS_2-POSS nanohybrid.* RSC Advances, 2020. **10**(35): p. 20579-20587.
388. Chen, Q., et al., *3D Hierarchical N, O Co–Doped MoS_2/NiO Hollow Microspheres as Reusable Catalyst for Nitrophenols Reduction.* ChemistrySelect, 2019. **4**(32): p. 9339-9347.
389. Atacan, K., N. Güy, and M. Özacar, *Preparation of gold decorated MoS_2/NiO nanocomposite in the production of a new electrochemical sensor for ascorbic acid detection.* Korean Journal of Chemical Engineering, 2022. **39**(8): p. 2172-2181.
390. Ahmed, R. and G. Nabi, *Enhanced Electrochemical Performance of Cr-doped NiO Nanorods for Supercapacitor Application.* Journal of Energy Storage, 2021. **33**: p. 102115.
391. Barzegar, F., et al., *Investigation of different aqueous electrolytes on the electrochemical performance of activated carbon-based supercapacitors.* RSC advances, 2015. **5**(130): p. 107482-107487.
392. Askari, M.B., et al., *$ZnFe_2O_4$ nanorods on reduced graphene oxide as advanced supercapacitor electrodes.* Journal of Alloys and Compounds, 2021. **860**: p. 158497.
393. Xue, J., et al., *N-doped two-dimensional ultrathin NiO nanosheets for electrochromic supercapacitor.* Journal of Materials Science: Materials in Electronics, 2020. **31**(22): p. 20611-20619.
394. Yang, K., et al., *Yolk-shell bimetallic metal-organic frameworks derived multilayer core-shells $NiCo_2O_4$/NiO structure spheres for high-performance supercapacitor.* Journal of Electroanalytical Chemistry, 2019. **851**: p. 113445.
395. Wu, M.K., et al., *MOF–derived hollow double–shelled NiO nanospheres for high–performance supercapacitors.* Journal of Alloys and Compounds, 2018. **734**: p. 1-8.
396. Riyas, Z.M., et al., *Synergistic effect of La_2O_3 -NiO nanocomposite based electrode for electrochemical high-performance asymmetric supercapacitor applications.* Journal of Energy Storage, 2022. **53**: p. 104988.

397. Zheng, Y., et al., *One-step microwave synthesis of NiO/NiS@CNT nanocomposites for high-cycling-stability supercapacitors.* Journal of Alloys and Compounds, 2019. **806**: p. 170-179.
398. Zhang, Z., et al., *Ni-MOF derived NiO/C nanospheres grown in situ on reduced graphene oxide towards high performance hybrid supercapacitor.* Journal of Alloys and Compounds, 2019. **801**: p. 158-165.
399. Zhao, X., et al., *MnO_2@NiO nanosheets@nanowires hierarchical structures with enhanced supercapacitive properties.* Journal of Materials Science, 2020. **55**(6): p. 2482-2491.
400. Yin, X., et al., *Multilayer NiO@Co_3O_4@graphene quantum dots hollow spheres for high-performance lithium-ion batteries and supercapacitors.* Journal of Materials Chemistry A, 2019. **7**(13): p. 7800-7814.
401. Sharma, V., I. Singh, and A. Chandra, *Hollow nanostructures of metal oxides as next generation electrode materials for supercapacitors.* Scientific Reports, 2018. **8**(1): p. 1307.
402. Kumar, R., et al., *Synthesis of porous electrode from $CH_3NH_3PbBr_3$ single crystal for efficient supercapacitor application: Role of morphology on the charge storage and stability.* Electrochimica Acta, 2021. **398**: p. 139344.
403. Tanwar, S., N. Singh, and A.L. Sharma, *Structural and electrochemical performance of carbon coated molybdenum selenide nanocomposite for supercapacitor applications.* Journal of Energy Storage, 2022. **45**: p. 103797.
404. Schoetz, T., et al., *Disentangling faradaic, pseudocapacitive, and capacitive charge storage: A tutorial for the characterization of batteries, supercapacitors, and hybrid systems.* Electrochimica Acta, 2022. **412**: p. 140072.
405. Shrivastav, V., et al., *Conductive and porous ZIF-67/PEDOT hybrid composite as superior electrode for all-solid-state symmetrical supercapacitors.* Journal of Alloys and Compounds, 2020. **843**: p. 155992.
406. Wang, T., et al., *Boosting the cycling stability of transition metal compounds-based supercapacitors.* Energy Storage Materials, 2019. **16**: p. 545-573.
407. Yan, L., et al., *Modulating the electronic structure and pseudocapacitance of δ-MnO_2 through transitional metal M (M = Fe, Co and Ni) doping.* Electrochimica Acta, 2019. **306**: p. 529-540.
408. Delbari, S.A., et al., *Transition metal oxide-based electrode materials for flexible supercapacitors: A review.* Journal of Alloys and Compounds, 2021. **857**: p. 158281.
409. Teli, A.M., et al., *Bismuth manganese oxide based electrodes for asymmetric coin cell supercapacitor.* Chemical Engineering Journal, 2022. **430**: p. 133138.
410. Ma, Y., et al., *High energy density and extremely stable supercapacitors based on carbon aerogels with 100% capacitance retention up to 65,000 cycles.* Proceedings of the National Academy of Sciences, 2021. **118**(21): p. e2105610118.
411. Le, Q.B., et al., *Effect of PANI and PPy on Electrochemical Performance of rGO/$ZnMn_2O_4$ Aerogels as Electrodes for Supercapacitors.* Journal of Electronic Materials, 2020. **49**(8): p. 4697-4706.
412. Bhattacharya, G., et al., *Novel π-conjugated iron oxide/reduced graphene oxide nanocomposites for high performance electrochemical supercapacitors.* RSC Advances, 2017. **7**(1): p. 327-335.

413. Zhu, Y., et al., *Ultrathin Nickel Hydroxide and Oxide Nanosheets: Synthesis, Characterizations and Excellent Supercapacitor Performances.* Scientific Reports, 2014. **4**(1): p. 5787.
414. Panda, P., R. Mishra, and S. Barman, *In-situ nano-engineering of amorphous MoS_2 nanosheets with carbon dots for enhanced supercapacitor performances.* International Journal of Energy Research, 2022. **46**(12): p. 17576-17589.
415. Wang, K., et al., *General solution-processed formation of porous transition-metal oxides on exfoliated molybdenum disulfides for high-performance asymmetric supercapacitors.* Journal of Materials Chemistry A, 2017. **5**(22): p. 11236-11245.
416. Wei, S., R. Zhou, and G. Wang, *Enhanced Electrochemical Performance of Self-Assembled Nanoflowers of MoS_2 Nanosheets as Supercapacitor Electrode Materials.* ACS Omega, 2019. **4**(14): p. 15780-15788.
417. Sun, J., et al., *Solvent-Controlled Morphology of Amino-Functionalized Bimetal Metal–Organic Frameworks for Asymmetric Supercapacitors.* Inorganic Chemistry, 2020. **59**(16): p. 11385-11395.
418. Ghosh, S., et al., *A cobalt(II) metal-organic framework featuring supercapacitor application.* Journal of Solid State Chemistry, 2020. **282**: p. 121093.
419. Wang, G., et al., *NiO/Ni Metal–Organic Framework Nanostructures for Asymmetric Supercapacitors.* ACS Applied Nano Materials, 2021. **4**(9): p. 9034-9043.
420. Zhong, Y., et al., *Homogeneous nickel metal-organic framework microspheres on reduced graphene oxide as novel electrode material for supercapacitors with outstanding performance.* Journal of Colloid and Interface Science, 2020. **561**: p. 265-274.
421. Azadfalah, M., et al., *Cobalt based Metal Organic Framework/Graphene nanocomposite as high performance battery-type electrode materials for asymmetric Supercapacitors.* Journal of Energy Storage, 2021. **33**: p. 101925.
422. Zhang, J., et al., *Constructing ultra-thin Ni-MOF@NiS_2 nanosheets arrays derived from metal organic frameworks for advanced all-solid-state asymmetric supercapacitor.* Materials Research Bulletin, 2021. **137**: p. 111186.
423. Du, Y., et al., *High-performance quasi-solid-state flexible supercapacitors based on a flower-like NiCo metal–organic framework.* RSC Advances, 2022. **12**(10): p. 5910-5918.